Attrition and Phase Changes during Agitated Filter Bed Drying

by

Wei Pin Goh

Submitted in accordance with the requirements for the degree of

Doctor of Philosophy

The University of Leeds

School of Chemical and Process Engineering

April 2019

The candidate confirms that the work submitted is their own, except where work which has formed part of jointly authored publications has been included. The contribution of the candidate and the other authors to this work has been explicitly indicated below. The candidate confirms that appropriate credit has been given within the thesis where reference has been made to the work of others.

Chapter 6 of this thesis has been prepared and will be submitted in the Journal International Journal of Pharmaceutics. The numerical simulation work based on CFD is the work of Dr Muzammil Ali. The other co-authors have had a supervisory role.

Acknowledgement

First of all, I am grateful and would like to express my deep sense of thanks and sincere gratitude to my supervisor, Professor Mojtaba Ghadiri for giving me the opportunity to embark on a research journey and his constant dedication and keen enthusiasm in supervising my work. This thesis would not have been possible without his timely advice and guidance. I am also indebted to my co-supervisor, Professor Frans Muller and previous co-supervisor, Dr Colin Hare for their sincere and valuable guidance and encouragement extended to me. Their support and advice have been invaluable on both an academic and a personal level, for which I am truly grateful.

I would like to express my appreciation to the technical and financial support of my sponsor, AbbVie Inc., Chicago, USA, particularly for the award of a research studentship that provided the necessary financial support for this research. My thanks also go to my industrial supervisors, Dr Nandkishor Nere, Dr Raimundo Ho, Dr Kushal Sinha, Dr Shailendra Bordawekar and Dr Ahmad Sheikh. I am thankful to the University of Leeds for the facilities and equipment provided, without which the experimental works would not have been possible. My gratitude also extends to Professor Bill Jones of University of Cambridge and Dr Jerry Heng from Imperial College London for their valuable suggestions towards this work. My gratitude also goes to Dr Grabriela Schneider Rauber for her constant encouragement and emotional supports throughout this voyage of research.

I am eternally grateful to my parents, Mr Ewe Tong Goh and Ms Ah Geck Teh, for the tremendous financial support they have provided me over these years in allowing

me to pursue my first degree abroad. I would also like to thank my parents and family members for all the moral support and encouragement.

I would like to take this opportunity to acknowledge and thank all the members in Ghadiri Research Group for making me feel welcomed. I really value for all the help and encouragement that they give during my research pursuit.

Last but not least, my thanks also go to all those who have helped me directly or indirectly in completion of this thesis.

Abstract

Active pharmaceutical ingredients (API) and excipients are normally present in crystal form, obtained by crystallisation, followed by filtration and drying. Filter bed drying is the unit operation of choice in the pharmaceutical industry, where the crystal suspension is first filtered, washed and then dried. Heat is applied to the filtered bed of crystals and agitated to promote heat transfer, and homogeneous moisture and temperature distributions as the bed dries. The agitation induces shear stresses within the bed, which can cause undesirable particle attrition and polymorphic transformations.

This thesis mainly addresses the research conducted in understanding the polymorphic phase transformation of carbamazepine dihydrate crystals and their breakage behaviour during agitated filter bed drying process. The coupled effect of thermal and mechanical stresses is isolated and studied. The dehydration and rehydration of the model crystals due to thermal and relative humidity gradients are studied under well controlled environmental conditions. The ramping rate of humidity is found to have some interesting effect of the water sorption capacity of the crystals.

The presence of cleavage planes in the acicular crystals or carbamazepine are investigated and related to their breakage behaviour due to impact using a novel aerodynamic dispersion method. Using this new approach, the breakability index of carbamazepine dihydrate crystals is determined. A new agitated filter bed test rig is developed to study the effect of process parameters on the breakage behaviour of the crystals. The breakage data correlates well with the input energy supply to the particle bed through impeller blade rotation. Rocky software based on Discrete Element Method

(DEM) is used to study the effect of particle shape on the particle dynamics as well as the stress and strain distributions in an agitated bed.

Table of Contents

List of Figures

List of Tables

Nomenclature

Latin Characters	*Definition*	*Unit*
A	Projected area	m^2
A_d	Projected area of debris	m^2
A_f	Projected area of feed particles	m^2
AR	Aspect ratio	-
B	Particle size distribution of interest	-
B_{ref}	Reference particle size distribution	-
d_T	Initial size	m
D_V	Square equivalent side length (volumetric)	m
E^*	Reduced modulus	Pa
E_a	Activation energy	kJ/mol
f_{mat}	Material parameter	-
F_{fr}	Fracture force	N
F_n	Contact force	N
G	Size distribution modulus	-
H	Hardness	Pa
j	Bin number	-
k_n	Contact stiffness	
K_C	Fracture toughness	$Pa.m^{0.5}$
K_G	Attrition constant in Gwyn equation	-
K_N	Attrition constant in Neil and Bridgwater model	-

K_O	Empirical fitting constant in Ouwerkerk model	-
l	Characteristic particle size	M
L_V	Particle length (volumetric)	M
m	Measure of spread of strength	M
m_G	Attrition constant in Gwyn equation	-
M_d	Mass of debris	kg
M_f	Mass of feed	kg
R	Radius	M
R^*	Extent of breakage	-
S	Difference in area percentage of bin number j	%
T	Temperature	K
U	Normal impact velocity	m/s
V_d	Particle volume of debris	m^3
V_f	Particle volume of feed	m^3
W_k	Mass-specific kinetic impact energy	$kg.m^2/s^2$
$W_{k,\min}$	Mass-specific threshold energy	$kg.m^2/s^2$
W_T	Mass passing size d_T	g
W_V	Particle Width (volumetric)	m
W	Extent of breakage	%

Greek Characters	***Definition***	***Unit***
α	Proportionality constant	-
α_o	Empirical fitting constant in Ouwerkerk model	-
β	Breakability index	-

β_N	Attrition constant	
ρ	Particle density	kg.m^3
Γ	Strain	-
ϕ	Volume fraction of particles	-
σ_1	Principal stress 1	Pa
σ_2	Principal stress 2	Pa
σ_3	Principal stress 3	Pa
σ_D	Deviatoric stress	Pa
σ_H	Hydrostatic stress	Pa
σ_S	Strength	Pa
σ_{scs}	Side crushing strength	Pa
σ_{ref}	Reference stress level	Pa
$\tau_{\max}$	Maximum shear stress	Pa
φ	Attrition constant in Neil and Bridgwater model	°
θ	Incident angle	kg/m^3

Chapter 1

Introduction

1.1 Attrition and Phase Changes during Agitated Drying

Crystalline solids may exist as different structures or polymorphs depending on environmental and stressing conditions they experience. Polymorphic transformations of active pharmaceutical ingredients (API) alter their mechanical, chemical, thermal and physical properties which could influence the API's stability and bioavailability. Filter bed drying is the unit operation of choice in the pharmaceutical industry for isolation of API after crystallisation. A typical agitated filter bed dryer comprises of an impeller which intermittently agitates to promote homogenous distribution of moisture and temperature throughout the bed during drying. Shear stresses induced by the impeller, together with the heat supplied to the filter bed dryer could lead to undesirable particle attrition and polymorphic transformation.

Attrition of particles in the filter bed dryer is closely related to the dynamics of the particle bed. Bagster and Bridgwater (1970) conducted a study on material flow in an agitated dryer and found that the dynamics of the bed is influenced by different process properties such as blade height, blade angle and bed height. Particle breakage could arise from both impact and shearing of bulk material, of which the latter is the dominant cause of particle attrition in filter bed dryer. Impact breakage due to particle to particle collisions

or particle to other mechanical parts in the filter bed dryer can be characterised and analysed using the single particle impact tester, first used by Yuregir *et al.* (1986). The agitating impeller induces breakage and shear deformation as the impeller blade pushes the particles forward, forming a heap before falling back behind the blade. To study bulk shear deformation, various shear cells were initially designed to study flow problems in bunker or hopper (Jenike, 1961; Walker, 1967; Carr and Walker, 1968), but Paramanathan and Bridgwater (1983) later developed a special one to study the mechanism of attrition in a defined failure zone such that the stress, strain and rate of strain are well controlled.

Polymorphic transformation or polymorphism of API during drug development is of paramount importance in the pharmaceutical industry. Transformation of one crystal structure to another could lead to the alteration of the physical and chemical properties of an API. This could have catastrophic consequences towards the formulated products as one polymorph may have lower bioavailability than another and this will seriously compromise the efficacy and drug delivery of the API. Polymorphic transformation is dependent on the environmental factors such as humidity and temperature (Otsuka *et al.*, 1986; Otsuka *et al.*, 1999). Studies of solid state transformation during milling are very well reported in literature (Willart *et al.*, 2001; 2005; 2007; Desprez & Descamps, 2006). Studies on polymorphism during drying however are very limited (Lee et al., 2011; Yu and Ng, 2002). This research therefore aims to fill this gap and to address the effect of the stress-induced transformation, incorporating the breakage that follows, towards the polymorphism of API in filter bed drying.

1.2 Aim and Objectives of the Research

The aim of this work is to develop a new method for assessing the extent of attrition as well as the phase changes and polymorphic transformations of API subjected to filter bed drying. This involves the use of both experimental and simulation work. The objectives of the thesis are as below:

i. Understand the effect mechanical stresses on the phase transformation of API.

ii. Analyse the dehydration and rehydration of a hydrate crystals due to the surrounding temperature and relative humidity.

iii. Analyse the breakage behaviour of acicular crystals and associate that with their crystal structure.

iv. Develop a method to predict the breakage of acicular crystals due to impact

v. Develop a lab-scale agitated filter bed dryer to study the effect of process parameters on the breakage of crystals.

vi. Study the effect of particle shape on the particle dynamics as well as the stress and strain distributions within an agitated filter bed dryer.

1.3 Structure of Report

The main research topic of this thesis concerns the attrition and phase changes of a pharmaceutical crystals during agitated filter bed drying, which is a unit operation of choice in the pharmaceutical industry for isolation of crystals from the mother liquor. The model compound studied in this thesis is the carbamazepine dihydrate, which is the active ingredient of a common anticonvulsant medication used for treating epileptic seizure. A series of initial characterisation of the material properties were performed and the results provided inputs to the other research areas addressed in this thesis. During agitated filter bed dryer, both the heat applied and the mechanical agitation induced by the rotating impeller impose stresses to the particles within the system. These stresses could both contribute to the phase transformation of the model compound studied in this thesis. Hence, the very first research area addressed in this thesis involved investigating the effect of mechanical (by subjecting the crystals to different stresses such as impact and compaction) and thermal stresses on the phase transformation of the model compound, as well as determining if there exists a coupled effect between these stresses. Being a hydrate, the model compound is prone to dehydration. The rate of crystal water loss as a function of temperature is studied. During agitated filter bed drying, dry gas is often supplied to the system to facilitate the drying of the wet cake. The relative humidity plays an important role in the phase changes of the model compound and is addressed through a series dehydration studies under controlled ambience.

Apart from the phase changes, the other focus of this thesis is on the attrition of the model compound as a result of the shear induced by the rotating impeller. The tendency of a particle to break is governed by its material properties. The ratio of the hardness and fracture toughness give a measure of the breakability of the material. A new impact-based approach is developed to determine the breakability of acicular crystals and to address the role of crystal structure in the breakage behaviour of the material. A

miniaturised agitated filter bed dryer unit was developed subsequently to simulate the agitation process. The breakage of the model as a result of different process conditions was characterised. Numerical simulation using Discrete Element Method (DEM) was performed to quantify the stress and strain distributions within an agitated bed, which are too difficult to obtain experimentally. The research areas detailed above are formulated into several separate chapters as shown below.

Chapter 1 gives a brief introduction of the thesis and the aim and objectives of this research work.

In chapter 2, review of the literature is documented, focusing on the particle breakage and phase transformation in an agitated filter bed drying. Particle breakage in an agitated dryer is caused by a combination of shear and impact. Different models to describe both impact breakage and shear breakage are reviewed here. In addition, an overview of Distinct Element Method (DEM) is given which summarises different contact models. Polymorphic Transformation of APIs could result in different polymorphic forms and is dependent on environmental factors such as temperature and moisture content. This is addressed in this chapter as well.

The summary of the material properties is documented in Chapter 3, concerning the characterisation of physical and mechanical properties of the study material used.

Chapter 4 aims to dissect the effect of thermal and mechanical stresses on the phase transformation of the model API.

A comprehensive study on the dehydration and rehydration of the model API under well-controlled temperature and humidity is discussed and that is documented in Chapter 5.

Chapter 6 relates the impact breakage behaviour of the model API to its crystal structure. A model is proposed to describe the impact breakage data obtained from a commercial particle size analyser, giving a measure of the breakability of the model API.

Chapter 7 covers the details of the development of a lab-scale agitated filter bed dryer test rig with an industrial partner. The newly developed test rig is used to study the effect of process conditions on breakage of the model API.

The simulations of agitated filter bed dryer by DEM, concerning the effect of particle shape and process conditions on the stress and strain distribution in the particle bed can be found in Chapter 8.

The conclusions of the thesis and future research recommended is summarised in Chapter 9.

Chapter 2

Literature Review

2.1 Particle Breakage and Attrition

2.1.1 Attrition in Agitated Dryer

Agitated drying of API is known to be a complicated process. Particle agglomeration or attrition are very common problems that occur during agitated drying and the tendency of API to undergo polymorphic transformation complicates the process even more. Normally, about 10-20% of moisture content is retained after filtration. Initially particle attrition is low and often negligible due to the presence of the solvent retained in the particle bed forming liquid bridges between the particles that reduces the frictional contact of particles to the impeller blade. As the particle bed dries, down until a critical moisture level (1.5 – 2%), particle breakage starts to increase and agglomerates are formed (Lekhal *et al.*, 2003; 2004). Although impact breakage is present in the dryer due to particle-particle and particle-mechanical component collision, breakage as a result of shearing of the particle bed (Neil and Bridgwater, 1994) is more pronounced and dominant, hence rendering the former negligible.

Attrition and agglomeration are constantly competing with each other during drying. There are many process parameters that could alter the behaviour of the particle bed in terms of particle breakage and agglomeration. Previous studies have shown that the final crystal properties are affected by process parameters such as agitation rate,

temperature and pressure (Lekhal *et al.*, 2003; 2004). Low drying rate and/or high shear rate tends to promote particle breakage, while agglomeration is dominant at high drying rate and/or low shear rate. Agglomeration during drying is found to affect the drying kinetics especially in those APIs which are capable of forming hydrates (Khoo *et al.*, 2010). One key thing that has to be taken into consideration when assessing the particle breakage in a lab scale dryer is the validity to scale up to industrial pilot scale. A recent study (Remy *et al.*, 2015) has proposed the importance of reproducing the range of hydrostatic pressures during scale-up drying process when conducting lab scale experiments.

2.1.2 Shear Failure

2.1.2.1 Attrition in Annular Shear Cell

Annular shear cell was first developed by Paramanathan and Bridgwater (1983) to study attrition in a shear band. Gwyn equation (1969) was initially developed to describe the attrition of catalysts in a fluidised bed and since then was used commonly as the base model in describing attrition in different contexts.

$$W = K_G t^{m_G} \tag{2-1}$$

where W is the extent of breakage, K_G and m_G are both attrition constants and t is time.

An improved model was developed by Neil (1986) to address the lack of stress component in Gwyn model. It was found experimentally that in some cases the extent of breakage increases with applied normal stress (Jørgensen *et al.*, 2005). The model developed by Neil assumes a fraction of the stress applied to the bed contributes to particle breakage.

$$W = K_N \left[\left(\frac{\sigma}{\sigma_{scs}} \right) \Gamma^{\varphi} \right]^{\beta} \tag{2-2}$$

where K_N, φ, and β_N are the attrition constants, σ_{scs} is the side crushing strength of the material and Γ is the shear strain. Schuhmann's (1940) model was found to correlate well with the size distribution of the breakage products (Neil and Bridgwater, 1994).

$$W = W_T \left(\frac{d}{d_T} \right)^G \tag{2-3}$$

where d_T is the initial size, W_T is the mass passing size d_T and G is the size distribution modulus. This model (Eq. 2-3) uses only one single value to describe the particle strength while in reality there exists a distribution of particle strength. Ouwerkerk (1991) proposed an alternative approach that incorporates the effect of stress and shear strain and found that the width of single particle crushing strength distribution actually influences the amount of breakage.

$$W = K_O \left[\left(\frac{\sigma}{\sigma_{ref}} \right)^2 \Gamma \right]^{\alpha_O} \tag{2-4}$$

where K_O and α_O are empirical fitting constants and σ_{ref} is the reference stress level. However, it is worth noting that Eq. 2-4 refers to a case of Neil's model in which the φ is assumed to be 0.5, hence giving less flexibility in comparison. Ghadiri *et al.* (2000) conducted a comprehensive study on the effect of shear toward attrition using porous silica catalyst carrier beads. Different breakage attrition models were tested in that study and it was found that both Ouwerkerk (1991) and Neil & Bridgwater (1994) models describe attrition data best when considering only fine debris. Attrition data which included bigger attrition products caused by fragmentation did not correlate well, hence suggesting that these models were suited better to describe surface damage rather than fragmentation.

2.1.3 Impact Breakage

2.1.3.1 Brittle Failure

In brittle failure, plastic deformation is not apparent before fracture takes place. Presence of pre-existing or surface flaws play an important role in affecting the strength and particle breakage. However, without the knowledge of the size, number, and position of these flaws, the only way to characterise the breakage is by empirical models. One common approach to fit the empirical data for this failure mode is based on Weibull analysis (Weibull, 1951) where the probability of breakage, S, is a function of applied stress, σ, characteristic flaw density, z, strength, σ_s and measure of spread of strength, m.

$$S = 1 - \exp\left[- z \left(\frac{\sigma}{\sigma_S} \right)^m \right] \tag{2-5}$$

In order to take material properties into consideration, Vogel & Peukert (2003) introduced two material parameters, f_{mat} and W_k into the equation above to describe impact grinding performance independently.

$$S = 1 - \exp\left[- f_{mat} x \left(W_k - W_{k,\min} \right) \right] \tag{2-6}$$

where f_{mat} reflects the material parameter, x is the initial particle size, W_k is the mass-specific kinetic impact energy and $W_{k,\min}$ is the mass-specific threshold energy for particle breakage.

2.1.3.2 Semi-Brittle Failure

In semi-brittle failure, plastic deformation takes precedence over crack propagation as plastic yield is reached. Fracture mechanics describes this failure mode successfully and it is governed by material mechanical properties such as Young's Modulus, E, Hardness, H, yield stress, σ_y, and fracture toughness, K_c.

Chipping

A mechanistic model has been developed by Ghadiri and Zhang (2002) to describe impact attrition of particulate solids in this failure mode. The model relates the extent of breakage to the material properties and impact condition.

$$R^* = \alpha \frac{\rho v^2 l H}{K_c^2} \tag{2-7}$$

where R^* is the extent of breakage, α is a proportionality constant ρ is the density of particle, v is the impact velocity, l is a characteristic particle size, H is the hardness and K_c is the facture toughness.

Fragmentation

There is no theory to predict the particle size distribution due to impact at the moment. However, the fracture force to fragment a sphere with diameter D can be estimated based on indentation fracture mechanics as proposed by Ghadiri and Zhang (2002) for crack extension.

$$F_{fr} \propto K_c^{\frac{4}{3}} D^{\frac{4}{3}} H^{\frac{-1}{3}} \tag{2-8}$$

Transition Velocity

Two important aspects of impact breakage are the plastic deformation to chipping and chipping to fragmentation transition velocities (Ghadiri, 2006). The critical plastic deformation to chipping transition velocity for round or relatively flat contact between a particle and target is defined as

$$V_{ch} \propto \left(\frac{K_C}{H} \right)^4 \frac{E}{H^{\frac{1}{2}}} \rho^{\frac{-1}{2}} D^{-2} \tag{2-9}$$

whereas the chipping to fragmentation transition velocity is defined as

$$V_{fr} \propto \left(\frac{K_C}{H}\right)^4 H^{\frac{1}{2}} \rho^{\frac{-1}{2}} D^{-2} \qquad (2\text{-}10)$$

Accurate measurement of the mechanical properties is the key to get reliable results using these models.

2.1.4 Breakage Pattern of Particles

Particles could break either through chipping, fragmentation or disintegration depending on the material strength as well as the stresses and strain rate applied. To plastically deform the particles and cause chipping, a minimum force is required. According to Hare 2010), the radial cracks will extend further toward the centre of the particles, causing fragmentation when the force applied is beyond a certain threshold. It is important to identify the breakage pattern of order to analyse the breakage data. The change of trend of the particle size distribution with the impact velocity was studied by Papadopoulus (1998). It was found that the trend of the curves obtained by plotting the cumulative percentage under size as a function of normalised size is very different for particles breaking through different pattern. The trends of the cumulative plot vs the normalised size for different breakage patterns are shown in Figure 2-1.

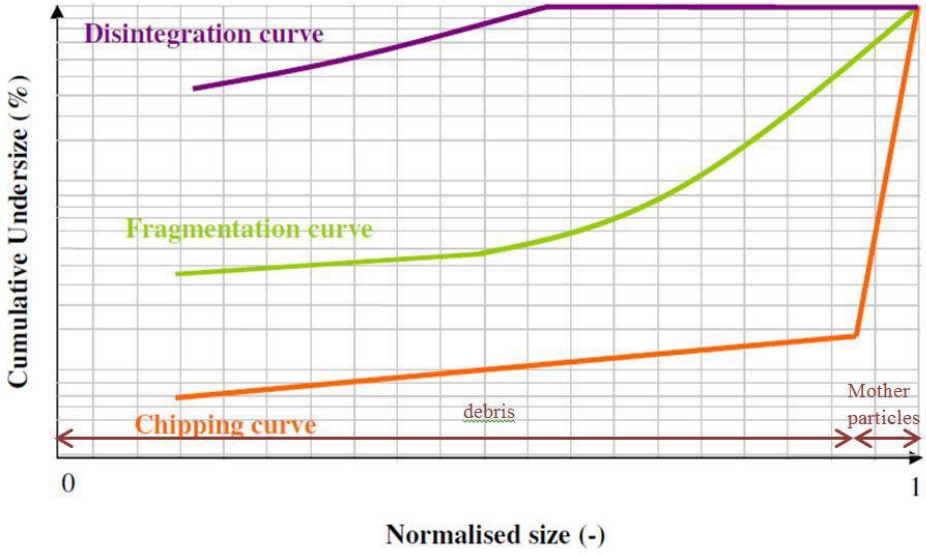

Figure 2-1 Breakage pattern of chipping, fragmentation and disintegration

2.2 Environmental Factors

2.2.1 Temperature Effect

Agitated drying is often operated at elevated temperature to speed up the drying rate and to drive out the solvent that could not be removed under standard ambient conditions. Material properties such as hardness and Young's modulus are temperature dependent (Wendy C Duncan-Hewitt and Weatherly, 1989). A study by Hassanpour *et al.* (2004) using α-lactose under sub-ambient conditions found that the breakage propensity reduces with temperature due to the increase in fracture toughness. A similar trend was observed by Olusanmi *et al.* (2010). The extent of breakage increases with the increase of temperature. An impact breakage model (Ghadiri and Zhang, 2002) was used in this work to analyse the data and the functional group H/K_c^2, representing the material properties was found to increase with temperature, suggesting that the fracture toughness, K_c decreases with temperature. It is however worth noting that these experiments were done in the absence of liquid in the particle bed. In an agitated dryer, where liquid is present, an increase in temperature leads to increase in particle size (Lekhal *et al.*, 2004). This is

however not a result of dissolution of finer API into the solvent that promote growth of larger crystal, but rather an outcome of increased solubility that agglomerates the crystal solids together (new crystal growth on the interfaces between the particles).

APIs can exist in different polymorphic forms. In enantiotropic systems, relative solubility of polymorphs is dependent of temperature. Changes of temperature could lead to previously stable polymorphs to transform into another polymorphic form. Glass transition temperature, T_g, is a common parameter used when describing polymorphic transformation. A lot of work has been done on investigating polymorphic transformation in milling with reference to T_g (Desprez and Descamps, 2006; Lefort et al., 2006; Descamps et al., 2015). Below T_g, milling is found to amorphise the sugars (lactose, trehalose, mannitol and sorbitol) while polymorphic transformation is found milling above T_g (Willart *et al.*, 2007). A study by Gan *et al.* (2002) shows that different polymorphic crystals are formed at different temperatures. It is also found that in a certain temperature range, different polymorphic forms of the crystals can coexist. Temperature also has an effect on hydrates or solvates where the crystallisation solvent is embedded into the crystal lattice. By subjecting them to high temperature, dehydration/desolvation could happen. Dehydration of α lactose monohydrate happens at 140 °C where the hydrate form of lactose transforms into the anhydrous form which is hygroscopic. A further heating will then convert the hygroscopic lactose into another polymorph which is stable (Garnier *et al.*, 2002). The glass transition temperature of carbamazepine dihydrate is ~53 °C and the dehydration process finishes by 75 °C (Kachrimanis and Griesser, 2012). Upon reaching the glass transition temperature, anhydrous form I of carbamazepine is first formed and transformed later into anhydrous form III at 190 °C. A fast water molecules removal leads to amorphisation whereas a slow process promote transformation to anhydrous crystalline form.

2.2.2 Moisture Effect

After filtration, the API is isolated and most of the solvent is removed from the particle bed. However, around 10-20% of the solvent still remains in the particle bed, interacting with the particles. Heat is then supplied to the particle-solvent mixture to remove the remaining solvent content that could not be removed by filtration.

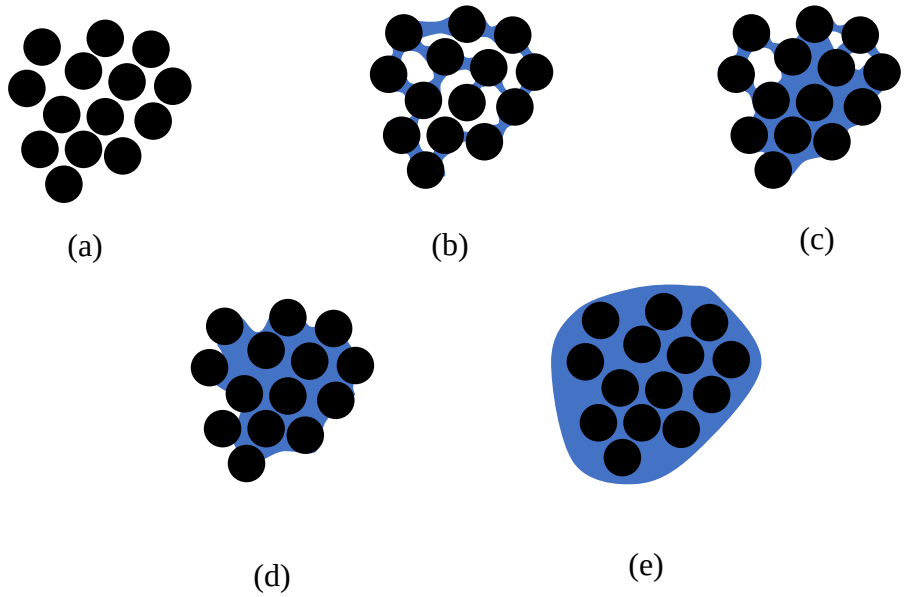

Figure 2-2 Schematic diagram of different liquid and particle interactions. (a) Dry (b) Pendular (c) Funicular (d) Capillary (e) Slurry

Figure 2-2 shows the schematic diagram of different liquid and particle interactions that occurs during the drying process. The end product of crystallisation is a mixture of crystal solids and solvent in slurry state which then undergoes isolation process to separate the crystal solids from the solvent. As the slurry dries, the liquid-particle interaction changes slowly from (e) to (a) as shown in Figure 2-2 (Newitt and Conway-Jones, 1958; Iveson et al., 2001). In slurry state, there is no cohesive interaction between the particles. Filtration process isolates the crystal solids formed from the slurry and drives the system into a capillary state where the particles are interacting with each other cohesively. Funicular state follows capillary state where both liquid bridges and liquid-filled pores coexist. Drying the system further gives rise to the pendular state, where particles are merely joined together by thin liquid bridges at the contact points. Dry state

describes the situation where liquid content is completely removed and cohesion effect is minimum or negligible. It is found that above the critical moisture level, the higher the amount of liquid present in the bed the lower the particle size reduction (Remy *et al.*, 2015). Viscosity of the liquid is proportional to the stress and is also found to affect the dynamic behaviour of granular matter (Chou and Hsiau, 2011).

2.3 Polymorphic and Phase Transformation

2.3.1 Phase Transformation

It is a standard procedure for a new chemical entity to undergo polymorph studies prior to any further development in the pharmaceutical industry. The combination of temperature, pressure and humidity selected for drying the API could favour the transformation of one polymorphic form to another (Bauer, 2008; 2009). In enantiotropic systems, one polymorph is the preferred and stable form within a certain temperature range as compared to the others. There are studies that show that by applying sufficient stresses at different temperatures, transformation could occur (Willart *et al.*, 2001; 2010; Desprez & Descamps, 2006). Normally, amorphisation occurs below glass transition temperature, $T_{g,}$ while above T_g polymorphic transformation takes place. While particle breakage is more pronounced at the later stage of drying, polymorphic transformation of API could happen at any stage of drying. It is hence of paramount importance to have a profound understanding of the thermal response of different polymorphic forms, especially in enantiotropic systems.

2.3.2 Polymorph Characterisation Techniques

Polymorphic transformation can be characterised by a wide range of techniques. Some of the main methods of analysis are microscopy, thermal methods, powder X-ray diffraction, Raman spectroscopies, inverse gas chromatography and dynamic vapour sorption. There is no technique that can accurately characterise every polymorphic form of a compound at the moment. Microscopy techniques such as Scanning Electron Microscopy (SEM) are capable of providing surface information of the crystals such as shape and size. Some of the polymorphs have distinguishable crystal shape which can be identified easily under SEM.

Differential Scanning Calorimetry (DSC) and Thermogravimetric Analysis (TGA) are two of the most commonly used thermal analytical techniques. DSC measures the heat flow when a sample is heated. Depending on the nature of the reaction, either endothermic or exothermic peak can be observed hence giving indications of temperature for melting, solid state transition, glass transitions, dehydration/desolvation etc. A lot of work has been reported using this technique (Rustichelli et al., 2000; Perrenot and Widmann, 1994; Grzesiak et al., 2003). TGA is a gravimetric technique that measures the change in weight as the sample is being subjected to heat. Unlike microscopy techniques, TGA provides the ability to quantify the phase changes due to dehydration/desolvation in terms of weight changes. Information regarding the physical phenomena (absorption, adsorption, desorption, crystalline transition etc.) and chemical phenomena (desolvation, dehydration, solid-state reactions etc.) can be obtained easily using TGA (Coats and Redfern, 1963).

Powder X-ray diffraction (PXRD) is a technique that makes use of the diffraction of X-rays to identify the crystal structure (Liss *et al.*, 2003). Since every material has their own unique diffraction pattern, PXRD allows the identification of different materials as well as the presence of impurities in the sample. A typical way to analysing the PXRD data is plotting the intensity of diffracted X-ray against 2θ where θ is the incident angle

of the X-ray. Figure 3-17 shows the PXRD of four different anhydrous forms of carbamazepine even though they all have the same chemical composition.

Instead of using X-ray, Raman spectroscopy technique utilises laser light and measures the scattered light (Raman and Krishnan, 1928). Most of the scattered light is of the same frequency as the source. However, a small amount of scattered light experiences an energy shift due to the interaction of the electromagnetic waves and the molecular vibrational energy levels. A Raman Spectrum is created by plotting the laser frequency and the shift in energy measured. Inverse gas chromatography (IGC) is a material characterisation technique that is used in surface analysis of solids. IGC requires a constant concentration of gas to be injected into the column packed with the sample and the retention time is measured. IGC can be used to measure isotherm, surface energy, heat of absorption, surface heterogeneity, permeability and diffusion (Thielmann, 2004). There is work reported using IGC to characterise polymorphic transformation, given by Cares-Pacheco *et al.* (2014; 2015).

Dynamic vapour sorption (DVS) is a gravimetric technique that measure the water sorption isotherms of a material. It is a technique typically used to study water uptake and stability of a material under various relative humidity steps. DVS can also be used to study the formation of hydrates and solvates (Buckton and Darcy, 1995; Vollenbroek et al., 2010). In order to do so, the sample must be able to react with the solvent readily to form hydrates/solvates. The formation of hydrates/solvates will result in weight gain hence allowing the transformation to be quantified.

2.4 Numerical Simulation

2.4.1 Distinct Element Method (DEM)

Discreet Element Method (DEM) is a numerical simulation method for computing or estimating the motion of a particles in a system, and the forces acting on them. DEM was initially introduced by Cundall in 1971 and this line of work was then further developed (Cundall and Strack, 1979) . DEM is based on Newton's second law of motion and force-displacement law which states that the acceleration is dependent on the net force and the mass of the object. The introduction of DEM has provided a way to study the behaviour of particles and it is able to provide information that is too difficult to be obtained experimentally. DEM is a cost effect approach and has been used widely nowadays to simulate particle flow in complex processes.

2.4.1.1 Contact Models

Linear Spring-Dashpot Model

The motion of particle resulting from the forces acting on it is determined by Newton's second law. The displacement of the particle can then be related to force-displacement law to find the contact forces. The deformation of particle is represented by allowing the overlapping of particles and contact force is dependent on the magnitude of the overlap (Cundall and Strack, 1979). The force-displacement takes the following form.

$$F_n = k_n \left(\Delta n\right)_t \tag{2-11}$$

where F_n is the contact force, k_n is the contact stiffness, Δn is the relative displacement between the particles and t is the time.

Hertz-Mindlin Contact Model

Hertz-Mindlin model is the most commonly used contact model in within EDEM and it assumes the contact between two particles to be elastic. The contact force is a function of reduced Young's modulus, *E*, reduced radius, *R* and normal overlap, α and it takes the form below(Zhu *et al.*, 2007).

$$F_n = \frac{4}{3} E^* R^{*\frac{1}{2}} \alpha^{\frac{3}{2}} \tag{2-12}$$

2.4.2 Particle Shape

Most of the DEM simulation software support only using sphere in the simulation due to its well defined geometry and simplicity. However, in real life not all particles are spherical and using spherical particles in the simulation will inevitably yield a non-representative result. To account for shape effect, rolling friction is normally introduced proposed by (Morgan, 2004). Clumped sphere method allows the approximation of the irregularity of the targeted particle while maintaining the accuracy and efficiency of spheres. Simulating particle shape in 2-dimensional systems had been attempted and reported in literature (Jensen *et al.*, 2001; Jensen *et al.*, 2001). 3-dimensional systems had been attempted by (Wang *et al.*, 2007) in which both clumped sphere and ellipsoid methods were implemented. It was found that clumped sphere method could represent the particle shape more accurately but it is more computationally expensive and more spheres are required. The ellipsoid method, on the other hand, provides less accuracy but more computational efficiency. A recent study has shown that by using clumped sphere method, satisfactory representation of particle shape for rapid shearing systems can be obtained (Pasha *et al.*, 2015). Superquadrics are another approach to simulate particle shape and they are described by similar equation as to ellipsoidal particles (Barr, 1981). Interlocking of particle is possible with this model however the aspect ratio has to be

significantly higher than one in the angle repose test to be representative as the particles generated have round corner (Masuda *et al*., 2006). DEM simulation has always been done using spherical particles where in the case of non-spherical particle shape is needed, clumped sphere method is implemented. Polyhedra have the advantages of preserving both mass and volume of the particle (without having to overlap the particles) compared to clumped sphere method. This approach was first commercially implemented in ROCKY DEM software. There is work reported (Mack *et al*., 2011; Nye *et al*., 2014) on DEM simulations using polyhedral, however it is relatively limited. A technical paper has been published discussing the DEM simulation in a transfer chute using polyhedra (Potapov and Donohue, 2013).

2.4.3 Particle Breakage

The advancement of DEM over the years has led to more capabilities being added to the model. Particle breakage is a complicated process and DEM alone is insufficient to describe particle attrition in different process. The Performance of comminution processes has been describe using empirical approach and mathematical models as of recently. To predict particle attrition, DEM simulation is often coupled with empirical data to describe attrition in specific processes. DEM simulations of ball milling have been successfully used to predict the breakage behaviour of the particles through post-processing of the simulation data (Tavares, 2017; Datta and Rajamani, 2002; Tavares and de Carvalho, 2009). A prediction of breakage in an agitated dryer has been reported (Hare, 2010; Hare *et al.*, 2011). Particle breakage was predicted by first characterising the particle breakage in a shear cell. The particle bed was separated into an array of domains which allow the stresses experienced at different region to be estimated. This method provided an insight into the stress and strain distribution of the particle bed and is applicable to systems that the attrition arises predominantly through shear. Similar work

was also reported by Lee *et al.* (2010) in predicting the breakage rate in a centrifugal/vibration mill. The DEM simulation impact energy of the mill was found to correlate linearly with the breakage parameter.

The work mentioned earlier were conducted without incorporating the breakage model into the DEM but correlating the simulation and empirical data instead. To date, three different approaches have been reported in the literature to describe particle breakage intrinsically with the DEM simulation and they are called the bonded-particle model (BPM) (Potyondy and Cundall, 2004), the discrete grain breakage model (DGB) (Potapov and Campbell, 1994) and the particle replacement model (PRM) (Cleary, 2001).

Potyondy and Cundall (2004) demonstrated that BPM approach was able to simulate the strain softening of granite in both confined and unconfined compression tests. PRM approach models the breakage using spherical particles is to replace the mother particle by smaller daughter particles if the impact energy is sufficient to cause breakage. Some recent work reported by Delaney *et al.* (2015) and Sinnott & Cleary (2015) have adopted this approach to simulate the particle breakage in an industrial scale cone crusher and impact crusher.

ROCKY DEM is a relatively new simulation package and they adopted DGB breakage model in their software package. The breakage model is based on a Voronoi fracture particle subdivision algorithm, and modified T_{10} approach proposed by Shi & Kojovic (2007). A technical article has been published using this breakage model to study coal breakage in conveyor transfer chutes (Potapov and Donohue, 2013). It was found that this model is capable of predicting breakage rates and fragment size distribution, provided the breakage strength of the particles is known. Figure 2-3 shows a ROCKY DEM simulation of polyhedra breakage in a crusher. The feed particles (Figure 2-4) are fed through the crusher where the particles experience stresses and fragment into smaller

particles. The fragmented particles (Figure 2-5) have a size distribution based on the breakage energy probability. Unlike PRM method, the daughter particles have the volume and mass as the feed particle. This model is very good in describing fragmentation of rocks and brittle materials.

A recent paper published by Jiménez-Herrera et al. (2018) has compared the three different breakage modelling approaches. It was found that BPM is capable of describing the force-deformation profile and the interaction of particles in the bed with the dropping ball. The breakage distribution however is difficult to be fitted. The computational effort required is also tremendously high. DGB model describe the interaction between the dropping ball and the particle bed well qualitatively. However, the measured force-deformation profile and progeny size distribution is not ideal. PRM method, despite being the crudest method amongst the three allows the size distribution of the progeny to be fitted well.

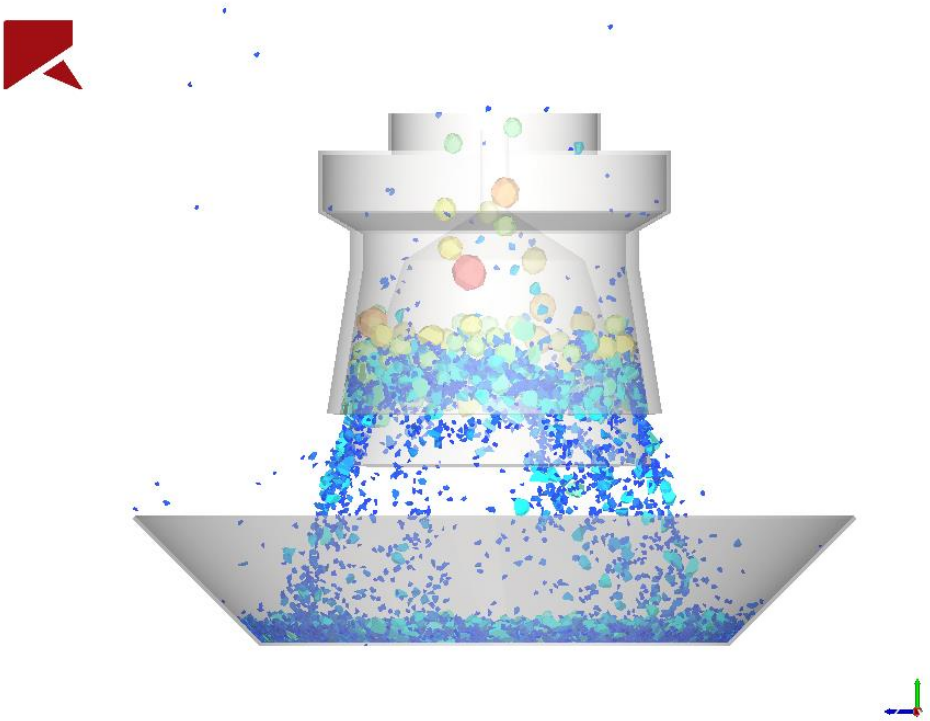

Figure 2-3 Rocky DEM – Breakage of polyhedra in a crusher (Image taken from the software)

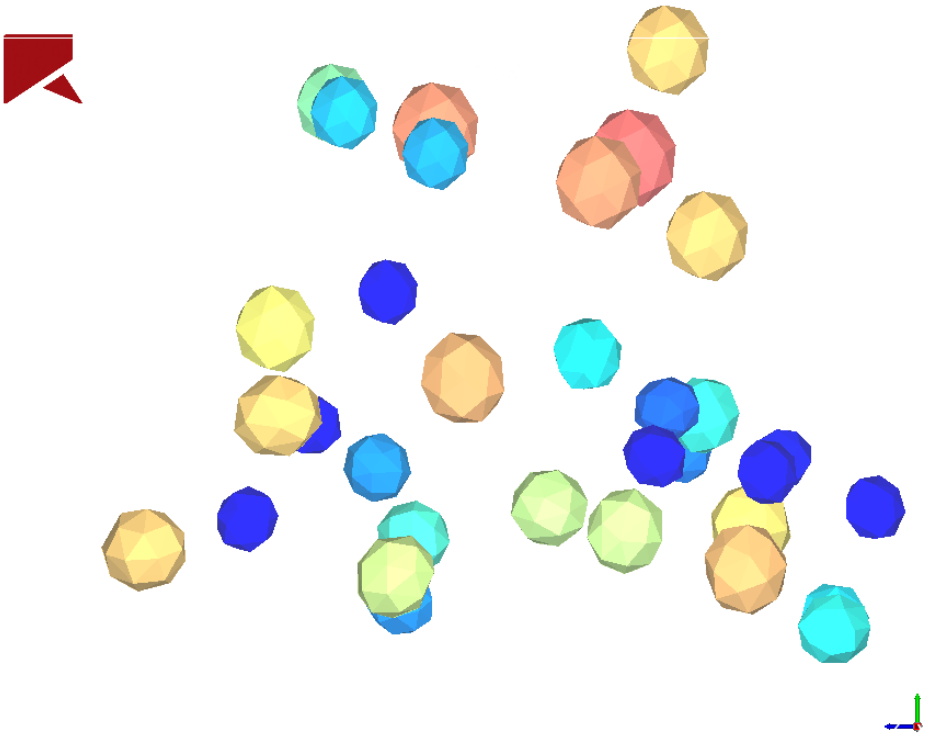

Figure 2-4 Rocky DEM – Polyhedra before being crushed (Image taken from the software)

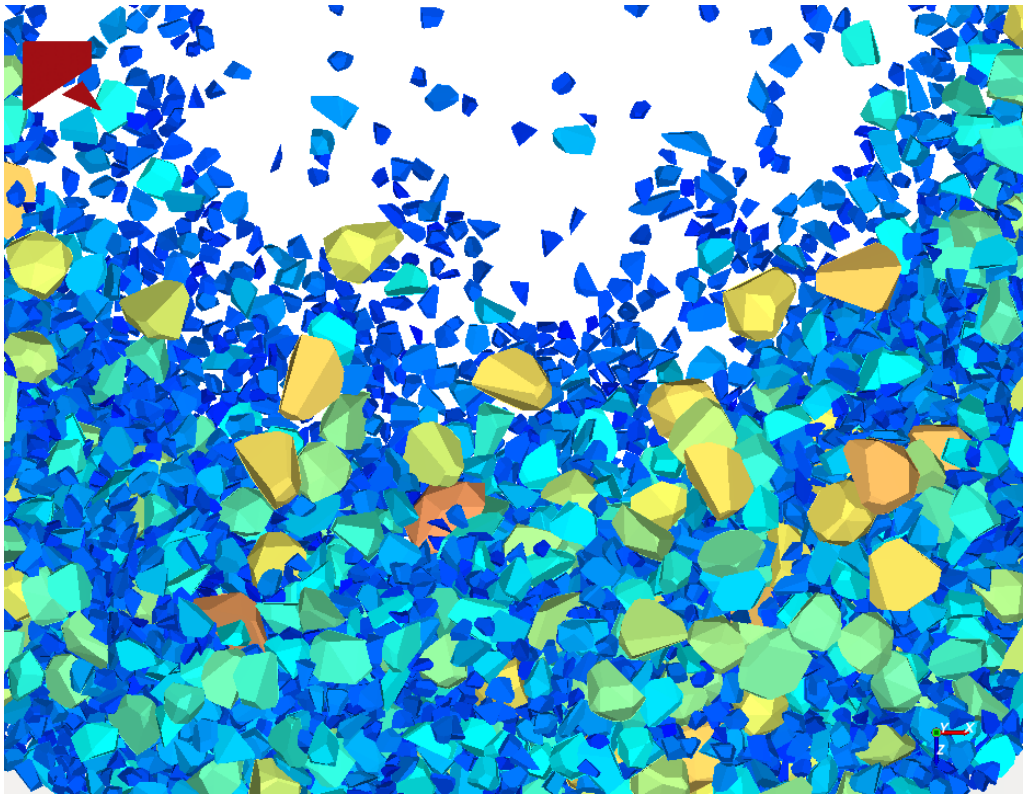

Figure 2-5 Rocky DEM – Polyhedra after being crushed (Image taken from the software)

2.4.4 DEM Simulation Validation Technique

2.4.4.1 Position Emission Particle Tracking (PEPT)

Validation is a very important aspect in any numerical simulation. For DEM simulations, one way to validate the particle flow in a system is to trace a single particle and observe the flowing pattern. Positron emission particle tracking (PEPT) is a technique developed at the University of Birmingham which was derived from the commonly used positron emission tomography (PET). In PEPT, a tracer particle which typically has the same size and density is irradiated so that it emits positrons. When a positron contacts an electron, they are annihilated and two collinear gamma rays are produced. The tracer particle is mixed together with other particles and the system is placed between two detectors, allowing the gamma rays to be traced. The position of the particle can then be estimated using a triangulation method, as shown in Figure 2-6 (Seville *et al.*, 2005). This technique has been used in literature quite often to validate DEM simulation of different processes

of particle flow (e.g. Hare, 2010; Marigo *et al.*, 2013). Multi-PEPT is an improved version of PEPT which was initially proposed by Yang *et al.* (2006) that could trace more than one particle by labelling the tracers with different radioactive levels. The algorithm was then improved to enable the tracking of free-flowing particles (Yang *et al.*, 2007).

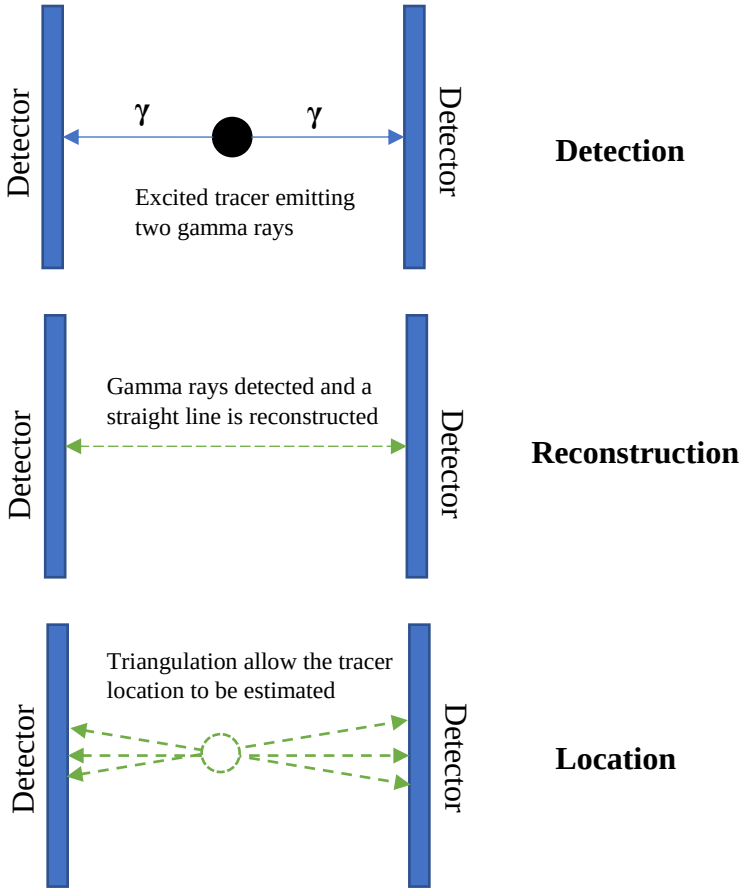

Figure 2-6 Determining tracer location in PEPT

2.5 Concluding Remarks

Attrition of APIs in agitated dryers is found to be dominant by shear deformation. Although breakage as a result of impact is present, it is less significant compared to attrition caused by shear deformation. The attrition shear cell has proven to be a useful tool to investigate particle attrition in a confined shear zone by making sure the particles are sheared against each other rather than moving together as a block. Single particle impact testers are useful in characterising the particle impact breakage as a function of

impact velocity and material properties. Various factors could result in the final particle size distribution to be shifted and yield undesirable product specification. Temperature is found to alter the particle material properties, though not by a significant margin, and could either promote or mitigate the breakage. Particle-particle interaction depends on the amount of liquid present in the particle bed and different regime could arise depending on the moisture level.

Apart from attrition, agitated drying could also induce phase transformation. APIs are known to exist in different polymorphic forms. Polymorphic transformation during agitated drying is undesirable as it may lead to poor drug delivery and low bioavailability. It could also cause some processing problems such as agglomeration. Stress and temperature have been found to have an effect on the polymorphism of APIs. Different combination of stress and temperature can favour the formation of different polymorphs. There is literature that investigates phase transformation of particles during milling. However, less has been attempted with agitated dryers to quantify the attrition and phase changes of the API.

The Distinct Element method (DEM) has provided a way to estimate the stress distribution in the particle bed which experimentally is too difficult to achieve. Empirical data obtained for assessing a given material under shear cell or impact tester could then be coupled with DEM simulations, providing a predictive tool to estimate the breakage in the agitated dryer. The introduction of polyhedra particles in DEM simulations has opened up another interesting area to assess particle flow and breakage as compared to the conventional way which uses only spherical particles.

Chapter 3

Material Characterisation of Carbamazepine Dihydrate Crystals and Methods

3.1 Introduction

Material characterisation is essential in the early development of a new product in the manufacturing industry. It is a necessary step in devising the process plan, especially when the product is brand new, to reduce the cost and time associated in the development. Knowing the material properties of a new compound, together with the constitutive models of the process of interest, allows one to predict its downstream processing behaviour. The model compound studied in this research work is carbamazepine dihydrate, a hydrate form of carbamazepine which is clinically used in the treatment of epilepsy and bipolar illness (Post et al., 2007). Carbamazepine dihydrate has two water molecules embedded to a carbamazepine molecule in a stoichiometric ratio. It is acicular in shape. Losing its crystal water through dehydration, the crystal lattice integrity of this hydrate is disrupted and it then subsequently phase transforms into anhydrous carbamazepine, which could exist in four different polymorphic forms (Grzesiak et al., 2003), depending on the environmental conditions it is subjected to. The acicular nature of this compound and its potential to phase transform into different anhydrous polymorphs makes it an ideal candidate for the study of crystal polymorphic transformation and attrition during processing. A process stage where this readily occurs

is the agitated filter bed drying. In this chapter, the material properties of carbamazepine dihydrate are characterised extensively and the results serve as the basic foundation of the research work documented in the chapters that follow.

3.2 Material Preparation

Anhydrous form of carbamazepine was purchased from Sigma Aldrich and recrystallised into carbamazepine dihydrate by Dr Kushal Sinha at AbbVie Inc. (Chicago, US) before being shipped to the University of Leeds for this research work. Two separate batches of carbamazepine dihydrate were produced at different times, both having distinctive physical features that differs from each other. The very first batch of carbamazepine dihydrate provided by AbbVie is of the smaller scale, at 1 kg, while the second batch is a scale-up version, at 9 kg. While the solid-state properties of these two batches remain the same, the physical properties (size and aspect ratio) of these crystals are different and will be further discussed in the following sections. The first batch of carbamazepine dihydrate (batch no.: CBZ.2H_2O_B2016) was produced according to the procedure below.

Forward Addition of Anti-solvent into Carbamazepine-Ethanol Solution

1. Anhydrous carbamazepine is first charged to crystallizer. A mixture of ethanol:water (80:20 w/w%) is then charged to the pot. The solution is stirred at 250 RPM and brought to 65 °C for complete dissolution.
2. The temperature is then reduced to 41 °C and wet-milled seeds of carbamazepine dihydrate (previously prepared) are added into the solution.
3. The crystalliser is then allowed to come to equilibrium for an hour.
4. Anti-solvent (water) is then charged into the solution at 41 °C at 13.6 ml/min.

5. Once the addition of anti-solvent is complete, two heat/cool cycles are performed, one at 0.1 °C/min and other at 0.05 °C /min. There is a hold time of 90 min at the end of each cycle.
6. The slurry is then filtered, and the cake is washed with water twice to isolate the crystals from the mother liquor.
7. The wet cake is then dried at room temperature.

The procedure to crystallise the second batch (Batch no.: CBZ.2H_2O_B2018) of carbamazepine dihydrate is detailed below.

In-situ Seed Generation and Forward Addition of Anti-solvent into Carbamazepine-Ethanol Solution

1. Anhydrous carbamazepine is first charged to crystallizer. A mixture of ethanol:water (75:25 w/w%) is then charged to the pot. The solution is stirred at 70 RPM and brought to 65 °C for complete dissolution.
2. 9 litres of the solution is taken out and cooled down to 41 °C to bring to supersaturation of 1.14.
3. Wet-milling of solution at 41 °C is then used for in-situ seed generation of carbamazepine dihydrate seeds.
4. A sample is then taken and verified to make sure the crystals are of the right form by powder X-ray diffraction (PXRD).
5. The prepared seeds are then added to the crystallization tank by pressure transfer from a port on top.
6. Another sample is taken a few minutes later to check the crystal form.
7. Two heat/cool cycles are performed, first one at 2 °C/hr and second at 4 °C/hr. A cooling end point is 22 °C and heating end point is 42 °C. A hold time of 1 hour is given at the end of cooling cycle.

8. The slurry is then pressure transferred to agitated filter dryer and filtered, and the cake is washed with mother liquor composition twice to isolate the crystals.
9. The wet cake is then humidified dried (RH not less than 30, was kept at 70) at 28 °C until loss on drying reaches the theoretical end point. Orthogonal measurements were done via Karl Fischer (KF) and quantitative Nuclear Magnetic Resonance (qNMR) to call off drying.

3.3 Physical Properties

3.3.1 Observation under Scanning Electron Microscopy (SEM)

The micrographs of the carbamazepine dihydrate crystals were taken using the Hitachi Tabletop Microscope TM3030 Plus. It has the ability of examining uncoated samples as it is operated under a low vacuum pressure, hence reducing the charge-up issues over sample that are typically found in the full-fledged SEM setup, though the clarity and resolution of the images taken are relatively inferior. The results of the forward addition of anti-solvent into carbamazepine-ethanol solution is crystals that have high aspect ratio as shown in Figure 3-1. The third dimension (thickness) of the crystals is significantly smaller compared to the first two dimensions (length and width) that constitute the dominant face of the crystals, leading to an acicular and plate-like crystal morphology.

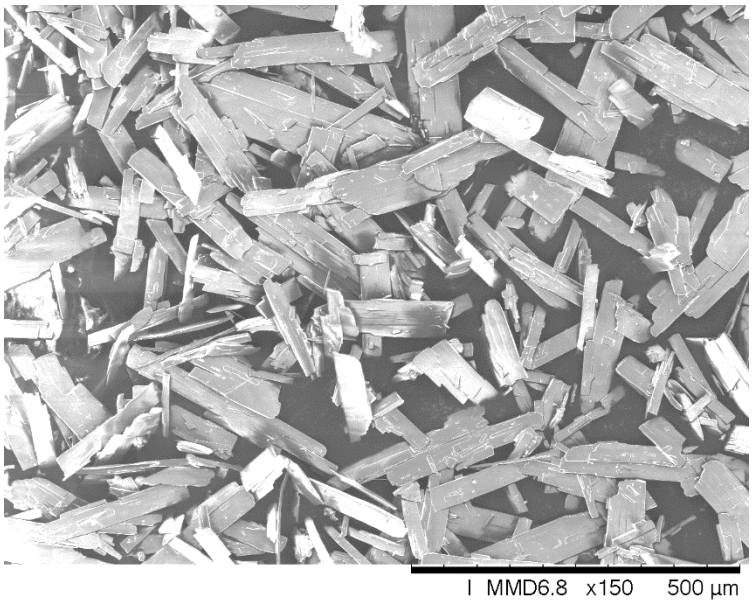

Figure 3-1 SEM image of carbamazepine dihydrate crystals (CBZ.2H_2O_B2016)

The physical attributes of the 9 kg batch carbamazepine dihydrate are shown in Figure 3-2. Similar plate-like feature is observed but the particles are bigger in size, and the aspect ratio is lower compared to the 1 kg batch. The particle size of the 9 kg batch also seems to have a wider distribution. This is inferred from the existence of the smaller crystals that are lying on top of the bigger crystals in the micrograph.

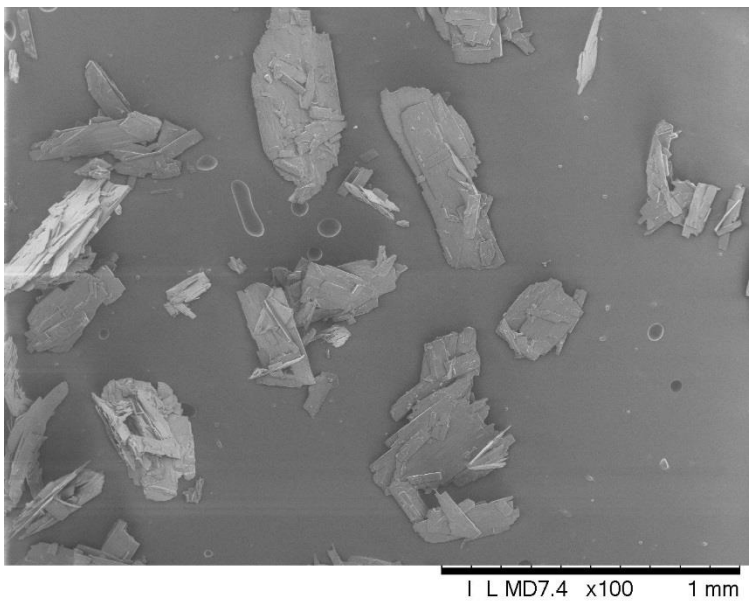

Figure 3-2 SEM image of carbamazepine dihydrate crystals (CBZ.2H_2O_B2018)

3.3.2 Shape and Size

Observation of the carbamazepine dihydrate using SEM provides only a qualitative image of the physical appearance of the crystals. To quantify the size and shape of carbamazepine dihydrate crystals, a commercial particle size analyser, Morphologi G3 from Malvern Panalytical is used. The device comprises an aerodynamic dispersion unit, an optical microscope and an automated XYZ stage. Standard operating procedure involves first dispersing the test sample (dry or wet) onto the glass slide and then subsequently capturing a series of micrographs of the dispersed sample with the aids of the XYZ. Image analysis is then performed on the micrographs captured to generate the distributions of different particle size and shape parameters of the test sample.

3.3.2.1 Setting Up Standard Operating Procedure (SOP) for Carbamazepine Dihydrate Crystals

The accuracy of image analysis is sensitive to the lightning conditions when the micrographs are taken. The reflective and refractive properties of a sample is material dependent and hence a dedicated SOP is needed to ensure the repeatability of the measurements. For carbamazepine the setup of the SOP is as below:

1. Sample Size : 7 mm^3
2. Dispersion Type : Dry
3. Dispersion Pressure : 0.5 barg
4. Light Source : Episcopic (top light)
5. Optics Selection : 5×
6. Z-Stacking : None
7. Threshold Range : 0 to 156
8. Scan area : 30 mm (radius)

Approximately 7 mm^3 of sample is measured using a volumetric spatula provided by the instrument and fed into the sample well of the dry dispersion unit. The pressure used to disperse the sample is 0.5 barg, which is the lowest allowable pressure of the instrument. Two different light sources can be used to provide the illumination needed for micrograph acquisition. In the case of carbamazepine, the episcopic light is used as it provides better contrast between the crystals and the background. Morphologi G3 comes with 5 optic lenses with different magnification levels ranging from 2.5× to 50×. The level of magnification has a significant impact on the scan time of the sample. The higher the magnification, the longer the scan time. It is found that 5× magnification works best for carbamazepine dihydrate crystals used in this work, as it produces clear micrographs that have enough pixels for both the large and small crystals to be detected by the image analysis suite. Z stacking is a useful feature for producing crisp micrographs of particles with a large variation of thickness by fusing a few micrographs captured at different depths into one. However, this feature is not adopted as the carbamazepine dihydrate crystals are platy and the variation of crystal thickness is small.

The micrographs captured using Morphologi G3 are 8-bit images with greyscale value ranging from 0 to 255. In order for the image analysis suite to differentiate the particles from the background, a technique called thresholding is performed to convert the 8-bit greyscale images to binary images. Thresholding is the simplest technique of image segmentation. It works by converting pixels that are not within the specified threshold range into white pixels (background) and those within into black pixels, essentially separating the pixels into two groups, background (white) and particle (black). Unfortunately, human intervention is needed to determine the optimal threshold range and hence the accuracy of the measurement is prone to subjective measurement error. Nevertheless, this error can be minimised, provided a set of criteria (will be discussed later on) is fulfilled by the threshold range selected. An example of image thresholding is

shown in Figure 3-3. The first image on the left (a) is a crop-out of the 8-bit greyscale image captured by the Morphologi G3 without thresholding. It can clearly be seen by eyes that only one single particle is present. This image, however, is difficult to be interpreted and analysed by the computer as it is made up of pixels with a wide range of greyscale value from 0-255. As can be seen in the second image (b), the pixels in blue are the "background" pixels that have been segmented by limiting the threshold range of interest between 0-200. The rest of the pixels make up the "particle" group and they will subsequently be subjected to particle size analysis. However, more than one particle will be detected if image (b) is now being subjected to particle size analysis. This is due to inadequate threshold range used to segment the image. Apart from the single crystal, the background noise is also assumed to be individual particles and taken into the particle size analysis. A more appropriate threshold range to be used is 0-150 and the result is illustrated in image (c). Using this threshold range results in a crystal with clean and clear edges while keeping the background noise at minimum. The void encircled by the edge will be filled automatically in the image analysis suite and hence would not affect the particle size measurement. Further narrowing down the threshold range could lead to incomplete particle where the edge is broken as shown in image (d) and analysing the size of the particle will incur substantial error in the measurement.

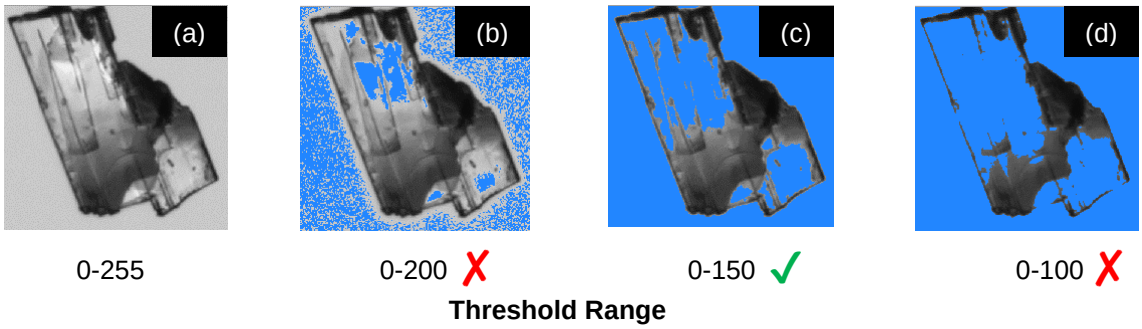

Figure 3-3 Thresholding of greyscale image

3.3.2.2 Exclusion of Particle Anomaly by Image Analysis

A pulse of pressurised air is used in Morphologi G3 to disperse the test sample from a sample well, breaking up any lumps present before the particles exit and settle down on a glass slide by gravity. In the process of doing so, it is possible for the particles to rain down on top of other particles that have already settled down on the glass slide, that will later on be captured by the instrument as clusters made up of conjoined particles as shown in Figure 3-4. Those clusters, if left untreated, will lead to false representations of the particle size and shape distribution.

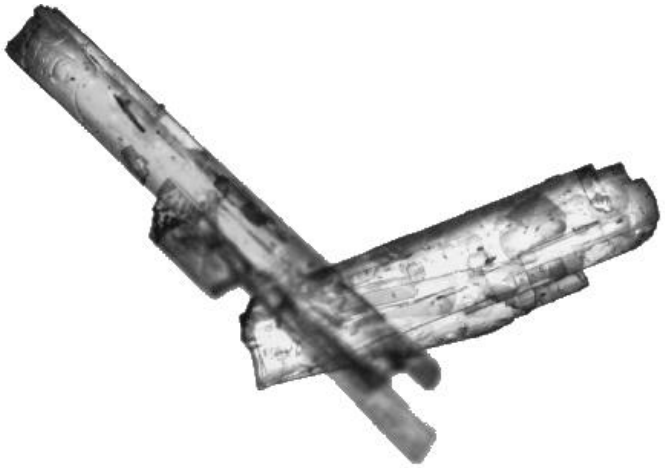

Figure 3-4 A cluster made up of two conjoined particles

Image thresholding provides a way to segment the particles from the background, but it could not differentiate a single crystal from a cluster of particles. Overlapping particles are undesirable in particle size analysis as they give a false impression that big particles are present in the sample, while these "big" particles are actually made up of smaller individual particles lying on top of each other. There are different ways that one could apply to remove those clusters. In this work, image filtration using two shape descriptors, namely convexity and solidity is adopted. Convexity is defined as the perimeter of the convex hull divided by its perimeter. Solidity, on the other hand is defined as the object area divided by the area of the convex hull. Both of these shape

descriptors give a measure of the particle “spikiness”. The illustration of the convexity and solidity calculation is shown in Figure 3-5.

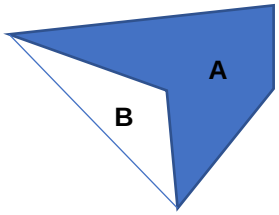

$$\text{convexity} = \frac{\text{Perimeter of (A + B)}}{\text{Perimeter of A}}$$

$$\text{Solidity} = \frac{\text{Area of A}}{\text{Area of of (A + B)}}$$

Figure 3-5 Illustration of convexity and solidity

A sensitivity analysis was performed to determine the optimal value for convexity and solidity. The scatter plot of solidity versus convexity of carbamazepine dihydrate crystals is shown in Figure 3-6 (a). The particle population density is centred around the top right corner of the scatter plot, inclining towards unity for both convexity and solidity. On the lower spectrum of convexity (region A), particles appear to be jagged and incomplete as shown in Figure 3-6 (b), whereas particles recorded with low solidity (region B) appear to be fibre-like as those found in Figure 3-6 (c). On the other hand, particles with convexity and solidity close to unity (region C) have standalone crystals with well-defined crystal shape. A series of values are tested for both convexity and solidity and the optimal value is determined. It is found that a value of 0.85 used for both of these shape descriptors yields the best result, removing most of the incomplete, overlapping and fibre-like particles. The result of the image filtration is shown in Figure 3-7. The image on top (a) contains the particles that have solidity and convexity higher than 0.85 and they will be used for further particle size analysis while the particles in the image below (b) are the outliers that will be excluded.

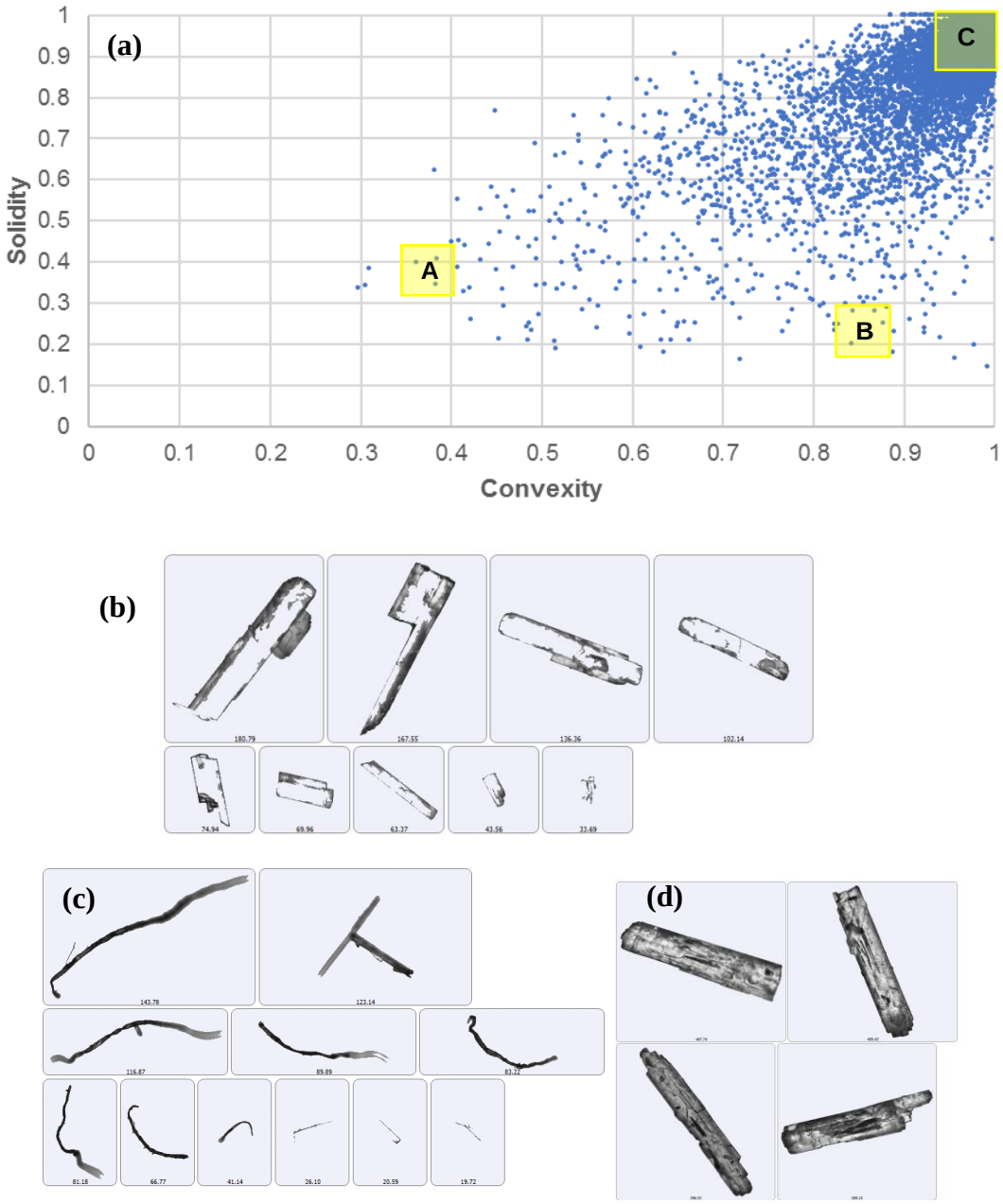

Figure 3-6 (a) Scatter plot of solidity vs convexity; (b) Particles at region A; (c) Particles at region B; and (d) Particles at region C

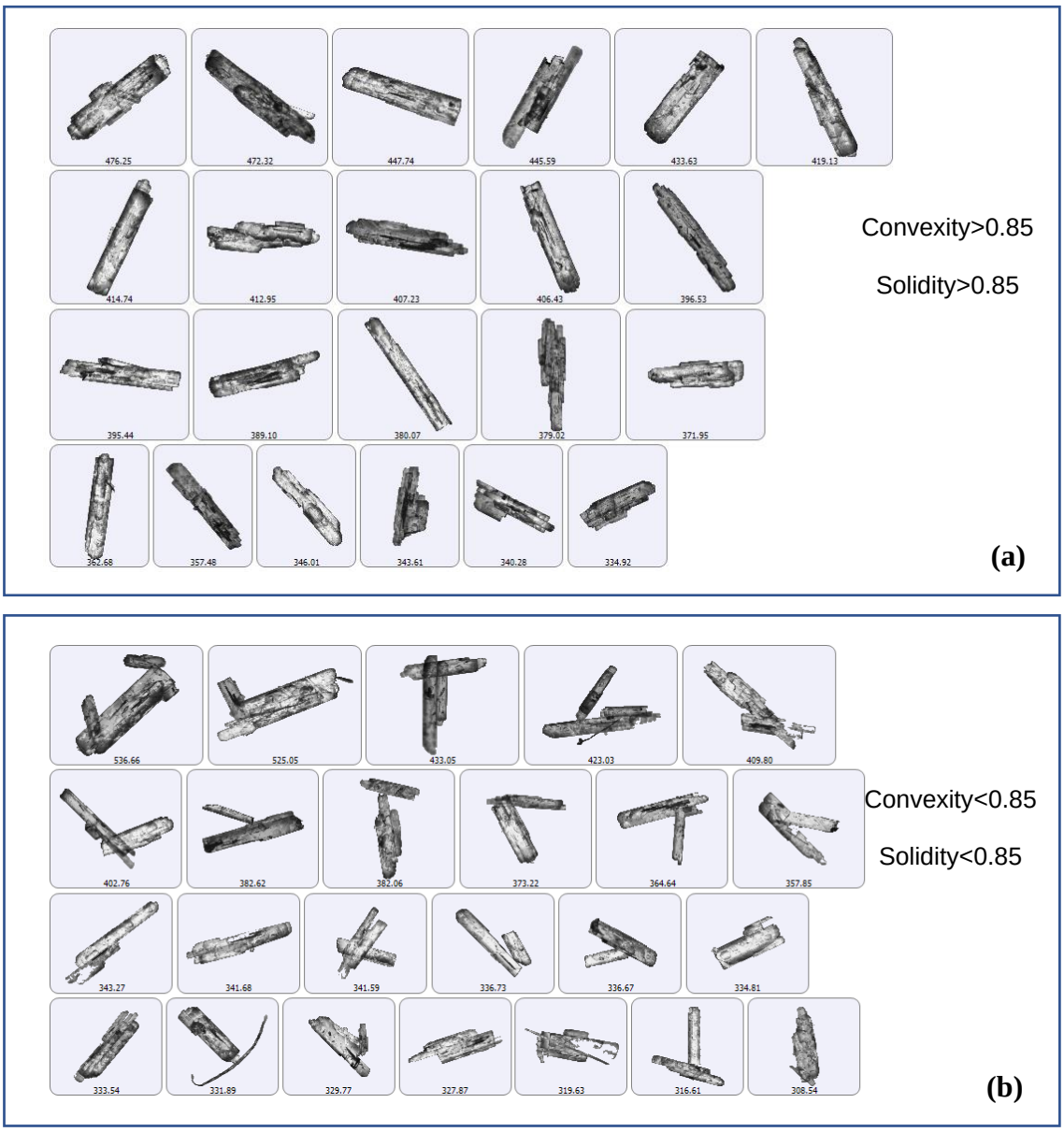

Figure 3-7 Remaining particles after filtration (a) and the particles that have been filtered out (b)

3.3.2.3 Particle Volume Estimation

Like most particle analysers, Morphologi G3 captures 2-dimensional information of the particles that lie on their maximum stable plane and converts the particle projected area into a circle equivalent area. The assumption that the particle volume approximates that of a sphere with equal projected area works relatively well with equant particles. However, this assumption falls short for highly acicular and platy particles in that it tends to overestimate the particle volume. Platy particles like carbamazepine dihydrate have a

third dimension that is significantly smaller than the other two dimensions. It is hence safe to assume that a constant thickness value can be applied across the particle projected area and still result in a reasonably representative volumetric-based particle size distribution. To avoid confusion, the particle size, *D* is represented by square equivalent side length rather than circle equivalent diameter. Square equivalent side length is defined as the side length of a square that has the same projected area as the particle. The PSD plots in this thesis are constructed based on such assumption.

3.3.2.4 Statistical Reliability and Data Smoothing

G3 Morphologi has miniscule sample size requirement, typically in milligram range for each measurement. However, small sample size is also associated with lower population of particles being measured and hence the local particle size distribution measured may not be representative of the global particle size distribution. Depending on the particle size and shape of the sample, multiple measurements may have to be performed to improve the statistical reliability of the measured particle size distribution. The particle size distribution of bigger and non-spherical particles, especially those with large aspect ratio, tends to have a wider scatter compared to those of smaller and rounded ones. Figure 3-8 shows an example of the PSDs of carbamazepine dihydrate dispersed and measured at 0.5 barg. An average of ~25000 are analysed in each measurement. Note that the particle size distribution measured using G3 Morphologi is in the form of discrete probability distribution but is presented as continuous probability distribution in this thesis for better visual presentation. The scatter of the PSD is large for each individual measurement. Hence, a summation of six of these measurements is performed to reduce the scatter. A moving average of 11 points is then applied to the PSD of the sum to iron out the peaks present due to the deficiency of particle population in the measurement. As

shown in Figure 3-9, a moving average of 11 points produces a reasonably smoothened plot and the overall distribution is not shifted excessively.

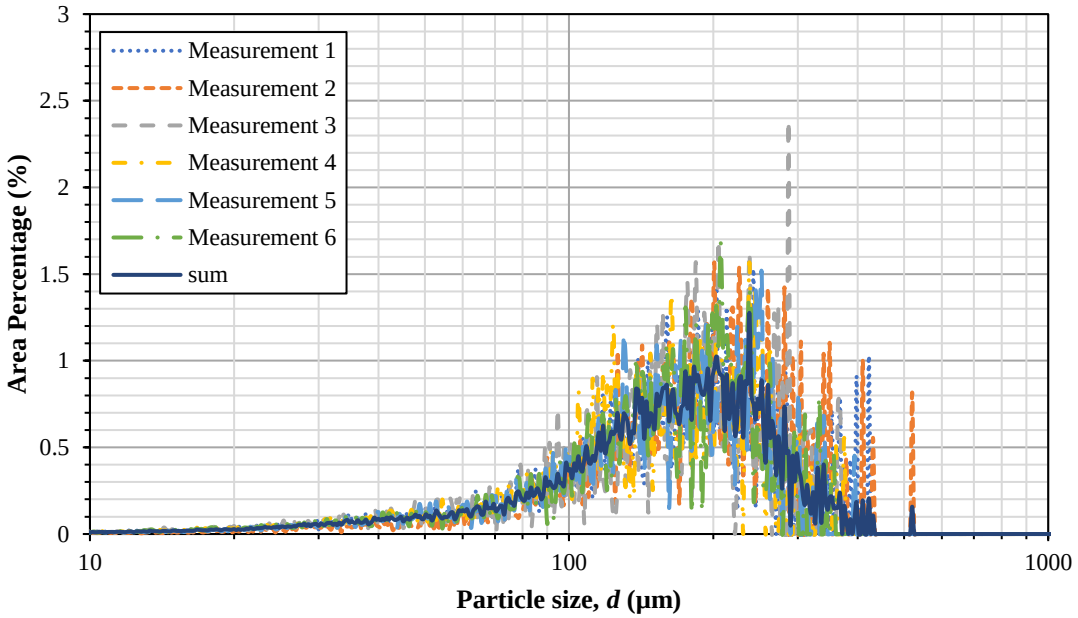

Figure 3-8 Measurements of PSD of carbamazepine dihydrate crystals dispersed at 0.5 barg

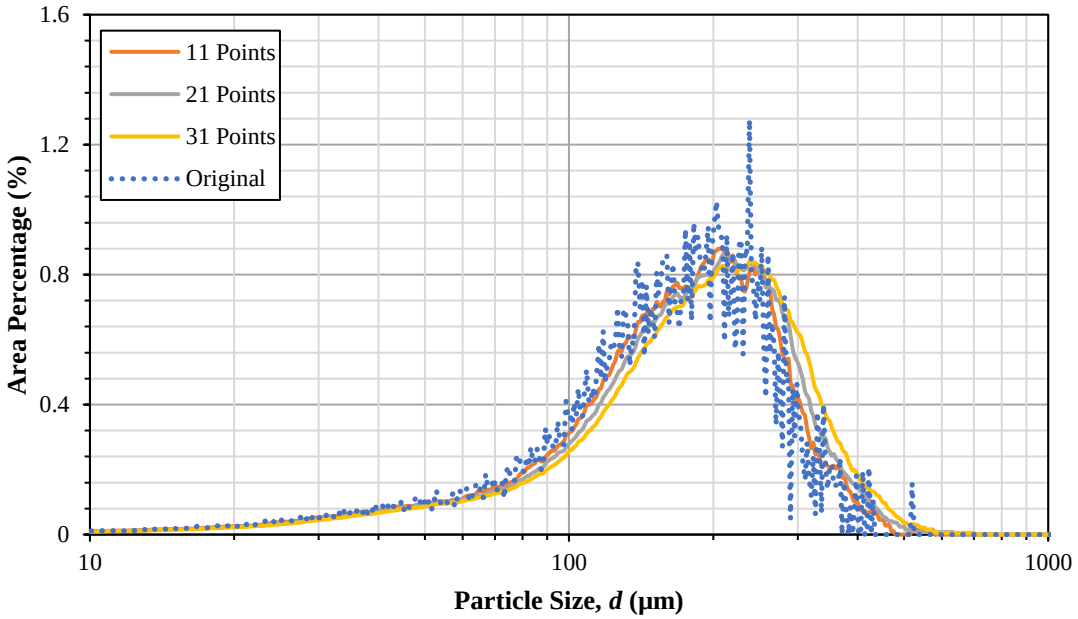

Figure 3-9 Moving average of PSD using different number of points

The particle size distribution of the two batches of carbamazepine dihydrate crystals are shown in Figure 3-10. It can clearly be seen that CBZ.2H_2O_B2018 has a

wider particle size distribution compared to CBZ.2H$_2$O_B2016 and this in in agreement with the visual observation made using SEM. The span of a volume-based size distribution gives a measure of the width of the distribution and is defined as:

$$Span = \frac{D_{V,90} - D_{V,10}}{D_{V,50}} \tag{3-1}$$

where D_V is the volumetric size and the subscript that follows after is the volume percentage below the size of interest that the sample contains. CBZ.2H$_2$O_B2018 has a span value of 1.56 while CBZ.2H$_2$O_B2016 has a lower span value of 1.29, indicating that the former batch has a wider distribution.

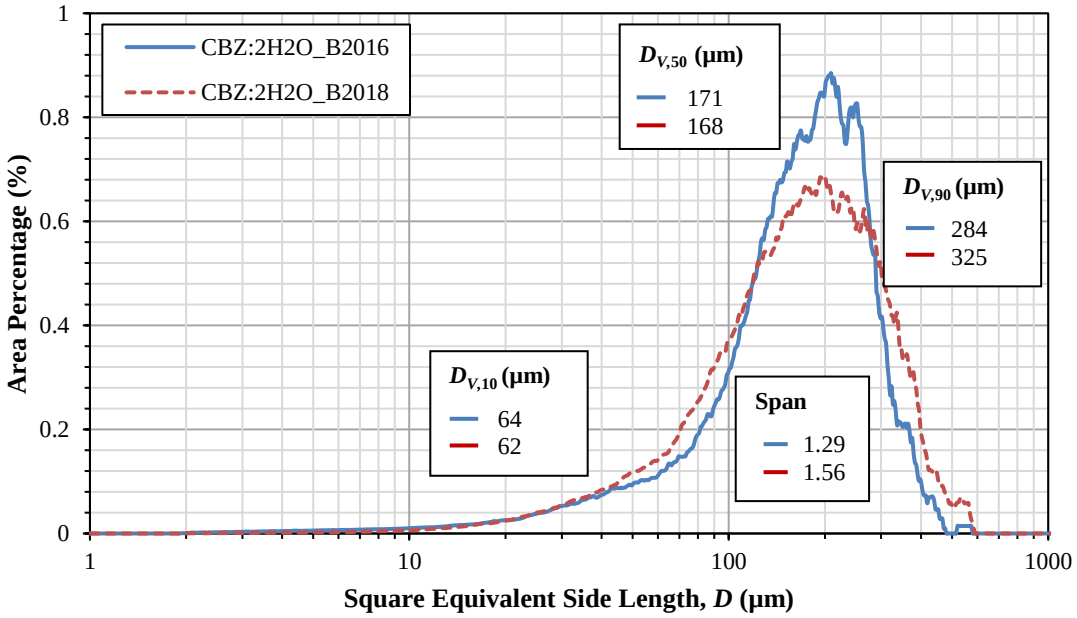

Figure 3-10 Particle size distribution of carbamazepine dihydrate crystals

Apart from the size, the shape distribution of the two batches also varies. The aspect ratio of the particles is of particular interest here and the distribution of this shape descriptor is shown in Figure 3-11. The aspect ratio, *AR*, is defined as the quotient of the particle width, *W* over the particle length, *L* as shown in Eq. 3-2. An equant particle will have an aspect ratio of about 1. The more elongated the particle, the lower the aspect ratio.

$$AR = \frac{W}{L} \tag{3-2}$$

As expected, the aspect ratio distribution of CBZ.2H$_2$O_B2016 is skewed towards the left, indicating that the particles are slender in shape. CBZ.2H$_2$O_B2018, on the other hand, has a shorter length and a distribution mode of ~0.5 that approximates a 2:1 ratio of the length and width.

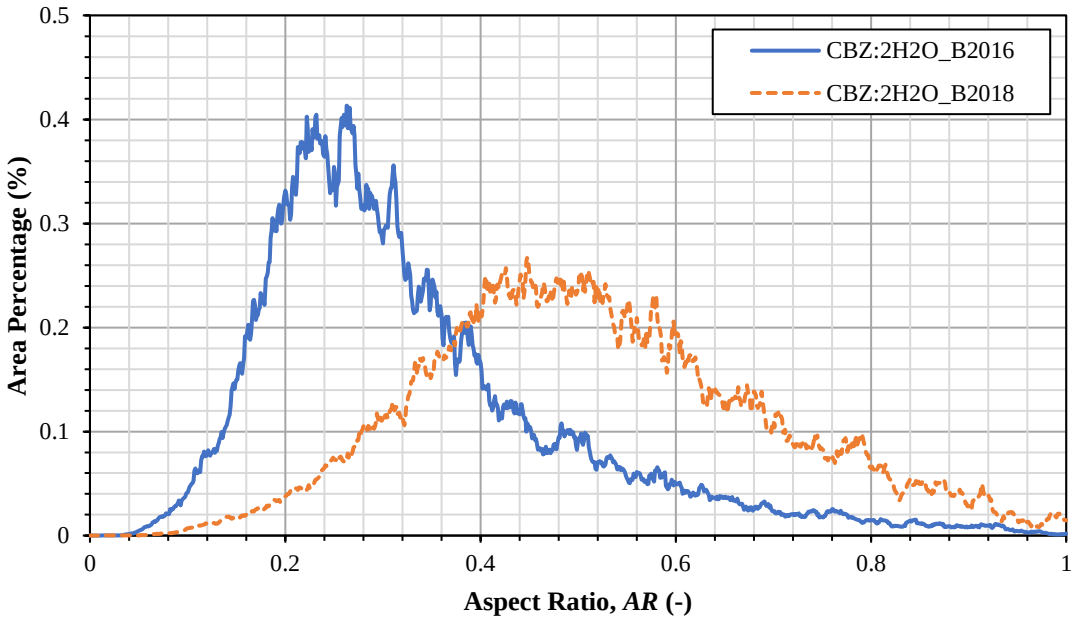

Figure 3-11 Particle aspect ratio distribution of carbamazepine dihydrate crystals

Both the size and shape distributions provide quantitative observations that agree very well with the SEM micrographs presented in the earlier section. The crystals of CBZ.2H$_2$O_B2016 are more acicular and have a narrower size distribution. CBZ.2H$_2$O_B2018, in contrast, appears to have wider size distribution and the crystals are bigger in size, but "thicker plates" in shape.

3.4 Solid State Properties

3.4.1 Classification of Organic Solids

Solid state characterisation is of paramount importance in pharmaceutical industry, as the end products are most commonly manufactured as organic solid materials. Figure 3-12 shows the classification of organic solids.

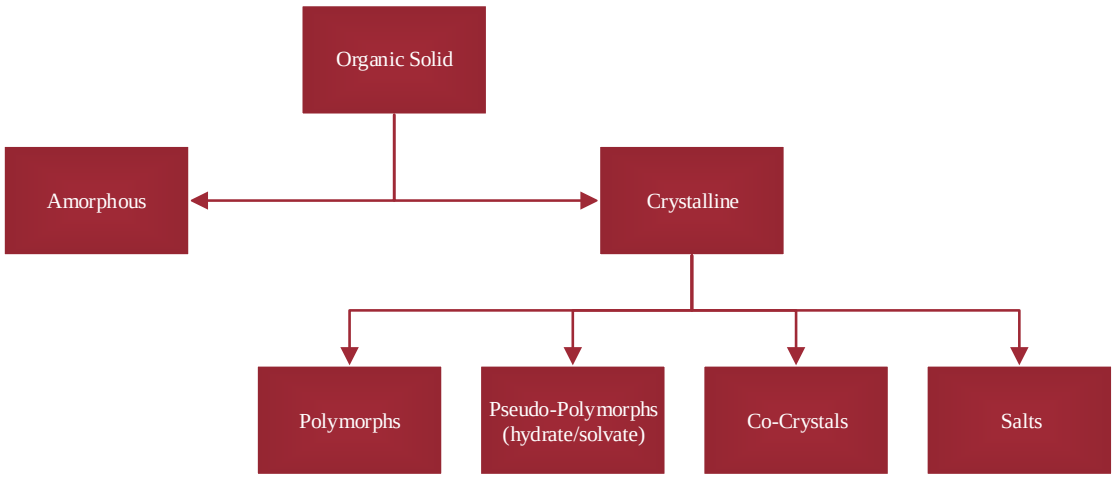

Figure 3-12 Classification of organic solids

In general, organic solids can be either amorphous or crystalline. The amorphous state describes the situation where the crystal structure is totally disrupted, and no orderly arrangement of the molecules is observed. Amorphous materials could be created intentionally, or they could be a result of phase transformation during crystallisation or post crystallisation processes. They are often undesirable due to the lack of distinct physicochemical properties and potential instability. Crystalline solids, on the other hand, consist of atoms, ions and molecules that are orderly arranged in repeating patterns. They can be further divided into four subclasses of polymorphs, pseudo-polymorph, co-crystals and salts.

Polymorphs refer to those crystalline solids that have the exact same chemical composition but different crystal lattice structure. Pseudo-polymorphism is the result of solvate or hydrate being entrapped in the crystal structure. Solvates are crystals that

contain solvent of crystallisation whereas hydrates are the products of crystallisation with water. Depending on the interaction between the solvent and the crystal, the stability of the solvates is varied. In the case where the solvent is forming part of the hydrogen network, the solvates formed are relatively more stable and more difficult to be desolvated/dehydrated compared to those cases where solvent is merely occupying the voids in the crystal. Compounds that have their molecules joined together by ionic bonding are known as salts. The formation of salts could alter the physicochemical properties of APIs such as stability, solubility and dissolution rate. Co-crystals are defined as 'crystalline solids composed of two or more molecules in the same crystal lattice' by FDA (Aitipamula *et al.*, 2012). In the crystal lattice of co-crystal, a neutral guest compound referred as conformer is bonded with the host API compound via non-ionic interaction.

3.4.2 Phase Transformation and Polymorphism

Solid state phase transformation refers to the process when one material changes its composition. It could be temperature driven and might involve the reaction with another material. For instance, subjecting a hydrate/solvate to high temperature could lead to the loss of crystal water/solvent, hence transforming the hydrate/solvate to anhydrate, referred to as dehydration/desolvation. Conversely, subjecting an amorphous phase material to humidity may lead to the phase transformation of the material to a more stable anhydrous crystalline form or even the formation of hydrate, if the system and ambient conditions allow it. Polymorphism occurs when a material changes its crystal lattice arrangement, but without altering the composition. The combination of temperature, pressure and humidity could favour the transformation of one polymorphic form to another (Bauer, 2008; 2009). In enantiotropic systems, one polymorph is the preferred and stable form within a certain temperature and humidity range as compared to the others.

Phase transformation and polymorphism of organic solids are dependent on factors such as temperature, humidity, pressure and mechanical stress. Studies have shown that a combined thermal and mechanical stresses could lead to the amorphisation of crystalline material (Willart *et al.*, 2001; 2010; Desprez & Descamps, 2006). Normally, amorphisation tend to occur below glass transition temperature, $T_{g,}$ while above T_g polymorphic transformation takes place.

Phase transformation and polymorphism during the manufacturing process could lead to off-specification end products and compromise drug performance, such as reduced bioavailability and stability of the API. In the worst-case scenario, these unwanted transformations could render the drug inefficient and hence, seriously impairing the efficiency of the treatment promised by the drug. A classic example is the Ritonavir manufactured by Abbott (now AbbVie), an antiretroviral medication used to treat HIV/AIDS that was called to be removed from the market due to unexpected polymorphic transformation of the compound. This drug was originally administered as an ordinary capsule comprising form I polymorph of the compound (the only polymorph discovered during the development of the drug). However, a more stable polymorph (form II) was discovered a few years later that has lower solubility, and thus lower bioavailability when taken orally (Bauer et al., 2001). The presence of polymorph form II, even in the slightest trace, could transform the therapeutic polymorph form I to the more stable polymorph form II. It has now become a standard procedure for a new chemical entity to undergo polymorph studies prior to any further development in the pharmaceutical industry.

3.4.3 Polymorphs and Hydrate of Carbamazepine

Carbamazepine is a model compound that has been used for decades to study polymorphism. To date, there are five anhydrous forms of carbamazepine, Form I, II, III, IV and V reported in the literature (Grzesiak et al., 2003; Arlin et al., 2011). However, there is only one hydrate form of carbamazepine that has been reported in the literature (Laine et al., 1984). Due to the large amount of research activities performed on carbamazepine, the nomenclature of the carbamazepine polymorphs and hydrate reported in the literature is not standardised, but most of them comply to the convention as illustrated in Figure 3-13.

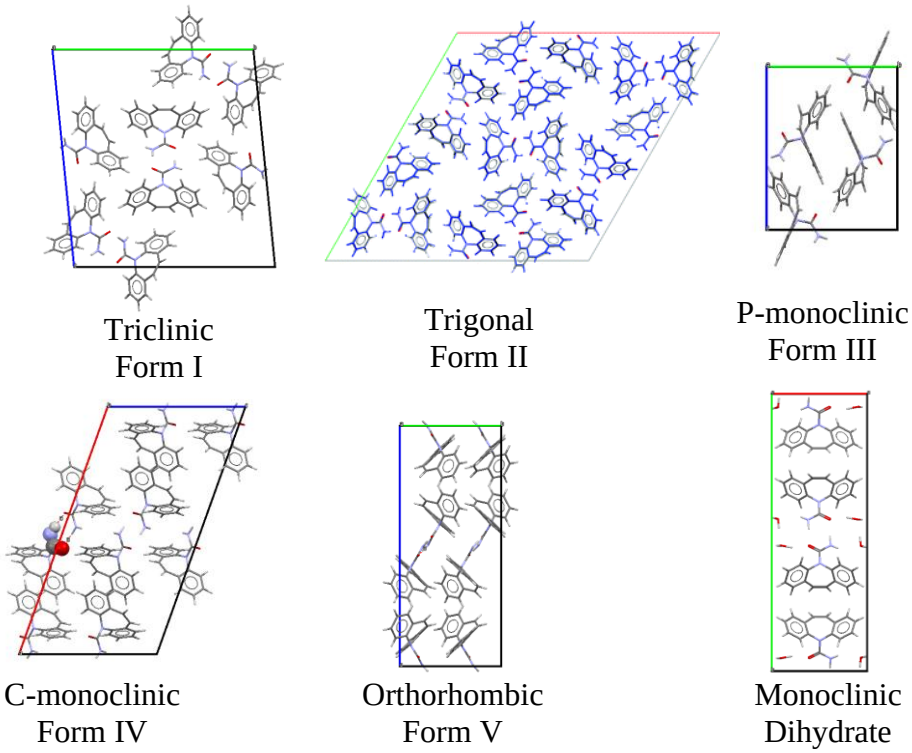

Figure 3-13 crystal arrangements of anhydrous polymorphs and hydrate of carbamazepine (obtained from Mercury Software)

The hydrate form of carbamazepine has two water molecules and the structure is found to be monoclinic (Harris et al., 2005). The systematic arrangement of water molecules forms channel-like structure that is parallel to the crystallographic axis *c*, as shown in Figure 3-14. The crystal morphology of carbamazepine dihydrate calculated using Mercury software is shown in this figure. The calculated morphology is acicular in

shape and it is in agreement with the carbamazepine dihydrate crystals observed under SEM in the previous section.

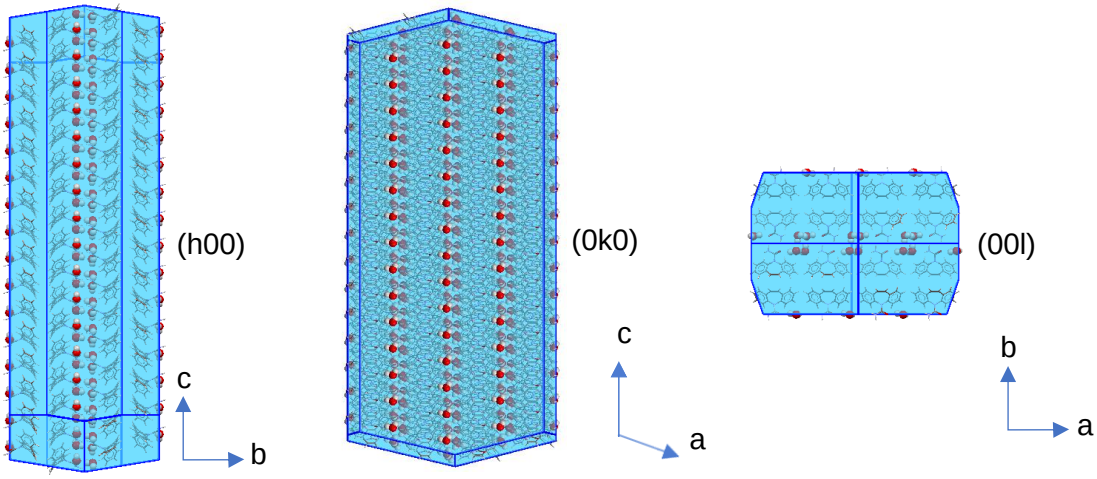

Figure 3-14 Calculated crystal morphology of carbamazepine dihydrate (obtained from Mercury Software)

Hydrates/solvates are generally more stable chemically and have lower solubility. In a study comparing the bioavailability of different polymorphs of carbamazepine, the hydrate form of carbamazepine shows no performance boost on dissolution rate and has lower bioavailability as compared to the anhydrous forms (Kobayashi *et al.*, 2000). Different salts of carbamazepine have also been reported in the literature (Buist *et al.*, 2013; 2015). Carbamazepine-nicotinamide and carbamazepine-saccharin are both co-crystals of carbamazepine and they are capable of undergoing another polymorphic transformation to form polymorphs of carbamazepine co-crystal (Porter *et al.*, 2008). Much like salts, co-crystals are of great interest to researchers nowadays to enhance the physico-chemical properties of APIs. Carbamazepine-saccharin salt was found to have better dissolution properties and higher oral absorption rate compared to the anhydrous counterparts (Hickey *et al.*, 2007). It was also found that by introducing conformers into intraconazole, the co-crystals formed exhibits better dissolution properties (Morissette *et al.*, 2004).

3.4.4 Polymorph Characterisation Techniques

Polymorphic transformation can be characterised by a wide range of techniques. Some of the main methods of analysis are microscopy, thermal methods, powder X-ray diffraction, Raman spectroscopies, inverse gas chromatography and dynamic vapour sorption. There is no technique that can accurately characterise every polymorphic form of a compound at the moment.

3.4.4.1 Microscopy Techniques

Microscopy techniques such as Optical and Scanning Electron Microscopy (SEM) are capable of providing surface information of the crystals such as shape and size (discussed in previous section). Some of the polymorphs have distinguishable crystal shape which can be identified easily under SEM. Figure 3-15 shows two SEM images of carbamazepine polymorph which have different crystal shapes. However, some polymorphs and other solvates or co-crystals might exhibit similar morphology hence making microscopy a qualitative rather than a quantitative technique for polymorph identification.

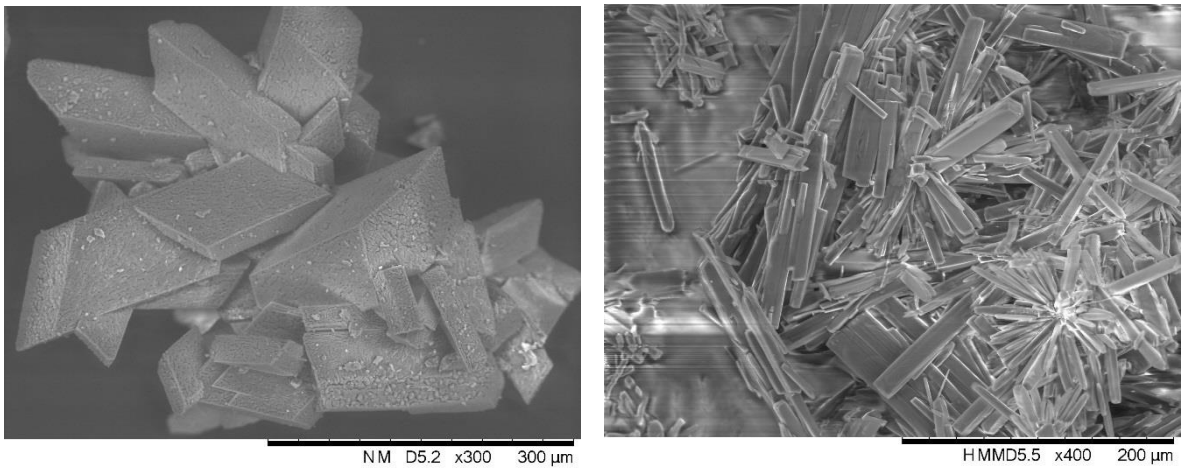

Figure 3-15 SEM images of anhydrous carbamazepine (left) and carbamazepine dihydrate (right)

3.4.4.2 Powder X-Ray Diffraction (PXRD)

Bragg's law is the fundamental law of X-ray crystallography and was derived by English physicists Sir W.H. Bragg and his son Sir W.L. Bragg in 1913 to explain why the faces of crystalline materials appear to diffract X-ray beam at certain angles of incidence, θ (Figure 3-16).

$$2d\sin\theta = n\lambda \tag{3-3}$$

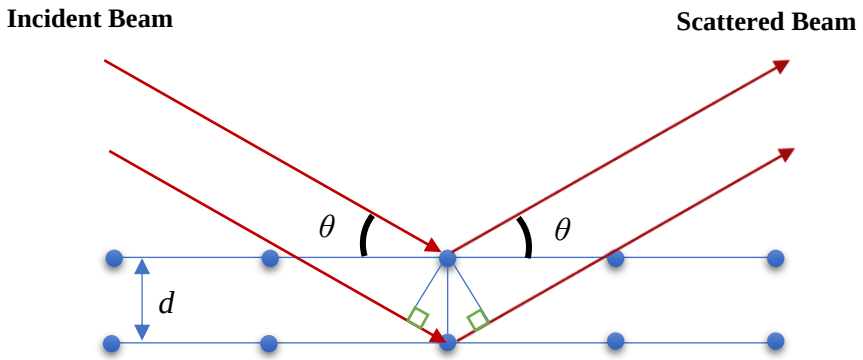

Figure 3-16 Bragg's law

Powder X-ray diffraction is a technique based on Bragg's law that makes use of the diffraction of X-rays to identify the crystal structure (Liss *et al.*, 2003). Since every material has their own unique diffraction pattern, PXRD allows the identification of different materials as well as the presence of impurities in the sample.

The X-ray diffraction patterns of the four anhydrous polymorphs of carbamazepine and its dihydrate calculated from Mercury software are shown in Figure 3-17. The anhydrous polymorphs of carbamazepine all have the same chemical composition but very different crystal lattice arrangement and that is reflected in their X-ray diffraction pattern. The X-ray diffraction pattern is a unique footprint of crystalline materials. Each peak in the X-ray diffraction pattern corresponds to a specific plane in the crystal lattice structure. The X-ray diffraction patterns of the two batches of

carbamazepine dihydrate are shown in Figure 3-18. They were performed using Bruker D8 Advance XRD device. The samples were scanned using Cu Kα radiation (λ = 0.15406 nm) from 5 – 40 ° with step size of 0.05 °/s at room temperature. The measured X-ray diffraction patterns of the two batches of carbamazepine dihydrate (b & c) appear to have less peaks compared to the calculated X-ray diffraction pattern (a). This is an artefact due to the preferred orientation of the crystals in the sample and it is always present. Ideally, the sample prepared for measurement should have its crystals arranged at complete random orientation. However, such situation will only happen if the particles are spherical. Both batches of carbamazepine dihydrate crystals are acicular and platy in nature. Even though these samples were manually ground down to mitigate the preferred orientation, the crystal fragments still have a strong tendency to lie flat on the surface, exposing mostly the dominant face (h00) of the crystals and hence enhancing the intensity of Bragg reflection of that particular face. The effect of preferred orientation is prominent in both carbamazepine dihydrate samples. The plane that gives rise to the sharp peak at ~9 ° is the (100) crystallographic plane, together with the other peaks identified, proves that the two samples tested are indeed carbamazepine dihydrate.

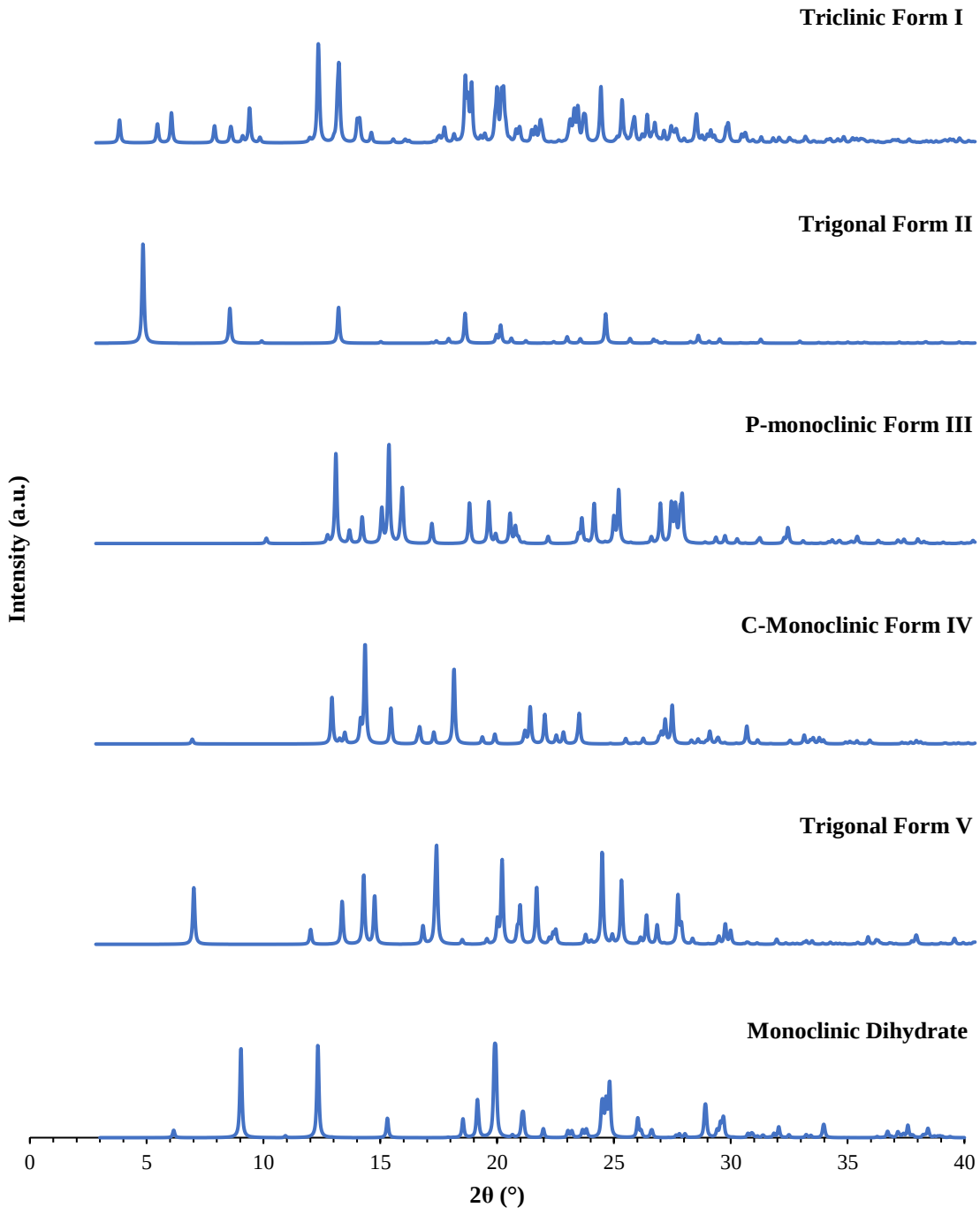

Figure 3-17 Calculated PXRD patterns of different anhydrous polymorphs of carbamazepine & its dihydrate calculated from Mercury software

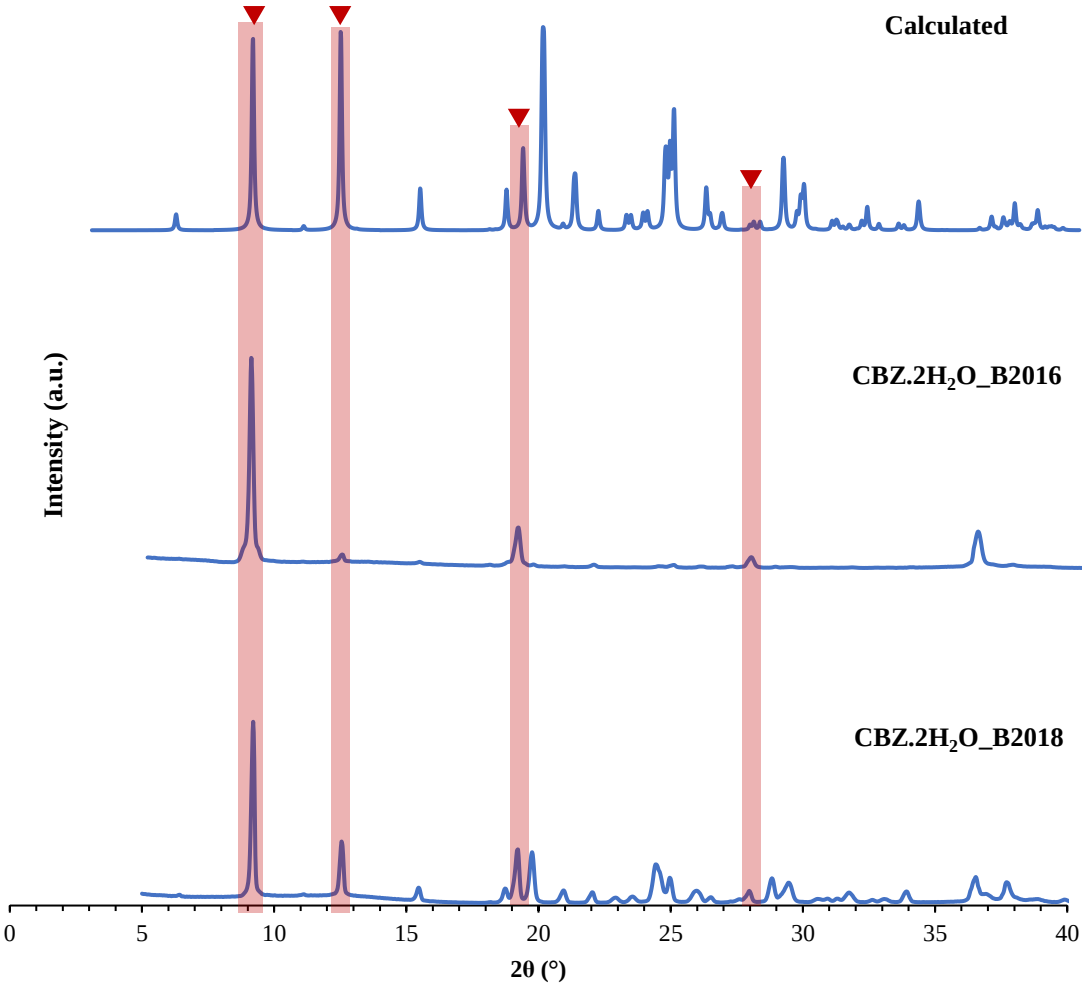

Figure 3-18 X-ray diffraction patterns of CBZ.2H$_2$O_B2016 & CBZ.2H$_2$O_B2018

3.4.4.3 Differential Scanning Calorimetry (DSC)

Differential Scanning Calorimetry (DSC) measures the heat flow against time or temperature when a sample is heated, in a specified atmosphere. DSC comprises two identical measuring cells that is made of the same material to keep the difference in heat losses to minimum. In a power-modulated DSC, when the sample cell containing the specimen is heated at the same rate as the reference cell (both have separate heater), a difference in temperature starts to occur due to the different thermal response of the specimen the additional power input supplied to compensate the temperature difference. The differential power signal (heat flow) is then recorded as a function of the actual

sample temperature. On the other hand, in a heat-flux DSC, only one heater is used and the temperature difference between the sample and reference cells, which is proportional to the heat flux difference, is used instead to compute the heat flow. Depending on the nature of the reaction, either endothermic or exothermic peak can be observed hence giving indications of temperature for melting, solid state transition, glass transitions, dehydration/desolvation etc.

The DSC thermographs of the four anhydrous polymorphs of carbamazepine acquired by Grzesiak et al. (2003) are shown in Figure 3-19 and their transition temperatures are listed in Table 3-1. According to Grzesiak's work (2003), all carbamazepine polymorphs eventually transform into Triclinic Form I if the temperature is increased to 200 °C. Form II carbamazepine recrystallises into Form I between the temperature range of ~140 to 160 °C (exotherm observed) and subsequently melts at ~192 °C (melting point of Form I carbamazepine). The DSC thermograph of Form III carbamazepine exhibits two endotherms and one exotherm. The first endotherm (~175 °C) corresponds to the melting of Form III carbamazepine, and recrystallisation to Form I (exotherm) is quickly followed afterward. The second endotherm at ~193 °C represent the melting of the recrystallised Form I carbamazepine. Form IV carbamazepine has very different DSC thermograph compared to the others. It has two endotherms that are very close to each other and the bigger of the two is recorded at ~188 °C, which corresponds to the melting of Form IV carbamazepine. The second and smaller endotherm corresponds to the melting of Form I. Unlike form III, recrystallisation exotherm is not observed in the DSC thermograph of Form IV. This is due to the heating rate used to collect the DSC thermographs (20 °C/min was used). A Lower heating rate at 5 °C/min reveals two distinctive endotherms which correspond to the melting point of Form IV and Form I, as well as a recrystallisation exotherm.

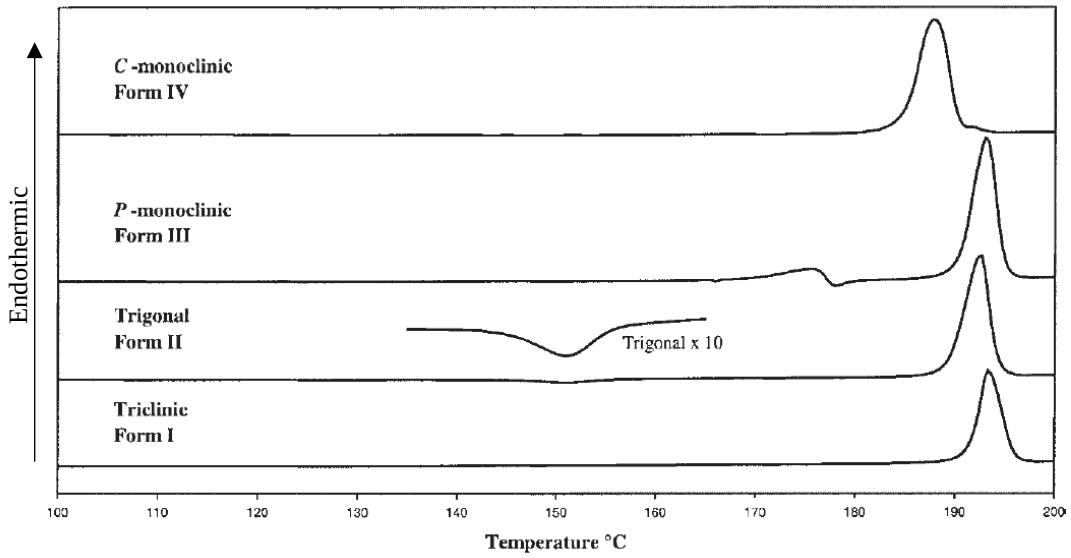

Figure 3-19 DSC thermographs of the four anhydrous polymorphs of carbamazepine (Grzesiak et al., 2003)

Table 3-1 DSC peak positions of the four anhydrous polymorphs of carbamazepine (Grzesiak et al., 2003)

	Triclinic Form I	Trigonal Form II	P-Monoclinic Form III	C-Monoclinic Form IV
Peak 1 (°C)	-	140-160	174.8	187.7
Peak 2 (°C)	193.5	192.1	193.2	191.5

The DSC thermograph of carbamazepine dihydrate recorded by Yoshihashi et al. (2002) is shown in Figure 3-20. The first endotherm corresponds to the dehydration of carbamazepine dihydrate, commencing at around 60 °C and finishing at ~90 °C. Subsequent heating results in the second endotherm which marks the melting point of the anhydrate.

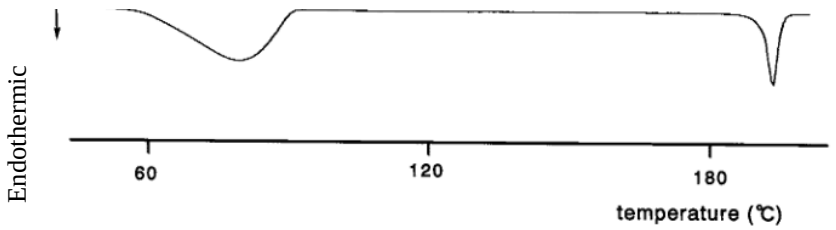

Figure 3-20 DSC thermograph of carbamazepine dihydrate (Yoshihashi et al., 2002)

The two batches of carbamazepine dihydrate were analysed using Mettler Toledo DSC1 under nitrogen purge (50 ml/min) over a temperature range of 40 to 200 °C at a heating rate of 10 °C/min. The DSC thermographs recorded are shown in Figure 3-21. It can clearly be seen that the two thermographs are almost identical to the one reported in the literature. These two samples go through dehydration (first broad endotherm) first and

the dehydrated crystals then melt at ~ 192 °C, confirming that these two batches of samples are indeed carbamazepine dihydrate and they both phase-transformed into anhydrous Form I carbamazepine due to dehydration before undergo melting.

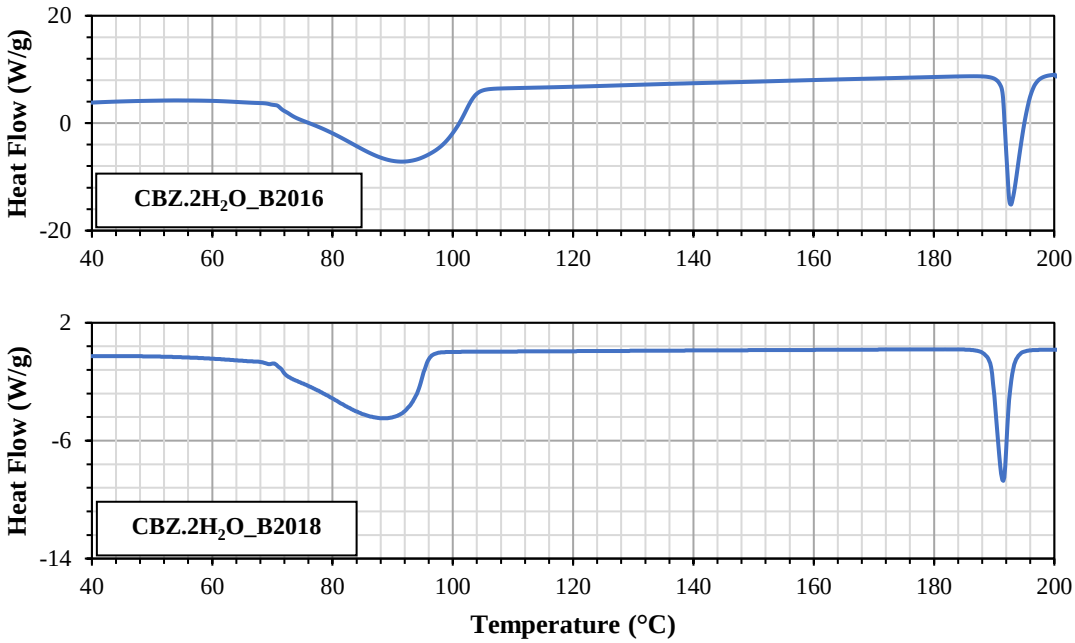

Figure 3-21 DSC thermographs of the two batches of carbamazepine dihydrate

3.4.4.4 Gravimetric Techniques

Gravimetric techniques make use of the weight change to identify the hydrate/solvate content present in a sample. There are a number of gravimetric techniques available but only thermogravimetric analysis (TGA) and dynamic vapour sorption (DVS) are used and discussed here. Carbamazepine dihydrate is a stoichiometric hydrate and it has a molecular mass of 272.3 g/mol and 13.2 % of the weight is contributed by the two water molecules (molecular mass of H_2O = 18.01 g/mol) embedded in the crystal lattice. Unlike non-stoichiometric hydrates, in which the water composition is variable depending on the water activity or relative humidity of the environment, the water composition in carbamazepine dihydrate is fixed. The difference in weight upon complete dehydration of the hydrate could provide a quantitative measure of the crystal water, hence inferring the crystallinity and purity of the sample.

Thermogravimetric Analysis (TGA)

TGA is a gravimetric technique that measures the change in weight as the sample is being subjected to heat. It consists of a high precision balance with a sample pan in a programmed-controlled furnace. Unlike microscopy techniques or PXRD, TGA provides the ability to quantify the phase changes due to dehydration/desolvation in terms of weight changes. Information regarding the physical phenomena (absorption, adsorption, desorption, crystalline transition etc.) and chemical phenomena (desolvation, dehydration, solid-state reactions etc.) can be obtained easily using TGA (Coats and Redfern, 1963).

The TGA studies of the two batches of carbamazepine dihydrate were performed using Mettler Toledo TGA under nitrogen purge (50 ml/min) over a temperature range of 30 to 120 °C at a heating rate of 10 °C/min. The resulting TGA thermographs of the two batches of carbamazepine dihydrate are shown in Figure 3-22. The crystal water content is calculated by subtracting the dry mass of the sample from the initial mass of the feed sample. The difference is then normalised with the initial feed mass and expressed in percentage. The water content in the two batches of carbamazepine dihydrate is found to be 13% and 12.9%, respectively. These results agree very well with the theoretical water content (13.2%) in carbamazepine dihydrate. The dehydration starts at ~60 °C and finishes at ~100 °C, which coincides with the DSC results discussed in previous subsection.

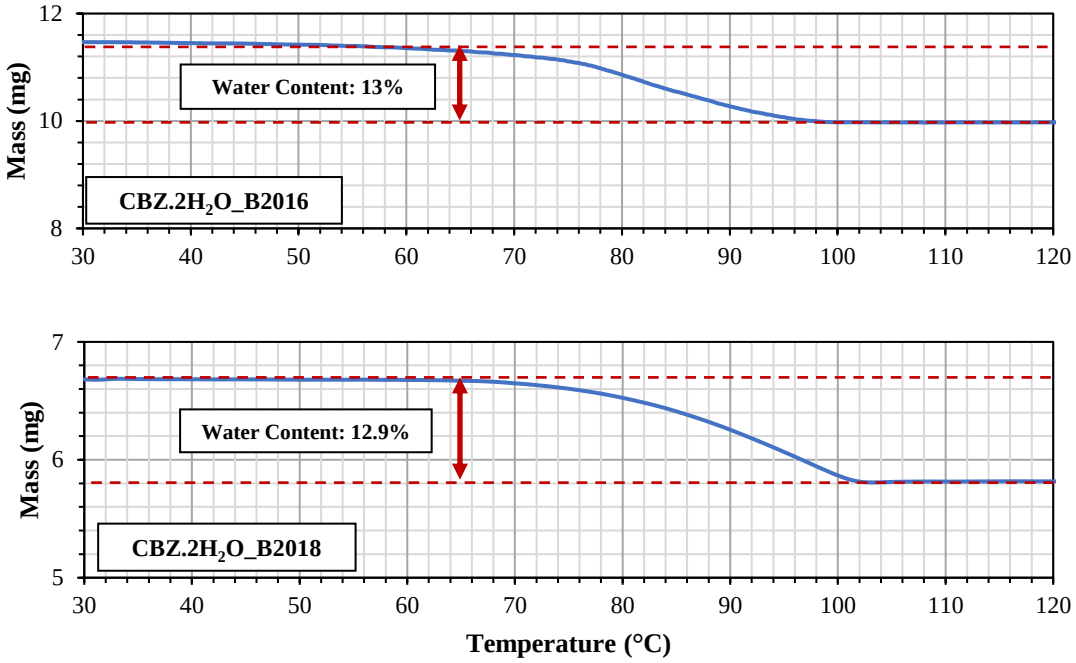

Figure 3-22 TGA curves of the two batches of carbamazepine dihydrate

Dynamic Vapour Sorption (DVS)

Dynamic vapour sorption (DVS) is a gravimetric technique that measure the water sorption isotherms of a material. It is a technique typically used to study water uptake and stability of a material under various relative humidity steps. DVS can also be used to study the formation of hydrates and solvates (Buckton and Darcy, 1996; Vollenbroek et al., 2010). In order to do so, the sample must be able to react with the solvent readily to form hydrates/solvates. The formation of hydrates/solvates will result in weight gain hence allowing the transformation to be quantified. On the contrary, the weight loss of can be used to quantify the solvent content of a hydrate/solvate.

The two batches of carbamazepine dihydrate were studied using Surface Measurement Systems DVS Advantage at 25 °C and at 0% RH. The sample is kept in the chamber until the change of mass per minute (DMDT) of the sample is less than 0.005 %/min. The initial mass of the sample and the final dry mass of the sample are used

to calculate the water content in the sample. Again, both batches appear to have water content that are comparable to the theoretical value, at 13% and 13.1%, respectively.

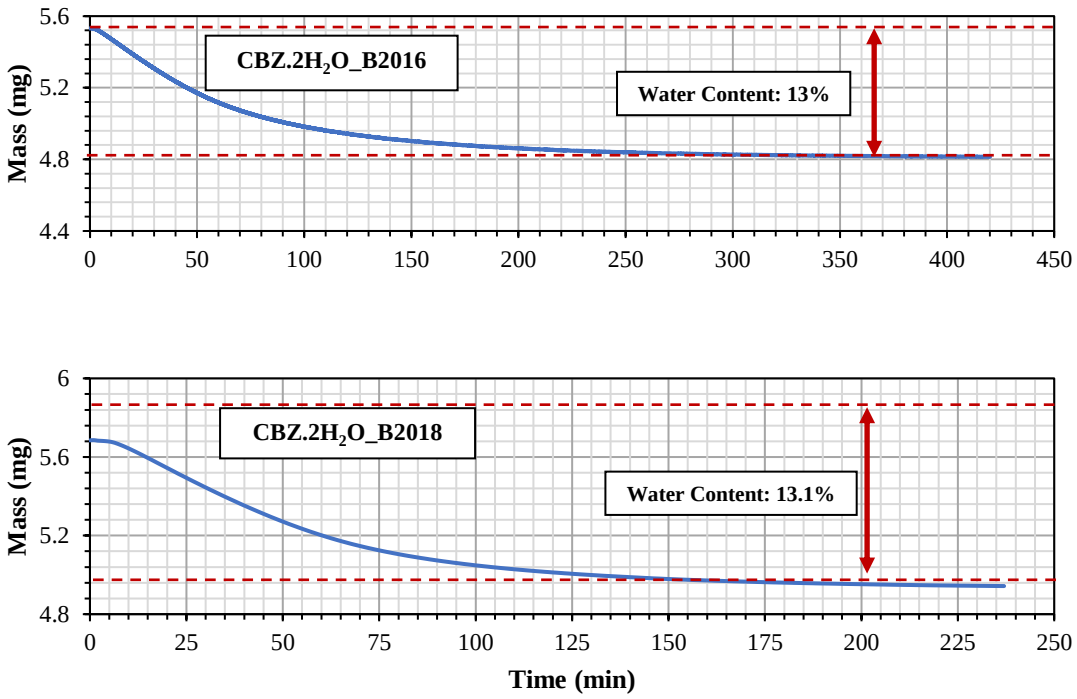

Figure 3-23 DVS curves of the two batches of carbamazepine dihydrate

3.5 Characterisation of Mechanical Properties using Nanoindentation Method

Nanoindentation is widely used to characterise mechanical properties of a material at the nano/microscale (Broitman, 2017). Its working principle involves probing an indenter into a surface under a specific load. The basic information that are required to perform nanoindentation are the penetration depth, area, time and load. Different indenter geometries can be used to perform various measurements such as Hardness, H, Young's modulus, E, fracture toughness, K_C, etc. The contact area is a function of the penetration depth and it varies with the type of indenter used (see Table 3-2). A typical indentation load-displacement curve is shown in Figure 3-24, consisting of an application of load followed by an unloading sequence.

Table 3-2 Projected area for various types of indenters (Fischer-Cripps, 2011)

Indenter type	Projected area
Sphere	$A \approx \pi 2Rh_c$
Berkovich	$A = 3\sqrt{3}h_c^2\tan^2\theta$
Vickers	$A = 4h_c^2\tan^2\theta$
Knoop	$A = 2h_c^2 \tan\theta_1 \tan\theta_2$
Cube corner	$A = 3\sqrt{3}h_c^2\tan^2\theta$
Cone	$A = \pi h_c^2\tan^2\alpha$

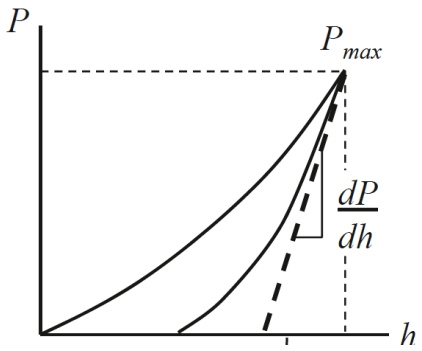

Figure 3-24 Typical indentation load-displacement curve (Fischer-Cripps, 2011)

Hardness is defined as

$$H = \frac{P}{A} \tag{3-4}$$

where P is the indentation load and A is the projected area of contact.

Indentation modulus, or reduced modulus, E^* is determined from the gradient/slope of the unloading curve at maximum load. It is defined as a function of dP/dh and the area of contact (calculated from the value of h_c) as shown below.

$$E^* = \frac{1}{2}\frac{\sqrt{\pi}}{\sqrt{A}}\frac{dP}{dh} \tag{3-5}$$

For the ease of performing the indentation, big lab-grown crystals of carbamazepine dihydrate were prepared and supplied by Dr Gabriela Schneider Rauber at the University of Cambridge and the tests were performed at the University of Leeds.

These crystals are (h00) face-dominant, similar to the two batches of carbamazepine dihydrate prepared by AbbVie. The indentations were performed using Berkovich indenter on the (h00) dominant face of the crystal, following a partial unloading approach. Four loads were used from 5 mN to 20 mN, with an interval of 5 mN (Figure 3-25). At each load increment, the sample is partially unloaded to allow the measurement of the stiffness of the contact. This enables the measurement of changes in modulus or hardness with penetration depth. The indentations were performed on six crystals. The mean hardness and reduced modulus are shown in Table 3-3, respectively. The error bars represent the standard deviation between the six different measurements. It can clearly be seen that hardness decreases with the indentation load. The reduced modulus on the other hand, is consistent regardless of the indentation load, and the mean reduced modulus is found to be 16.68 GPa.

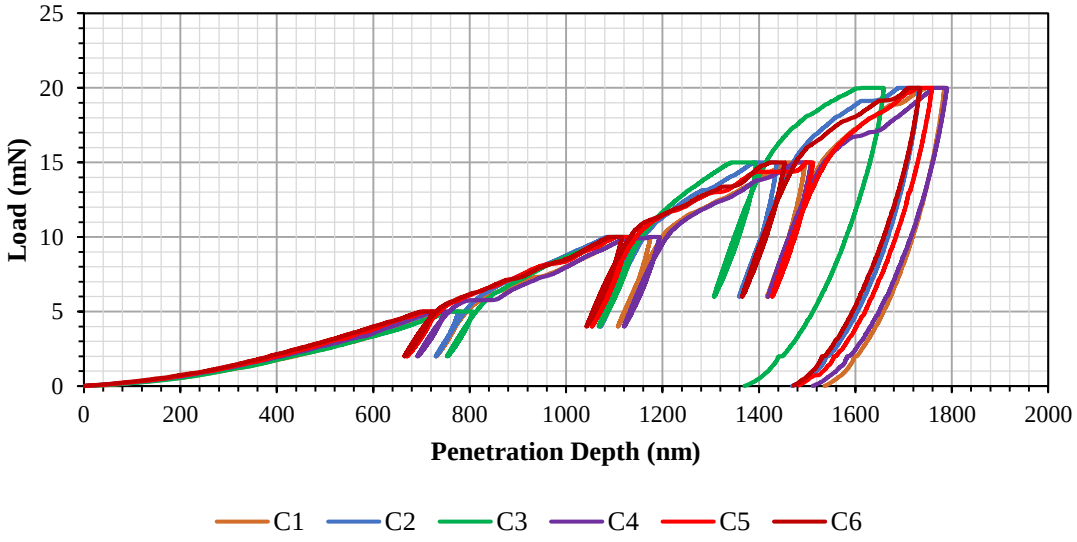

Figure 3-25 Load-displacement curves of carbamazepine dihydrate

Table 3-3 Mean hardness and reduced modulus at different loads

Test	Load (mN)	Hardness, *H* (GPa)	Standard Deviation (GPa)	Reduced Modulus, *E** (GPa)	Standard Deviation (GPa)
1	5	0.39	0.04	16.54	0.92
2	10	0.34	0.02	17.21	1.28
3	15	0.31	0.02	16.69	1.47
4	20	0.30	0.02	16.28	0.80

Chapter 4

Phase Transformation of Carbamazepine Dihydrate due to Mechanical and Thermal Stresses

4.1 Introduction

During agitated filter bed drying process of active pharmaceutical materials (API), the wet cake experiences both thermal and mechanical stresses induced by the heated jacketed vessel and the agitating impeller. Together, these stresses could lead to undesirable particle attrition and polymorphic transformation of the API. Thermal stresses are known to induce polymorphic transformation in enantiotropic crystal systems where one polymorph is the preferred and stable form within a certain temperature range compared to the others (Bauer, 2008; 2009). Mechanical stresses are also found to induce transformation of crystalline materials when sufficient stresses are applied at certain temperature (Willart et al., 2001; 2010; Desprez and Descamps, 2006). Normally, amorphisation occurs below glass transition temperature, T_g, while above T_g polymorphic transformation takes place (Willart et al., 2007). Carbamazepine dihydrate is prone to dehydration at elevated temperature and could phase transform to one of the five anhydrous polymorphs or loses its crystallinity completely if amorphisation takes place. Each polymorph has its own unique PXRD and DSC thermal footprint (shown in Chapter 2) that would help in identifying the polymorphic form of the dehydrated sample.

According to Remy et al. (2015), the hydrostatic pressure experienced by the particle bed is proportional to the scale of the agitated filter bed dryer. The range of pressure experienced by the particle bed can vary between 0.2 (50 g lab-scale dryer) to 3.0 kPa (500 kg commercial scale dryer). The scale of different agitated filter bed dryers and their corresponding hydrostatic pressure is shown in Table 4-1.

Table 4-1 Hydrostatic pressure experience by different scale of agitated filter bed dryer (Remy et al., 2015)

Scale	Pressure (kPa)
Traditional lab dryer (50 g)	0.2
Pilot plant dryer (150 kg)	1.4
Commercial Scale dryer (500 kg)	3.0

The focus of this chapter is to assess the effect of mechanical and thermal stresses, separately and concurrently, on the phase transformation of carbamazepine dihydrate crystals. Mechanical stresses are induced to the crystals by subjecting them to impact and bulk crushing. On the other hand, thermal stresses are induced through heating the crystals in an oven. DSC and PXRD analyses are then performed to assess the phase transformation of the crystals from hydrate form to anhydrous form.

4.2 Phase Transformation due to Mechanical Stress

Mechanical stresses induced by the impeller is one of the two major stresses that the particle bed experiences during agitated filter bed drying process. This study aims to investigate the influence of mechanical stresses (impact and bulk crushing) on the phase transformation of the carbamazepine dihydrate crystals.

4.2.1 Materials and Methods

CBZ.2H_2O_B2016 crystals were used in this study. The crystals were subjected to impact by using the dry dispersion unit, Scirocco, of Malvern Panalytical Mastersizer 2000,

which is a commercial particle size analyser based on laser diffraction technique. The scirocco unit comprises an L-elbow that is designed to break down agglomerates present in the measuring sample. The dispersion pressure of the unit is controllable, hence making it a suitable device for inducing impact damage to the crystals. Four different dispersion pressures were used, and 2 g of crystals were used in each test.

Apart from impact, the crystals were also subjected to bulk crushing using Instron material testing device. 1 g of sample was fed into a 20 mm die and flattened before being loaded by a piston at a displacement rate of 1 mm/min until the maximum load was reached. The maximum loads tested were, 0.1, 0.5, 1 and 5 kN and the corresponding pressures exerted to the particle bed are shown in the table below.

Table 4-2 Maximum loads and their corresponding pressures during bulk crushing

Maximum Load (kN)	Pressure (GPa)
0.1	0.3
0.5	1.6
1	3.2
5	15.9

The stressed crystals were collected, and wet dispersion technique was used to measure their size distributions. The collected samples were also analysed using Bruker D8 Advance XRD to assess the associated phase transformation due to impact and bulk crushing.

4.2.2 SEM Observations

SEM micrographs were collected after each test and the comparison between them are shown in Figure 4-1. It can clearly be seen that carbamazepine dihydrate crystals are very prone to impact breakage. A significant size reduction can be observed even at the lowest dispersion pressure, at 0.5 barg. As the dispersion pressure increases, the progeny size decreases. The broken crystals appear to be “blocky” with sharp edges, suggesting the

presence of cleavage planes in the crystal. The presence of cleavage planes in the crystals and their influence on breakage behaviour is discussed comprehensively in Chapter 6.

On the other hand, bulk crushing does not cause as much size reduction as compared to impact. The SEM micrographs of the crystals after being crushed with different loads are shown in Figure 4-2. At 5 kN, the reduction of crystal size becomes conspicuous through visual observation. In addition to the obvious size reduction, agglomeration of particles also become prominent as the load increases as illustrated in Figure 4-3. Huge agglomerates that appear to have fused together are found when the crystals are crushed at 5 kN. Substantial deformation of the crystals is observed too after bulk crushing. An interesting example is given in Figure 4-4 where it can be seen clearly that the crystal (circled), after being crushed at 0.5 barg, is deformed but no evidence of breakage is observed.

Bulk crushing and impact are two very different loading methods where the former is quasi-static while the latter is dynamic. During impact, particles are being accelerated by the air in the Scirocco disperser before hitting on the L-elbow. Even though the experiments were performed in bulk, the particle-particle interactions are in fact very infrequent along the air stream that carries the particles, mimicking that of single particle impact. Upon impact, the incident kinetic energy is dissipated either in the form of particle relocation/reorientation or, if the energy is large enough, initiating cracks on the crystal and subsequently leading to crystal breakage. On the contrary, the energy is distributed across the particle bed during bulk crushing where the crystals are in multiple-contact with their neighbouring crystals, providing support to each other. This then gives rise to the occurrence of agglomerates and deformed crystals in the sample upon being loaded as the particle bed is experiencing increasing compressive normal and hoop stresses while the space available for particle relocation and reorientation is reducing.

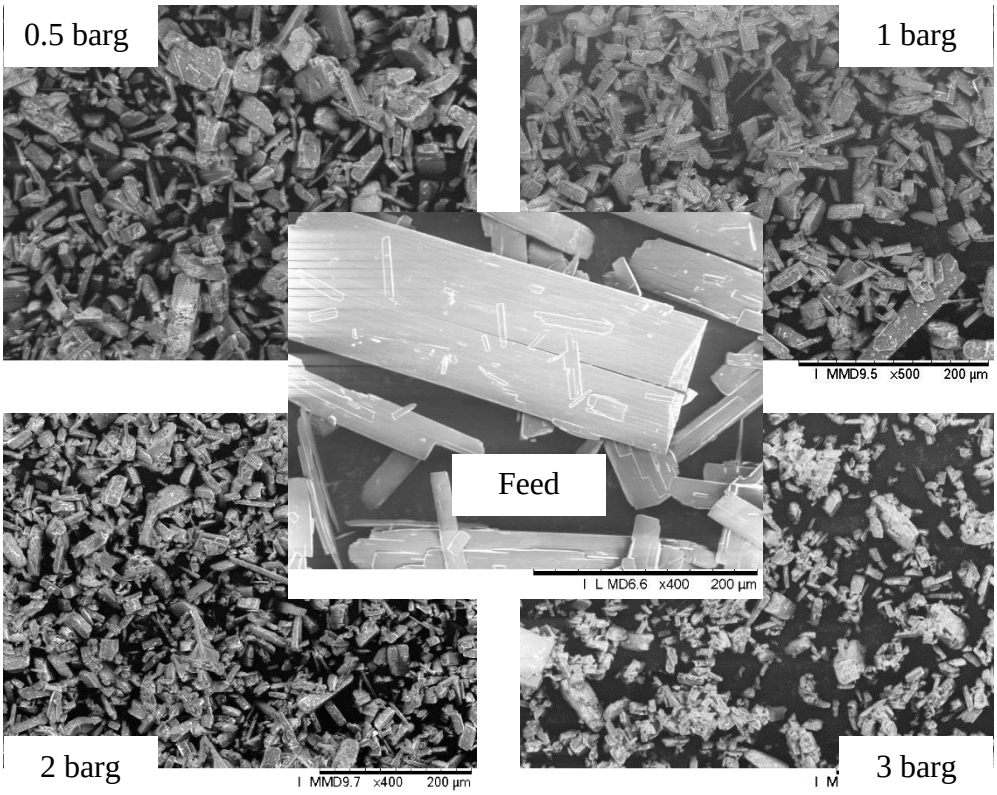

Figure 4-1 SEM micrographs of the feed and collected samples after being dispersed at 0.5 1, 2 and 3 barg

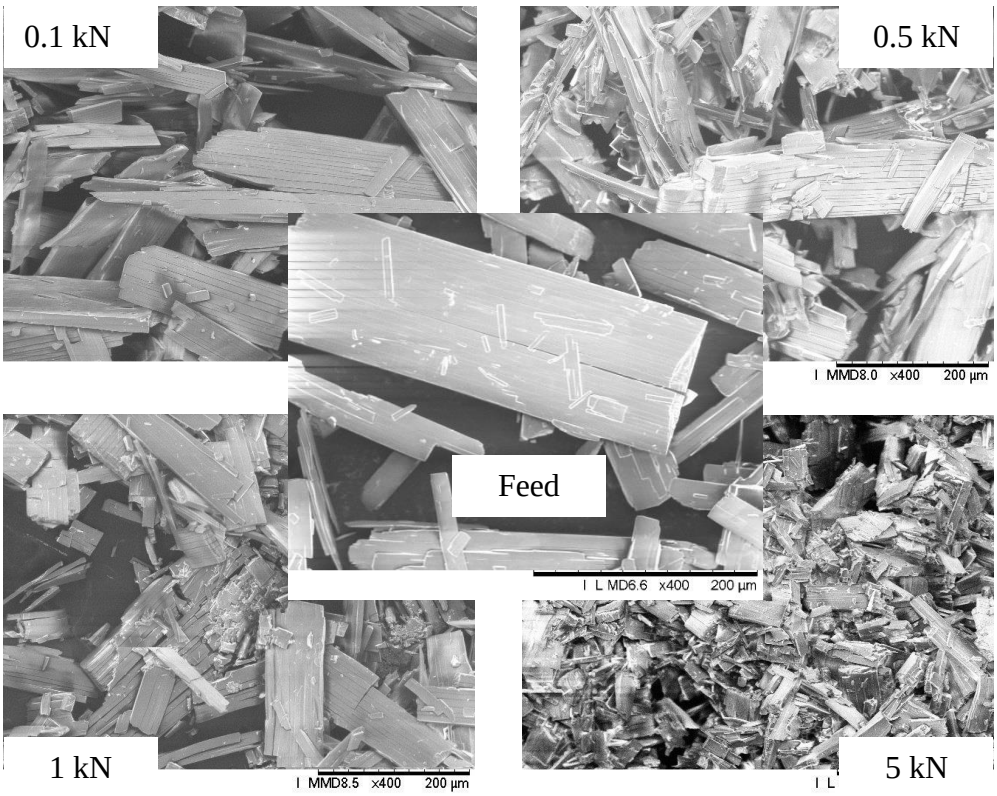

Figure 4-2 SEM micrographs of the feed and collected samples after being crushed at 0.1, 0.5, 1 and 5 kN

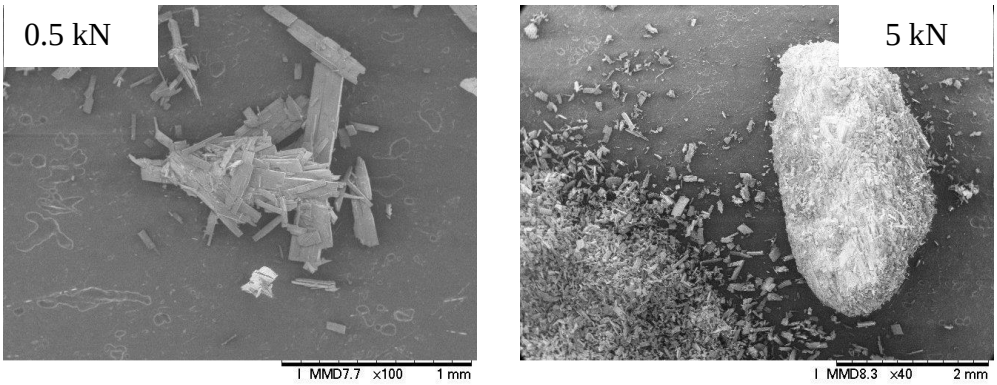

Figure 4-3 Formation of agglomerates due to bulk crushing

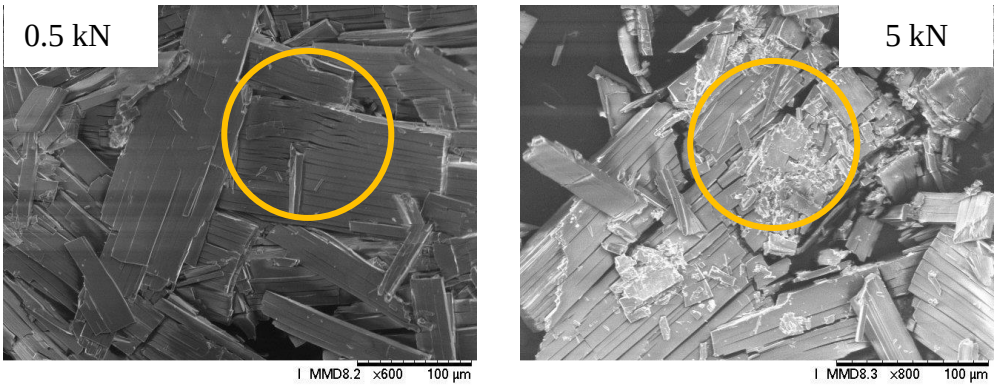

Figure 4-4 Crystal deformation due to bulk crushing

4.2.3 Particle Size Analysis by Wet Dispersion Technique

The collected samples were dispersed in cyclohexane and their size distributions were analysed using Hydro 2000S, the wet dispersion unit of the Mastersizer 2000. The volume-based size distributions of the impacted and crushed samples analysed are shown in Figure 4-5 and 4-6. Shifting of the particle size distributions to the left is observed for both impact and bulk crushing, indicating significant size reduction of the crystals upon impact, though to a lesser extent in the latter case. This result is in line with the observations made from SEM micrographs in the previous section. The feed distribution appears to be trimodal and that can be attributed to the limitation of laser diffraction technique. Laser diffraction technique is suitable for analysing the particle size distribution of equant particles but falls short when it comes to highly acicular particles.

Using optical imaging technique, the size distribution of the same sample appears to be monomodal as depicted in chapter 3. The trimodal appearance of the distribution is in fact the manifestation of the diffraction of the three highly varied dimensions (length, width and thickness) of carbamazepine dihydrate crystals. The reduction in particle size expressed in the shift of specific surface area, $\Delta SSA/SSA_0$ as a function of dispersion pressure and maximum load is shown in Figure 4-7 and 4-8, respectively. ΔSSA is defined as the difference of specific surface area between the feed (SSA_0) and the sample of interest. $\Delta SSA/SSA_0$ gives a measure of the extent of generation of the new surface area. At 0.5 barg, the $\Delta SSA/SSA_0$ is ~3. This is a relatively significant increase in the specific surface area compared to the other subsequent dispersion pressures. As for bulk crushing, at 0.1 kN, the $\Delta SSA/SSA_0$ is ~2.5. increasing the maximum load from 0.5 to 1 kN does not result in observable increase of the $\Delta SSA/SSA_0$. The specific surface area of the sample after being loaded at 5 kN is ~4.5 times the specific surface area of the feed.

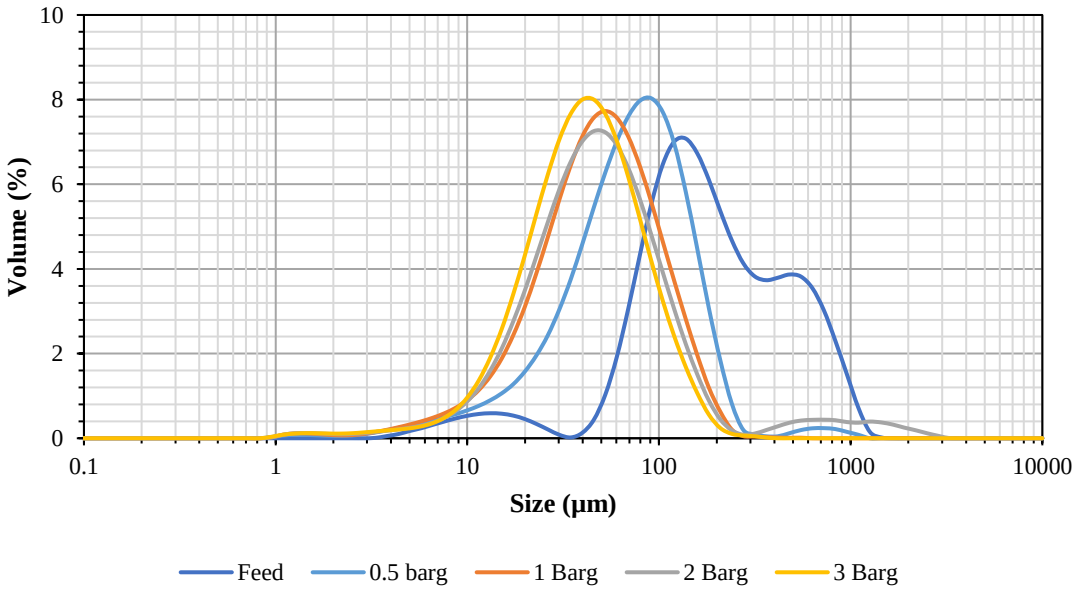

Figure 4-5 PSDs of impacted CBZ.2H₂O crystals at different dispersion pressures

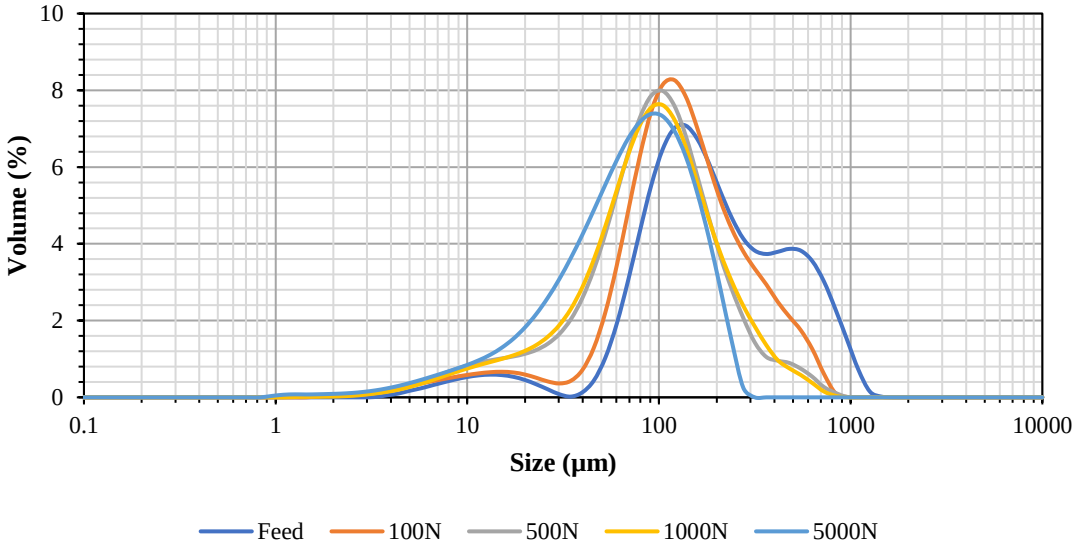

Figure 4-6 PSDs of crushed CBZ.2H₂O crystals at different maximum loads

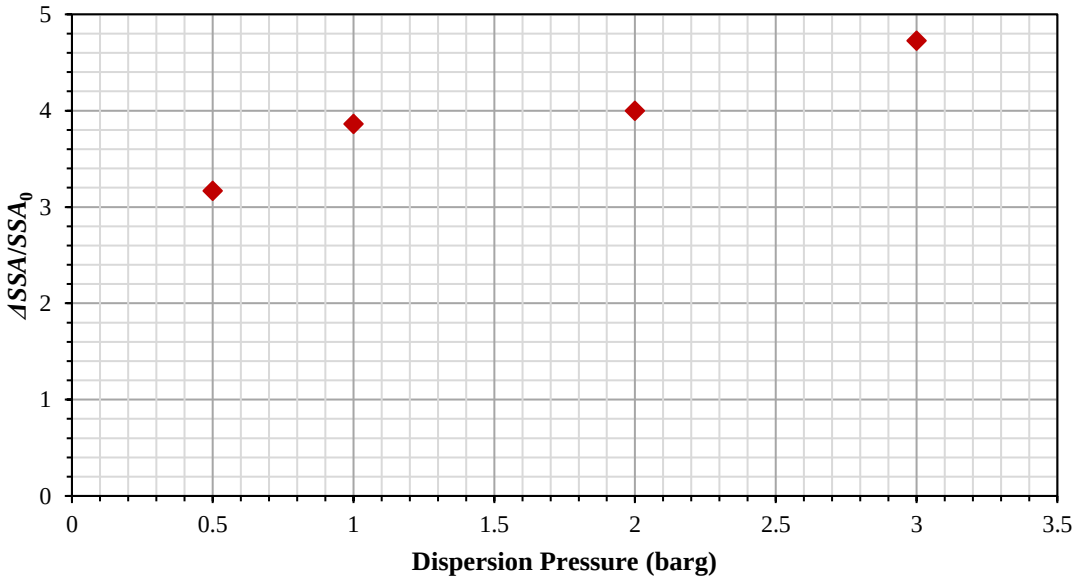

Figure 4-7 Shift of specific surface area as a function of dispersion pressure

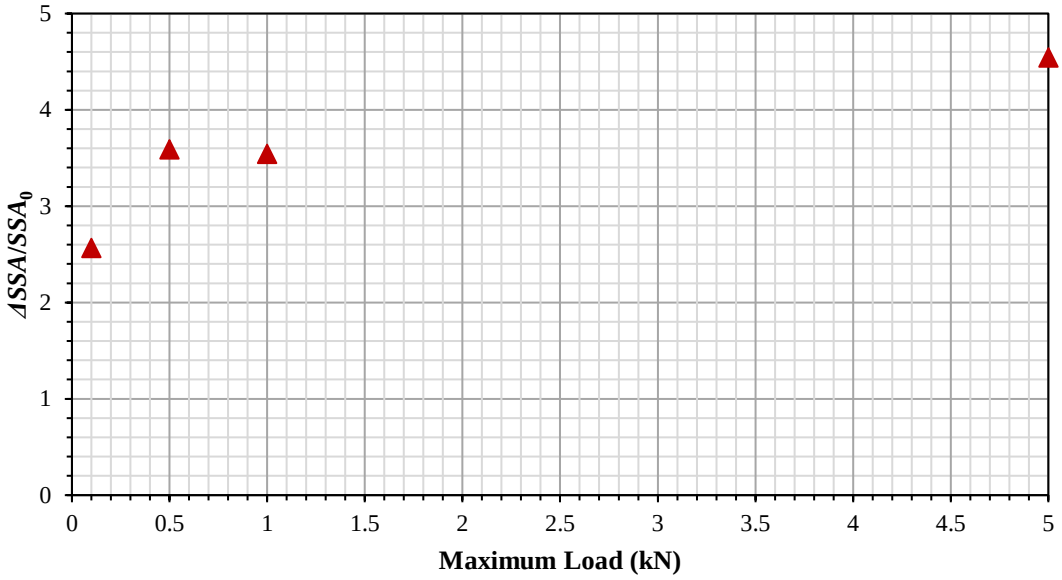

Figure 4-8 Shift of specific surface area as a function of maximum load

4.2.4 Phase Transformation Study using PXRD

The diffraction patterns of the CBZ.2H_2O crystals are shown in Figure 4-9. The first diffraction pattern shown is the calculated pattern of carbamazepine dihydrate from Mercury Software. Compared to the reference, the diffraction pattern of the feed appears to have less diffraction peaks. As previously discussed in Chapter 2, acicular crystals of CBZ.2H_2O have a very high tendency to orient themselves in a particular direction, hence exposing the dominant face (h00) of the crystals in the measurement of their diffraction pattern. This is reflected in the diffraction pattern as a very sharp peak at ~9 °, which corresponds to the (100) plane of the crystal. As the dispersion pressure is increased and the particle size is reduced, the artefact caused by preferred orientation of the crystals becomes less prominent, revealing the peaks that were previously masked out by the strong diffraction signal from the (100) plane. The peaks highlighted in yellow boxes are some of the characteristic peaks of CBZ.2H_2O crystals. The peaks corresponding to (040) and (140) get more discernible as the crystal size gets smaller, along with other peaks of CBZ.2H_2O. These diffraction patterns are compared against the diffraction patterns of the

anhydrous polymorphs of carbamazepine and no obvious evidence of phase transformation is discerned. Similar results are obtained from the diffraction patterns of crushed samples. Increasing the maximum load of bulk crushing reduces the crystal size and hence reducing the effect of preferred orientation on the diffraction pattern of the crystals (Figure 4-10). The diffraction peaks of non-dominant faces become clearer as the particle size becomes smaller. No apparent phase transformation is observed for the crushed samples. These results suggest that carbamazepine dihydrate crystals do not undergo phase transformation within the range of mechanical stressing conditions tested. Even though the crystals have undergone significant breakage, their crystal structure remains intact.

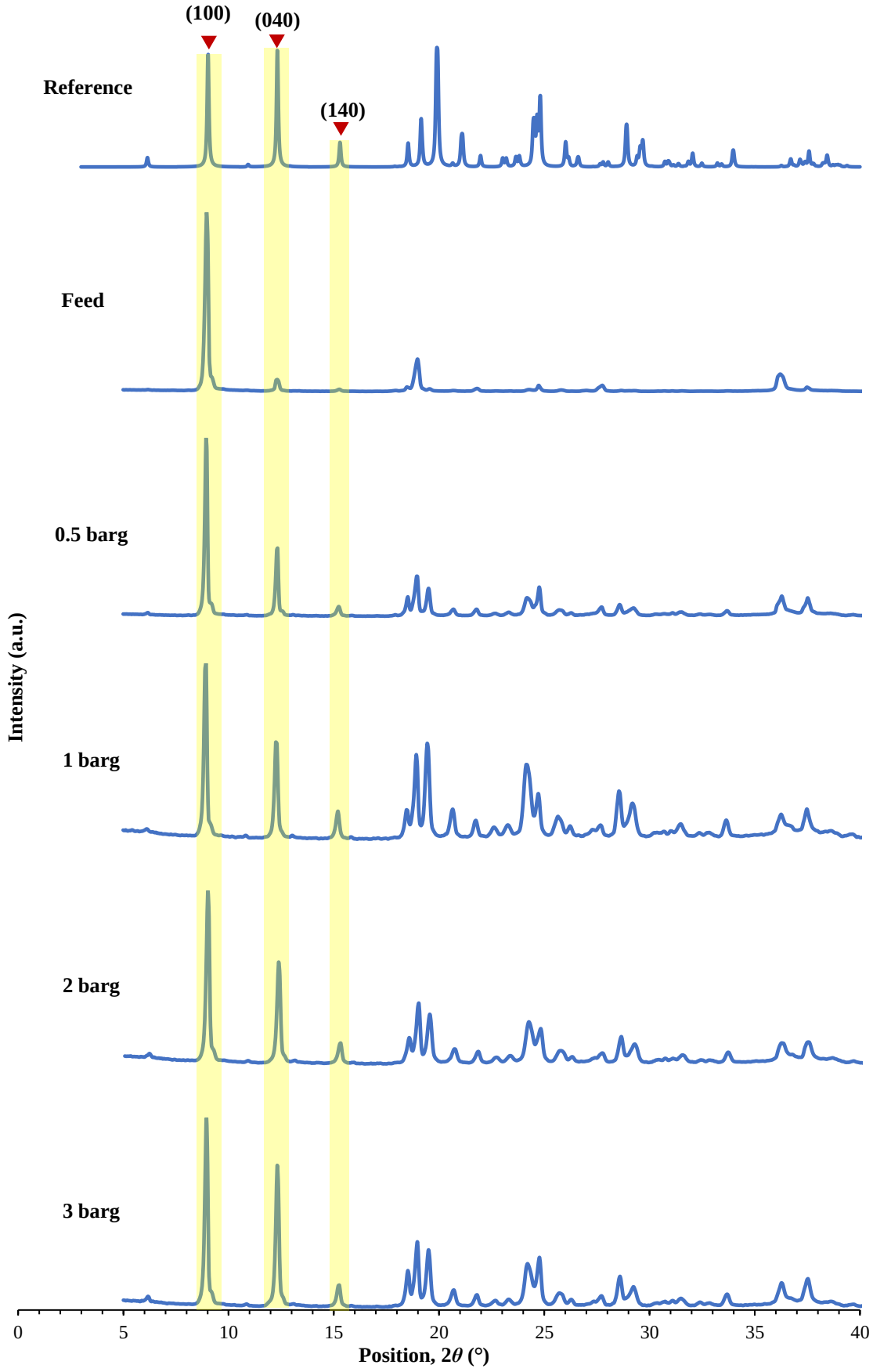

Figure 4-9 X-ray diffraction patterns of CBZ.2H₂O samples impacted at different dispersion pressures

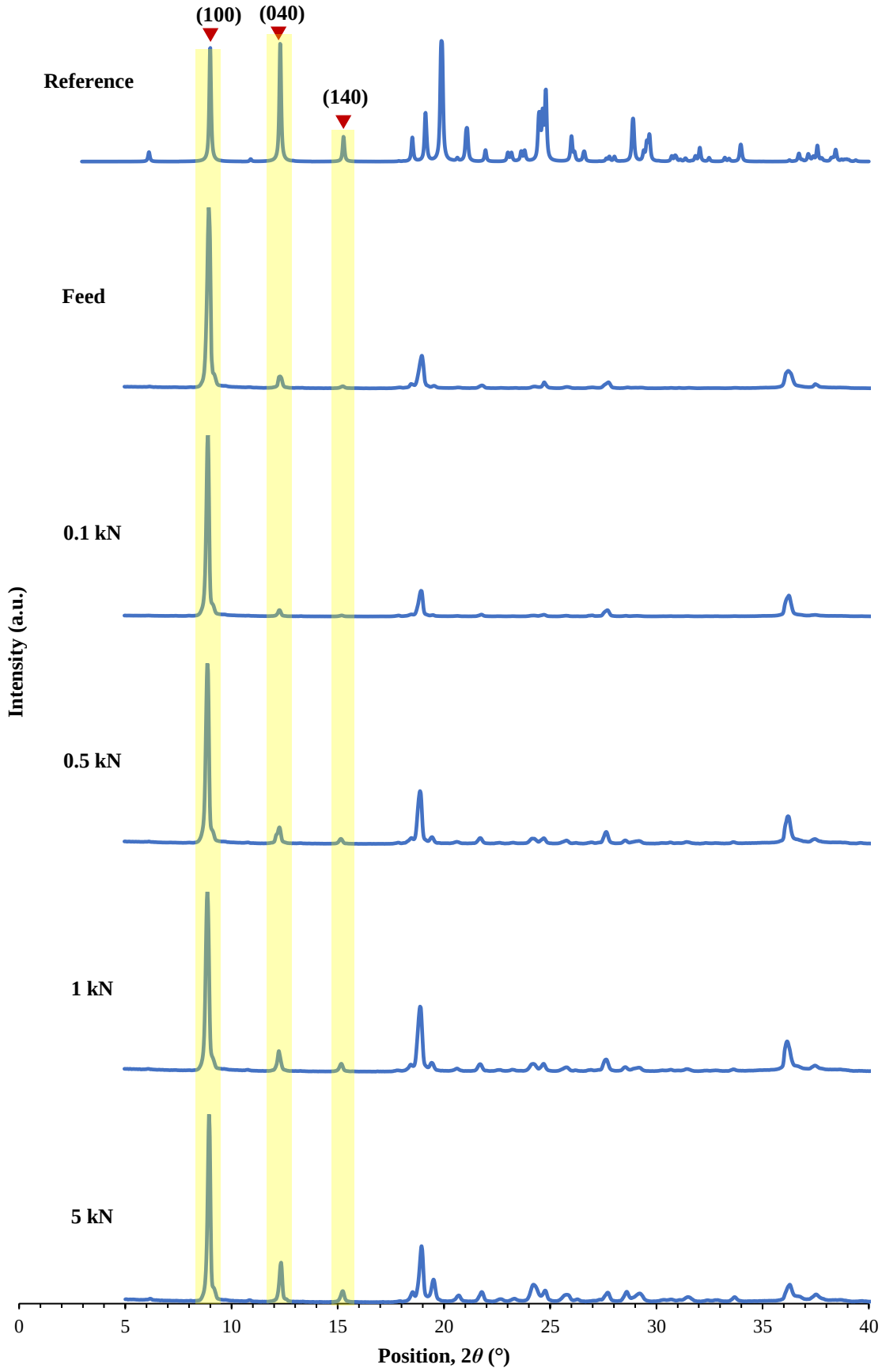

Figure 4-10 X-ray diffraction patterns of CBZ.2H₂O samples crushed at different maximum loads

4.3 Phase Transformation due to Thermal Stresses

4.3.1 Materials and Methods

4.3.1.1 Thermal Analysis using DSC

CBZ.2H_2O_B2016 crystals were used in this work. The thermal behaviour of these crystals was studied using DSC at different heating rates. The experiments were carried out at six different heating rates of 2, 6, 10, 15, 20 and 30 °C/min. The temperature range tested was from 30 to 230 °C with a nitrogen flow of 50 ml/min over the sample. A sample size of ~ 5 mg was used for each test. The aluminium crucibles were crimped, and a hole was punched on top of the lid to allow the water vapour to escape.

4.3.1.2 Inducing Phase Transformation through Oven Heating

CBZ.2H_2O_B2016 crystals were spread evenly in a petri dish and subjected to heating at 48 °C. Nine samples were heated at 1, 2, 3, 4, 5, 6, 7, 8 and 24 hours. The samples were collected and analysed using DSC and PXRD right after each test to assess the phase transformation. The experimental setup for DSC is similar to the one used for thermal analysis in the previous section (4.3.1.1), but the heating rate is fixed at 10 °C/min. As for the PXRD characterisation, the operating conditions are the same as the one described in Section 4.2.1.

4.3.2 Thermal behaviour of Carbamazepine Dihydrate under DSC

The DSC thermographs of CBZ.2H_2O_B2016 as a function of heating rate are shown in Figure 4-11. Two endotherms can be observed in all the thermographs. The first represents the dehydration/vaporisation of crystal water, while the latter corresponds to

the melting of the dehydrated carbamazepine. The DSC thermal characteristics of each carbamazepine polymorphs reported by Grzesiak et al. (2003) are summarised below:

Form I

i. One endothermic peak at ~193 °C, corresponding to the melting point of this polymorphic form.

Form II

i. One small endotherm in the range between 140 – 160 °C followed by an exotherm that corresponds to the recrystallisation to Form I.
ii. Subsequent increase in temperature lead to the melting of Form I at ~193 °C.

Form III

i. Endotherm that corresponds to melting and recrystallisation of Form III between 162 and 175 °C.
ii. Endothermic peak at ~193 °C, corresponding to the melting point of Form I

Form IV

i. An endothermic peak at ~187 °C (corresponding to the melting of Form IV)
ii. Another endothermic peak at ~192 °C (corresponding to the melting of Form I)

Heating rate has a pronounced effect on the dehydration of the samples. The onset, peak and endset temperatures of the dehydration endotherms are shown in Figure 4-12 (the onset temperature presented here is the extrapolated onset temperature which is defined as the intersection between the extrapolated baseline and the extrapolated edge of the transition. See Figure 4-13). Increasing the heating rate increases the onset temperature of dehydration though the change is small. The effect of heating rate is most discernible on the peak and endset temperature of dehydration. At a heating rate of

2 °C/min, the dehydration commences at ~48 °C and finishes at ~76 °C, while at 30 °C/min, the dehydration commences at ~58 °C and finishes at 120 °C. These dehydration temperatures are in agreement with the literature reported (Li et al., 2000; Yoshihashi et al., 2002). The melting of the dehydrated crystals, on the other hand, are not affected by the heating rate. The endotherms appear sharp and the peak melting temperature is independent of the heating rate, remaining at ~190 °C. This corresponds to the melting temperature of anhydrous polymorph Form I of carbamazepine, indicating the polymorphic form of anhydrous carbamazepine that the crystals dehydrate to. The onset, peak and endset melting temperatures of CBZ.2H_2O_B2018 as a function of heating rate are shown in Figure 4-14.

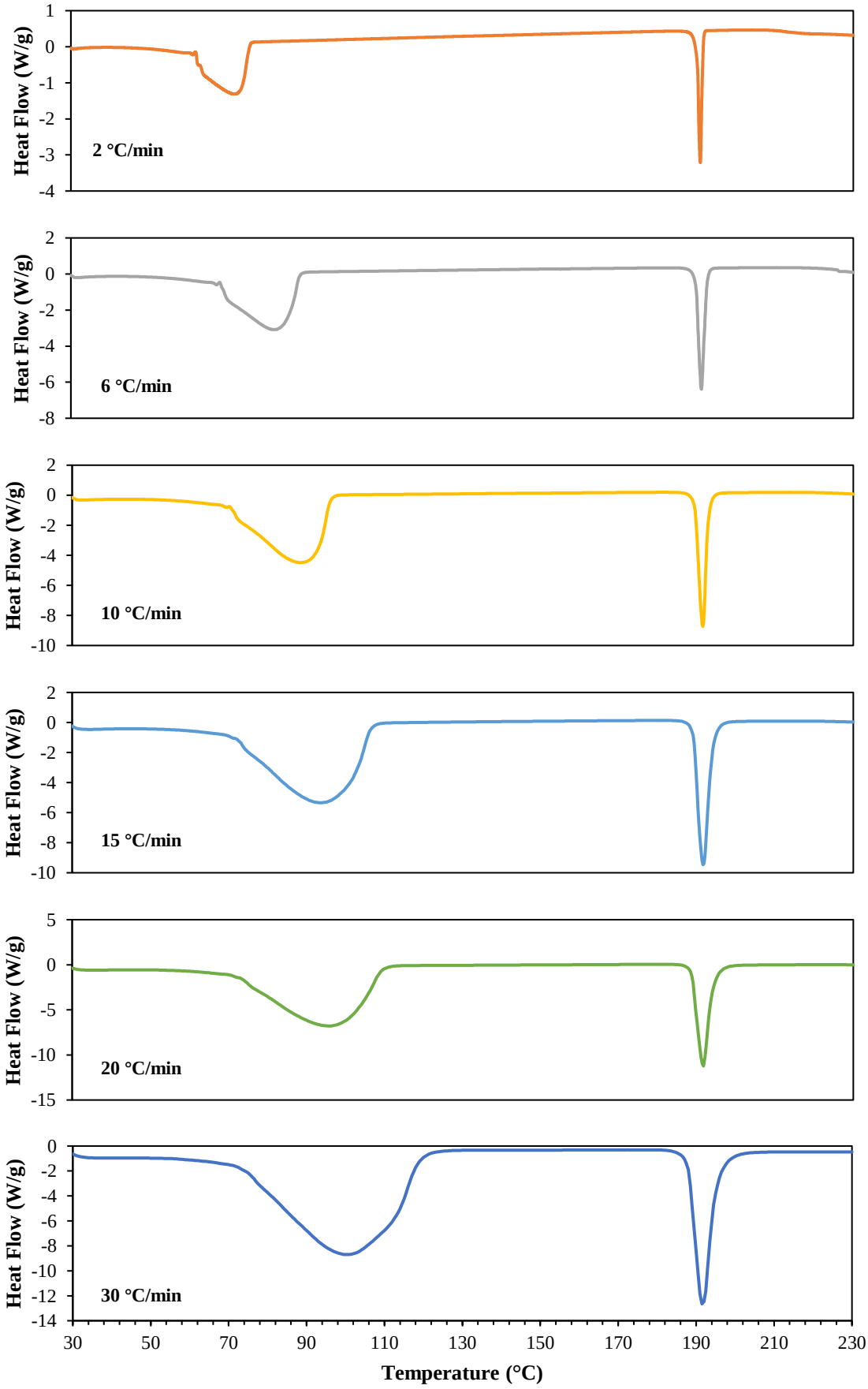

Figure 4-11 DSC thermographs of CBZ.2H$_2$O_B2018 at different heating rates

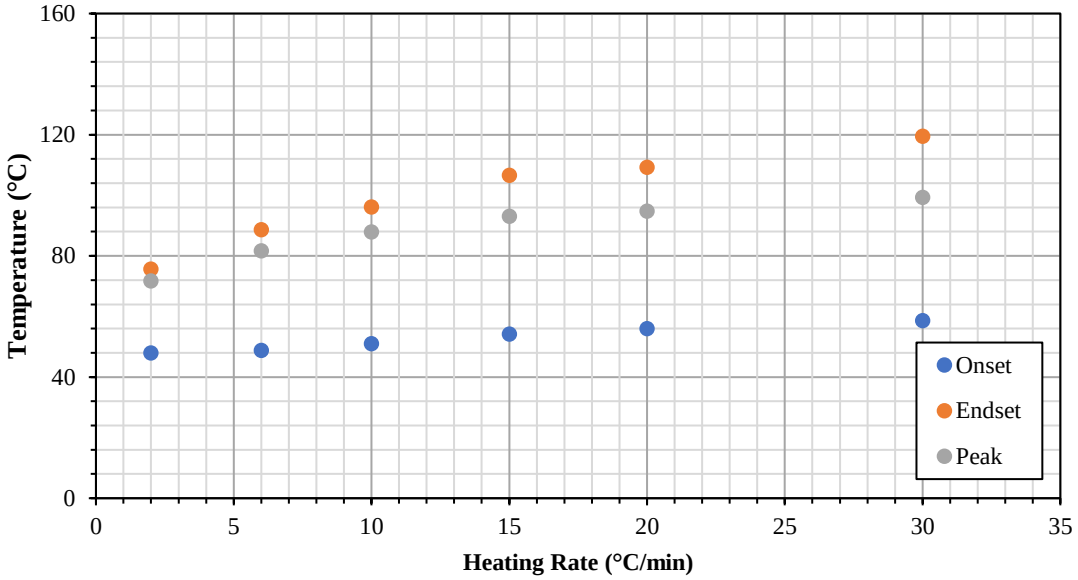

Figure 4-12 Onset, peak and endset dehydration temperatures of CBZ.2H$_2$O_B2018 as a function of heating rate

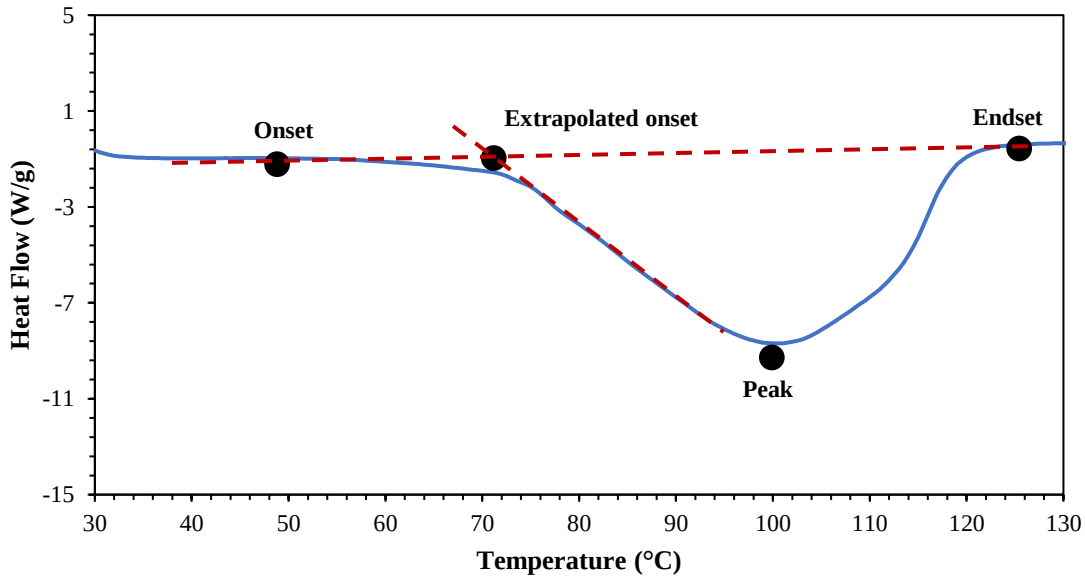

Figure 4-13 Illustration of onset, extrapolated onset, peak and endset temperatures

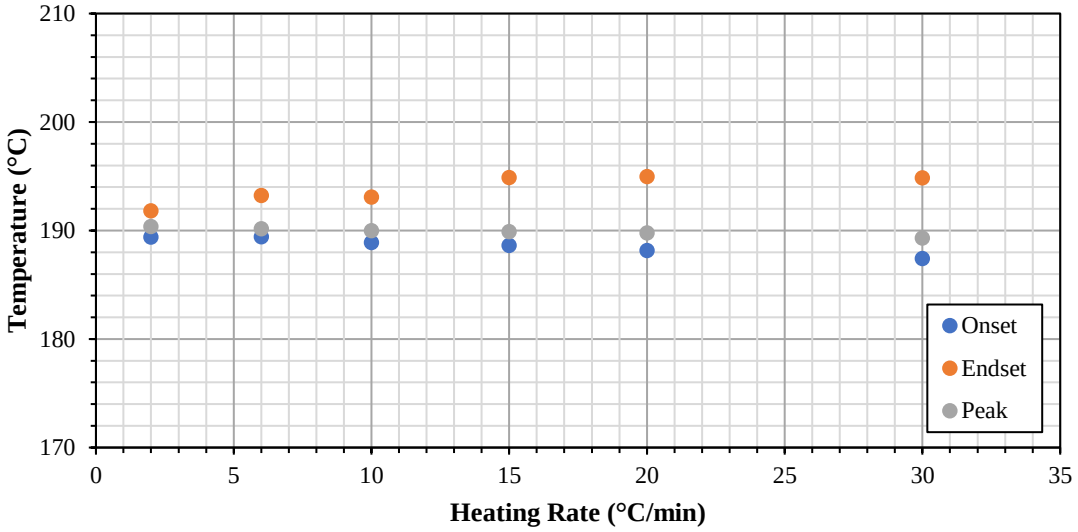

Figure 4-14 Onset, peak and endset melting temperatures of CBZ.2H₂O_B2018 as a function of heating rate

The thermal kinetics of dehydration of carbamazepine dihydrate can be modelled using Arrhenius equation (Arrhenius, 1889) as shown below.

$$k = A\exp\left(\frac{-E_a}{RT}\right) \tag{4-1}$$

where k is the rate constant, A the pre-exponential factor, E_a the activation energy, R the gas constant and T the temperature. The Arrhenius parameters can be obtained from the DSC thermographs by using the Kissinger method (1957), which assumes the reaction rate reaches maximum at the peak temperature of the reaction and it takes the form below.

$$\ln\left(\frac{\beta}{T_P^2}\right) = \ln\frac{AR}{E_a} - \frac{E_a}{R}\frac{1}{T_P} \tag{4-2}$$

where β is the constant heating rate, T_P the peak temperature of the reaction, E_a, the activation energy, A the pre-exponential factor and R the gas constant. The Kissinger plot is shown in Figure 4-15. It can be seen that the Kissinger method fits the DSC data very well, having achieved a coefficient of determination, R^2, of 0.99.

Another commonly used method to determine the Arrhenius parameters is the Ozawa method (1965) as shown below.

$$\ln(\beta) = const - 1.052\frac{E_a}{RT_P} \tag{4-3}$$

where β is the heating rate, E_a the activation energy, R the gas constant and T_P the peak temperature of the reaction. The DSC data fitted with Ozawa method is depicted in Figure 4-16. A very clear linear relationship between the heating rate and the Arrhenius parameters can be observed. A summary of the Arrhenius parameter for dehydration is shown in the table below. The results are in agreement with the literature reported by Liu et al. (2013).

Table 4-3 Summary of Arrhenius parameters for dehydration

	Kissinger	Ozawa
Activation Energy, E_a (kJ/mol)	96.4	97.5
R^2 (-)	0.9958	0.9963

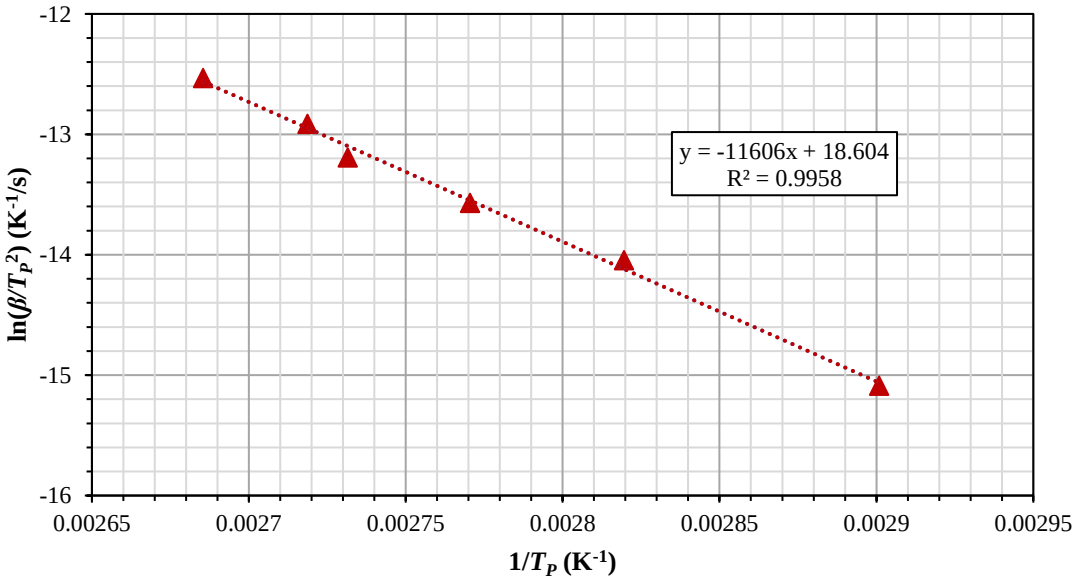

Figure 4-15 Linear relationship established according to Kissinger equation for dehydration

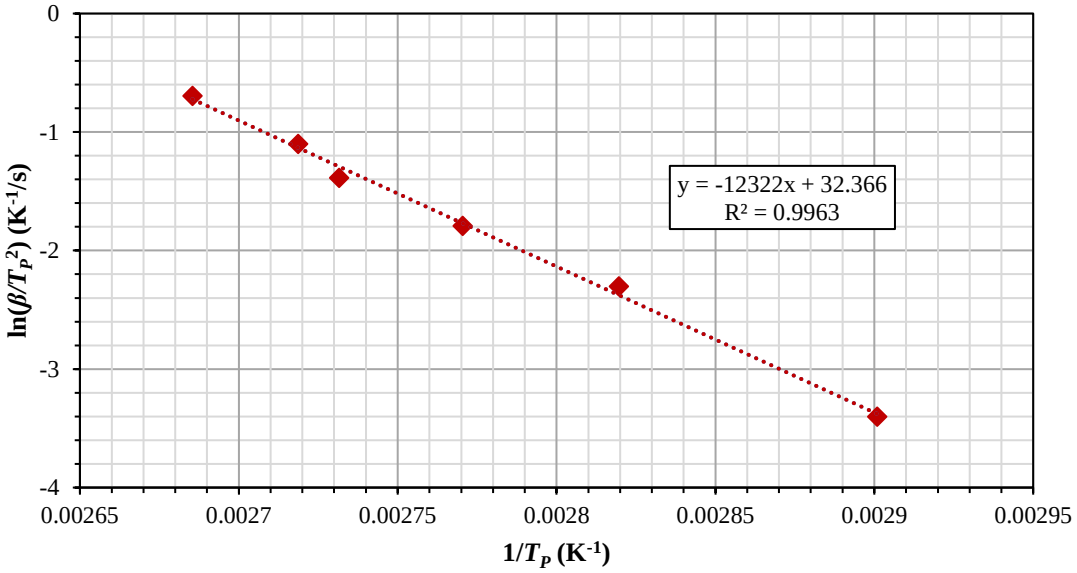

Figure 4-16 Linear relationship established according to Ozawa equation for dehydration

4.3.3 Phase Transformation of Dihydrate to Anhydrous Carbamazepine

4.3.3.1 Physical Changes of Crystal Morphology of CBZ.2H$_2$O upon Heating

From the thermal analysis using DSC, it was found that the dehydration commences at 48 °C at the lowest heating rate tested. This temperature was then used to heat up CBZ.2H$_2$O crystals at different lengths of time in an oven to study the progressive changes of the crystal morphology as a function of time under SEM. The SEM micrographs of the CBZ.2H$_2$O samples being heated for 1 up to 24 hours are shown in Figures 4-17 and 4-18. Under low magnification, the crystal shape appears to remain identical to the original crystals even after it was heated for 1 hour, little change is observed (A1 & A2). However, a closer look at the surface of the crystals reveals the formation of whisker-like features on the dominant (h00) face. After being heated for 2 hours, notwithstanding the patchy surfaces of the crystals, the overall crystal structure still remains intact and preserves the platy-like morphology (B1 & B2). At this point, the surface coverage of whisker-like features is found to have increased but not covering the whole crystals. Apart from increasing the surface coverage of the whisker-like features

and roughening of the crystal surfaces, heating the crystals for extended period does not impose any significant change to the macroscopic crystal morphology of CBZ.$2H_2O$. The transformation of the crystals seems stop progressing after four hours of heating. The whisker-like features are ubiquitous all over the surface of the crystals (see Figure 4-19). The formation of whiskers has been reported in the work of Khoo et al. (2013) in which the crystals were subjected to vacuum pressure dehydration. It was found that those whiskers are in fact Form I carbamazepine that nucleates on the surface of the crystals upon dehydration. PXRD and DSC analyses confirmed the dehydrated crystals are indeed Form I carbamazepine, agreeing with the literature (discussed in the following sections). These dehydrated crystals are porous as shown in figure G3, where the edge of one of the crystals is chipped off, exposing the crystal internal structure.

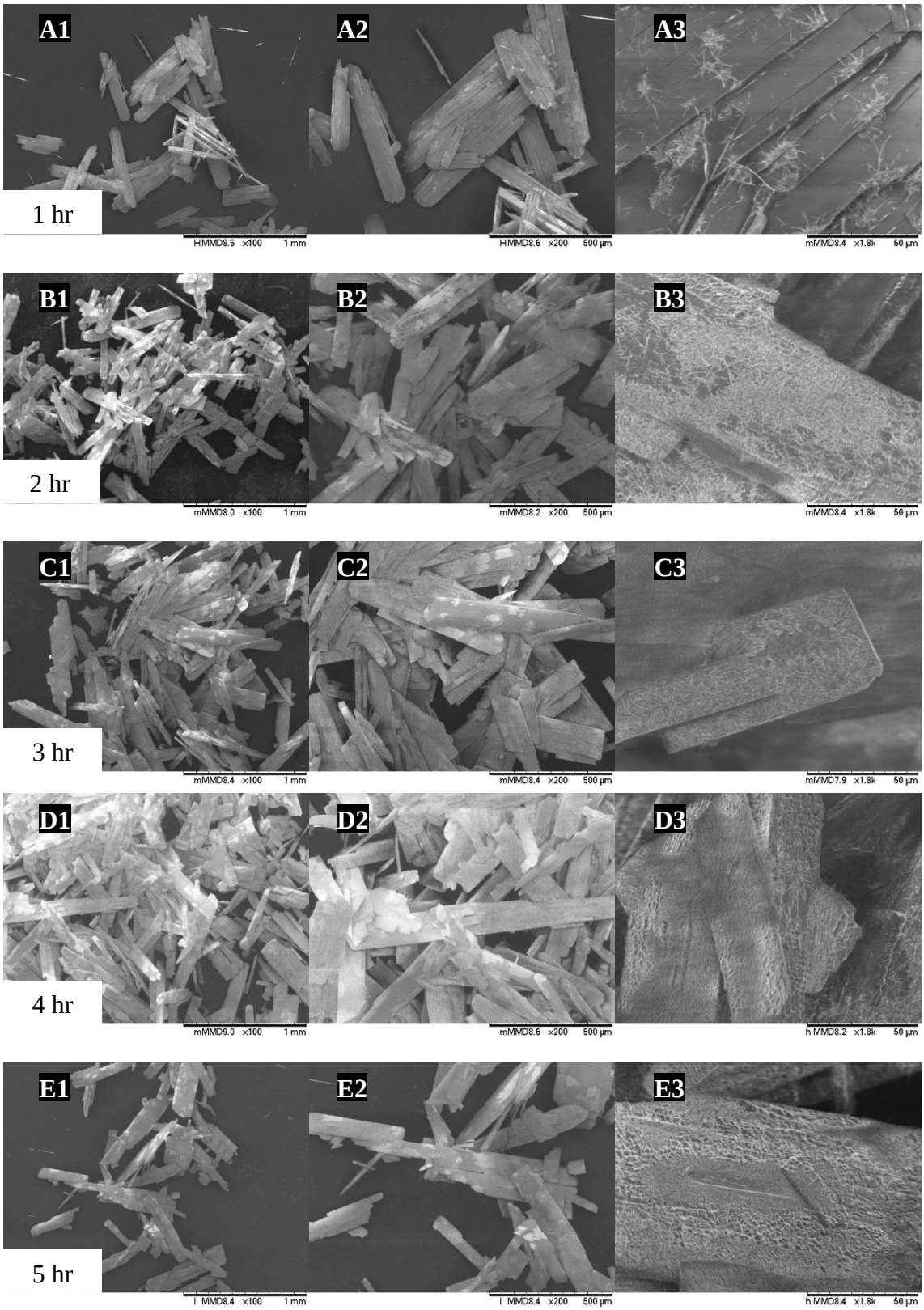

Figure 4-17 Morphological changes of CBZ.2H$_2$O at 48 ° as a function of time (1 – 5 hours)

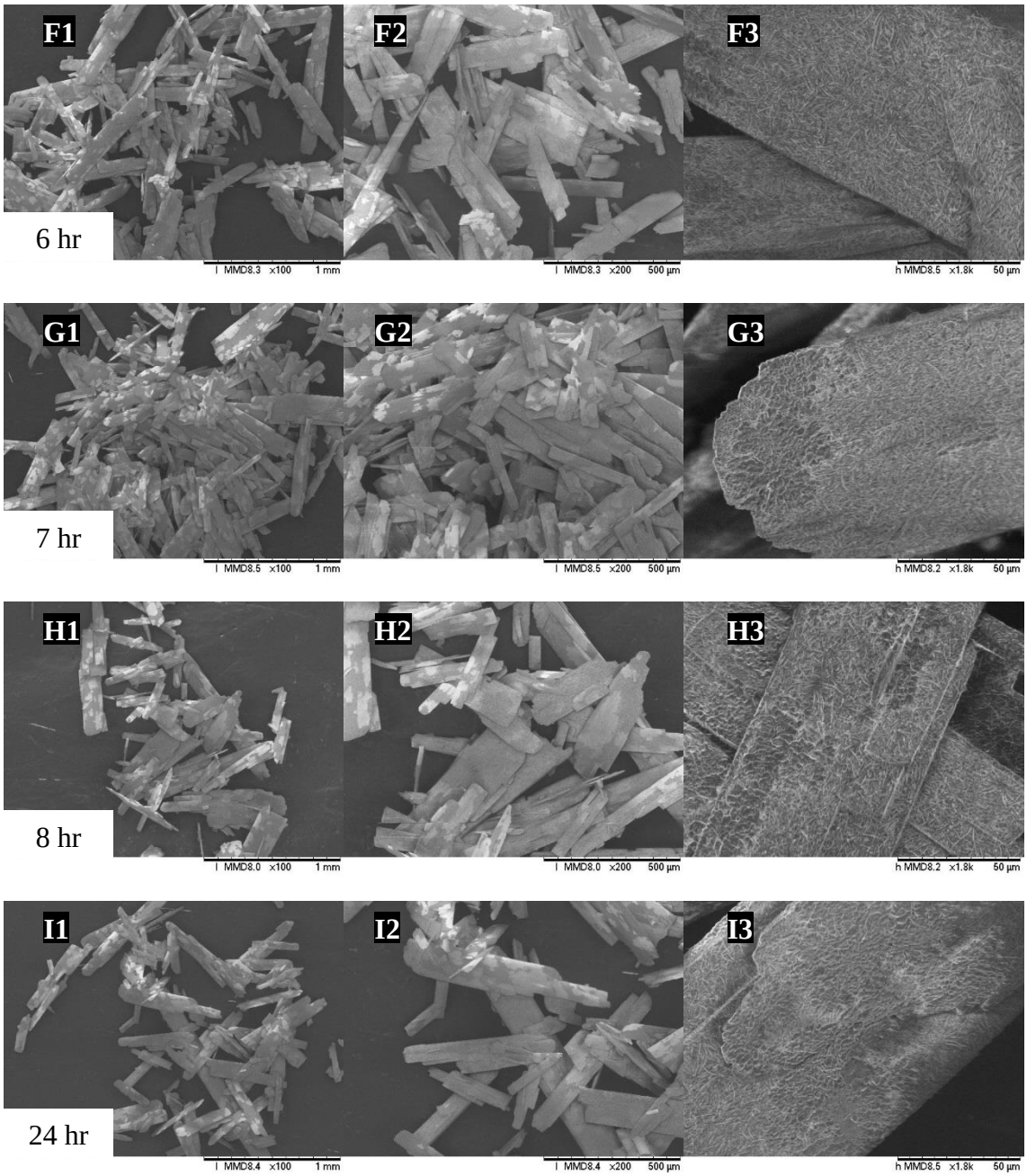

Figure 4-18 Morphological changes of CBZ.2H$_2$O heated at 48 °C as a function of time (6 – 24 hours)

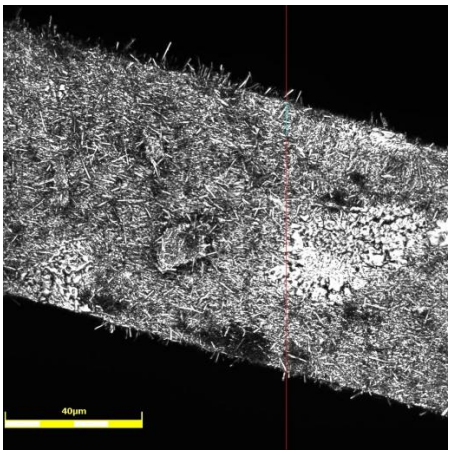

Figure 4-19 CBZ.2H_2O crystals fully covered in whiskers after being heated for 24 hours (captured using confocal laser microscope)

4.3.3.2 Solid-state Characterisation of Heated CBZ.2H_2O

The diffraction patterns of CBZ.2H_2O crystals heated for different periods are shown in Figures 4-20 and 4-21. The CBZ.2H_2O sample that has been heated for one hour has almost identical diffraction pattern as the feed sample (dihydrate) even though the whiskers (Form I carbamazepine) are already present on the surface of the crystals as shown in previous section. However, the amount of whiskers formed is very small and hence they go undetected by the PXRD. The change only becomes more discernible when the sample is heated for two hours. The diffraction pattern of the sample shows traces of both dihydrate and Form I carbamazepine (Peaks capped by ▼ and ▼ are the characteristics peak for dihydrate and Form I carbamazepine, respectively). The intensity of the peak that represents the (100) plane of the dihydrate gradually reduces and eventually disappear after four hours of heating, indicating the sample is now fully dehydrated. Further increase in the heating period results in no changes of the diffraction patterns, even after twenty-four hours.

The DSC thermographs of the CBZ.2H_2O samples heated for different periods are shown in Figures 4-22 and 4-23. It can clearly be seen that as the heating period is increased, the enthalpy of dehydration reduces, suggesting that the amount of water

molecules present in the sample reduces as a function of time. The dehydration enthalpy ceases to exist after the samples are heated for four hours. This observation is in agreement with the PXRD results discussed earlier. The second sharp peak recorded at ~193 °C in each sample provides evidence of the anhydrous polymorphic form into which the crystals dehydrate, which is characteristic to Form I carbamazepine. No sign of glass transition is observed in the DSC thermographs, indicating the dehydration of the crystals under conditions tested is a solid-state transformation from one crystalline form to another without going through amorphisation.

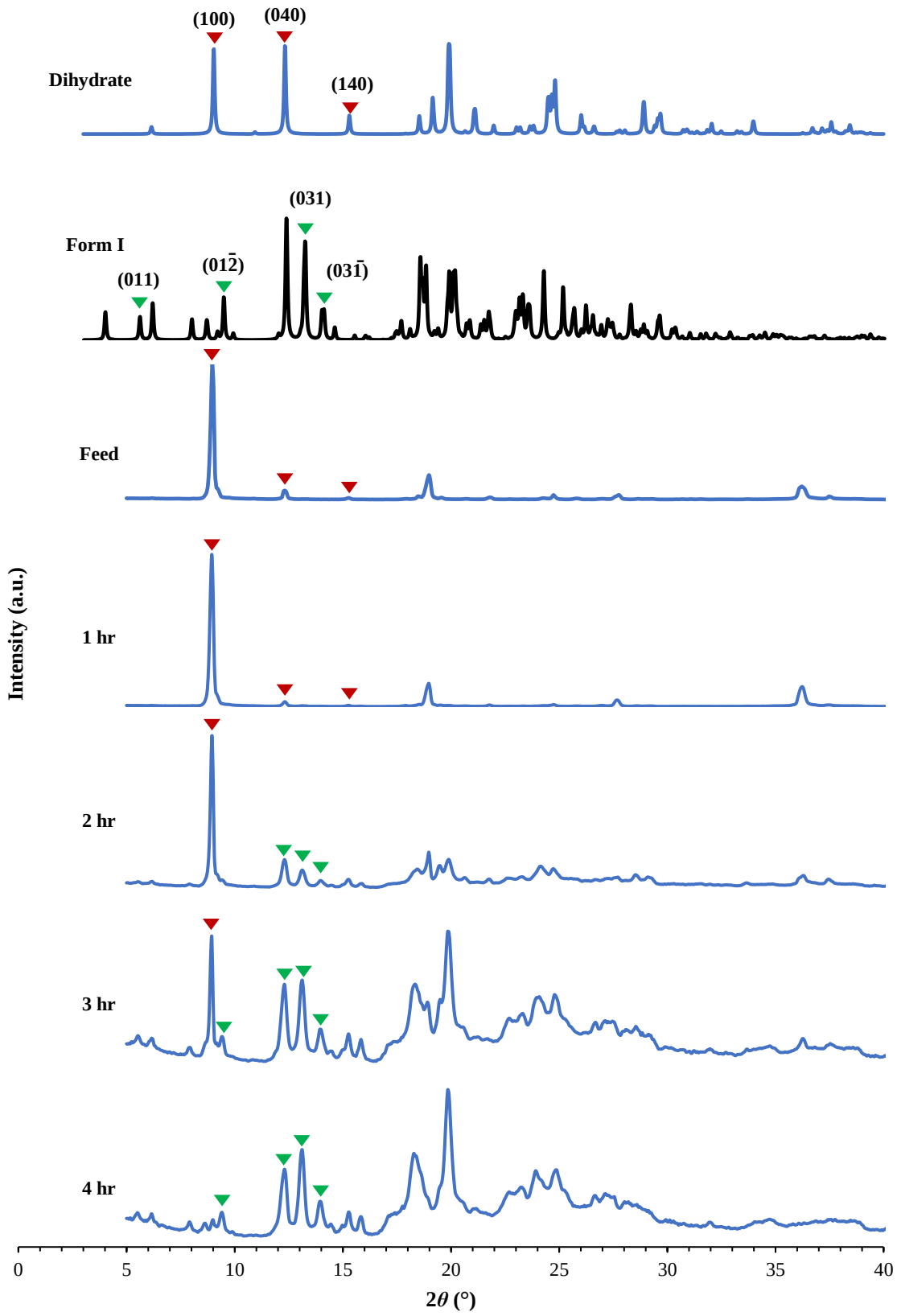

Figure 4-20 Diffraction patterns of CBZ.2H$_2$O heated at 48 °C as a function of time (1 – 4 hours)

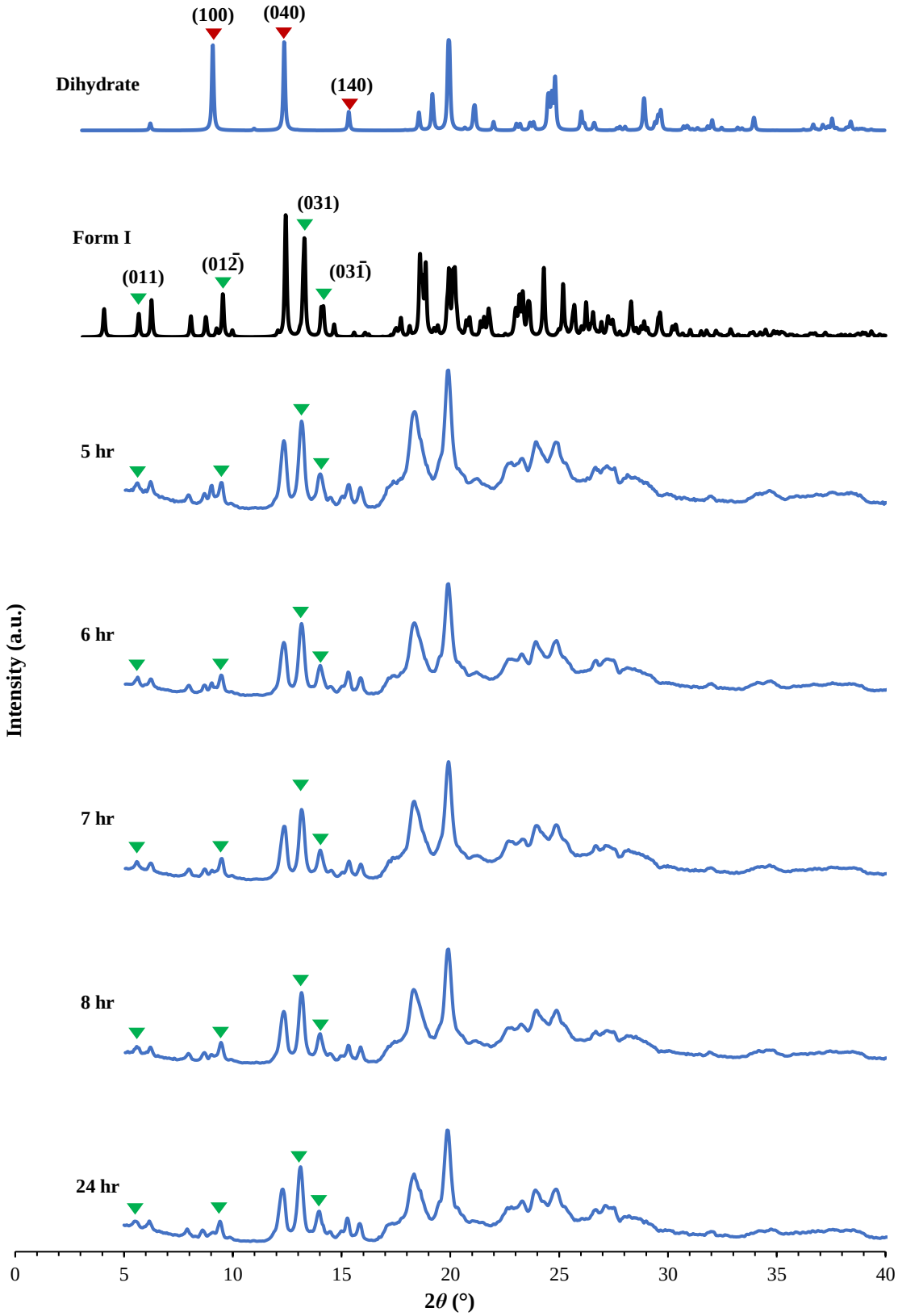

Figure 4-21 Diffraction patterns of CBZ.2H₂O heated at 48 °C as a function of time (5 – 24 hours)

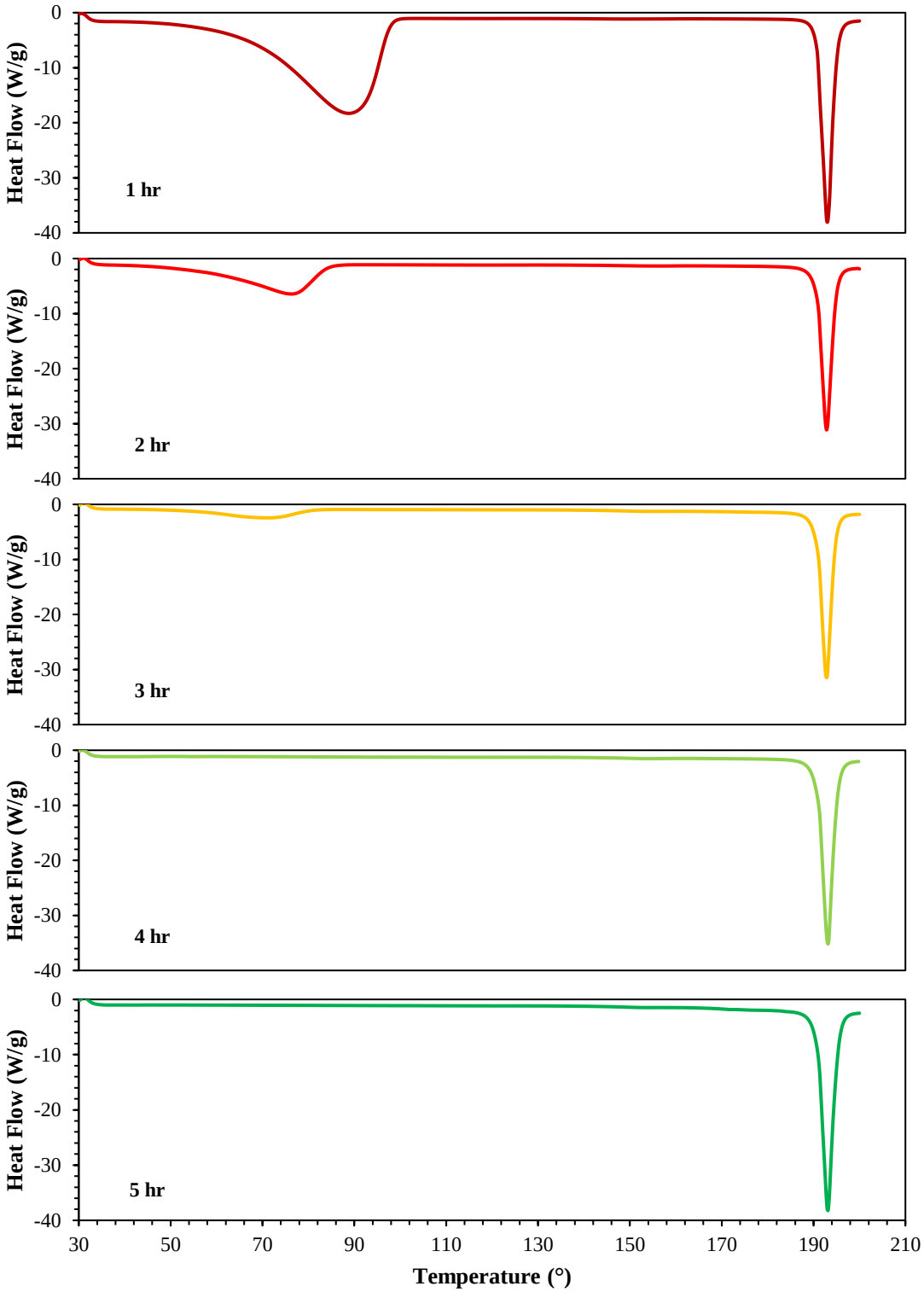

Figure 4-22 DSC thermographs of CBZ.2H₂O samples heated at 48 °C collected at different times (1 – 5 hours)

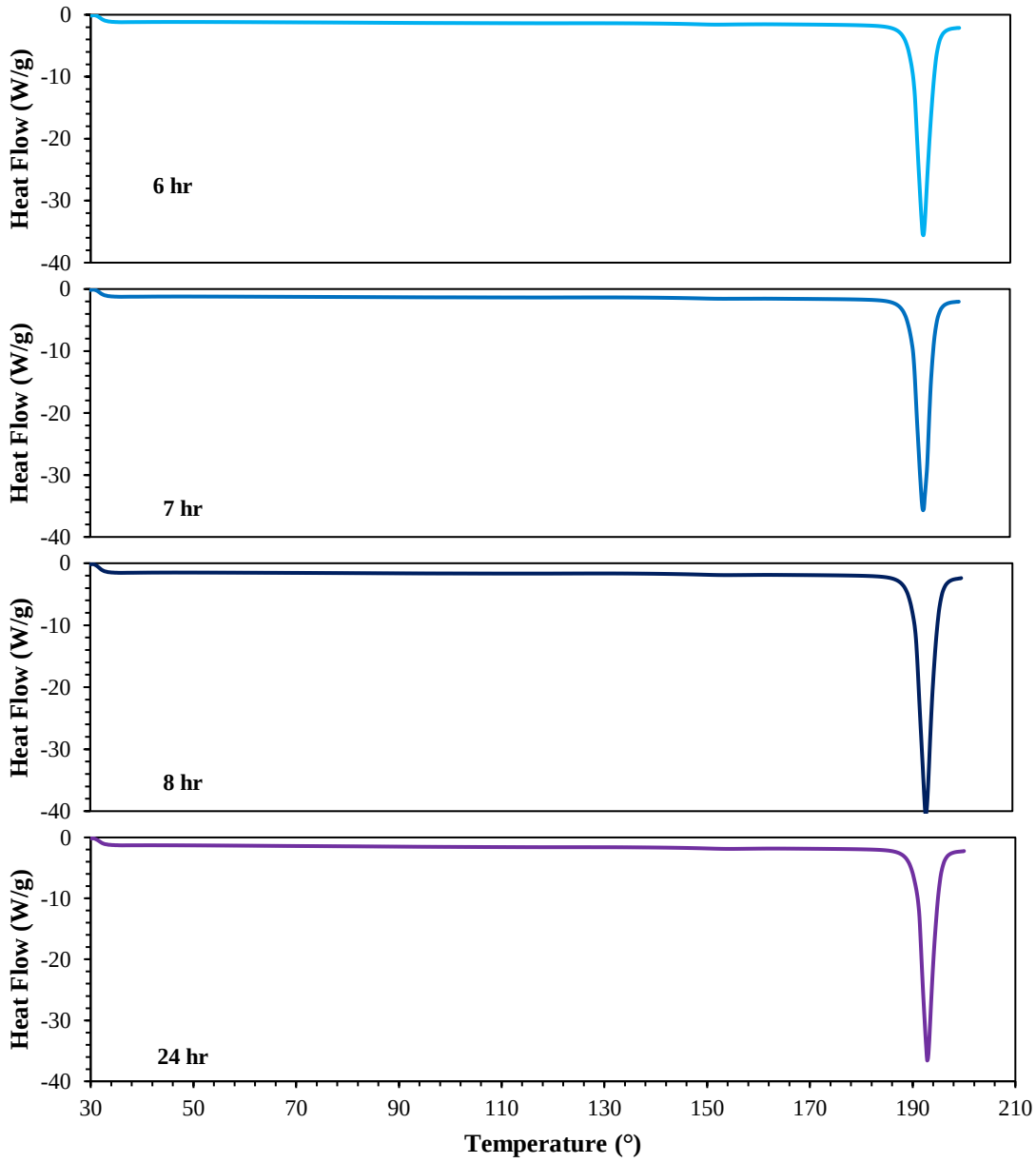

Figure 4-23 DSC thermographs of CBZ.2H₂O samples heated at 48 °C collected at different times (6 – 24 hours)

4.4 Coupled Effect of Thermal and Mechanical Stresses on the Phase Transformation of Carbamazepine Dihydrate

In an agitated filter bed dryer, the particle bed is experiencing both thermal and mechanical stresses concurrently. Thermal stresses have been shown to induce phase transformation in CBZ.2H_2O through DSC and PXRD analysis discussed in previous sections. On the other hand, mechanically stressing the crystals does not yield any discernible transformation. However, a question which naturally arises is whether there exists a coupling effect on the phase transformation of the CBZ.2H_2O crystals between thermal and mechanical stresses. To study that, partial dehydration is induced on the crystals prior to subjecting them to mechanical stresses. The partial dehydration introduces defects to the crystals, and it is hypothesised that by applying mechanical stresses to such crystals, the transformation should get accelerated if coupling effect does exist.

4.4.1 Materials and methods

It was found in the previous experiments that CBZ.2H_2O crystals fully dehydrated after being heated for four hours at 48 °C. Based on this information, three partially dehydrated samples were prepared by subjecting them to 1, 2 and 3 hours of heating. A lower heating temperature at 35 °C was also tested. Bulk crushing was then performed to induce mechanical stresses to the crystals. The diffraction patterns of the crystals were collected before and after bulk crushing to investigate the influence of mechanical stresses on partially dehydrated crystals.

4.4.2 PXRD Analysis

The diffraction patterns of the partially dehydrated CBZ.2H_2O crystals at 48 °C (crushed and uncrushed) are shown in Figure 4-24. For the sample that was heated for one hour, the crystals remain predominantly as dihydrate, and that is reflected by the sharp peak recorded at ~9 °. The diffraction patterns before and after the bulk crushing are almost identical, but with some peaks that have slightly higher intensity compared to the others. The concurrence of dihydrate and Form I carbamazepine is observed in the diffraction patterns of the sample that was heated for two hours (Figure 4-24). Crushing the sample does intensify the smaller peaks that were previously masked out by the strong (100) peak of the dihydrate but that is mainly due to the increased randomness of the crystal orientation in the packing as the particle size reduces. The sample heated for three hours shows almost no difference in the diffraction pattern and that is attributed to the fact that the crystals were dehydrated and transformed to Form I carbamazepine fully before being crushed. Hence, the diffraction patterns of crushed and uncrushed samples remain almost identical.

Similar experiments were performed but at lower temperature (35 °C). No observable transformation is observed in the diffraction patterns of the samples before and after being crushed (Figure 4-25). This indicates that there is not coupling effect between the thermal and mechanical stresses in the phase transformation of carbamazepine dihydrate.

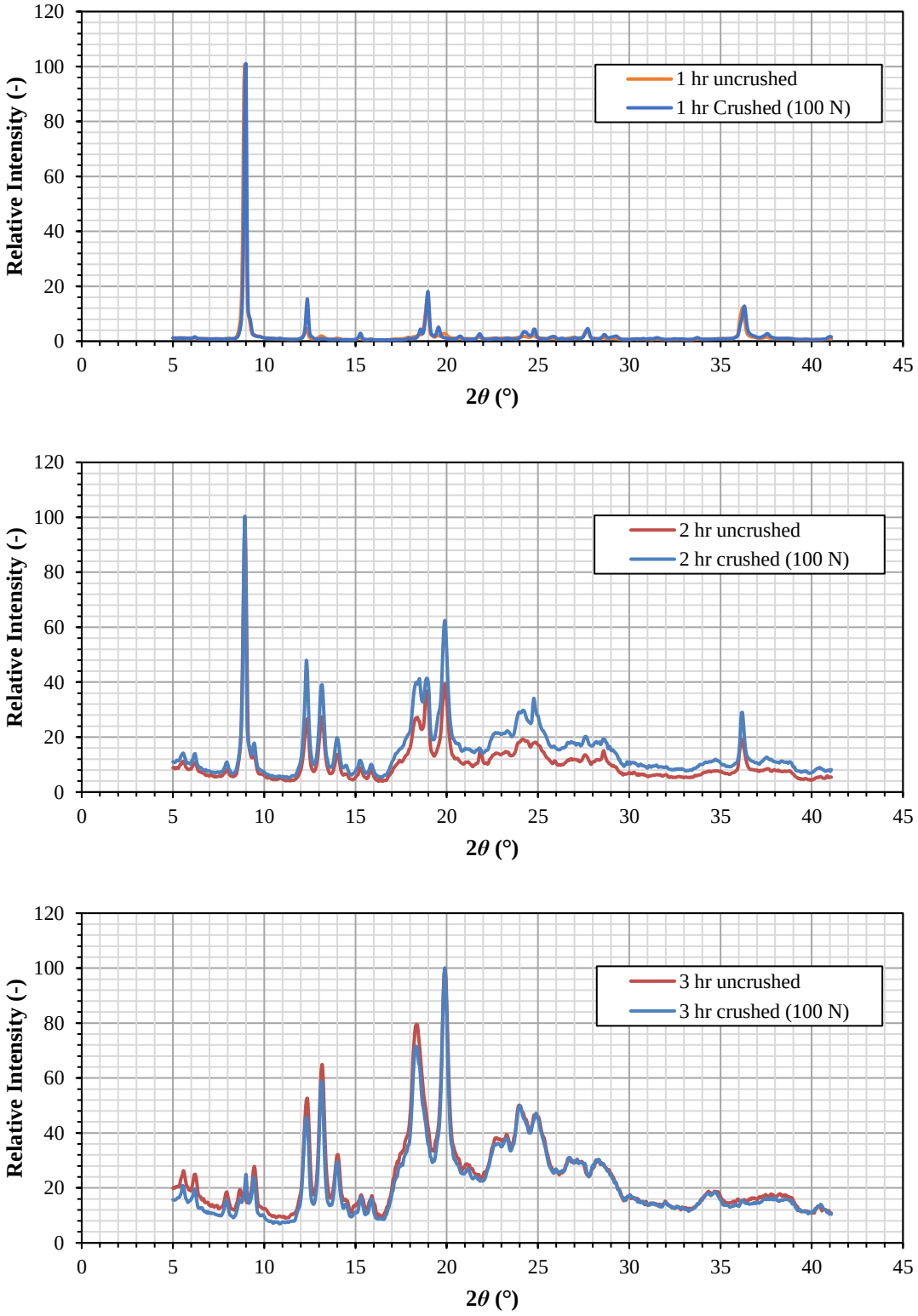

Figure 4-24 Diffraction patterns of crushed and uncrushed CBZ.2H$_2$O samples at 48 °C

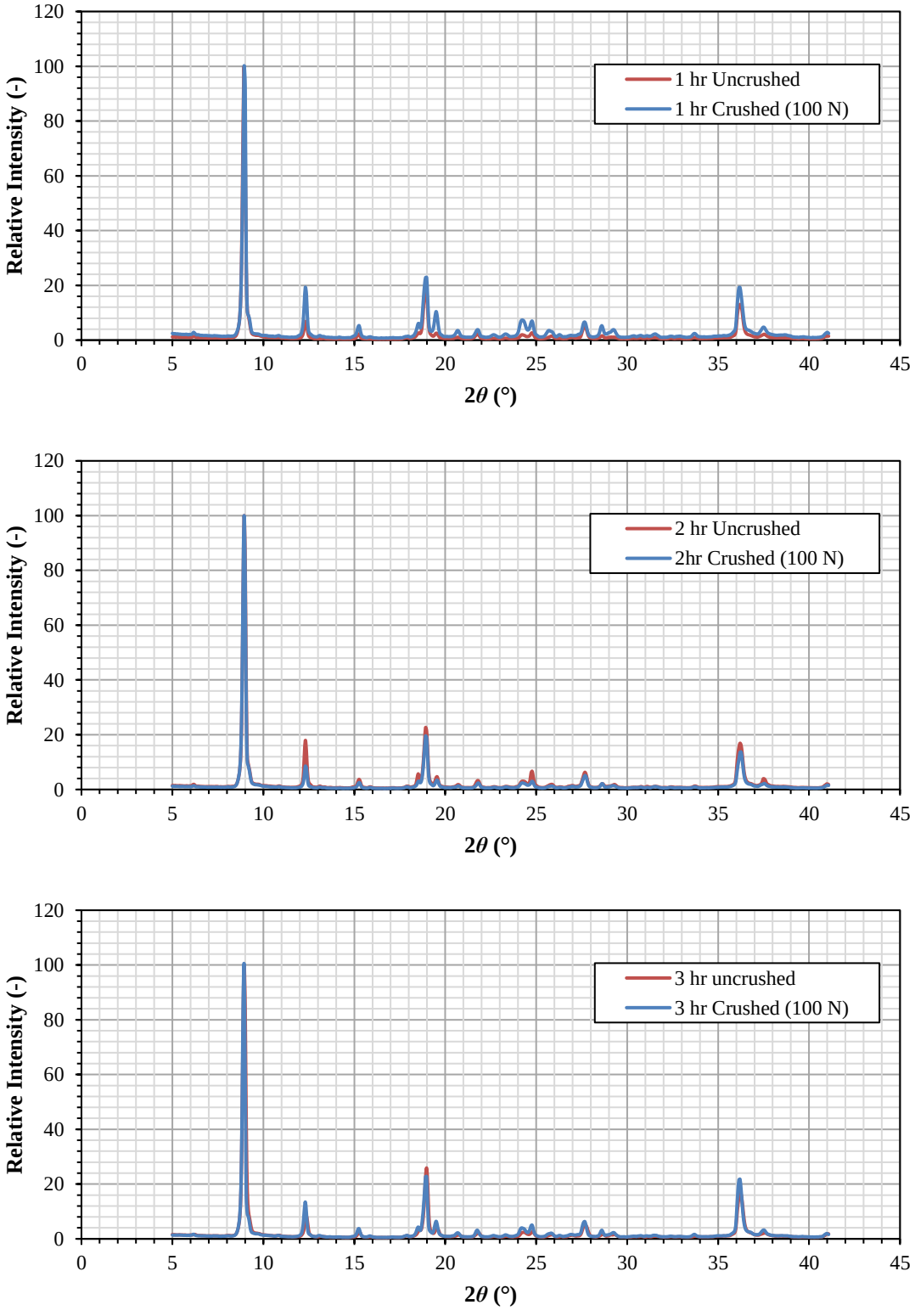

Figure 4-25 Diffraction patterns of crushed and uncrushed CBZ.2H₂O samples at 35 °C

4.5 Conclusions

The effects of mechanical and thermal stresses on the phase transformation of CBZ.2H_2O crystals have been investigated in this chapter. Subjecting the crystals to impact and bulk crushing both yield a noticeable amount of crystal breakage. The crystals are very prone to impact breakage and that is evident in the rapid shifting of the PSD, even at the lowest dispersion pressure tested (0.5 barg). On the other hand, bulk crushing too leads to a considerable amount of breakage, but to a lesser extent compared to impact. Both impact and bulk crushing introduce damage to the crystals, but the breakage mechanisms are different. The crystals break by snapping into fragments almost instantaneously upon impact whereas they are stressed for a long period of time in bulk crushing at low strain rate. Deformed crystals are observed when the crushing loads are higher that 1 kN. In spite of the significant physical damage done to the crystals, the PXRD analysis of the broken samples reveal no discernible phase transformation from dihydrate to anhydrous or amorphous form of carbamazepine.

CBZ.2H_2O is susceptible to thermal stresses and dehydrates very easily at elevated temperature above 40 °C. The activation energy of the dehydration of CBZ.2H_2O from the DSC thermal analysis is found to be small, suggesting that CBZ.2H_2O is a weak hydrate. In the range of the temperature tested (DSC 30 – 230 °C purged with N_2), CBZ.2H_2O dehydrates at ~48 °C to anhydrous Form I carbamazepine. The polymorphic form is confirmed by the melting point of the dehydrated sample, at ~192 °C, which is the characteristic melting point of Form I carbamazepine. Ex-situ study of the effect of thermal stresses as a function of time in a temperature-controlled oven also reveals similar results. The dehydration of CBZ.2H_2O forms of "whiskers", which grow on the surfaces of the crystals. As the heating period is prolonged, the growth of the "whiskers" spread over the crystal surface. The dehydration of the crystals is catastrophic, i.e. the loss of

water molecules leads to the complete collapse of the crystal lattice, even though the macroscopic crystal shape is preserved.

The coupled effect of thermal and mechanical stresses is investigated, and the results show that CBZ.2H_2O crystals dehydrate readily when being stressed thermally but not mechanically. Subjecting partially dehydrated crystals to mechanical stresses does not increase the transformation rate of the hydrate to anhydrous carbamazepine, at least not to an observable extent by PXRD.

Chapter 5

Dehydration and Rehydration of Carbamazepine Dihydrate Crystals under Controlled Temperature and Humidity Conditions

5.1 Introduction

Carbamazepine dihydrate is very prone to dehydration due to the stresses induced by thermal gradient. Apart from the temperature, the surrounding relative humidity also plays a role in affecting the dehydration of the crystals. Depending on the surrounding conditions, carbamazepine dihydrate could dehydrate to either the anhydrous form of carbamazepine or its amorphous counterpart (Li et al., 2000; Khoo et al., 2010; Kachrimanis and Griesser, 2012). The effect of temperature and relative humidity on the dehydration and rehydration of carbamazepine dihydrate is a complex process and is not very well understood. In this chapter, the dehydration and rehydration of carbamazepine is studied thoroughly under controlled temperature and humidity conditions. Several different techniques have been deployed to study some of the important aspects, such as the critical humidity, kinetics, and polymorphic transformations during the dehydration and rehydration process.

5.2 Stepwise DVS Isotherms

The Dynamic Vapour Sorption (DVS) isotherms of carbamazepine dihydrate at 25, 30, 35 and 40 °C were collected using, DVS Adventure of Surface Measurement Systems. The amount of sample used in each test was ~5 mg. The solvent was distilled water and the air was purged at 200 SCCM. The DVS experiments were performed on a stepwise basis where the relative humidity (RH) of the system was first stepped down from 90 to 0%, and then stepped back to 90 with an interval of 10%. In another set of experiments, the RH was stepped down from 90 to 10% first before reducing the step size to 2% RH from 10 to 0 % RH to increase the resolution of the data below 10% RH. The relative humidity of the system stepped forward when the change of the mass of the sample per minute was less that 0.01 percent.

5.2.1 10% RH Step

The DVS isotherms of carbamazepine dihydrate crystals collected at 25, 30, 35 and 40 °C are shown in Figure 5-1. It can be seen that at all temperatures, the sample mass fluctuates initially at the first 90% RH step. The reduction of sample mass is small when the RH is stepped down from 90 to 10% but then becomes significant when the RH is brought further down from 10% to 0%. The equilibrated change of sample mass at each RH step is recorded and shown in Figure 5-2. The change in the sample mass is less than 5% when the RH is stepped down from 90 to 10% and this is observed at all the temperatures tested. The reduction in sample mass from 90 to 10% RH is associated with the evaporation of the sample surface water. On the other hand, the prominent decrease in the sample mass between 10% RH to 0% RH is associated with dehydration of the crystal water. The dehydration process has the same pattern for all the temperature tested. It is evident that temperature plays a notable role in the reabsorption of water into the crystal system. When

the system is brought back to 90% RH from 0% RH, only the sample collected at the lowest temperature (i.e. 25 °C) manages to re-absorb water and gains weight. The higher the temperature, the lower the amount of water reabsorbed by the dehydrated sample (Figure 5-3).

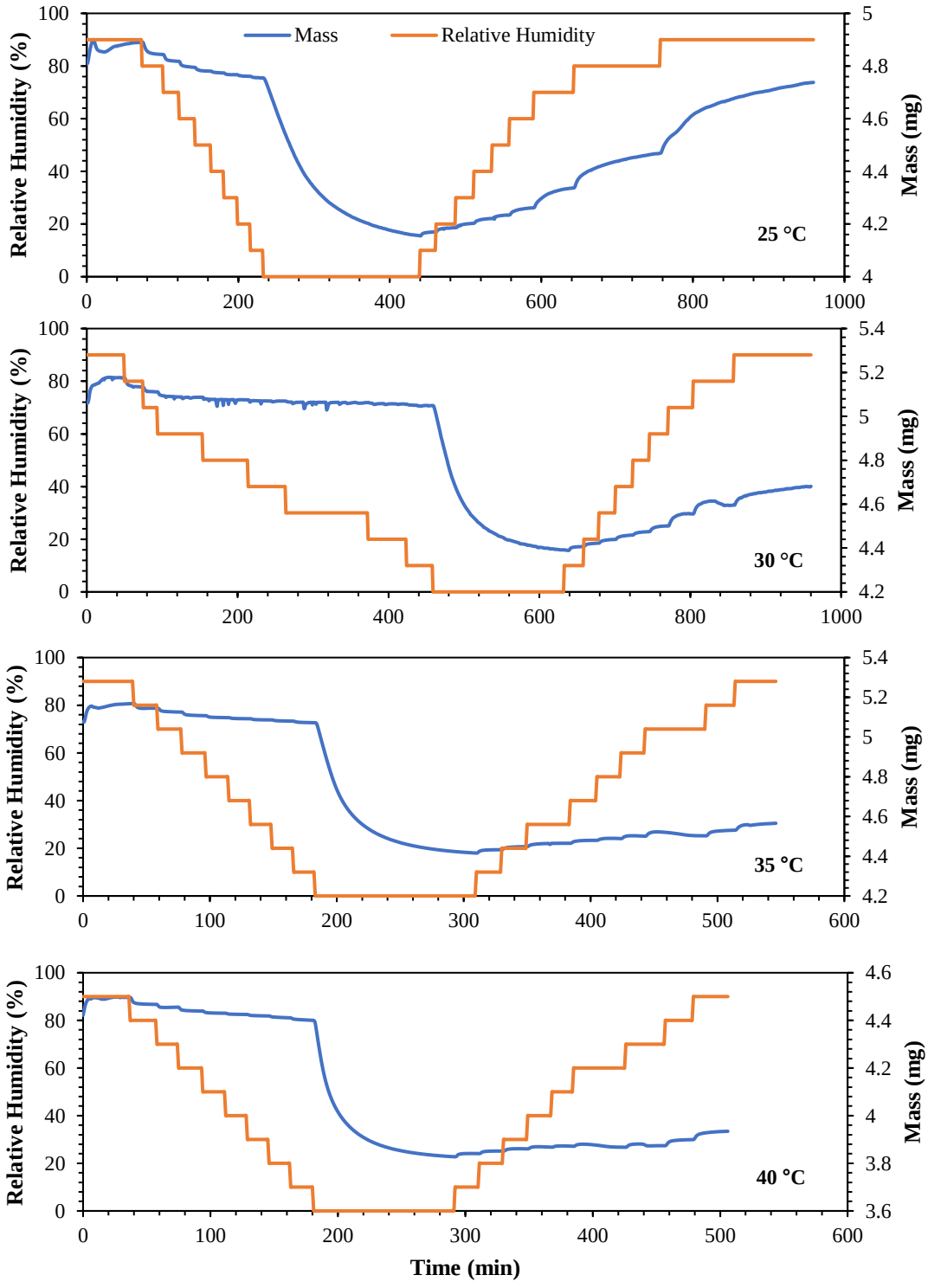

Figure 5-1 DVS isotherms of carbamazepine dihydrate at 25, 30, 35 and 40 °C (10% RH step)

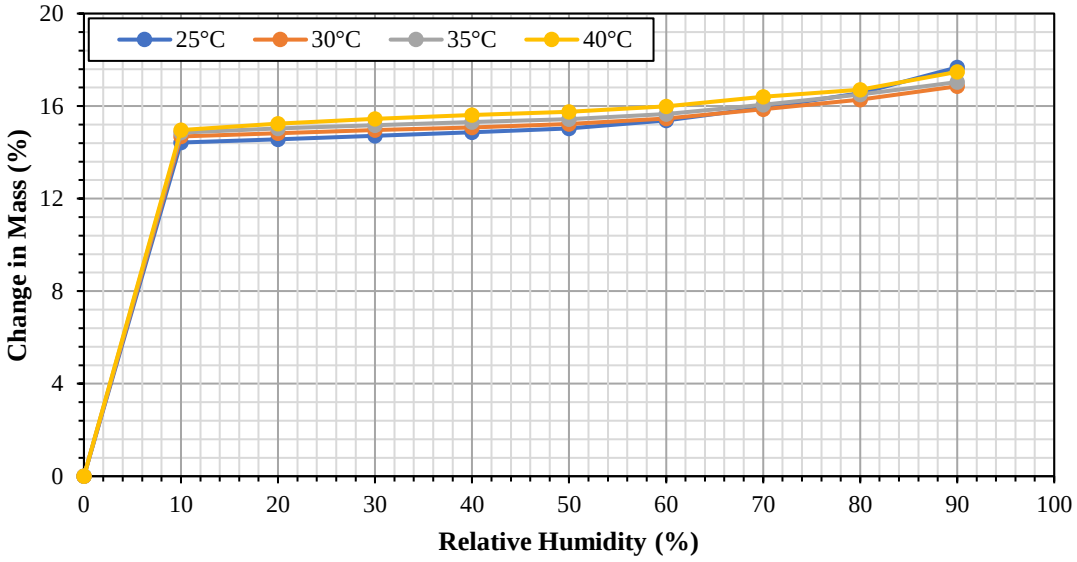

Figure 5-2 Equilibrated percentage change in mass at each RH step, 10% interval (dehydration phase)

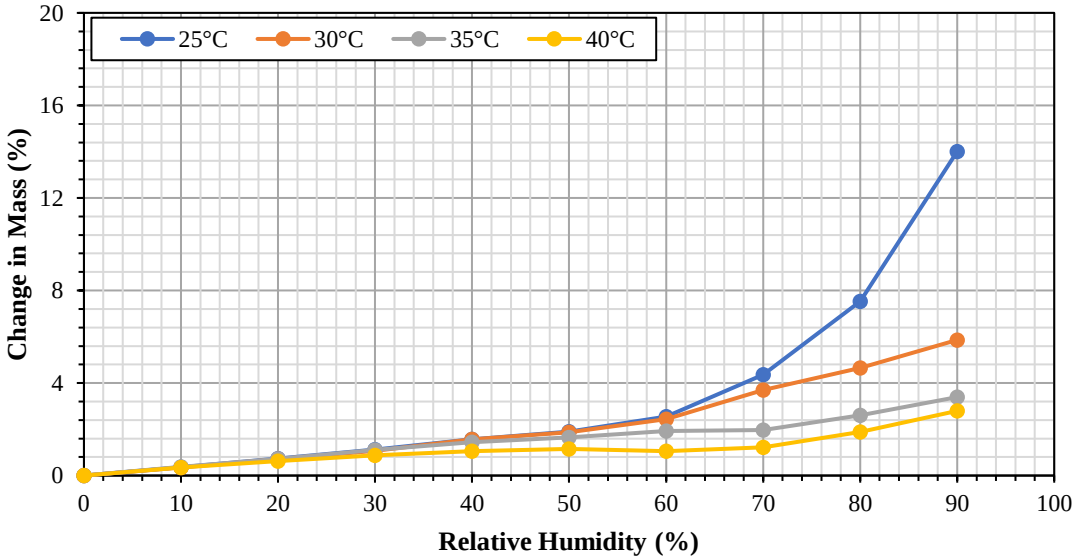

Figure 5-3 Equilibrated percentage change in mass at each RH step, 10% interval (rehydration phase)

5.2.2 2% RH Step

The results from previous section (10% RH step) indicate that carbamazepine dihydrate crystals dehydrate when the RH is less than 10% but the dehydration could commence at any point between 0 – 10% RH. In order to better understand the dehydration behaviour of carbamazepine dihydrate, the step size between 0 and 10% RH is reduced to 2% to improve the resolution of information gathered between this RH range. The DVS isotherms (dehydration and rehydration) of the samples collected at increased RH resolution are shown in Figure 5-4 and the mass change of the sample (dehydration) at different temperatures between 0 to 10% RH is shown in Figure 5-5. At 25 °C, the dehydration of the crystals commences at ~3% (indicated by the abrupt change in the sample mass recorded when the RH is stepped down from 4 to 2%) and this critical dehydration RH point increases when the temperature is increased. It is found that the dehydration starts at ~5% RH instead when the sample is kept at 30 °C. The critical dehydration point is shifted to ~7% RH at 35 °C and 10% RH at 40 °C. Unlike those samples kept at the lower temperatures, at 40 °C, the dehydration of the crystals initiates at 10% RH and finishes even before stepping down to 8% RH, indicating a very fast dehydration kinetic. These observations are summarised in Figure 5-6 where the plot of equilibrated change in mass at RH steps below 10% is shown. As far as the rehydration process is concerned, compared to the results collected in the previous section (10% RH step), subjecting the dehydrated samples to rehydration yields reveals similar crystal rehydration behaviour, where increasing the temperature hinders the water reabsorption ability of the dehydrated sample. The equilibrated percentage change in mass at each RH step, 2% interval during rehydration is shown in Figure 5-7.

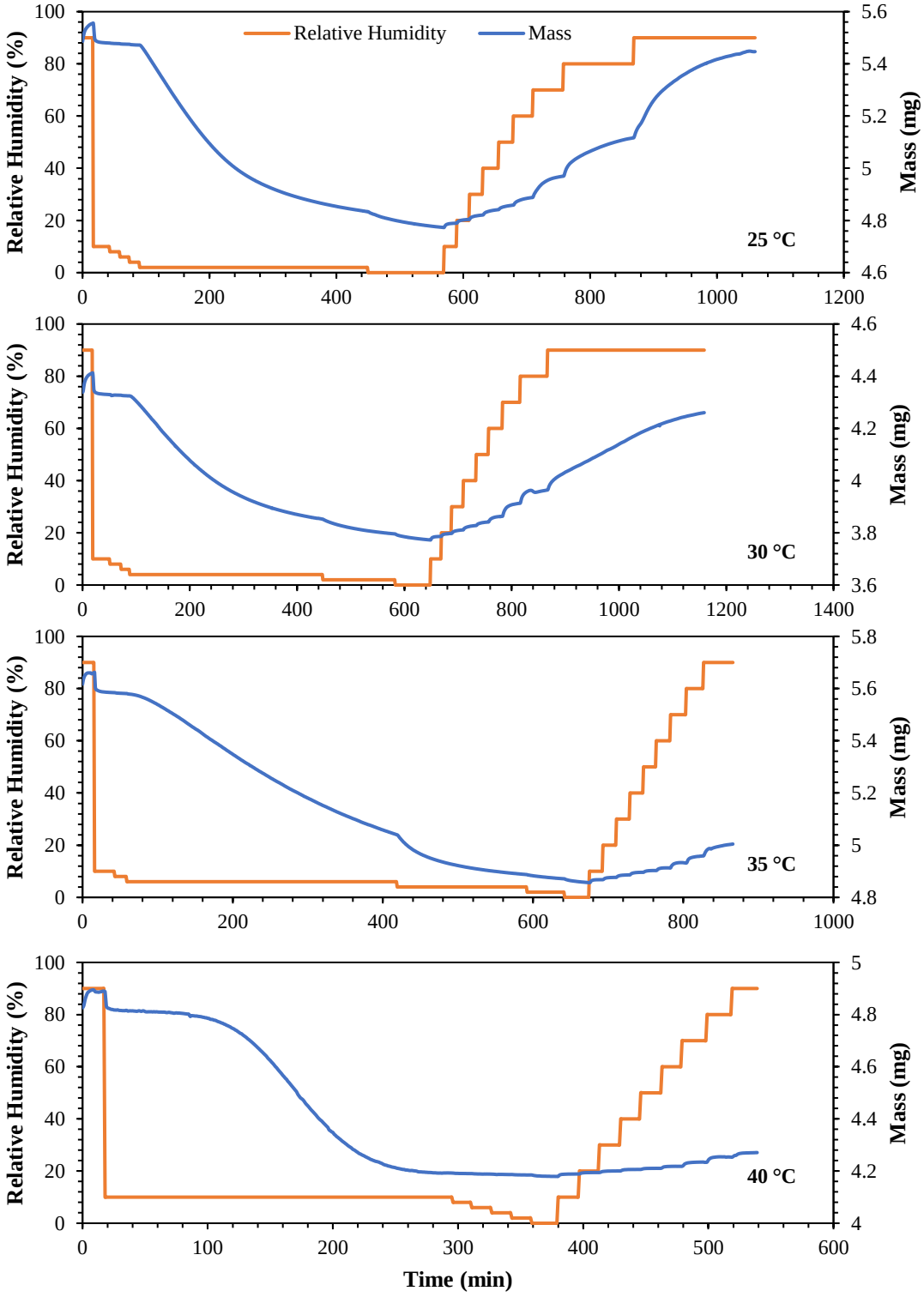

Figure 5-4 DVS isotherms of carbamazepine dihydrate at 25, 30, 35 and 40 °C (2% interval from 10% RH to zero)

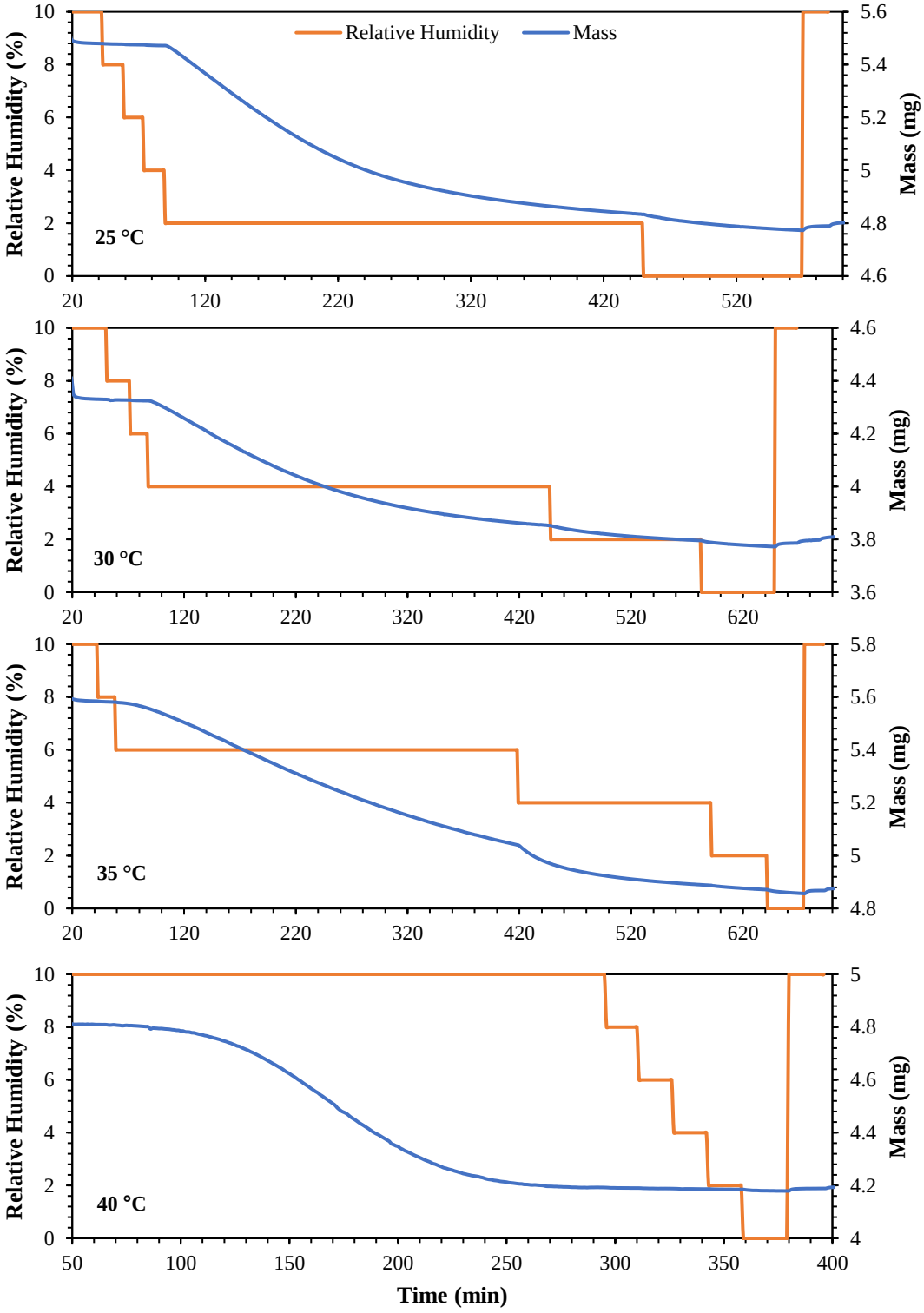

Figure 5-5 DVS isotherms from 10 to 0% RH (2% RH step)

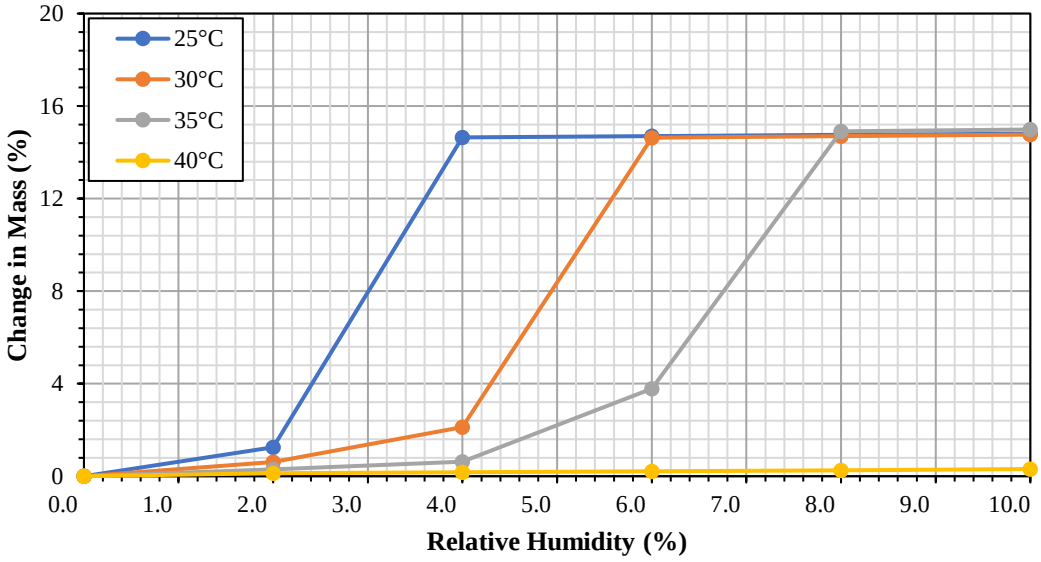

Figure 5-6 equilibrated percentage change in mass at each RH step, 2% interval (dehydration phase)

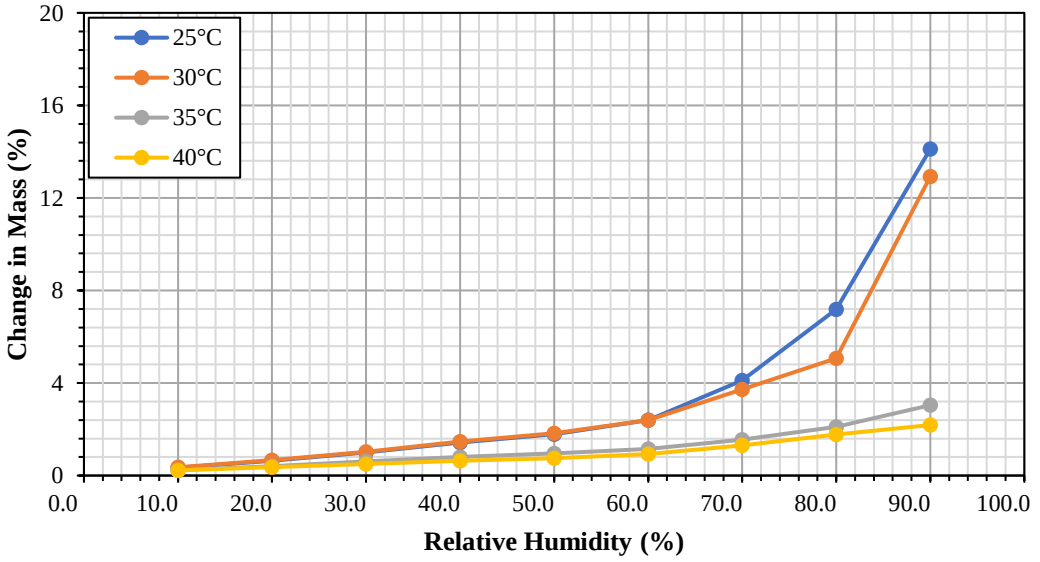

Figure 5-7 equilibrated percentage change in mass at each RH step, 2% interval (rehydration phase)

5.2.3 SEM Observations and PXRD Analysis

The samples were collected at the end of each test (dehydration and rehydration cycle) and studied under scanning electron microscope to investigate the effect of temperature and humidity on the macroscopic structure of the crystals. The SEM micrographs of the samples that have been subjected to dehydration and rehydration cycle are shown in

Figure 5-8. Interestingly, after substantial crystal water loss, all the samples seem to retain their crystal morphology, at least macroscopically. The difference between the samples begins to unfold when attention is paid on the surface of the crystals. The rehydrated sample at 25 °C seems to retain its macroscopic crystal structure. The surface of the crystals appears to be smooth and no apparent damage or structural damage is observed on the surface. At 30 °C, whiskers are found on the surfaces of the sample collected, indicating structural change of the crystals. Subjecting carbamazepine dihydrate crystals through dehydration and rehydration at 35 °C results in crystals that have whiskers grown on them and the surface of the crystals appears to be very rough. At low magnification, the dehydration of the crystals does not seem to have any detrimental effect on the integrity of the crystals. However, a high magnification observation on the surface of the crystals suggests otherwise. At 40 °C, the high temperature which leads to very fast dehydration rate promotes the growth of whiskers that is in fact a manifestation of the phase transformation from dihydrate to Form I carbamazepine through recrystallisation.

PXRD analysis on these samples provides complementary support to the observations made through SEM (Figure 5-9). Out of the four temperatures tested, only the sample tested at 25 °C has the ability to revert back to its original hydrate state. The diffraction pattern shows a sharp peak at ~ 9 °, which is a characteristic of carbamazepine dihydrate. However, the conversion back to dihydrate is not complete, as some other peaks which correspond to Form I carbamazepine are recorded in the diffraction pattern too. At 30 °C, the characteristic peak of the dihydrate is not observed and the diffraction pattern corresponds to carbamazepine Form I. Similar diffraction pattern is seen for both samples dehydrated/rehydrated at 35 and 40 °C, though the latter shows broader peaks, indicating the possible presence of amorphous content in the sample.

These studies reveal that, in order for dehydrated carbamazepine to revert back to dihydrate, the dehydration rate has to be slow. According to Garnier et al. (2002), there

are two kind of dehydration mechanisms. A smooth dehydration happens when the water molecules depart from the crystal in a non-destructive and allow the reorganisation of the crystal lattice to the nearest possible crystalline packing through relaxation. A destructive dehydration, on the other hand, causes the crystal lattice to collapse due to rapid water molecule departure. Such detrimental process usually results in the loss of crystallinity and the formation of amorphous material, which could later on evolve into anhydrous form of the material through nucleation and growth mechanism. The dehydration of carbamazepine dihydrate at 25 °C seems to follow that of a smooth dehydration where the loss of water molecules does not destroy the crystal structure (see the SEM micrograph in Figure 5-8). Hence subsequent rehydration of the crystals leads to the formation of dihydrate as confirmed by PXRD. At higher temperature, the dehydration of carbamazepine is detrimental to the crystal structure, new crystal domains exhibiting in the form of whiskers grown on the surface of the crystals is observed. It is most evident for the case where the test was performed at 40 °C, whiskers are found fully covering the crystals. Those samples which had gone through destructive dehydration process are found not being able to get rehydrated and transform back to the hydrate form at 90% RH, as shown in their diffraction patterns. This is also reflected in their ability to reabsorb water as a function of temperature. Only the sample dehydrated at 25 °C is able to pick up the water in the air during rehydration phase and regain mass that is equal to the amount of crystal water loss during dehydration phase.

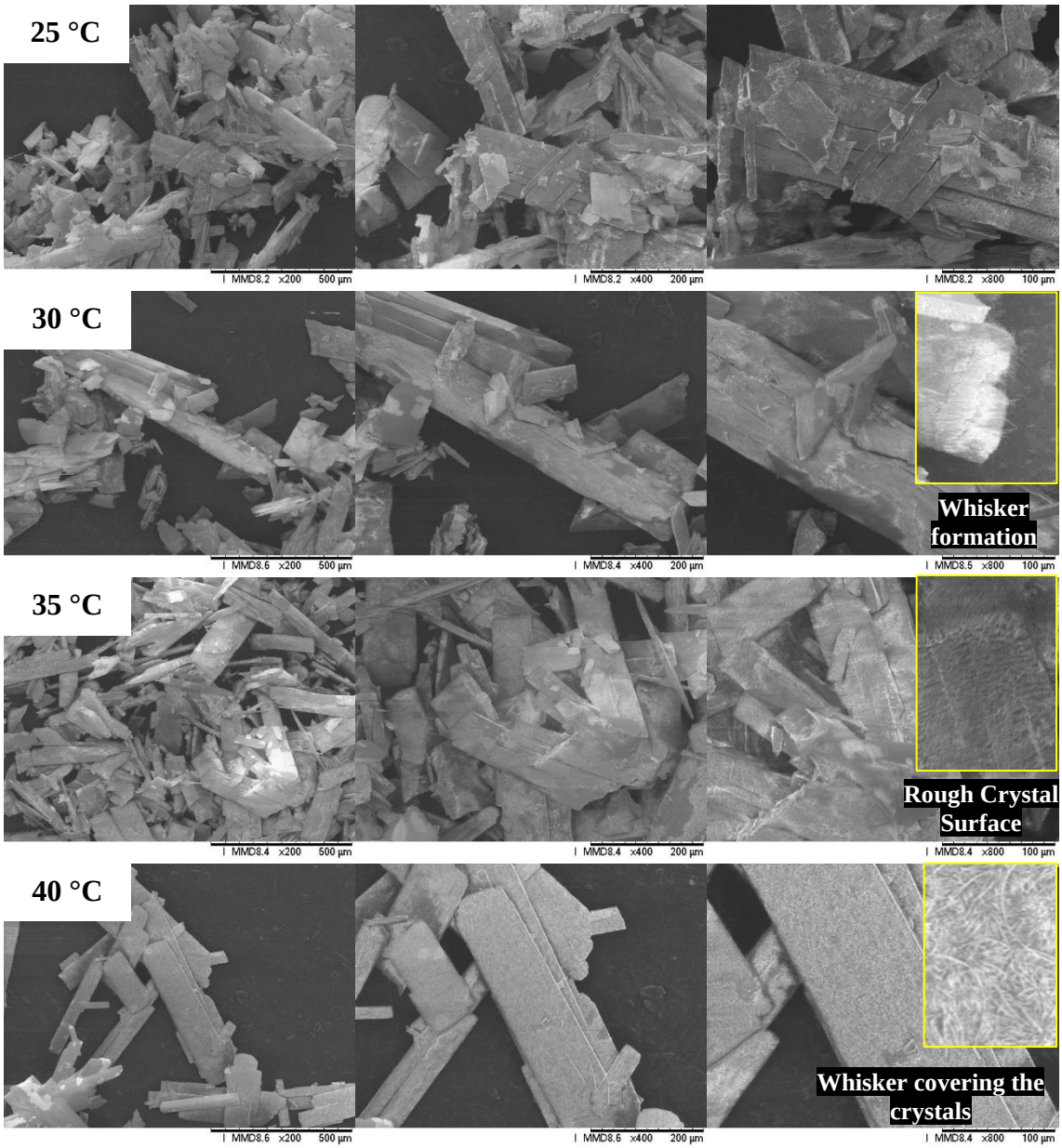

Figure 5-8 SEM micrographs of the crystals after the dehydration and rehydration cycle

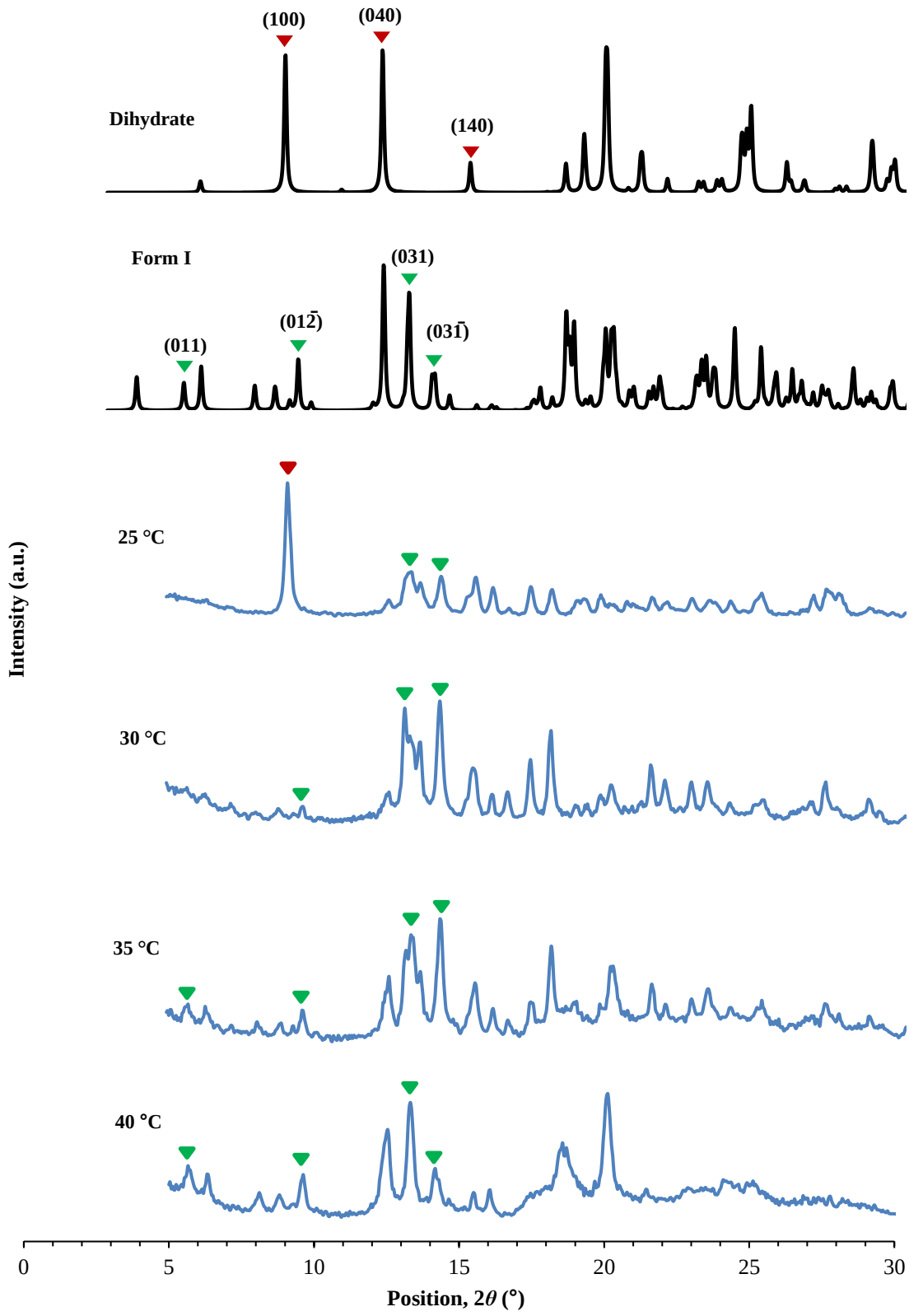

Figure 5-9 Diffraction patterns of the samples collected at the end of each dehydration/rehydration cycle at different temperatures

5.3 Rehydration of Carbamazepine at >90% RH

It was shown in previous section that the rehydration of dehydrated carbamazepine is temperature dependent. It was found that at 90% RH, only the sample dehydrated at 25 °C could pick up the water content. In this section, the rehydration of carbamazepine at the RH higher than 90% is investigated. The highest allowable RH of the DVS Adventure is used (~98%) to induce rehydration of dehydrated carbamazepine. The DVS isotherms of carbamazepine rehydrated at 98% RH at different temperature are shown in Figure 5-10. Similar to the experiments conducted at 90% RH, the dehydrated carbamazepine at 25 °C has the capability to reabsorb water in which the amount is equivalent to the crystal water loss during dehydration. Interestingly, samples that were dehydrated and rehydrated at 98% RH at 30, 35 and 40 °C show very different behaviour compared to when they were rehydrated at 90% RH. At 98% RH, all the samples manage to rehydrate and regain the mass that was loss during dehydration. The plot of percentage crystal water regain versus time is shown in Figure 5-11. It can clearly be seen that temperature plays a role in the rehydration rate of the samples. The higher the temperature, the slower the rate of rehydration. At 40 °C, there is a huge deviation of the rehydration curve from the others, indicating that the full rehydration of the crystals at temperature higher than 35 °C is considerably more difficult to achieve.

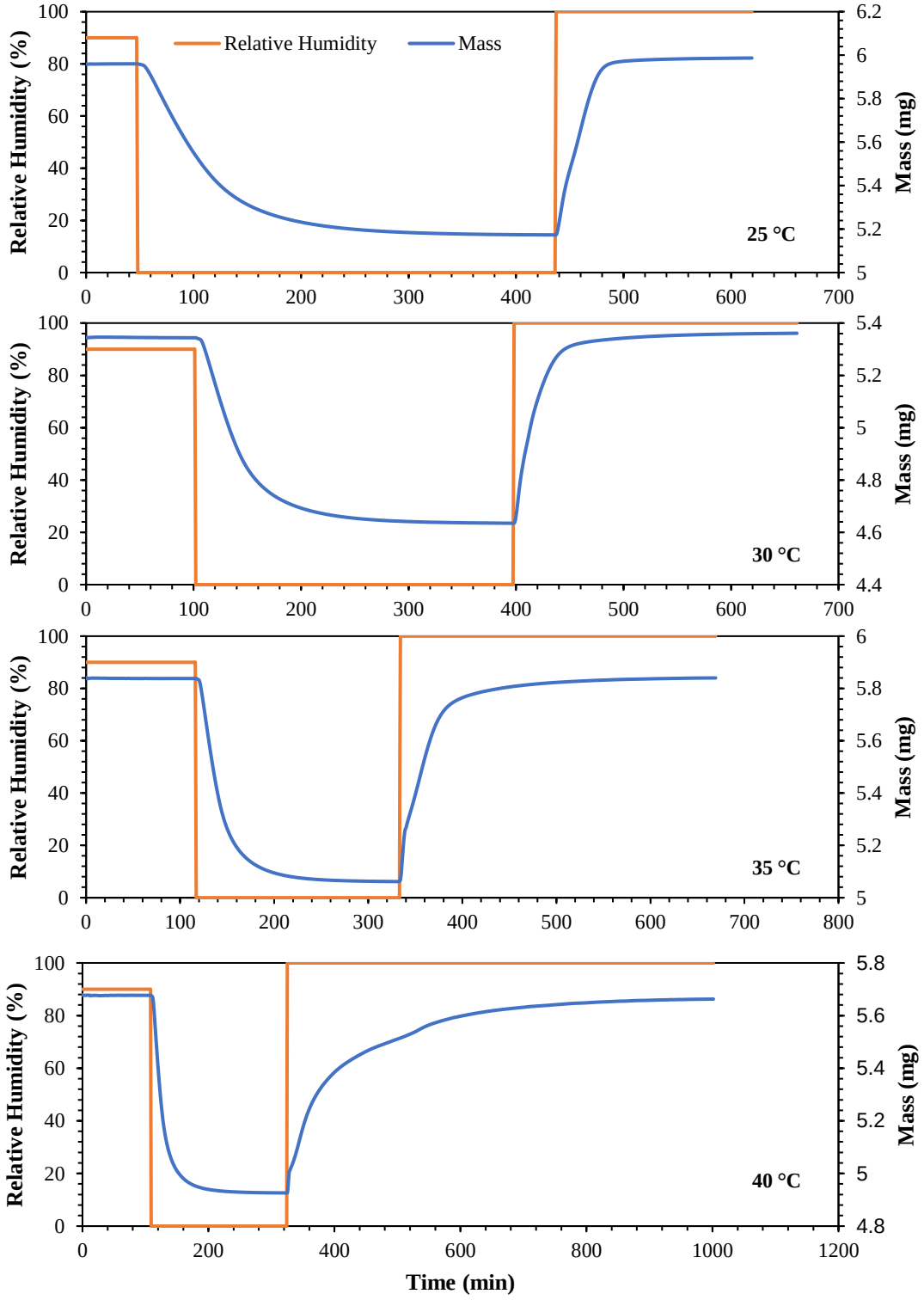

Figure 5-10 Rehydration of carbamazepine dihydrate at different temperatures

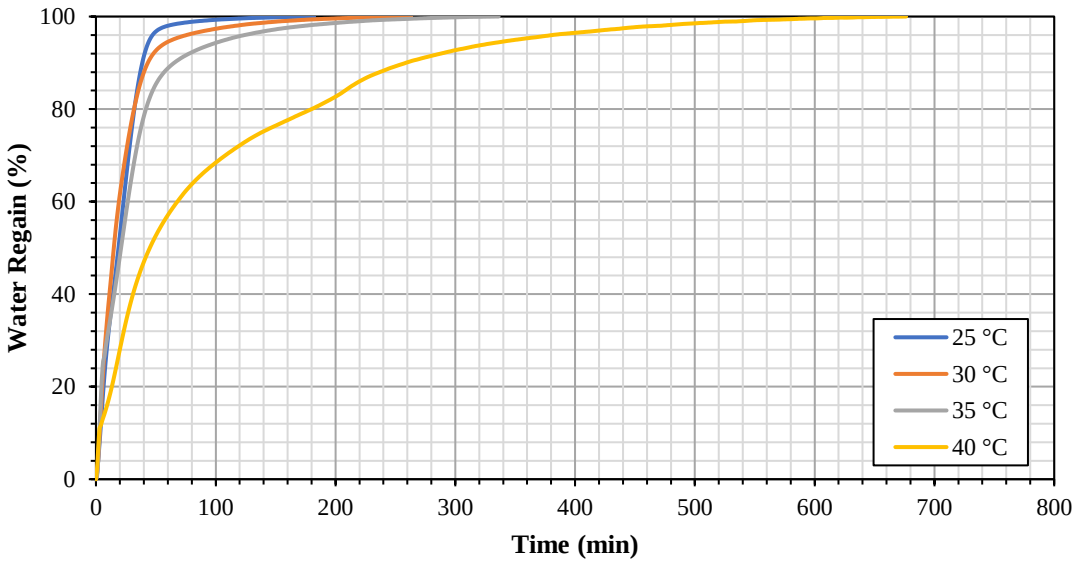

Figure 5-11 Percentage of crystal water regain during rehydration at 98% RH

5.4 Kinetic Study of the Dehydration of Carbamazepine Dihydrate

5.4.1 Dehydration of Carbamazepine Dihydrate at 0% RH

It has been shown in earlier section that carbamazepine dihydrate dehydrates at different rate depending on the temperature and humidity to which it is subjected. In this study, the kinetic of dehydration of carbamazepine dihydrate at 0% RH is studied as a function of temperature. Only two humidity steps are involved in the DVS programme to obtain the isotherm data for dehydration kinetic study. The RH of the system is stepped down from 90 to 0% when the sample mass reaches its equilibrium at 90% RH. The DVS isotherms of the samples dehydrated at 25, 30, 35 and 40 °C are shown in Figure 5-12. It can be seen that the dehydration commences as soon as the RH of the system is stepped down to 0%. The trend suggests a first-order rate process and this is analysed in the next section.

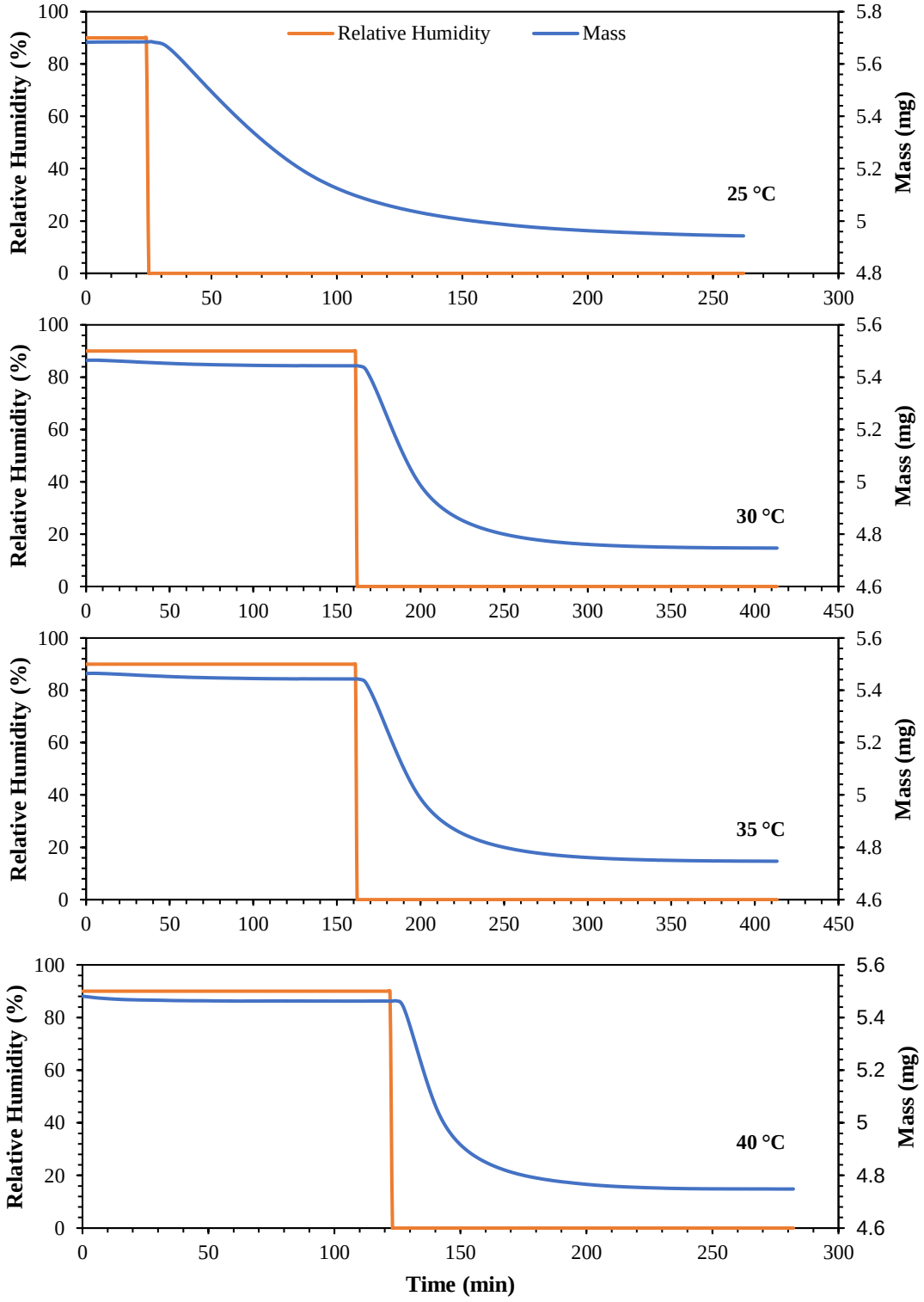

Figure 5-12 Dehydration of carbamazepine dihydrate at 0% RH at different temperatures

5.4.2 Fitting Dehydration Kinetics

The isotherms data collected can be divided into two segments as shown in Figure 5-13. The first segment corresponds to the time period where the sample is kept at 90% to equilibrate. In this segment, the sample mass fluctuates initially but eventually stabilise at the equilibrated point, y_o. The second segment involves the actual dehydration process where the sample environment is switched to 0% RH. Depending on the temperature, the dehydration rate of this segment will vary accordingly. t_o marks the start of crystal dehydration of carbamazepine dihydrate. The dehydration process of carbamazepine dihydrate can generally be expressed by the equation below:

$$CBZ.2H_2O\ (Solid) \xrightarrow[Dehydration]{} CBZ\ (Solid) + 2H_2O\ (Vapour) \qquad (5\text{-}1)$$

The reduction in sample mass can be converted to fraction mass loss, α which is commonly used in kinetic study. The dehydration kinetics of carbamazepine dihydrate is found to follow that of natural exponential disassociation, which takes a first-order form.

$$-\ln(1-\alpha) = kt \qquad (5\text{-}2)$$

where α is the fractional mass loss, k the dehydration rate constant and t the time.

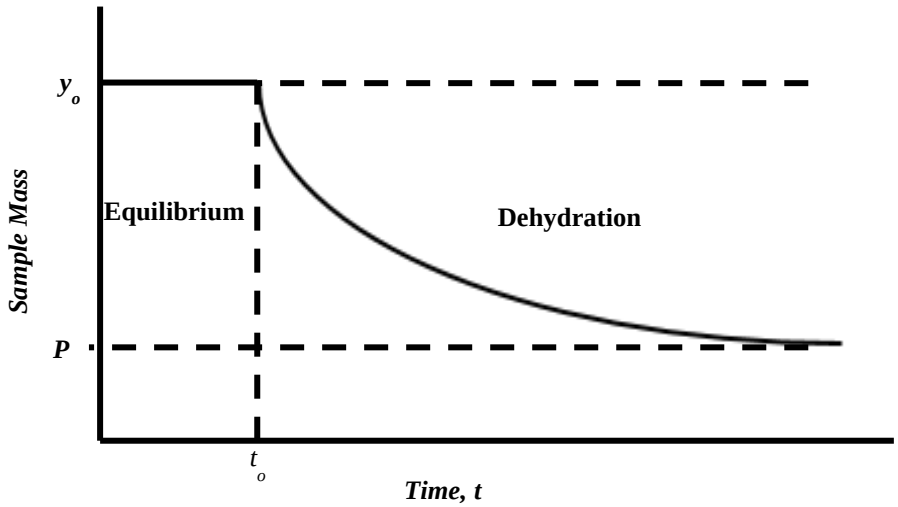

Figure 5-13 DVS isotherm data interpretation

The dehydration rate constant, *k*, determined at different temperatures is shown in Figure 5-14. The higher the temperature, the faster the kinetic of dehydration. Activation energy can be defined as the energy barrier that the system has to overcome to bring about the dehydration process. By using Arrhenius equation (given in Chapter 3), the activation energy of the dehydration process is found to be ~68.65 kJ/mol (Figure 5-15). This is in agreement with the work of Han and Suryanarayanan (1998) in which the activation energy reported was 68.8 kJ/mol at 0% RH. Arrhenius plot describes the temperature dependence of the dehydration rate constant and is a very useful tool to understand the dehydration process of carbamazepine dihydrate, particularly in designing the drying protocol for the material.

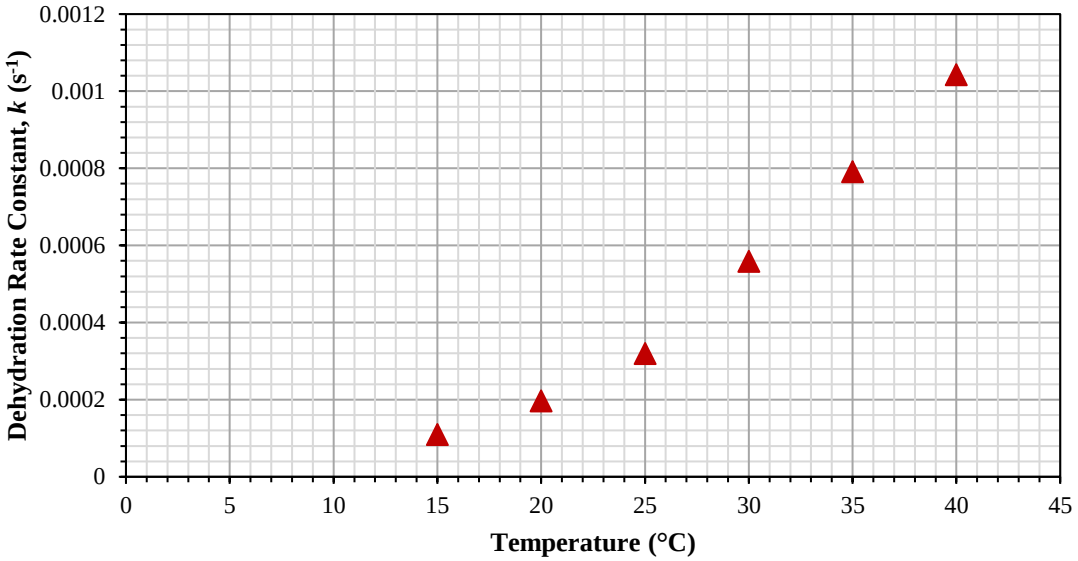

Figure 5-14 Dehydration rate constant as a function of temperature

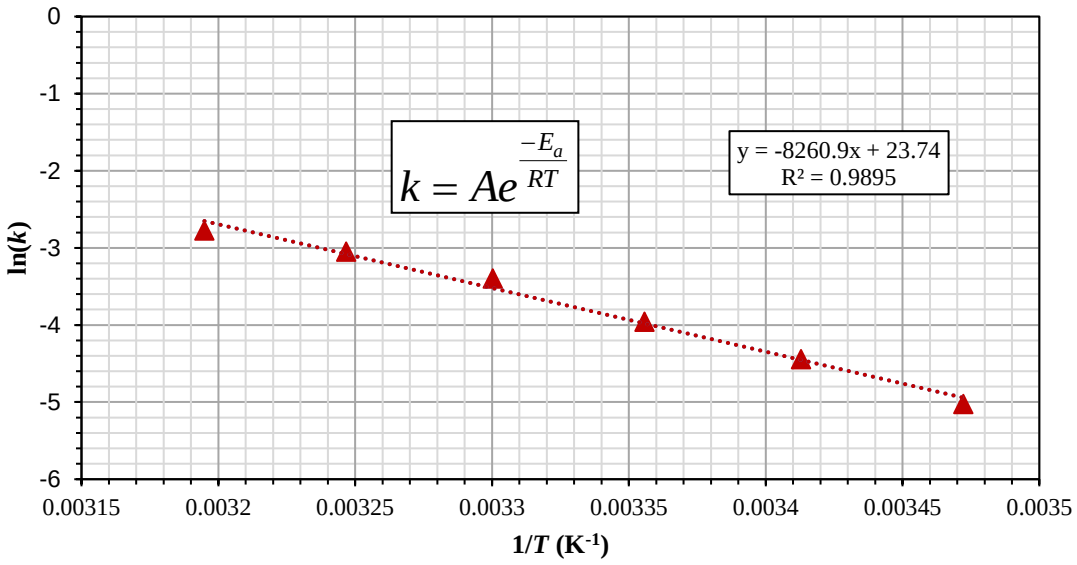

Figure 5-15 Activation energy determination through Arrhenius plot

5.5 RH Ramping Experiments

5.5.1 Determining Critical Dehydration RH of CBZ.2H$_2$O using RH Ramping Method

Dehydration of carbamazepine dihydrate is very sensitive to the surrounding conditions, among which the temperature is one of the most influential factors. The relative humidity of the surroundings also plays a very important role in the dehydration of CBZ.2H$_2$O. Carbamazepine dihydrate is found to be very prone to dehydration at elevated temperatures (discussed in Chapter 4). The higher the temperature, the faster the rate of dehydration. The effect of relative humidity on the dehydration of CBZ.2H$_2$O, however, is not very well understood. Therefore, the main focus here is to investigate the effect of relative humidity on the dehydration of CBZ.2H2O under varying RH ramping rates and temperatures.

CBZ.2H$_2$O samples were subjected to RH ramping rates of 2, 4, 8 and 10%/hr from 90 to 0% RH, at 25, 30, 35 and 40 °C. An example of the DVS isotherm of

carbamazepine dihydrate recorded across the RH range tested is shown in Figure 5-16. It can be seen that the mass of the sample remains almost constant until it reaches a critical RH point where a substantial decrease in sample mass is observed. This critical RH point can be determined by finding the intersection point between the baseline of the sample mass and the line that corresponds to the region where the deviation of the sample mass from the baseline is observed.

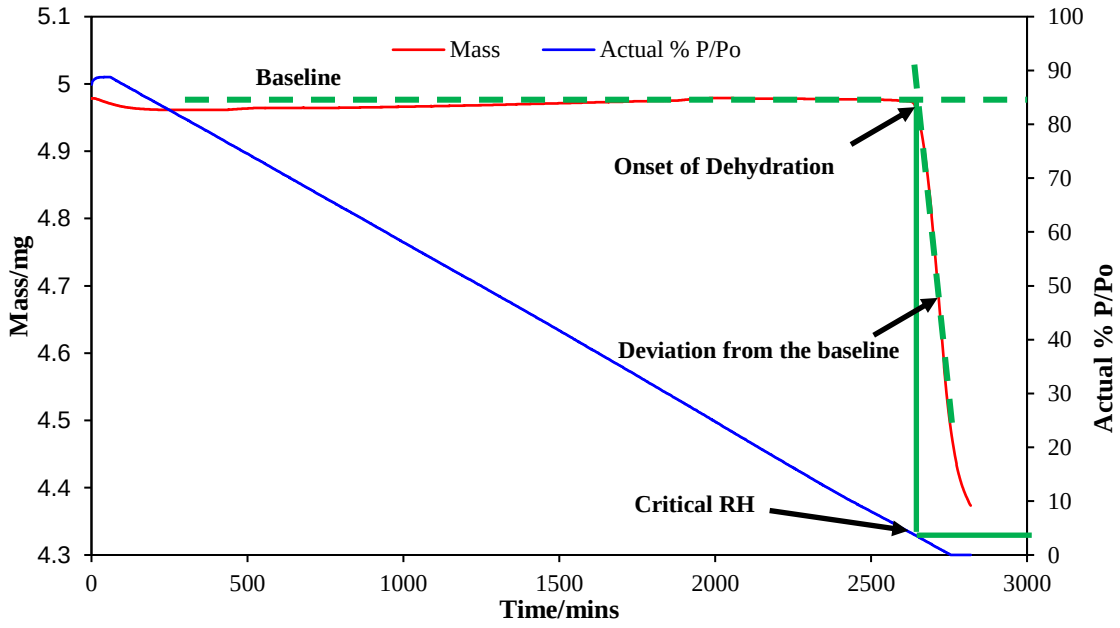

Figure 5-16 Determination of critical RH for dehydration

The DVS isotherms of carbamazepine dihydrate subjected to different ramping rates and temperature are shown in Figure 5-17. The samples appear to be very stable at 25 °C. Even RH below 10%, there is no visible change in the sample mass regardless of the RH ramping rate. Visible decrease in sample mass, which indicates the sample dehydration, is only observed at RH lower that 5%. At 25 °C, the ramping rate does not seem to affect the onset of sample dehydration.

At 30 °C, the dehydration of CBZ.2H_2O at the ramping rate of 2%/hr commences at a critical RH value (~18%) that is higher compared to the other ramping rates. Interestingly, there exist a secondary transition point below which below the rate of change of mass increases. At other ramping rates, only one transition point is observed

for dehydration and they remain almost identical to the ones obtained at 25 °C, at approximately 5%.

The occurrence of secondary transition point becomes more frequent when the temperature is increased, and it seems to be independent of the ramping rate. At 35 °C, both ramping rates of 2 and 4%/hr show secondary transition point at ~5% RH. At 2%/hr, the dehydration commences at ~20% RH, while at 4%/hr, the onset of dehydration is found to be ~17%.

For dehydration at 40 °C, the secondary RH transition point for both 8 and 10%/hr is found to be at ~6%. However, the secondary transition point ceases to exist in the cases where the sample was dehydrated at 2 and 4%/hr at 40 °C. This is due to the fact that the samples had fully dehydrated before the relative humidity was ramped down to ~5 %.

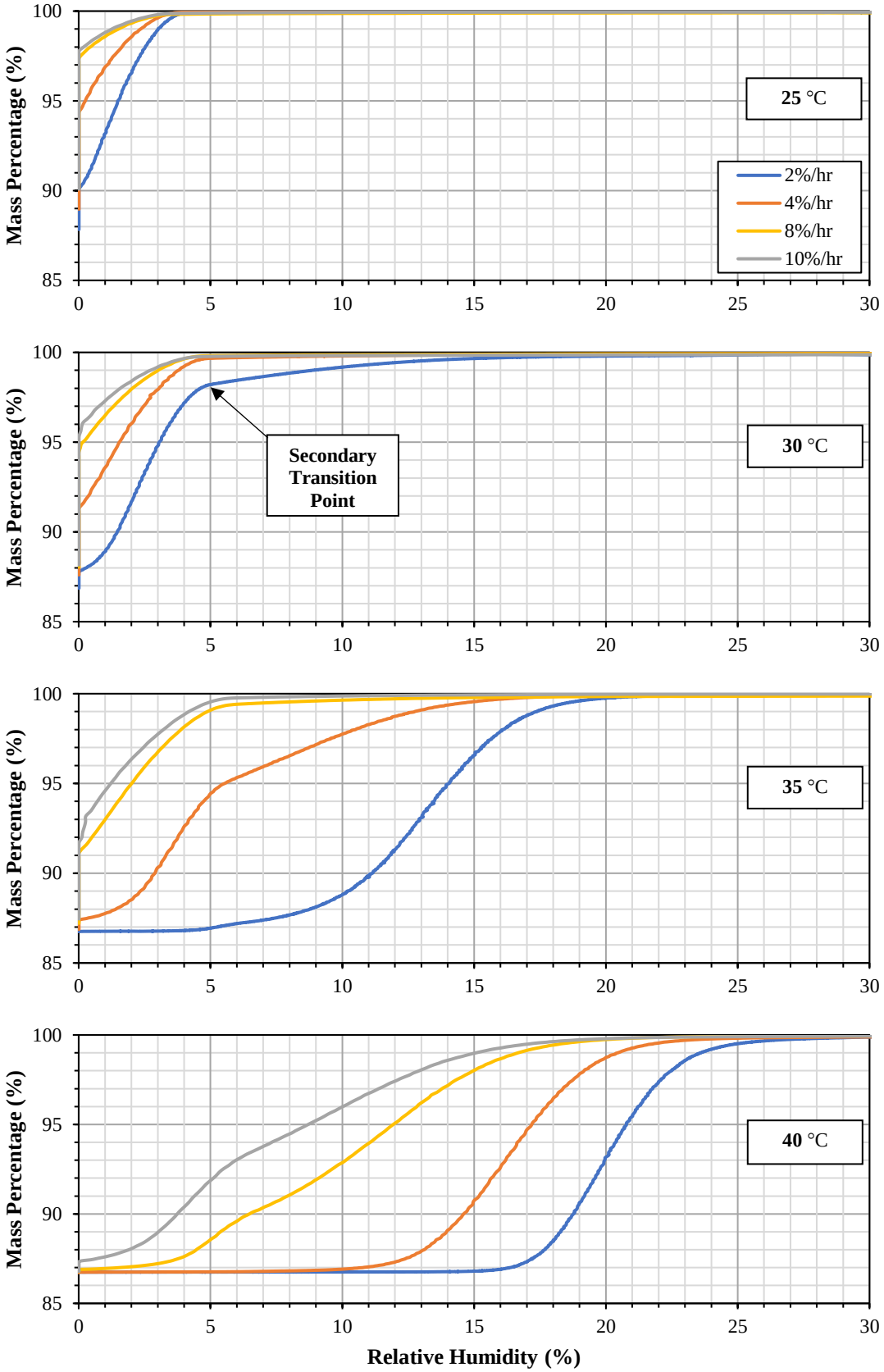

Figure 5-17 Dehydration of carbamazepine dihydrate as a function of ramping rate at different temperatures

The onset RH for $CBZ.2H_2O$ dehydration at different ramping rates and temperatures is shown in Figure 5-18. It can clearly be seen that the critical RH for dehydration is a function of temperature. The higher the temperature, the higher the onset RH for dehydration. The effect of temperature on the onset of dehydration RH is most prominent when the ramping rate is low (2 and 4%). At higher ramping rates (8 and 10%/hr), the effect of temperature is less significant except at 40 °C. Increasing the temperature from 25 to 35 °C does not affect the critical dehydration RH of carbamazepine dihydrate. However, at 40 °C, the critical RH is shifted by a considerable amount from ~5% to 16%.

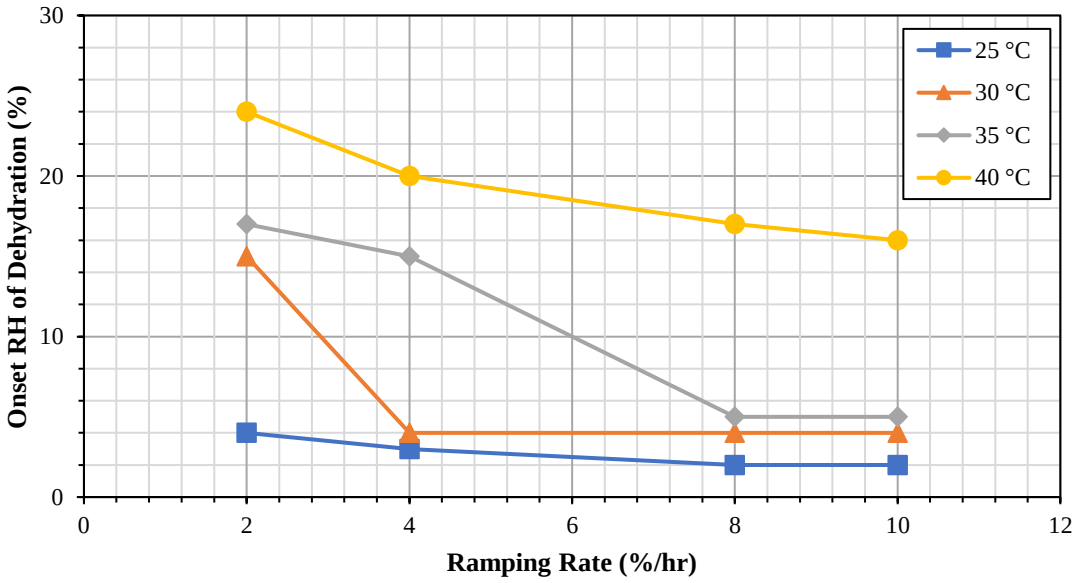

Figure 5-18 Onset of dehydration at different ramping rates and temperatures

By comparing the DVS isotherms of the same ramping rate, the effect of temperature and relative humidity on the dehydration kinetics of $CBZ.2H_2O$ can be investigated. The change of mass of carbamazepine dihydrate as a function of relative humidity at different temperatures and RH ramping rate is shown in Figure 5-19. It is evident that the higher the temperature, the faster the kinetic of dehydration. In some cases, there exist a transition point (~5 % RH) where the rate of dehydration is changed. These observations reveal the significance of relative humidity as the driving force in the

dehydration kinetics. Below the transition point, the dehydration rate is large while above that, the dehydration is significantly slower. A higher RH indicates a larger amount of water vapour in the air (smaller driving force) and hence the evaporation rate of crystal water is reduced. This only happens when the dominant driving force for loss of crystal water by diffusion is the humidity. At higher temperatures, where the dominant driving force for crystal dehydration is the thermal, such transition point does not exist.

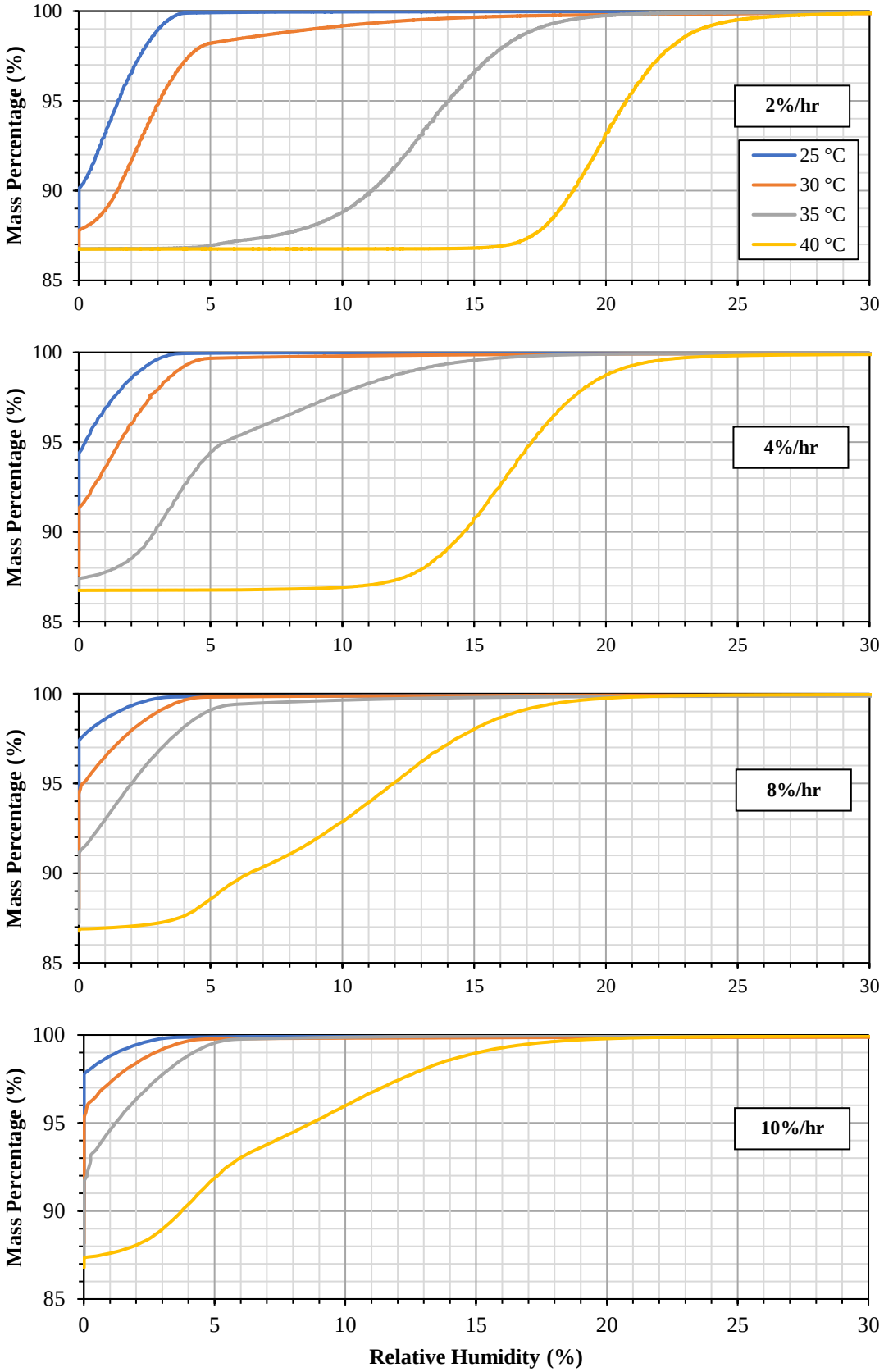

Figure 5-19 Dehydration of carbamazepine dihydrate as a function of temperature at different ramping rates

5.5.2 Rehydration Behaviour of CBZ.2H_2O under Dynamic Humidity Conditions

It has been discussed earlier that the carbamazepine dihydrate crystals used in this work have a high tendency to dehydrate into the anhydrous Form I of carbamazepine. Depending on the temperature and humidity to which it is subjected, the dehydrated carbamazepine may transform back to the hydrate form. It was found that low temperature favours the rehydration of carbamazepine, while a high temperature hinders such transformation. However, that limitation could be overcome by subjecting the dehydrated sample to RH higher than 90%, even at elevated temperature of 40 °C. Previous stepwise experiments have demonstrated the ability of the dehydrated carbamazepine dihydrate to reabsorb water that is equivalent to the stoichiometric ratio of the dihydrate in a constant relative humidity condition. That information is very useful for understanding the stability of the material under well controlled environment. However, in real life situation, the relative humidity could fluctuate through the day. The sorption behaviour of the dehydrated carbamazepine under dynamic humidity environment is still an open field that requires further studies. The purpose of this work is to fill that gap by studying the sorption and rehydration of dehydrated carbamazepine through RH ramping experiments.

Burnett et al. (2004) proposed a new method of characterising the vapour-induced transformation by using vapour sorption technique. Based on their findings, amorphous materials go through a series of transformation events, which are reflected in the change of mass of the material when they are being subjected to increasing relative humidity condition. An example of the sorption behaviour of amorphous material is shown in Figure 5-20. When an amorphous material is first being subjected to increasing humidity, it only adsorbs water onto its surfaces. Water is a plasticising agent, and hence as more and more water gets adsorbed onto the material, it transforms from a glassy state to a rubbery state, where the molecules have higher molecular mobility. Further increase in

the humidity results in a change in the moisture sorption characteristic of the material as the high molecular mobility now allows water absorption into the bulk. The transition point is known as the glass transition point. High humidity above the glass transition could favour recrystallisation of the material and that usually can be reflected as a "peak" in the sorption data. The water sorption capability of amorphous material is much higher (due to the lack of structural arrangement of the molecules) compared to its crystalline counterpart. After recrystallisation, the water sorption capacity of the crystal becomes less compared to when it was in amorphous form, thus resulting in a drastic loss of sample mass.

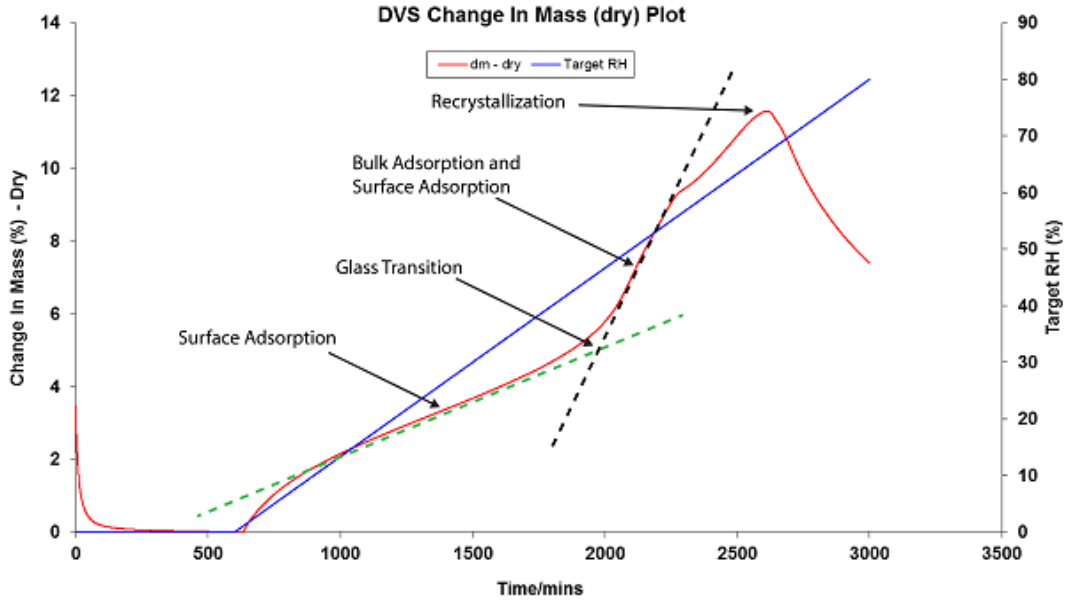

Figure 5-20 Sorption behaviour of amorphous material under dynamic humidity condition (Burnett et al., 2004)

Following this approach, the effects of temperature and RH ramping rate on the sorption behaviour of CBZ.2H_2O are studied in this work. CBZ.2H_2O crystals were first dehydrated by subjecting them to 0% RH at different temperatures in DVS Adventure. Once the crystals were fully dehydrated (indicated by the change of mass per minute), the RH of the system was then ramped up from 0 to 100% using different ramping rates.

5.5.2.1 Effect of Ramping Rate and Temperature

The water uptake of the dehydrated samples as a function of ramping rates at different temperatures is shown in Figure 5-21. At 25 °C, it can be seen that the water uptake increases with the relative humidity. Interestingly, the water uptake of the dehydrated sample seems to be affected by the ramping rate of the relative humidity. Increasing the ramping rate increases the rate of water sorption of the dehydrated sample. This trend is consistent within the range of ramping rate tested. At the ramping rate of 10%/hr, the water uptake at the highest RH (98%) is ~6%. However, the water uptake is only 1% at 98 % RH when the ramping rate used is 2%/hr at 25 °C. This huge difference signifies the importance of RH ramping rate in the water sorption of dehydrated carbamazepine. Unlike the example shown earlier, the water sorption of dehydrated carbamazepine at 25 °C does not show any characteristic (glass transition point) that suggests the presence of amorphous content in the sample. Instead, the dehydrated carbamazepine seems to undergo recrystallisation as indicated by an increase followed by a decrease in the water uptake. This is in line with the X-ray diffraction data presented in the previous chapter, which suggest CBZ.2H_2O dehydrates to anhydrous crystalline Form I carbamazepine in the dehydration conditions tested in DVS. This change of water sorption affinity (indicated by the "peak" below 70 % RH) implies the transformation of the dehydrated carbamazepine from one crystalline form to another. This "peak" gets narrower and occurs at higher RH levels with the RH ramping rate. At 2%/hr, the maximum point of the peak is found at ~35% RH and the span of that peak is huge, ranging from 0 to 60% RH. At 10%/hr, the commencement of the peak gets delayed and shifted to higher RH. The peak is now narrower (ranging from ~65 to 75% RH) and the maximum point is found to be at ~70% RH at 25 °C.

Similar trend is observed for the samples rehydrated at 30 °C. The recrystallisation peak gets broader and shifted to higher RH with the ramping rate. The same applies to

the samples dehydrated at 35 °C, but secondary peak starts to appear at RH higher than 90% (2 and 4%/hr). The occurrence of secondary peak gets more prominent when the temperature is increased to 40 °C. It is evident that the dehydrated samples go through two cycles of transformation events. The first one happens below 50% RH and the maximum point increases with the ramping rate. The second transformation event commences at RH higher than 50% but the maximum point of the peak (~90%) does not vary much regardless of the ramping rate. At some cases, the water uptake is seen to increase again after the plummet, such as the series 4%/hr at 35 °C and 10%/hr at 40 °C.

The water uptake of the dehydrated samples replotted as a function of temperature at different ramping rates is shown in Figure 5-22. Ramping the relative humidity at the same rate does not yield similar water sorption behaviour of the sample. It can clearly be seen that the water sorption of $CBZ.2H_2O$ is temperature dependent. Increasing the temperature reduces the ability of the dehydrated sample to adsorb water into the bulk structure of the crystals. At 2%/hr, the water sorption of the dehydrated carbamazepine at 25 and 30 °C shows an upward behaviour, whereas the water uptake plummets at 35 and 40 °C, at RH higher than 90%. Only very little water uptake is observed at 35 and 40 °C, with the highest water uptake being not more than 0.5 %.

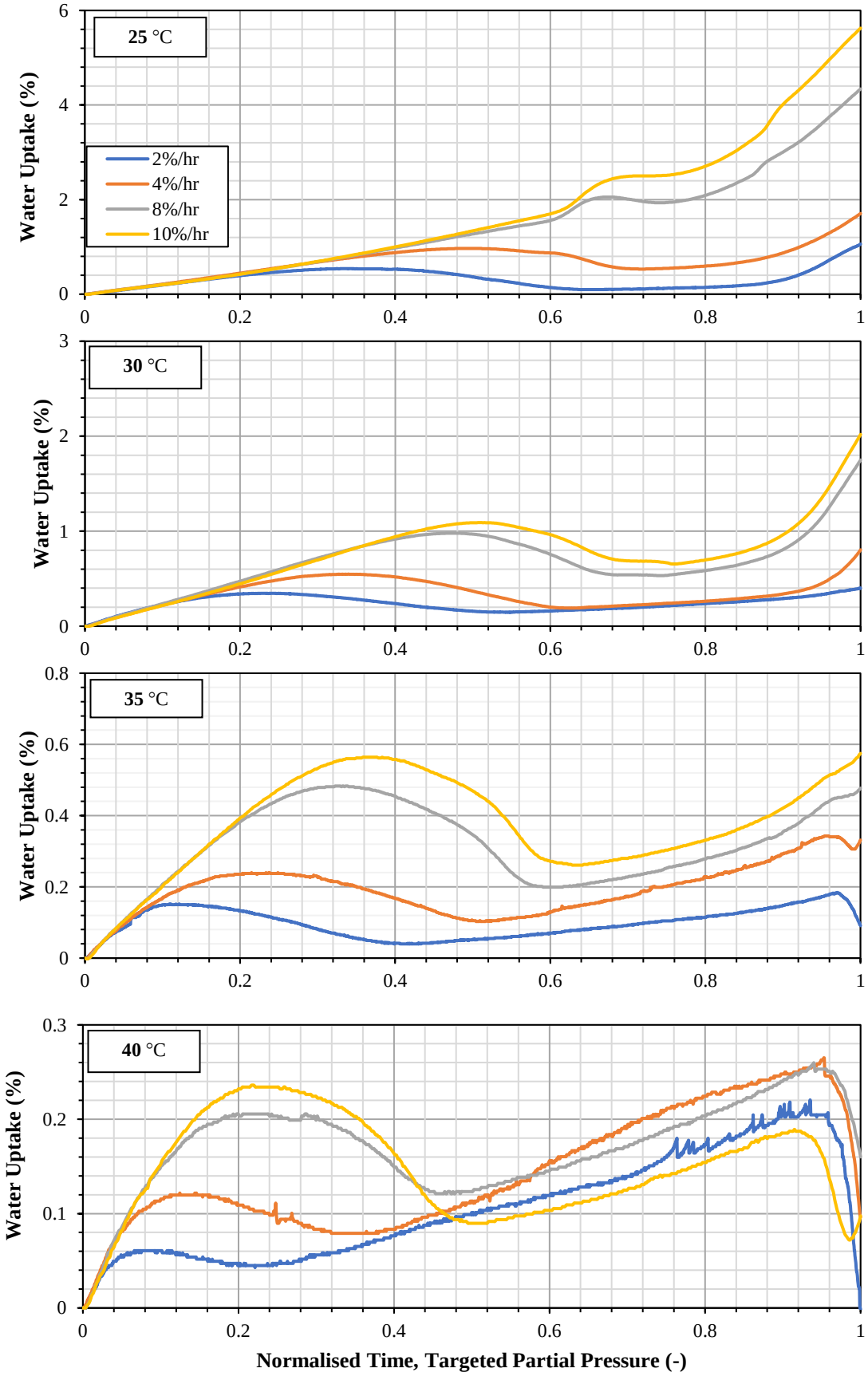

Figure 5-21 Water sorption behaviour of the dehydrated samples as a function of ramping rates at different temperatures

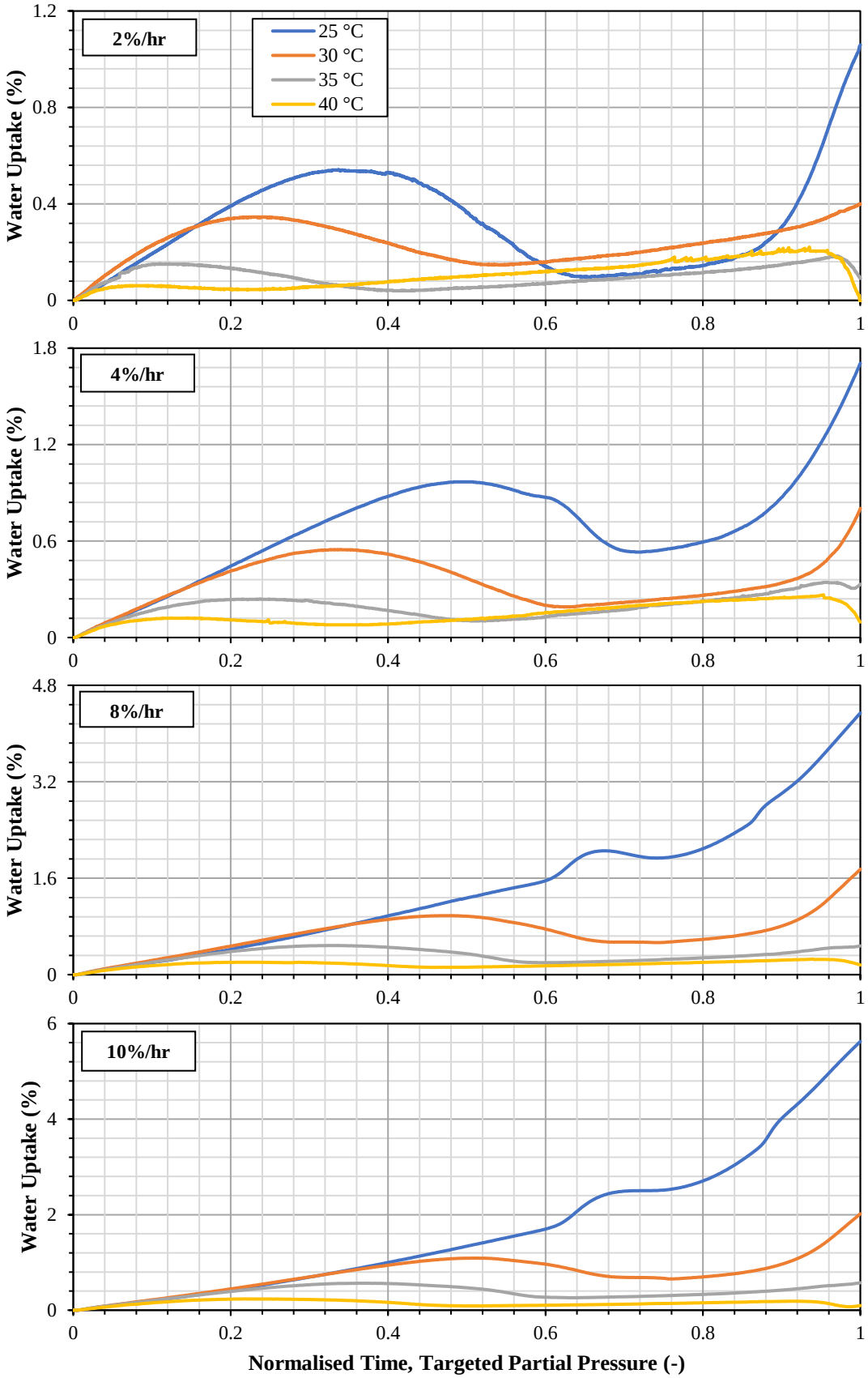

Figure 5-22 Water sorption behaviour of the dehydrated samples as a function of temperature at different ramping rates

5.6 Conclusions

A series of experiments have been performed to study the dehydration and rehydration of carbamazepine dihydrate. DVS experiments at 10% RH step suggest that the dehydration commences at below 10% RH and the rehydration of the dehydrated carbamazepine is dictated by the sorption temperature. Out of all the temperatures tested, the dehydrated carbamazepine seems to be able to regain the crystal water loss at 90% RH only through dehydration at 25 °C. A further experiments involving smaller RH steps reveal the dehydration of carbamazepine commences at RH varying from 2 – 4 %, depending on the temperature. The higher the temperature, the higher the critical RH for dehydration.

SEM analysis reveals macroscopic structural difference of CBZ.2H_2O dehydrated at different temperatures. At 25 °C, the macroscopic structure of the crystals remains intact. As the temperature is increased, secondary crystal domains are found growing on the crystal surfaces and have been identified as Form I "whiskers" through PXRD. The formation of such whiskers is most prominent when the sample was dehydrated at 40 °C.

Further experiments involve subjecting the dehydrated crystals to 98% RH. Interestingly, the crystals are now able to pick up water that is equivalent to the crystal water loss, indicating transformation back to the hydrate form of carbamazepine. These experiments highlight the role of relative humidity in the rehydration of carbamazepine. At RH lower than 90%, the rehydration of carbamazepine is limited by the temperature. That limitation is broken when the surrounding air is saturated with water vapour, at 98% RH.

The kinetics of dehydration have been successfully modelled using a first-order rate model. The dehydration kinetics of carbamazepine dihydrate at 0% RH fit nicely using Arrhenius equation. The activation energy for dehydration calculated agrees very

well with the literature reported. Arrhenius plot describes the temperature dependence of the dehydration of carbamazepine and is very useful of industrial process design.

The dehydration of CBZ.2H_2O has also been studied by ramping the RH from 90 to 0% at different ramping rate. There exists a transition region (~5-7 % RH) where the rate of dehydration changes significantly. At low temperatures, the onset of dehydration is driven by the relative humidity while at higher temperature it is dominated by the dehydration temperature.

The sorption and rehydration of dehydrated carbamazepine have also been studied using vapour sorption method. Ramping the RH from 0 to 100% reveals a series of transformation events of the dehydrated carbamazepine. The change of the crystal affinity to water suggests a polymorphic transformation of the dehydrated crystals. At higher temperatures, two peaks are observed, implying that the sample may have gone through secondary transition at RH higher than 90%, suggesting that the high temperature and high RH may favour the transformation to another polymorphic form of carbamazepine.

Chapter 6

Assessment of Carbamazepine Dihydrate Failure Patterns and Breakability using an Aerodynamic Dispersion Method

6.1 Introduction

Active pharmaceutical ingredients (APIs) are generally crystallised for stability and purity considerations, but are very often milled to obtain desired characteristics that are essential for further downstream processing, such as bioavailability of the drug, compactability and tabletability (Rowe, 2006). Particle breakage could also be unintentional, such as the particle attrition during filtration, drying, storage and transportation in the case of weak crystals, which eventually leads to the degradation of product quality and handling issues. This situation is often exacerbated in the case of acicular crystal shape, which is the subject of study here.

Breakage of particulate solids is the result of complex interactions of material properties, environmental conditions and the loading mode (Tavares, 2007). The breakage behaviour of particles is governed by their mechanical properties such as fracture toughness, K_C hardness, H and Young's modulus, E (Ghadiri et al., 2019). Moreover, for the case of organic crystals, these properties are strain-rate and temperature-dependent (Wendy C. Duncan-Hewitt and Weatherly, 1989; Hassanpour et

al., 2004; Olusanmi et al., 2010). The ratio of hardness, H, to fracture toughness, K_C is proposed by Lawn and Marshall (1979) as a measure of the brittleness of material under quasi-static indentation. Under dynamic impact loading conditions, the particle breakage propensity is described by the ratio H/K_C^2 (Ghadiri and Zhang, 2002).

Crystalline materials readily break by fracturing on cleavage and slip planes (if present), and/or on planes influenced by the tensile and shear stress fields. Breakage on cleavage planes produces smooth surfaces, whilst on other planes it is often associated with uneven and irregular fracture surfaces (Klein et al., 1985). Cleavage planes have low fracture surface energy and are therefore weaker than other planes within the structure. Consequently, they are more prone to failure compared to the others. Good examples are sodium chloride, a simple cubic crystal system which is known to readily cleave on the (100) planes (Pratt, 1953) and aspirin, which also cracks preferentially on cleavage planes (100) under both quasi-static and impact loading conditions, even though the cracks originate from plastically-deformed regions (Olusanmi et al., 2011). Generally speaking, crystals with cleavage planes tend to break into bigger fragments under the same stressing energy. In contrast, for particles with no cleavage plane, a higher energy is needed to forge the crack ahead and hence the breakage progeny is smaller in size.

Being able to assess the processability issues prior to mass production is of great interest of the pharmaceutical industry, especially when the formulation is still in clinical trial stage, and the available quantity of the material is scarce. Though there exists a wide range of assessment techniques (both quasi-static and dynamic conditions) in the literature, those testing devices are often not commercially available. The demand of having a breakability assessment tool commercially available has led to the work of Bonakdar et al. (2016) in which they developed a novel method based on Ghadiri and Zhang (2002) model to assess the breakability of materials using the dry dispersion unit of a commercial particle size analyser, the Scirocco disperser of Mastersizer 2000. The

breakage propensity is expressed as the shift of specific surface area, which can be easily calculated from the size distribution measured by laser diffraction technique. This new assessment technique has proven to agree very well with the results obtained from the single particle impact tester. However, a good fraction of pharmaceutical materials is highly acicular in shape, and laser diffraction is known to give false representation of the particle size of high aspect ratio particles. Hence using LDA for acicular particles is inadequate. A better technique to measure the size distribution of acicular particles would be by optical image analysis, where the actual particle size and shape are measured directly and not inferred from laser light scattering data.

The focus of this work is on the breakage of acicular crystals of carbamazepine dihydrate under impact loading. The mechanistic model of particle impact breakage of Ghadiri and Zhang (2002) is used here to analyse the breakage. Morphologi G3 of Malvern Panalytical, a particle size analyser based on static optical imaging analysis technique, is used to assess the breakage of carbamazepine dihydrate crystals under impact loading. The impact energy comes from the dry dispersion unit of the device, where a pulse of pressurised air is applied, by which the particles in the sample well (Figure 6-1) are dispersed and impact on to the internal walls of the spool before settling down onto a glass slide for subsequent size and shape analysis.

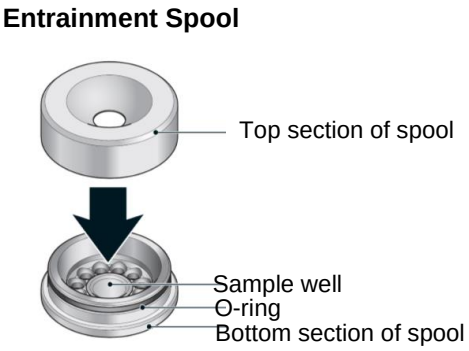

Figure 6-1 Dispersion spool of the dry dispersion

The transient fluid flow field is calculated by CFD modelling using Fluent. The particle trajectories are calculated using the same approach as of Ali and Ghadiri (2017) by adopting a Lagrangian method of calculation of particle velocity. The correlation of Ganser (1993) is used to account for the effect of particle shape on the fluid drag. The particle size is measured and the shift in its distribution is then used following the approach of Bonakdar et al. (2016) to estimate the breakability. In addition, the length and width of the particles are measured to reveal the breakage mechanism of in connection with the cleavage plane present in the crystal lattice structure.

6.2 Materials and Methods

6.2.1 Carbamazepine Dihydrate Crystals

CBZ.2H_2O_B2016 crystals were used in this work. Two water molecules are embedded in its lattice structure, forming channels of water molecules along the largest dimension of the macroscopic crystal, parallel to the crystal axis *c* (Figure 6-2). Its structure is monoclinic with a space group $P2_1/c$ (Harris et al., 2005). It is acicular and platy, owing to the fact that the growth rate of the first two dimensions which constitute the dominant faces (h00) and (0k0) of the crystals is substantially higher than the third dimension (Figure 6-3). Crystal axes *b* and *c* correspond to the particle length and width of the grown crystals. The orderly arrangement of water channels in the lattice structure leads to the

formation of cleavage planes (0k0) that are perpendicular to the dominant face (h00) of the crystal. These planes are very weak and are known to get exposed easily upon dehydration due to the macroscopic strain imposed (Khoo et al., 2013). The formation of cracks on h00 face is shown in Figure 6-4. They are parallel to the crystal axis *c* as a result of the detachment of water molecule from the crystal lattice channels (Rauber, 2018).

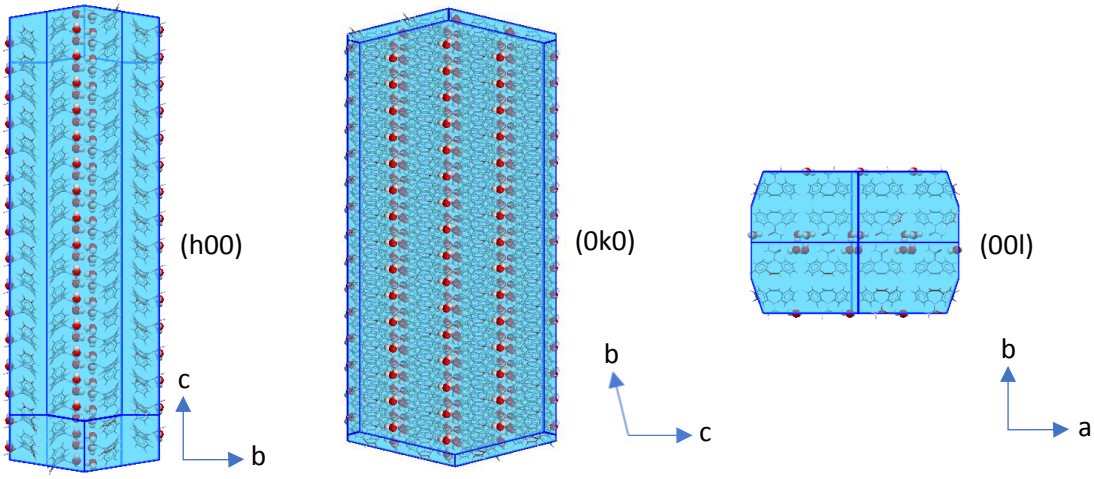

Figure 6-2 Calculated BFDH crystal morphology of carbamazepine dihydrate

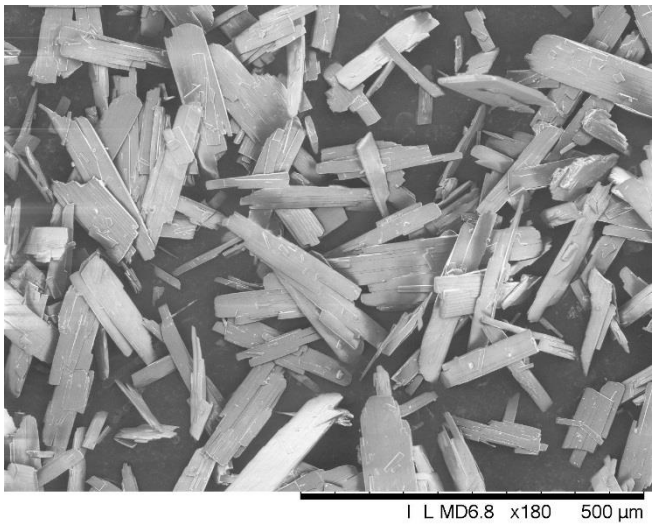

Figure 6-3 Carbamazepine dihydrate crystals viewed by scanning electron microscope (SEM)

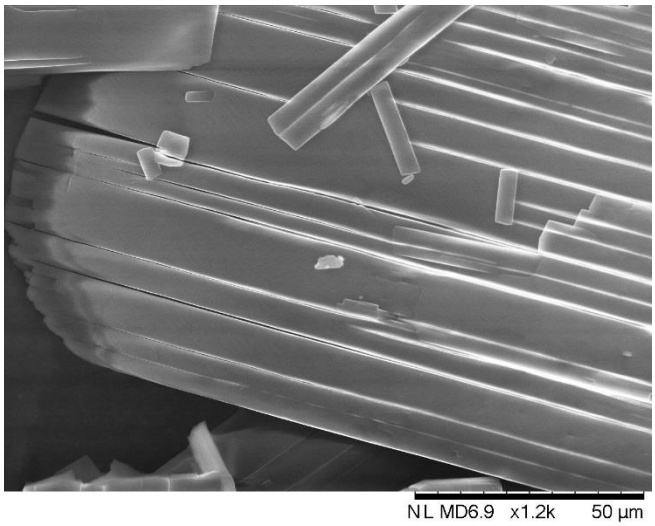

Figure 6-4 Formation of cracks on weak cleavage planes along h00 face under vacuum in the SEM chamber due to dehydration

6.2.2 Experimental Setup

A small amount of sample (~5 mm^3) is first placed into the dispersion spool of the dry dispersion unit of Morphologi G3. A pulse of pressurised air is then applied to disperse the particles, as a result of which they impact against the internal walls of the spool and possibly break before they exit the disperser and settle down onto the glass slide inside the collection chamber. The dispersion pressures used in this work ranges from 0.5 barg to 5 barg (with 0.5 barg interval between the consecutive tests). A series of grayscale images covering the whole scan area are captured by the microscope unit of the device with the aids of the automated XYZ stage under episcopic lighting condition. Image thresholding is performed to convert the grayscale images into binary images and isolate the particles from the background. The individual particle morphological properties are then analysed using the built-in image analysis suite.

6.2.3 Exclusion of Particle Anomaly by Image Analysis

A series of tests were performed initially to determine the optimal sample size, which has the largest particle population while attaining the minimum occurrence of particle overlaps. Nevertheless, there still existed some particles that laid on top of each other, appearing as a clump of particles (Figure 6-5). If left unattended, these will be treated as single particles in the image analysis, leading to false representations of the particle size and shape distribution, hence causing errors in the breakage analysis. Filters based on particle convexity and solidity are applied to remove them (discussed in Chapter 2). Both of these shape parameters give a measure of the "spikiness" of the particle. A clump that is made up of multiple particles will appear to be more spiky than individual crystal. A sensitivity analysis was performed to determine the optimal values for convexity and solidity, and it was found that a value of 0.85 used in both parameters filtered out most of the overlapping particles while keeping the individual particles intact.

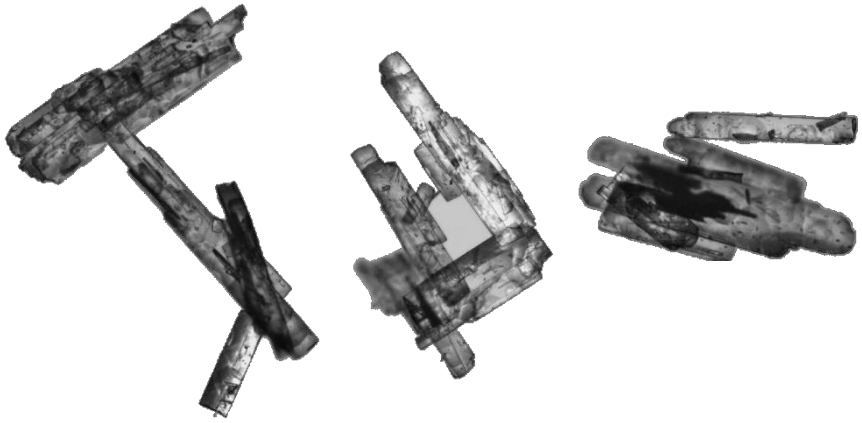

Figure 6-5 Clumps of carbamazepine dihydrate crystals

6.2.4 Particle Volume Estimation

Like most particle analysers, Morphologi G3 captures 2-dimensional information of the particles, as they lie on their maximum stable plane. Carbamazepine dihydrate crystals are platy and their third dimension is significantly smaller than the other two dimensions.

Therefore, the volumetric particle size distribution is calculated based on the crystal projected area, assuming constant thickness.

6.2.5 Statistical Reliability and Data Smoothing

Particle size and shape analysis by G3 Morphologi uses a miniscule sample, typically in milligram range for each measurement. However, a small sample size is also associated with lower population of particles being measured and hence the particle size distribution may not be fully representative. Depending on the particle size and shape of the sample, multiple measurements may have to be performed to improve the statistical reliability of the measured particle size distribution. The particle size distribution of bigger and non-spherical particles, especially those with large aspect ratio, tends to have a wider scatter compared to those of smaller and rounded ones. An example of the PSD of carbamazepine dihydrate dispersed at 0.5 barg is shown in Figure 6-6. The particle size distribution measured using G3 Morphologi is in the form of discrete probability distribution but is presented here as continuous probability distribution for better visual presentation. The scatter of the PSD is large for each individual measurement as the population number is small. Summing six of these measurements reduces the scatter. Undoubtedly, increasing the number of measurements will further smoothen out these peaks. A moving average of 11 points is applied to the sum of PSD at every dispersion pressure tested to iron out the peaks present, due to the deficiency of particle population in the measurement. As shown in Figure 6-7, a moving average of 11 points produces a reasonably smoothened plot and the overall distribution is not shifted excessively.

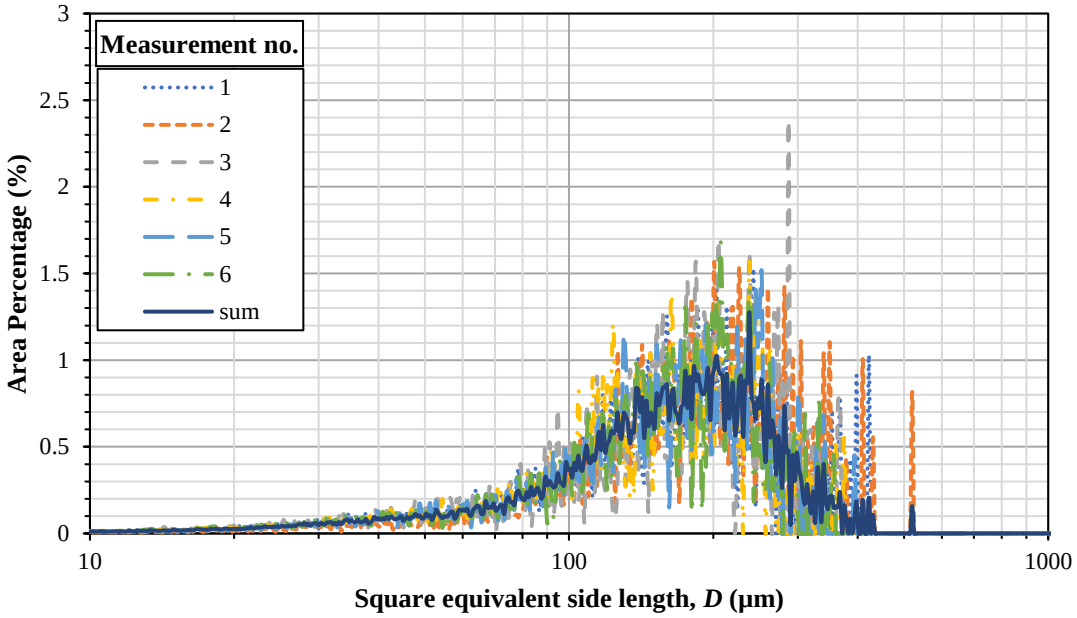

Figure 6-6 Measurements of PSD of carbamazepine dihydrate dispersed at 0.5 barg

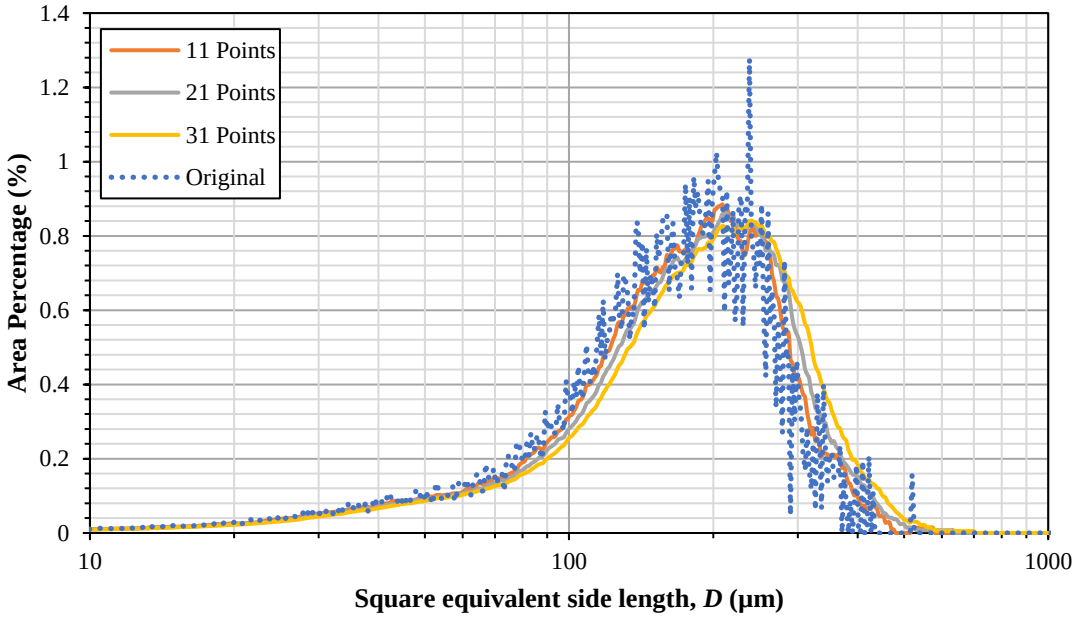

Figure 6-7 Moving average of PSD using different number of points

6.3 Impact Velocity Prediction by Computational Fluid Dynamics (CFD)

The CFD calculations of this work were performed by Dr Muzammil Ali, University of Leeds. Prediction of impact velocity of particles is carried out using transient three-

dimensional CFD modelling of G3 Morphologi disperser to take into account the effect of air flow and turbulence on the trajectories of particles. Commercial CFD software Ansys Fluent (2017) is used to solve the continuous (air) phase flow equations. To assess the impact of inlet pressure pulse on the impact velocities of particles, the simulation is carried out using inlet air pressures of 0.5 to 5 barg in 0.5 barg progression. Each simulation is run at the specified inlet pressure for 20 ms, thereafter the pulse is stopped by changing the pressure to 0 barg. The simulation is allowed to run until all the particles exit the domain. Details of the CFD modelling methodology, numerical solution method and the mesh used in the CFD simulations can be found in an earlier work carried out by Ali and Ghadiri (2017) in which triboelectric charging of particles in G3 disperser was studied using CFD modelling.

6.3.1 Modelling of particle trajectories

The discrete phase is considered to comprise thin cuboid-shape particles with constant width and thickness of 100 µm and 20 µm, respectively and length of 100, 250, 500 and 1000 µm. The density of particles is considered to be constant with a value of 1270 kg/m^3. The particles are initially placed in the sample well and dispersed by a pulse of pressurised air. The trajectories of particles are computed by solving the equation of motion of particles considering the drag and gravitational forces. For these particles shapes, the drag coefficient is calculated using correlations given by Ganser (1993). The rotation of particles is not considered. One-way coupling is assumed between the particles and the air, i.e. the air flow influences the trajectories of particles, but the momentum exerted by the particles on the air is ignored. The interaction between the particles is also not considered. The maximum impact velocity of particles in the disperser takes place at the wall just above the sample well (Figure 6-1). For the purpose of predicting the impact velocity, the velocity of particles colliding with this region of the wall is recorded and the

impacted particle is eliminated from the computational domain. To get a statistically representative impact velocity, 1000 particles are tracked for each size and the average value is used.

6.4 Experimental Results and Discussions

6.4.1 Size Reduction of Carbamazepine Dihydrate Crystals

The averaged PSDs of carbamazepine dihydrate at different dispersion pressures are shown in Figure 6-8. Gradual shifting of the size distribution to the left is observed as the dispersion pressure is increased. The reduction in the number of the larger particles, while the distribution remains skewed indicate that the particle breakage is dominated by fragmentation upon dispersion. Extensive breakage was observed above 4 barg pressure. The characteristic sizes, $D_{V,10}$, $D_{V,50}$ and $D_{V,90}$ are determined from the cumulative volume plots of these distributions (not shown in this paper) and the relationship between these attributes and the dispersion pressure is depicted in Figure 6-9. The subscript that follows after D_V is the volume percentage below the size of interest. Similar notation is given to the characteristic length, L_V, width, W_V and aspect ratio, AR_V, respectively. $D_{V,90}$, the characteristic particle size below which 90% of the particle population by volume lie, is normally associated with the large particles present in the sample and the change of this value shows a very clear trend of the evolution of particle size over the dispersion pressure range tested. It can be seen that the $D_{V,90}$ value at 5 barg, the highest dispersion pressure tested, is almost half of the one at 0.5 barg, indicating a reduction in particle volume by approximately a factor of four (assuming 2D dominant shape of the crystal). $D_{V,10}$ on the other hand, shows that the volume of the smaller particle at 5 barg is ~140 times smaller than those at 0.5 barg, indicating the particles undergo a significant size reduction upon being dispersed at 5.0 barg.

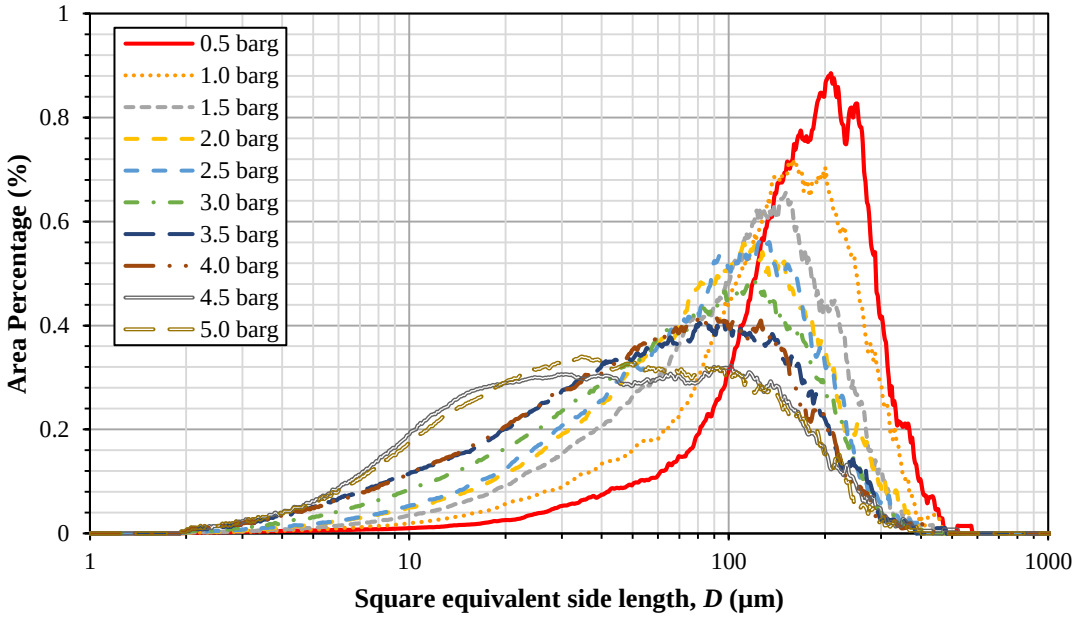

Figure 6-8 Particle size distribution of carbamazepine dihydrate crystals dispersed at different pressures

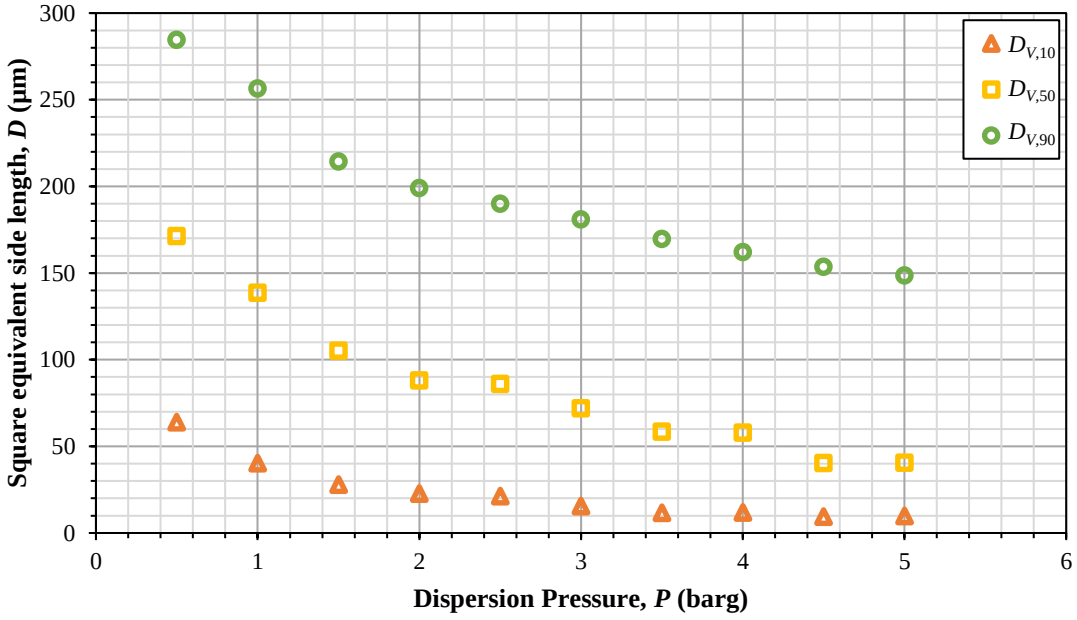

Figure 6-9 Characteristic volumetric intercept values of square equivalent side length, $D_{v,10}$, $D_{v,50}$ and $D_{v,90}$

6.4.2 Extent of Breakage

The extent of breakage, *R** gives a measure of the amount of debris produced after a breakage event, normally expressed on gravimetric basis, given by Eq. 6-1. This

gravimetric ratio can be converted to volumetric ratio as the density is the same for all the particles.

$$R^* = \frac{M_d}{M_f} = \frac{V_d \times \rho}{V_f \times \rho} = \frac{V_d}{V_f} \tag{6-1}$$

where M_d is the mass of debris, M_f is the mass of feed, V_d and V_f are the cumulative particle volumes (not the bulk volume) of debris, and the feed, respectively and ρ is the density of the particles. This relationship can further be simplified and expressed as a ratio of projected areas if the thickness term is considered constant for all sizes:

$$R^* = \frac{M_d}{M_f} = \frac{V_d}{V_f} = \frac{A_d \times h}{A_f \times h} = \frac{A_d}{A_f} \tag{6-2}$$

where h is the thickness of the particles, A_d the projected area of debris and A_f the projected area of feed particles. A_d / A_f can be obtained by subtracting the reference PSD (subjected to the lowest dispersion, 0.5 barg) from the PSD of interest. The integral of the positive difference as illustrated in Figure 6-10 can be calculated using Eq. 6-3 and Eq. 6-4.

$$S_i = B_i - B_{ref,i} \tag{6-3}$$

$$R^* = \sum_{i=1}^{n} S_i \left[S_i > 0 \right] \tag{6-4}$$

where S_i is the difference between the area percentage of the reference PSD, $B_{ref,I}$ and the PSD of interest, B_i of the particle size bin number I and R^* the sum of the positive differences between the two PSDs up to bin number n (the particle size is segmented into 1001 bins in the Morphologi G3, maximum particle size being 2 mm). The extent of breakage of carbamazepine dihydrate crystals as a function of the dispersion pressure is illustrated in Figure 6-11. The data points presented are the mean extent of breakage calculated from the six repeated measurements and the vertical bars being the standard deviation (SD). It can clearly be seen that as the dispersion pressure increases, the extent

of breakage increases too. The extent of breakage does not increase linearly with the dispersion pressure. This could be attributed to the fact that the particles have a limited travel distance in the dispersion spool to accelerate before impacting on the wall and hence increasing the dispersion pressure does not increase the impact velocity much at higher pressure.

It is evident that the particles break more as the dispersion pressure increases, though at lower dispersion pressures (below 2 barg), an increase in the extent of breakage is more prominent. The extent of breakage is in the range from 20% at 1 barg up to 60% at 5 barg with respect to the reference size distribution measured at 0.5 barg. This observation agrees very well with the qualitative comparison of the PSDs and quantitative investigation of characteristic sizes discussed in the previous section, which further stipulates that the carbamazepine dihydrate crystals are highly prone to breakage upon dispersion.

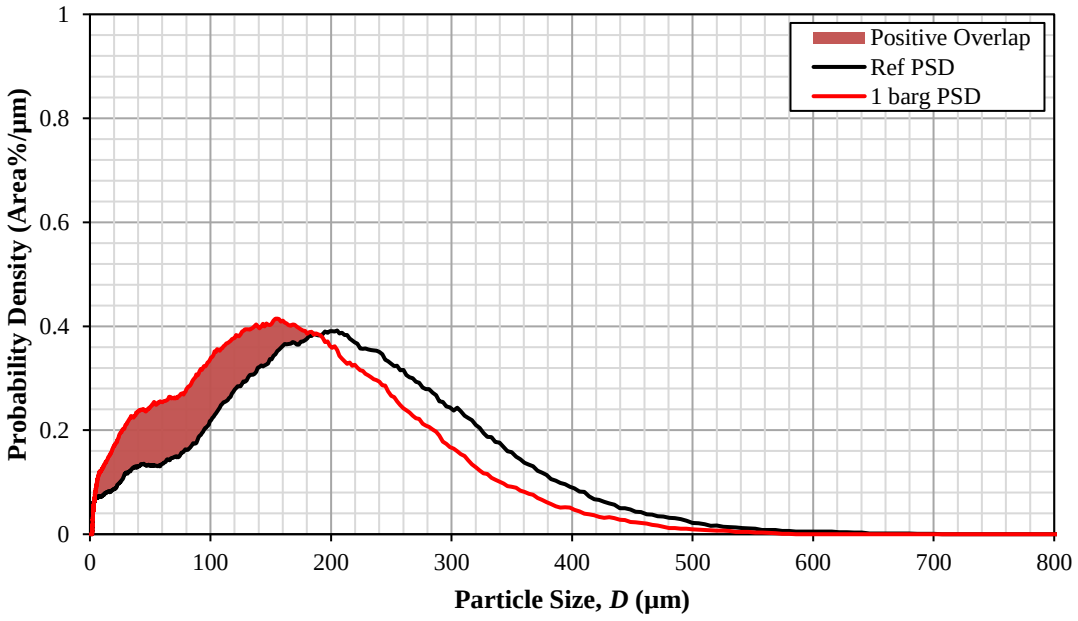

Figure 6-10 Calculation of R in the form of* A_d/A_f *(%)*

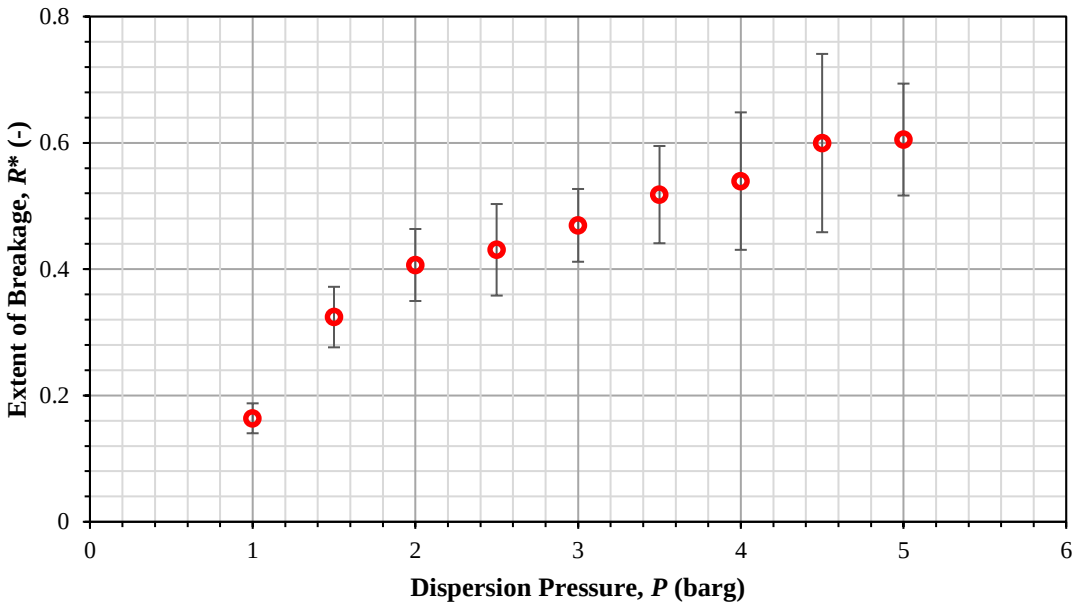

Figure 6-11 Extent of breakage of carbamazepine dihydrate crystals at different dispersion pressures

6.4.3 Shifting of Particle Length, Width and Aspect Ratio

The mode of breakage of carbamazepine dihydrate is very different compared to that of equant particles. High aspect ratio particles experience bending moments along their long axis and could snap along the length. The presence of cleavage plane on the dominant face (h00) complicates the breakage pattern further. Even though breakage on cleavage planes requires low energy and is often the preferred route for crack propagation, the geometric effect of the high aspect ratio of carbamazepine dihydrate could make breakage along the length more dominant. Figures Figure 6-12 and 1-13 show the length and width distributions of carbamazepine dihydrate crystals, dispersed at different pressures. Much like the volume distribution, length and width distribution of carbamazepine dihydrate widens and shifts to the left as the dispersion pressure is increased. The trend of breakage of acicular particles across their largest dimension is supported by the change of characteristic length, L_V at 90% particle volume (Figure 6-14). The change of particle length between each pair of consecutive pressures is notable, especially at lower

dispersion pressures up to 2 barg. Despite the presence of cleavage planes that are parallel to the particle length (Rauber, 2018), carbamazepine dihydrate crystals fracture across the particle length upon impact. This is a clear evidence that the geometric effect of bending of carbamazepine dihydrate is significant. Breakage across its width (along planes parallel to the long axis) is also observed due to cleaving and follows a similar pattern of Figure 6-15, but not shown here for brevity. The reduction of both particle length and width take place at a fast rate at lower pressures, but it slows down, approaching an asymptotic level, as the dispersion pressure is increased. There exists a transition point at 2 barg above which the changes in particle length and width between each pair of consecutive pressures become less conspicuous. These results show that unlike other acicular crystals, such as β-glutamic acid (Saifoori, 2018), carbamazepine dihydrate crystals do break in a noticeable degree along both their length and width. Though not to the same extent as the particle length, there is a substantial reduction in the particle width from 180 to 100 μm (~44%). Micrographs by SEM in Figure 6-16 (a) clearly show cracks along the particle length, parallel to the crystal axis *c* where the cleavage planes (0k0) exist. On the contrary, the fracture along the particle length, i.e. on planes perpendicular to axis *c*, has a more irregular edge (Figure 6-16 (b)). This is in agreement with the crystal lattice structure of carbamazepine dihydrate, as no slip/cleavage plane has been identified perpendicular to the particle length.

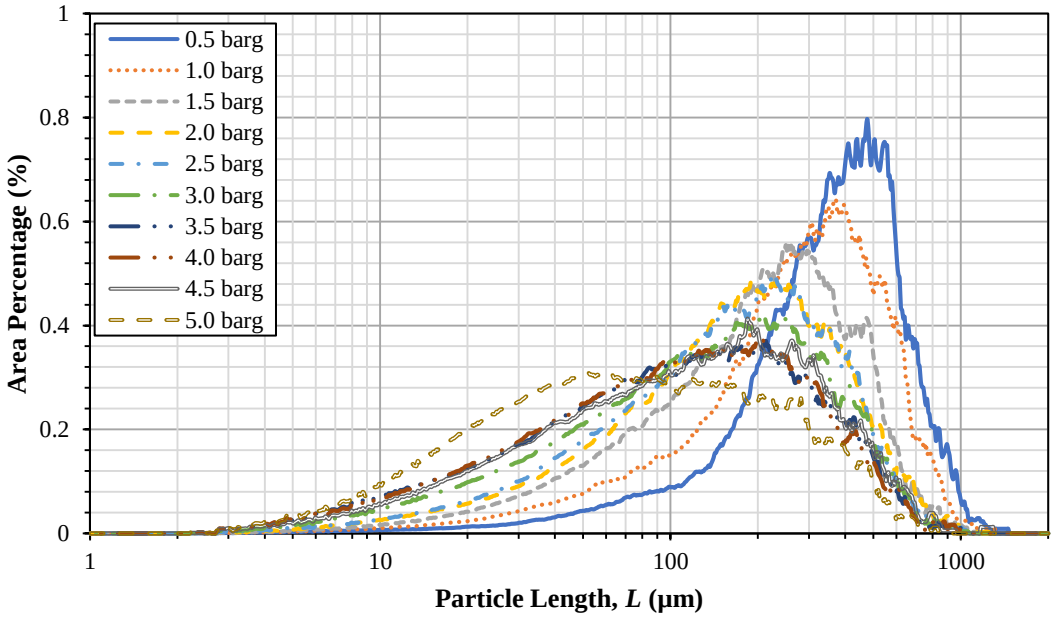

Figure 6-12 Particle length distribution of carbamazepine dihydrate crystals dispersed at different pressures

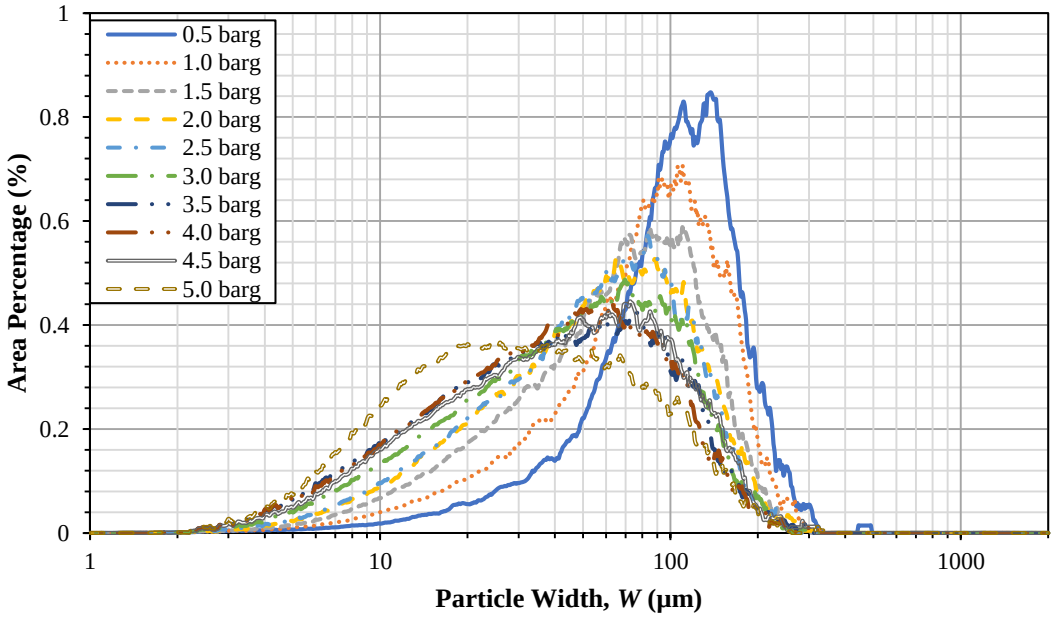

Figure 6-13 Particle width distribution of carbamazepine dihydrate crystals dispersed at different pressures

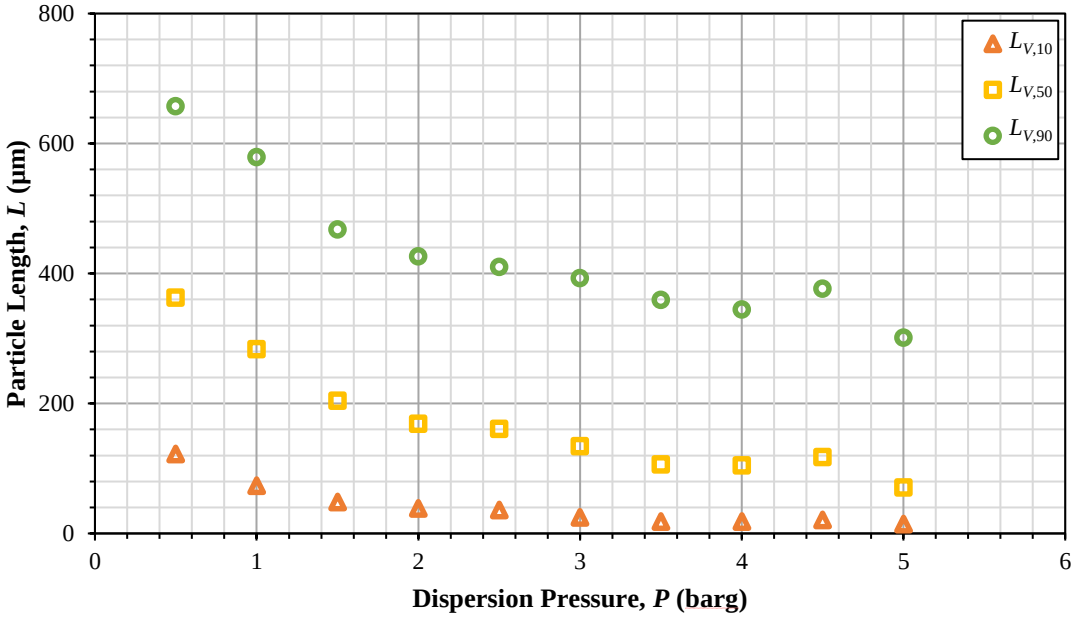

Figure 6-14 Characteristic volumetric intercept values of particle length, $L_{v,10}$, $L_{v,50}$ and $L_{v,90}$

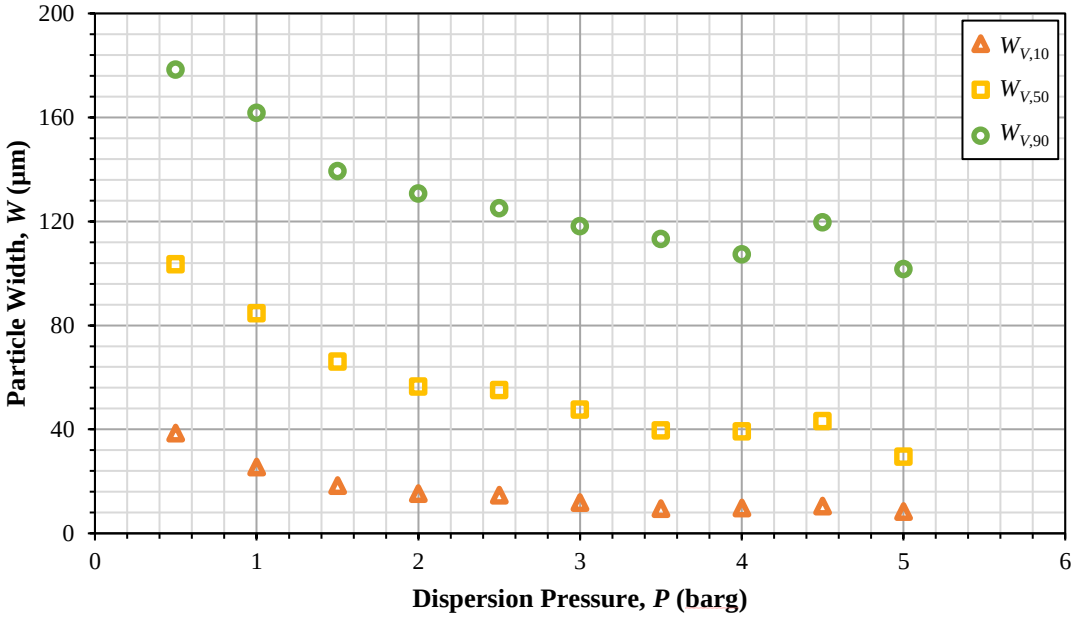

Figure 6-15 Characteristic volumetric intercept values of particle width, $W_{v,10}$, $W_{v,50}$ and $W_{v,90}$

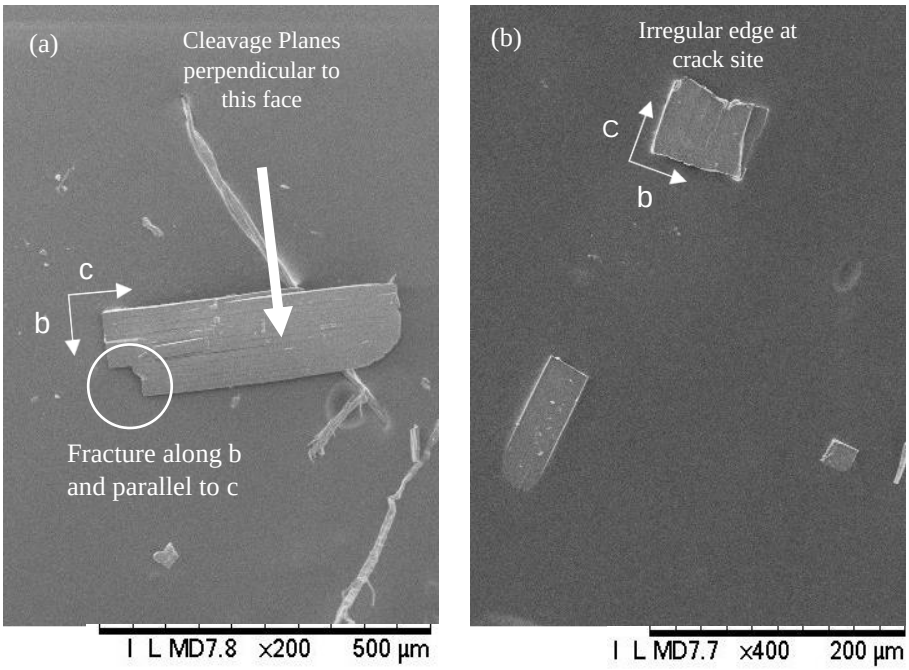

Figure 6-16 Fracture of carbamazepine dihydrate crystal along its (a) width and (b) length

The distributions of particle aspect ratio, defined as width over length, at different dispersion pressures are shown in Figure 6-17. The distributions are initially positively-skewed and with increase in pressure, the skewness reduces, indicating that the crystals undergo a higher extent of breakage along their length. The evolution of the characteristic values of aspect ratio as the dispersion pressure is increased is shown in Figure 6-18. A more prominent change is observed for the $AR_{V,90}$ series, the characteristic aspect ratio of larger particles, indicating a higher tendency for the larger particles to undergo size reduction and shape modification. Above 3 barg, the aspect ratio of the particles does not change much and remains at around 0.8, indicating that the originally acicular carbamazepine dihydrate is now more equant. This provides an explanation to the two different regimes observed from plots of particle size, length and width. Initially when the particles are acicular, they undergo substantial fragmentation due to the geometric effect of the particles. However, as the dispersion pressure increases, it reaches a point where the particles are no longer acicular but more equant and hence leads to a change of breakage mode from fragmentation to chipping where the reduction of size is smaller in comparison.

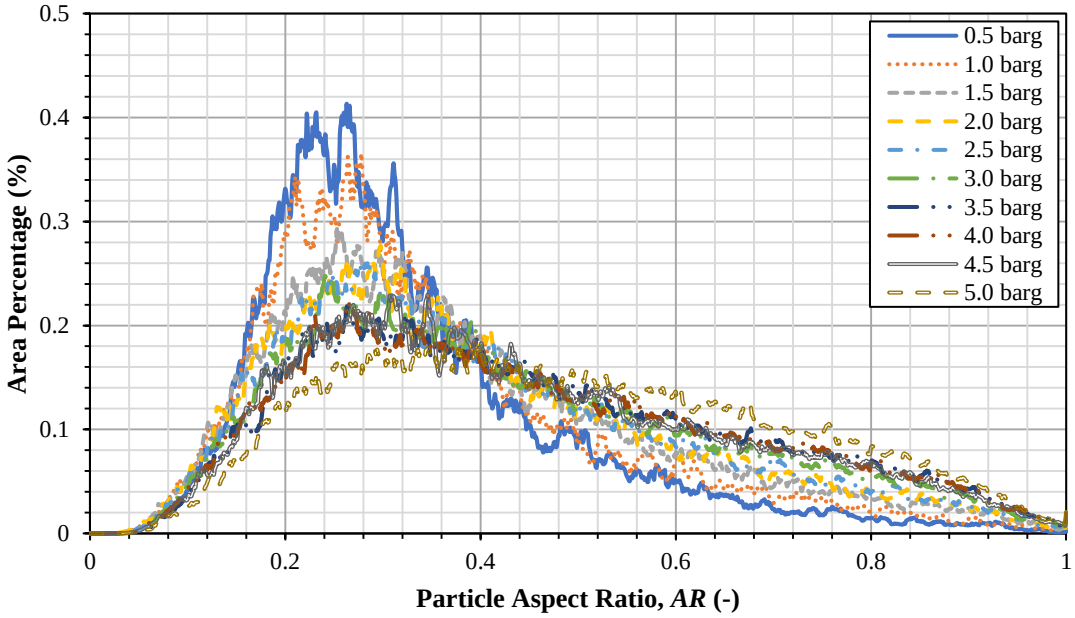

Figure 6-17 Particle aspect ratio distribution of carbamazepine dihydrate crystals dispersed at different pressures

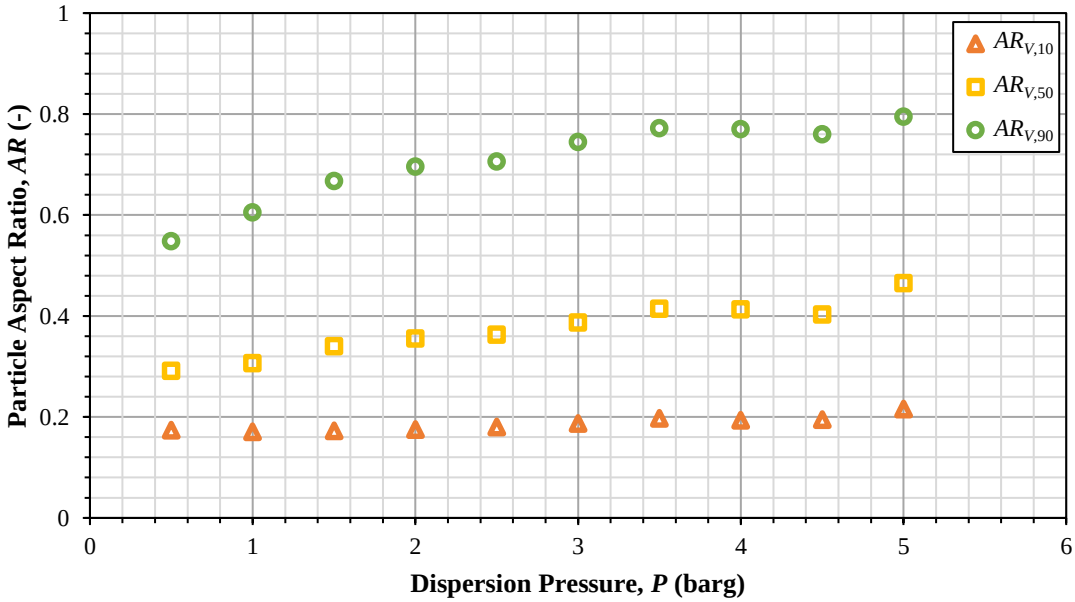

Figure 6-18 Characteristic volumetric intercept values of aspect ratio, $AR_{v,10}$, $AR_{v,10}$ and $AR_{v,10}$

6.4.4 Impact Breakage Assessment of Carbamazepine Dihydrate

Impact is the main cause of breakage in the dispersion spool of G3 Morphologi. For correlating the extent of breakage of particles and their intrinsic physical and mechanical

properties, the impact breakage model of Ghadiri and Zhang (2002) is used, given by Eq. 6-5.

$$R^* = \alpha \frac{H}{K_c^{\,2}} \rho D U^2 \tag{6-5}$$

where $R*$ is the extent of breakage, α the proportionality constant, H the hardness, K_C the fracture toughness, ρ the particle density, D the particle size and U the particle impact velocity. The functional group of $\alpha \frac{H}{K_C^{\,2}}$ governs the breakage propensity of a material and is known as the breakability index.

For highly acicular particles like carbamazepine dihydrate crystals, it is difficult to classify them into narrow size classes by length or width. Therefore, a full range of particle sizes present in the sample is used instead. The original breakage model is therefore modified so that it could accommodate the full-size distribution of the sample. The volume fraction of particles in different size classes in the original feed sample is taken into account in the modified impact breakage model and is presented below.

$$R^* = \beta \rho \sum_{i=1}^{n} \phi_i D_i U_i^{\,2} \tag{6-6}$$

where β is the breakability index, ρ the particle density, i the bin number, ϕ the volume fraction of the particles, D the representative particle size, and U the corresponding particle impact velocity in the bin *i*.

The impact velocities of particles with different sizes and aspect ratios in the dispersion spool at different dispersion pressures are depicted in Figure 6-19. The calculated particle normal impact velocity at different dispersion pressures is plotted as a function of the particle length. Interestingly, the variation of impact velocity with particle length is not notable, except for smaller particle lengths.

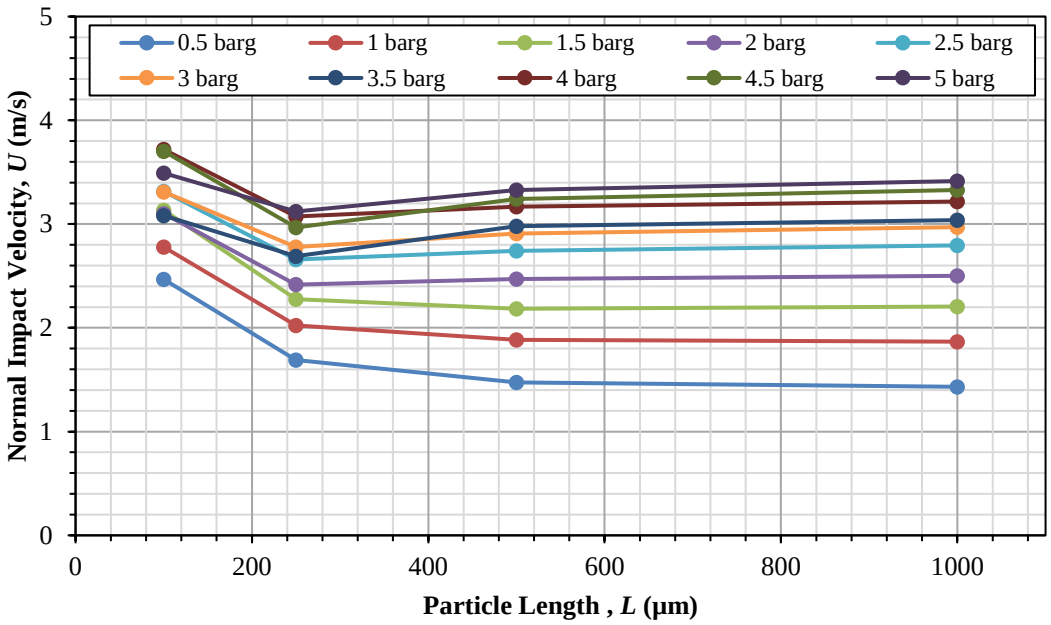

Figure 6-19 Normal impact velocity of carbamazepine at different dispersion pressure as a function of particle length

Particle length is proportional to the square equivalent side length as shown in the scatter plot in Figure 6-20. A simple linear relationship can be established using the equation below

$$L = kD \tag{6-7}$$

where L is the particle length, D the particle square equivalent side length and k the slope of the linear regression line. The impact velocity of the representative particle size of bin I in Eq. 6-6 can then be obtained using Eq. 2-1 (k is found to be 2.14).

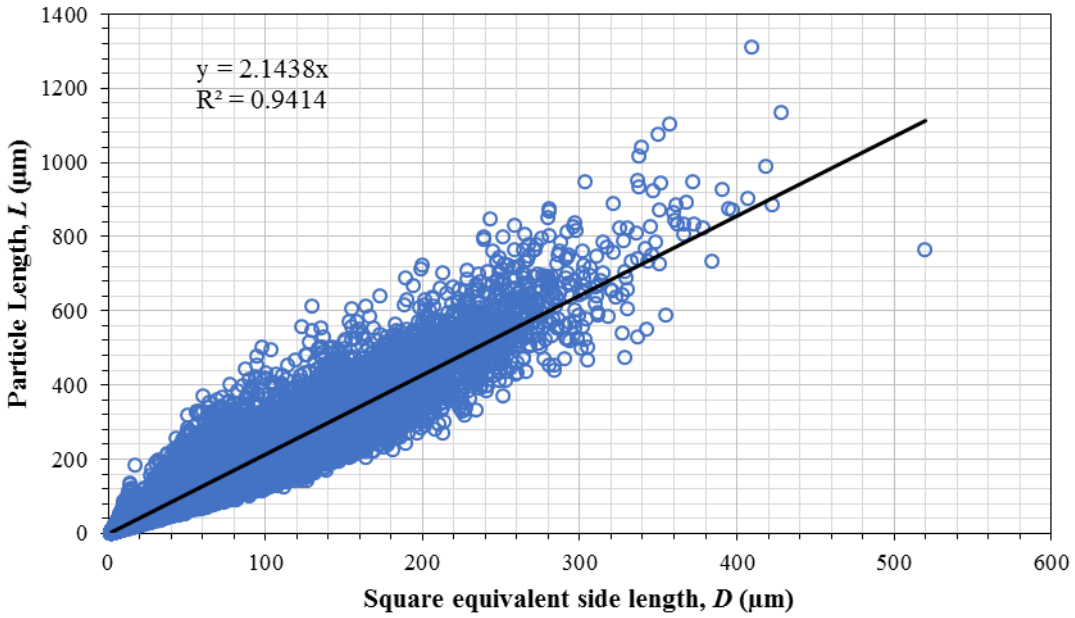

Figure 6-20 Scatter plot of particle length vs square equivalent side length

The impact velocities calculated from the particle length are used in to calculate the extent of breakage and the results are plotted in Figure 6-21. The slope of the regression line represents the breakability index of the carbamazepine dihydrate. Considering only the normal component of the impact velocity, the breakability index of the carbamazepine dihydrate is found to be 0.253. The plot shows a reasonably good agreement with the regression line, having achieved a coefficient of ~ 0.94. However, having one single global breakability index may not be representative, as two regimes can be distinguished, as discussed previously. These regimes are taken into consideration and segmented regression is performed on the data instead. Figure 6-22 shows the plot of R^* versus $\sum_{i=1}^{n} \rho D U^2$, the red broken regression line corresponds to the first regime where carbamazepine crystals are snapping off along their largest dimension and the blue regression line corresponds to the second regime where particles would also break by other mechanisms. For this region, the rate of particle breakage declines. The rapid breakage regime (red) has a breakability index of 0.47, while the second breakage regime has a breakability index of 0.20. β-glutamic acid crystals which are slender in width and

more needle-like, too exhibit two different breakage regimes within the range of dispersion pressure tested (Saifoori, 2018). The breakability index of the first breakage regime is 1.88 and the second is 0.77. The comparison between these two crystalline materials indicates that α-glutamic acid is approximately four times more likely to break compared to carbamazepine dihydrate in both the rapid breakage regime (fragmentation) and the slower second regime (chipping). Ghadiri and Zhang (2002) breakage model was developed based on chipping and was not tested rigorously with particles that undergo fragmentation. However, Olusanmi et al. (2011) show that Ghadiri and Zhang (2002) model fits the fragmentation data of aspirin very well. The model also fits the breakage data of carbamazepine dihydrate crystals that undergo rapid fragmentation.

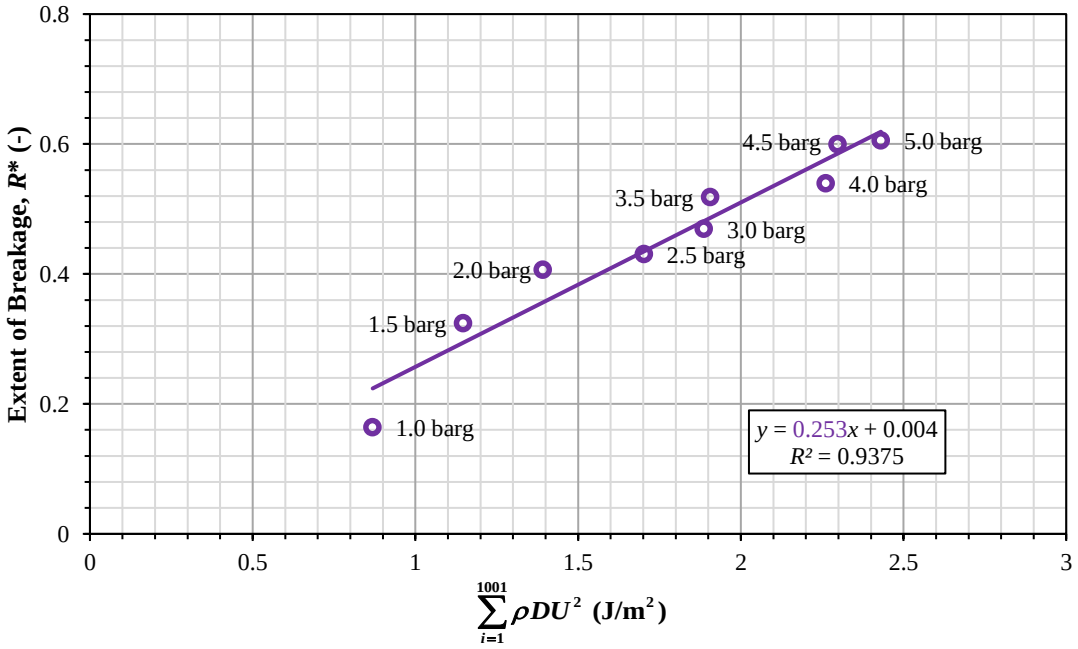

Figure 6-21 Extent of breakage as a function of $\sum_{i=1}^{n} \rho DU^2$ *(normal impact)*

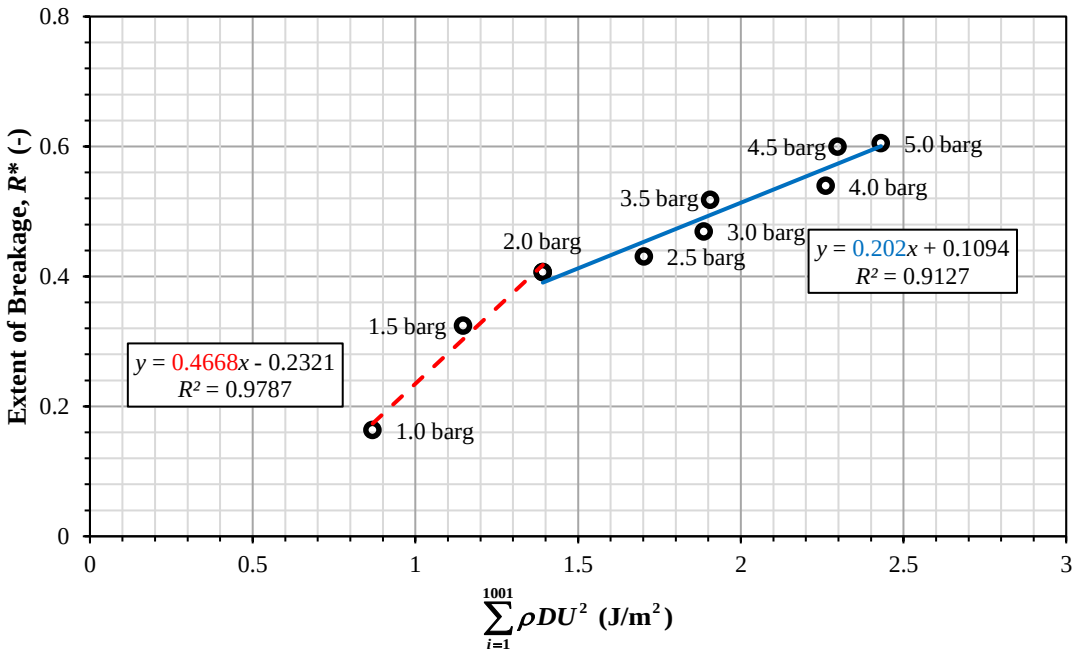

Figure 6-22 Segmented regression of R^* *versus* $\sum_{i=1}^{n} \rho DU^2$ *(normal impact)*

6.5 Conclusions

A new assessment technique has been used to study the breakability of acicular particles of carbamazepine dihydrate. Using the G3 Morphologi, the crystals are dispersed by a pressure pulse of air, causing impact breakage. The shift of particle size, length, width and aspect ratio are analysed, indicating that carbamazepine dihydrate tend to break along their largest dimension, due to bending arising from the geometric effect of the high aspect ratio and in spite of the presence of cleavage planes. Nevertheless, breakage along the crystallographic cleavage plane of weakness is also observed to a minor extent. These observations suggest that the breakage of carbamazepine is dominated by both fracturing perpendicular and cleaving parallel to the particle length.

A full particle size distribution is used in the test due to difficulty of classifying the crystals in narrow size ranges. The breakability index of carbamazepine dihydrate is

determined by plotting the graph of R^* versus $\sum_{i=1}^{n} \rho DU^2$, where a non-linear relationship is noted. There exists a transition point at which the rate of change the particle size is reduced, corresponding to a switch in the breakage mode. The first breakability index is higher than the second one and corresponds to the snapping of the particles along their length, while the latter smaller one is associated with chipping. This work demonstrates that by using a combination of image analysis and modified impact breakage model, the role of crystal structure properties, particularly the existence of cleavage planes, together with the physical geometric properties on the breakage behaviour of carbamazepine dihydrate crystals can be isolated and studied individually.

Chapter 7

Assessment of Particle Breakage during Agitated Filter Bed Drying

7.1 Introduction

Agitated filter bed drying is the unit operation of choice in pharmaceutical industry for isolation of active pharmaceutical ingredient (API). Heat is supplied to the wet cake and an impeller is agitated intermittently to promote homogenous drying of the drug product. It is a closed equipment that minimises the exposure of the operator to the active pharmaceutical ingredients that are being dried, which could potentially be potent or toxic.

In this chapter, the development of a new lab scale agitated filter bed dryer (AFBD) is presented. The newly developed AFBD device is used to study breakage behaviour of two materials (sodium chloride and carbamazepine dihydrate) with very different morphology. Several process parameters were studied, such as the impeller clearance size, rotational speed, number of impeller revolutions and solvent content. The resulting breakage is quantified using sieving analysis (for equant particles) and a new approach proposed (for platy crystals) in the previous chapter by assessing the degree of shifting of the size distribution of the broken crystals from the feed.

7.2 Standard Operating Protocol

The standard operating procedure of performing agitated filter bed drying is detailed here after a thorough discussion with the industrial collaborator of this project, AbbVie. Though the standard practice that AbbVie adopted might not be applicable for every pharmaceutical company, it serves as a reference of how agitated filter bed drying is performed on a stepwise basis.

Agitated filter bed dryer varies in scale and could accommodate sample mass of 1 up to 250 kg. During the drying process, the impeller is rotated intermittently. The diameter of the impeller can be as small as 0.08 m and as large as 2 m for a pilot scale dryer. The typical rotating speed of the impeller ranges from 0 – 25 RPM, though for smaller scale dryer, the speed could go up to 100 RPM or more. The impeller can be programmed to go upward and downward and as per need basis, but the clearance of the impeller from the base of the vessel at lowermost position is typically limited at ~10 mm. The same applies to the gap between the impeller blade tip and the vessel wall, typically a clearance of 10 mm is used. The operating volume of wet cake is dictated by the uppermost and lowermost position of the impeller. However, to ensure the efficiency of the drying process, normally a bed height of two to three times the impeller blade height is used.

The steps involved in agitated filter bed drying are as below:

Filtration and Washing

Right after the completion of crystallisation, the slurry is transferred to the filter to remove the mother liquor from the crystallised product. A number of washes are applied where appropriate to flush out the impurities using wash solvent that has similar composition to the mother liquor. Once the mother liquor is filtered and the wet cake settled, vacuum can then be applied to deliquor the excess unbound wash solvent. Blowdown of the wet cake

using nitrogen gas to drive the solvent out could also be done if necessary. During the deliquoring and blowdown process, smoothing of the wet cake using the impeller is performed (typically 3 – 5 impeller rotations) to remove any crack formation on the free surface, ensuring the efficiency of solvent removal.

Drying with Heating

Blowdown and deliquoring will not remove all the solvent in the wet cake. Very often, the wet cake is heated up to the upper temperature dictated by the thermal stability of the API to facilitate the drying process. The heating rate is governed by the loss on drying (LOD) of the solvent content and propensity of hardening of the wet cake (very likely to happen when the drying rate is fast). Vapour removal can be accelerated by applying nitrogen gas to the closed system either through headspace purging or through the wet cake itself from the base of the vessel. Vacuum can be applied too from the top or bottom based on the type of drying employed.

Intermittent Agitation

Upon reaching the desired drying temperature and LOD, the impeller is then lowered to agitate the partially dried cake intermittently to accelerate the drying. The typical speed used is approximately 5 to 10 RPM. 2 RPM is used lowermost for material that is very prone to attrition. Heat supply through the impeller is very common in most of the filter bed dryer to enhance the drying rate of the partially dried cake. The intermittent mixing of the partially dried cake is continued until an acceptable solvent content is achieved, according to International Conference on Harmonization (ICH) Standard. The typical drying time can range from 8 hours to a couple of days. It is a function of the API physical properties to be controlled, crystal form and the type of solvent used.

7.3 Development of a Laboratory Scale Agitated Filter Bed Dryer

Having a lab-scale device that could simulate and monitor the conditions during agitated filter bed drying is very essential in the development of pharmaceutical processes. However, the availability of such device in the commercial market is scarce. As part of this research work, a development programme was established between the University of Leeds and Freeman Technology (Tewkesbury, UK) to make an agitated filter bed drying test rig based on the design of the FT4 powder rheometer. Freeman Technology FT4 powder rheometer is a commercial dynamic powder characterisation device. The abilities of the device in measuring the impeller torque and the normal load applied as well as its smaller footprint make it an ideal surrogate vessel for AFBD modification work. The new AFBD unit is developed with some of the main features listed below in mind.

AFBD features required:

1. Interchangeable impeller blade geometry
2. Wide impeller rotational velocity range, ideally matching the tip speed of larger filter bed dryer impeller
3. Programmable impeller motion
4. Heating capability
5. Filtration capability with high chemical resistance
6. Vacuum capability
7. Array of sensors probing the temperature, pressure and humidity at various stages during agitated filter bed drying

The schematic and picture of the actual prototype of the AFBD unit are shown in Figure 7-1. It is jacketed so that hot fluid can be circulated through the vessel to heat up the wet cake. The inner vessel is 25 mm in diameter, and it is equipped with interchangeable impeller. The impeller is a geometrically scaled down replica (24.5 mm

in diameter) of a conventional AFBD impeller (adopted from Hare's thesis (2010)) . It was 3D printed by laser sintering as the unique curvature of the blade is difficult to be fabricated through traditional CNC machining. The blade has an inclination of 60 ° to the horizontal and the edge of the blade is chamfered to 15 ° as shown in Figure 7-2. The functions of the impeller are directional, in a sense that rotating the impeller in clockwise direction impose a “spreading” effect to the powder bed while in anti-clockwise direction, the impeller is conditioning the powder bed.

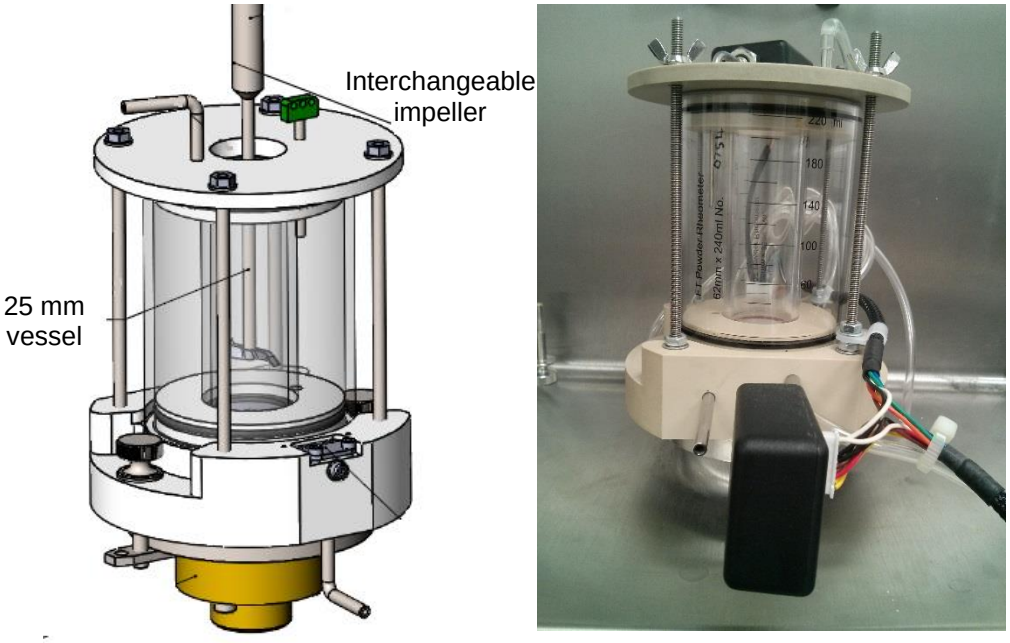

Figure 7-1 Schematic of the AFBD unit (left) and the image of the actual prototype (right)

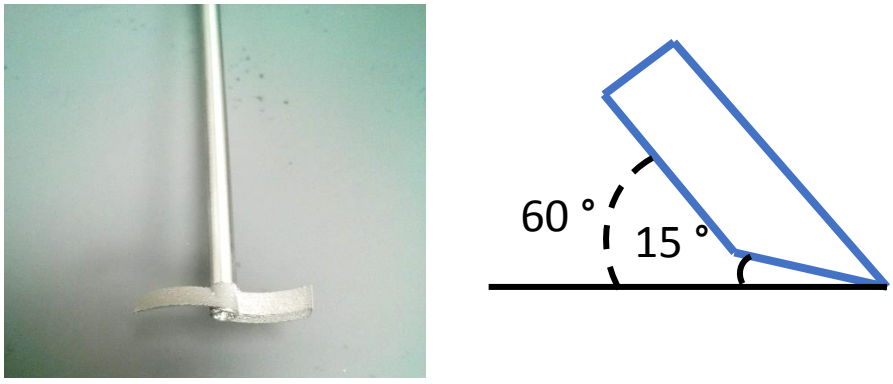

Figure 7-2 Scaled down conventional AFBD impeller blade (laser sintered)

To fully realise the features listed previously, several other auxiliary units are needed, together with the new AFBD unit developed. The overview of the complete AFBD system in shown in Figure 7-3. The filtration capability is added to the system by attaching a vacuum pump to the bottom of the AFBD unit. To be able to circulate hot fluid through the jacketed vessel, a water pump is used to draw the hot fluid from the temperature-controlled water bath back and forth to the AFBD unit. A Raspberry Pi data acquisition module is used to receive real-time data from the array of sensors attached to the AFBD unit. Collection of the data is performed by a laptop computer through wireless ad hoc network. The GUI of the data acquisition software and the list of the parameters that the AFBD unit could monitor are shown in Figure 7-4.

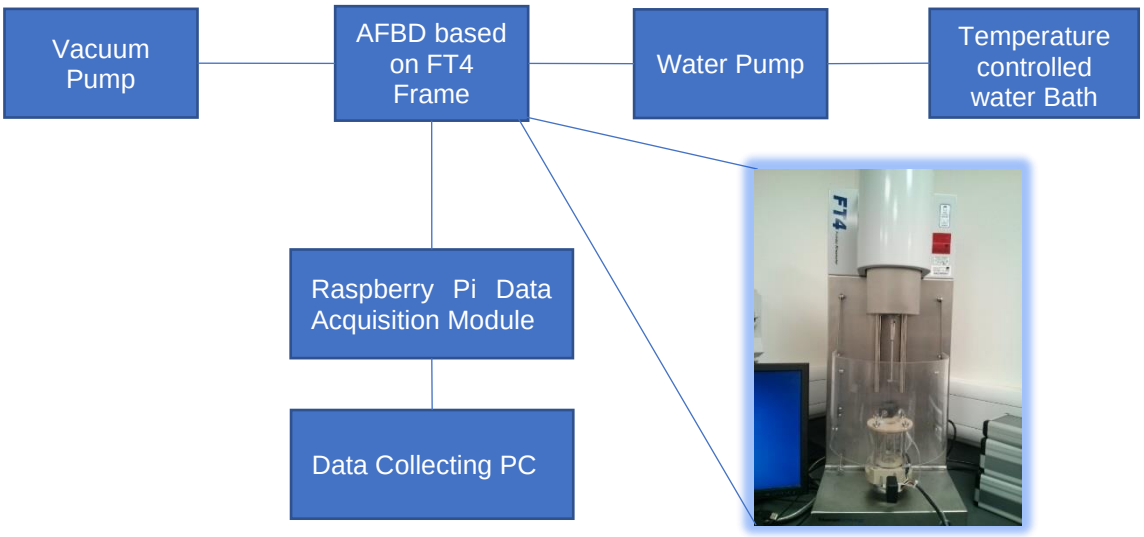

Figure 7-3 System overview of the new AFBD device

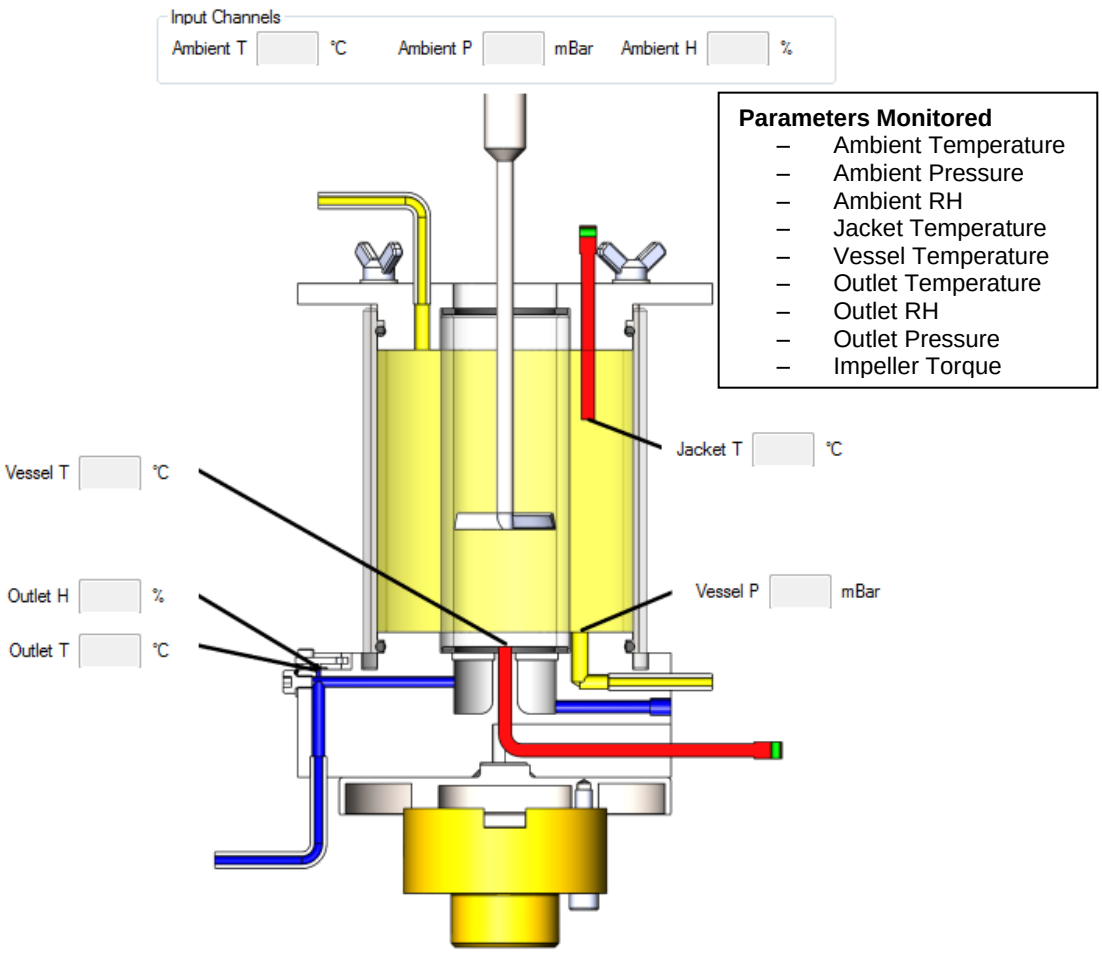

Figure 7-4 Software GUI and the list of parameters monitored

The newly developed system was put to test by drying a slurry of sodium chloride and isopropyl alcohol to see if it could capture the changes of the powder bed dynamic by analysing the impeller torque data recorded by the FT4 rheometer. The experimental setup is as below:

- Sample: Sodium chloride crystals
- Sample size: ~15 g
- Liquid carrier: Isopropyl alcohol (IPA)
- Jacket temperature: 40 °C

Drying sequence

1. Impeller moving slowly into the vessel
2. Impeller driving through the powder bed until it reaches the minimum allowable clearance (helix angle: -5 ° & tip speed: 30mm/s)
3. Impeller remains at that height and keeps rotating at 100 RPM for 30 s
4. Impeller retreats from the powder bed
5. Repeat steps 2-4 until the powder bed is dried

The average torque recorded when the impeller is rotating at step 3, both with and without suction applied, are shown in Figure 7-5. It can clearly be seen that two very different torque profiles are recorded. IPA is a very volatile solvent, with suction applied, it dries up very quickly and hence the average torque recorded quickly reduces and eventually reaches a plateau when the IPA is dried up completely. The torque profile becomes more interesting when there is no suction applied to the system, exhibiting a parabolic behaviour where the magnitude of the average torque of the impeller first gets reduced and then increased later. When the drying sequence first starts, a high volume of

IPA is present in the wet cake and act as a lubricant between the crystals and the impeller, hence reducing the resistance of the impeller to plough through the wet cake. As the IPA dries up gradually, the system enters a partially dry state where the capillary action of IPA between the crystals becomes dominant, increasing the resistance to flow of the wet cake. Beyond a critical point, the flow resistance of the powder bed reduces (reflected in the torque profile as a decrease in the magnitude of the torque) as the IPA dries up, slowly reverting back to the dry and free flowing state of sodium chloride crystals. This quick test has demonstrated the ability of the new AFBD unit in performing agitated filter bed drying of the crystals and the torque metre of FT4 in capturing the change of particle bed dynamic during the drying process.

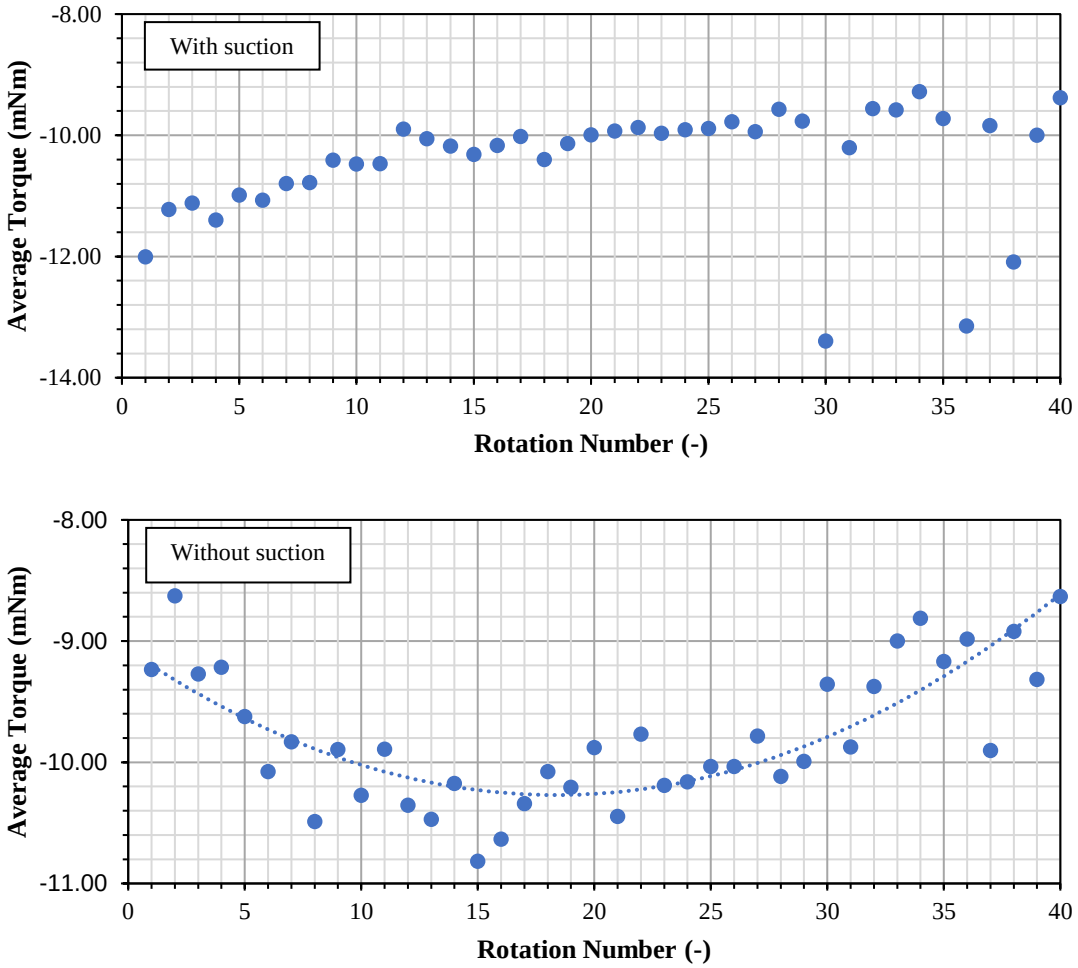

Figure 7-5 Impeller torque data recorded by FT4 powder rheometer

7.4 Effect of Process Parameters on the Breakage of Sodium Chloride Crystals in AFBD

7.4.1 Materials and methods

Sodium chloride crystals were used in this work to study the effect of process parameters on the breakage of equant particles. The crystals were first sieved to three different BS410 sieve cuts of 300 – 355, 355 – 425 and 425 – 500 µm, respectively. These sieved crystals were then washed with IPA to remove the fine particles on the surface of bigger crystals. The washed crystals were then dried in an oven at 50 °C to remove the residual IPA in the particles and sieved for a second time when the crystals are dried. The SEM images of the washed and sieved sodium chloride crystals are shown in Figure 7-6.

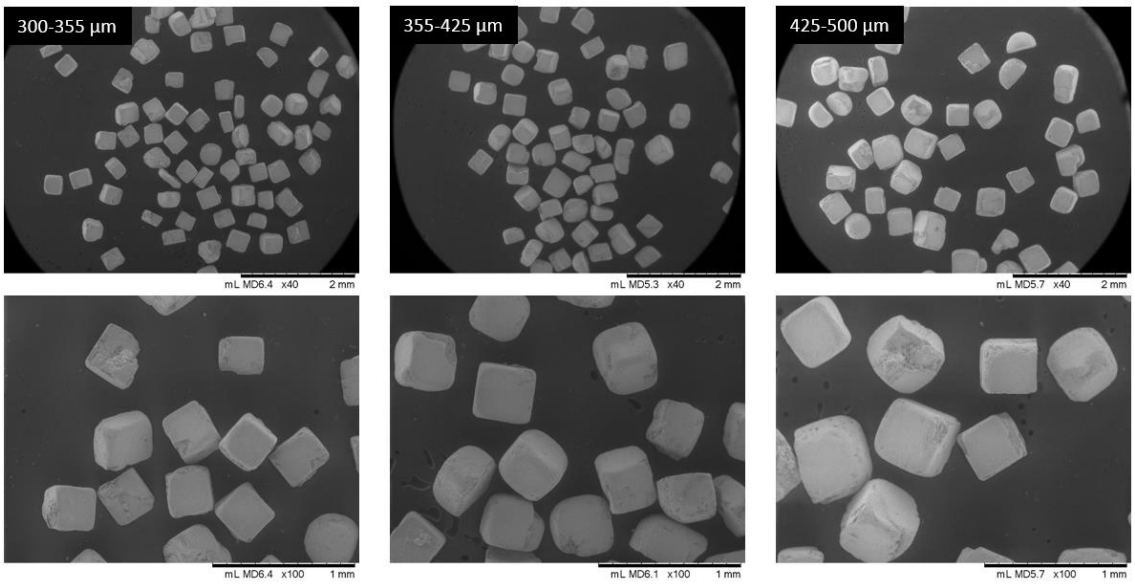

Figure 7-6 SEM micrographs of washed and sieved sodium chloride crystals

The sieved crystals were then subjected to different process treatments and the resulting breakage was assessed using sieving method. The extent of breakage, R^* is defined as the ratio of the mass of debris, M_d to the sum of the mass of the mother particles, M_m and debris, expressed in percentage.

$$R^* = \frac{M_d}{M_m + M_d} \times 100\% \qquad (7\text{-}1)$$

The mass of debris is defined as the mass of the broken crystals collected from a sieve which was two sieve cuts below the feed sieve cut.

7.4.2 Effect of Impeller-Base Clearance

425 – 500 µm sodium chloride crystals were used to study the effect of the clearance size between the impeller blades and the vessel base. Four different clearance sizes of 1, 3, 5 and 10 mm, corresponding to 2, 6, 10 and 20 particle diameters were used. The impeller was rotated at 120 RPM for 10 minutes for each of the tests and the broken crystals were classified by sieving. 10 g of sample was used for each test. The extent of particle breakage as a function of clearance size is shown in Figure 7-7. It can be seen that the extent of breakage is dependent on the clearance size and is highest when the clearance between the impeller and the base is 1 mm, amongst all the clearance sizes tested. As the clearance size is increased, the extent of particle breakage is reduced and eventually comes to a plateau when the clearance size is above 5 mm.

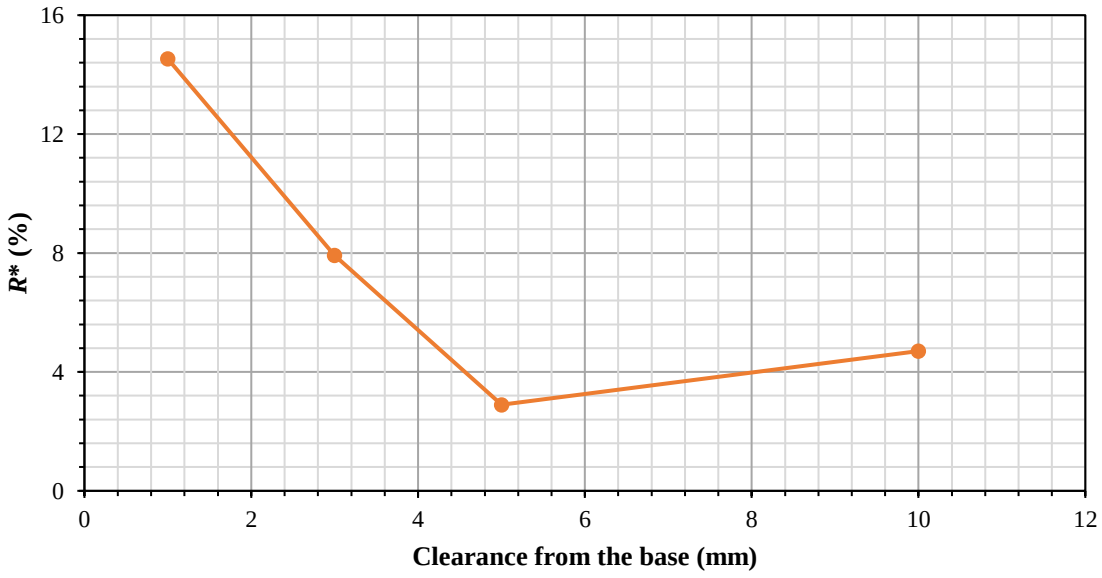

Figure 7-7 Effect of impeller clearance on R of sodium chloride*

7.4.3 Effect of Normal Load

The effect of normal load on the extent of breakage was studied by changing the sample mass used for the test. By changing the sample mass, the hydrostatic stress experienced by the particles at the bottom of the particle bed can be altered. Three sample masses were used to induce three varying degree of normal loads to the particle bed. Similar to the previous section, the particle bed was agitated at a speed of 120 RPM for 10 minutes and the extent of particle breakage was analysed. The result is shown in Figure 7-8, where it indicates that extent of particle breakage increases with the decrease in the sample mass. It was expected that the higher the sample mass (hence higher load), the higher the extent of breakage. However, the result suggests otherwise. A plot of the mass of debris as a function of the impeller-base clearance (Figure 7-9) shows that the amount of debris collected at each clearance size tested is actually superimposed on each other regardless of the sample mass. The problem actually lies in the fact that the particle breakage in an agitated filter bed dryer is regional and not homogenous. During agitation, only the particles that are within proximity to the impeller experiences shear deformation when the impeller is rotated. When additional load is applied to the powder bed in the form of increased sample mass, the fraction of particles that are being sheared becomes smaller as now the reference feed sample size is increased. This is not to say that analysis of the breakage data using R^* is inadequate, but it rather alludes the need of ensuring the reference sample mass is consistent for the tests in comparison. Nevertheless, it is shown in Figure 7-9 that increasing the normal load does not increase the extent of breakage of sodium chloride within the experimental conditions tested.

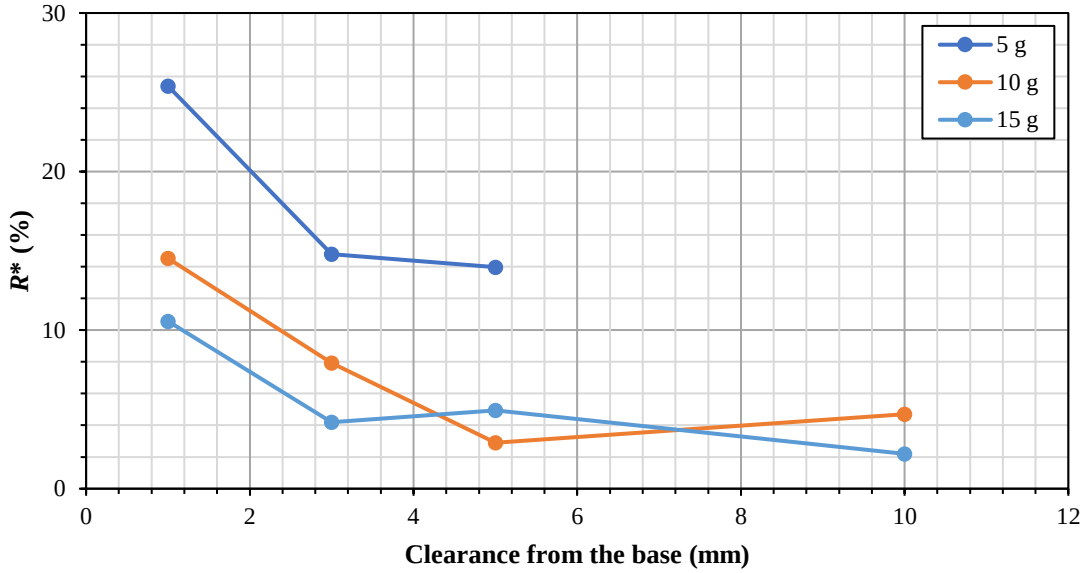

Figure 7-8 R vs impeller-base clearance as a function of sample mass of sodium chloride*

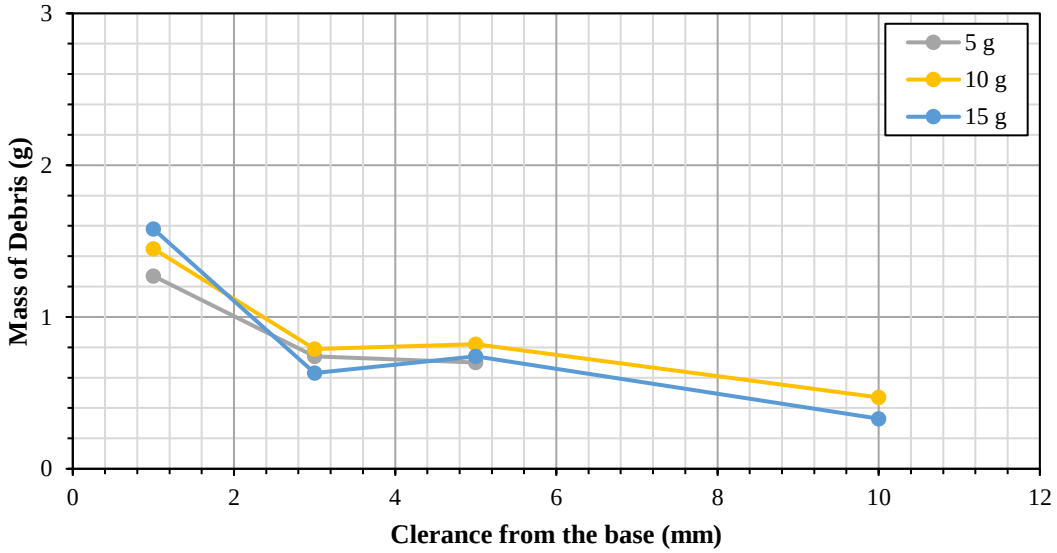

Figure 7-9 Mass of the debris of sodium chloride

7.4.4 Effect of Impeller Rotational Speed

The effect of impeller tip speed on the extent of breakage of sodium chloride crystals in an AFBD is investigated using four different impeller rotational speeds (25, 60, 90 and 120 RPM) at a clearance size of 5 mm. The number of revolutions is kept constant at 600 revolutions so that the results obtained are comparable. 10 g of 425 – 500 µm crystals were used in each test. The extent of breakage as a function of the impeller speed is shown in Figure 7-10. It is evident that the breakage of sodium chloride crystals is independent of the impeller rotational speed, maintaining at ~5% across the velocity range tested. The SEM images of the mother particle and debris at each rotational speed tested in shown in Figure 7-11. It can be seen that the dominant breakage mode of sodium chloride crystal in an AFBD is through chipping off the corner of the feed particles and surface abrasion (indicated by the fines generated). No significant difference can be observed amongst the SEM images of the broken crystals of sodium chloride agitated at different rotational speeds. The result of full sieving analysis of the broken sodium chloride crystals is shown in Figure 7-12. The size distributions of the broken particles seem to exhibit some slight variations amongst each other. The amount of particles collected at one sieve cuts below the feed size (355 – 425 µm) increases with the impeller rotational speed while for the rest of the sieve cuts, the trend reverses. This implies that while the impeller speed does not increase the amount of debris collected two sieve cuts below the feed, it does affect the size distribution of the broken particles, albeit to a very small degree.

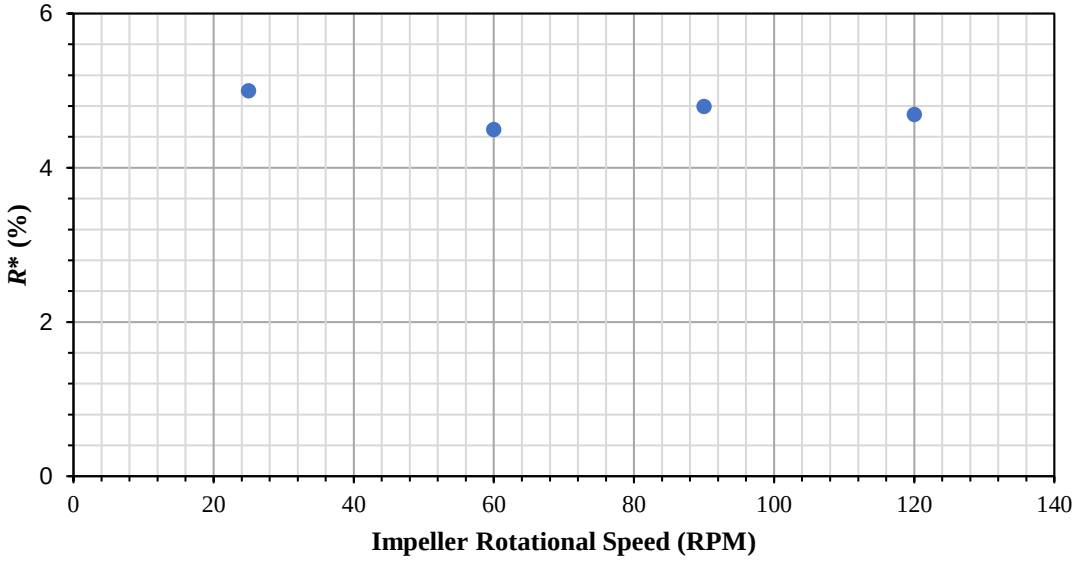

Figure 7-10 Effect of impeller speed on the R of sodium chloride*

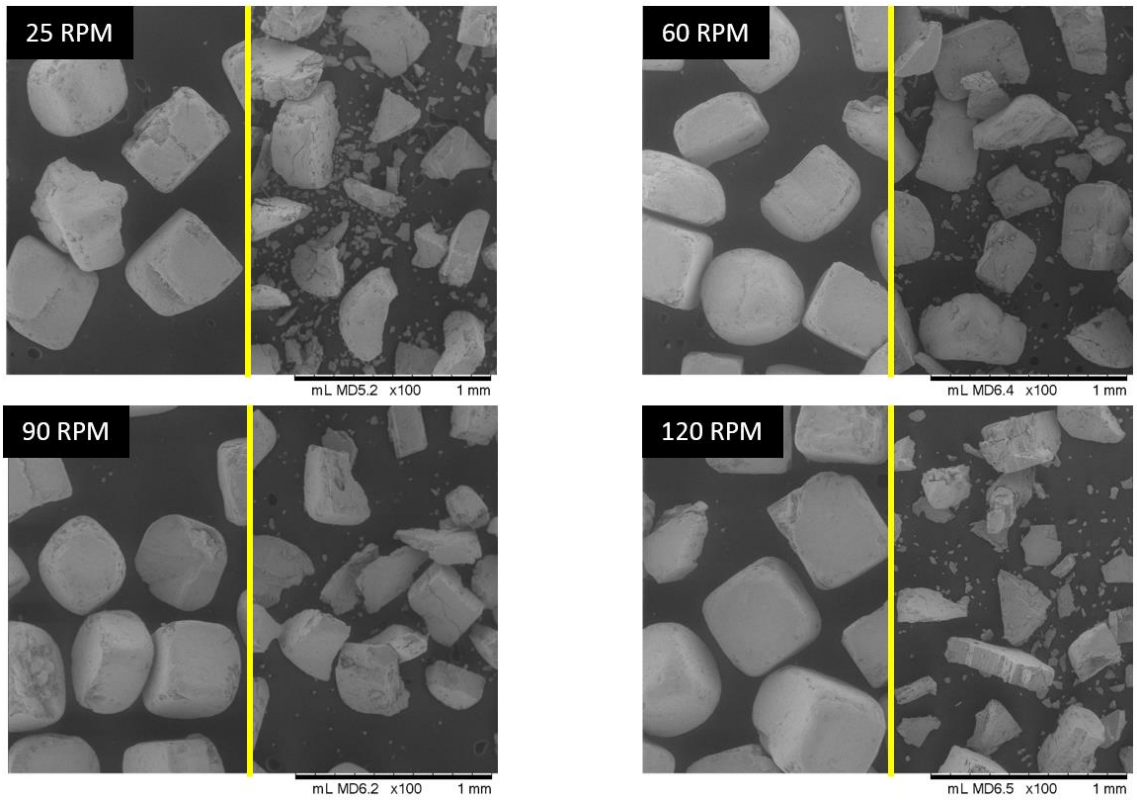

Figure 7-11 SEM micrographs of mother particles(left) and debris (right) of sodium chloride

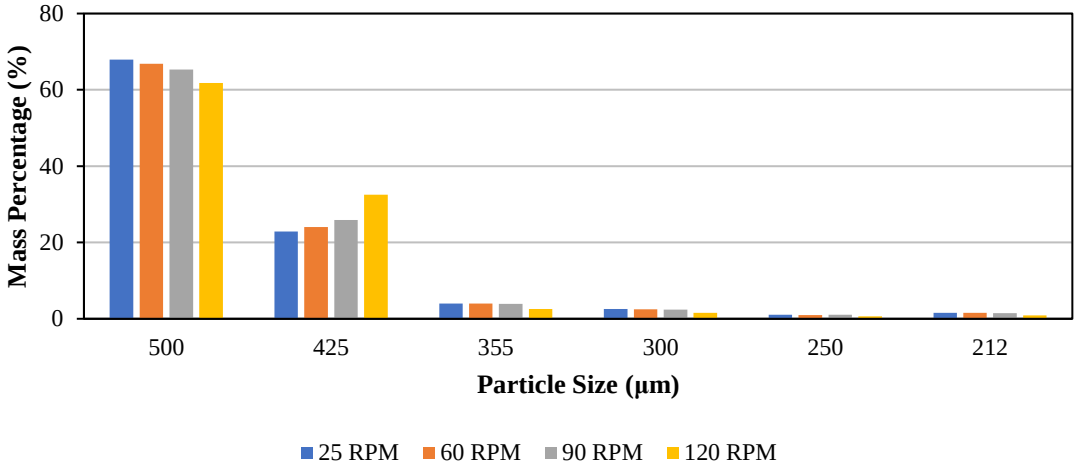

Figure 7-12 Sieving analysis of sodium chloride broken at different impeller speed

7.4.5 Effect of Number of Impeller Revolution

The three different sieve cuts of sodium chloride crystals were also used here to study the effect of the number of impeller revolutions on the extent of particle breakage. The rotational speed used was 120 RPM and the angular displacement of the impeller is altered by controlling the number of revolutions that the impeller can rotate. Each sieve cut of sodium chloride crystals was agitated for 300, 600, 1200, 2400 and 4800 revolutions. The resulting breakage of the crystals was then analysed, and the results are shown in Figure 7-13. A strong linear relationship is observed for all the particle sizes tested. The higher the number of impeller revolutions, the higher the extent of breakage. The breakage of 300 – 355 µm sodium chloride is of lesser extent compared to the other two sieve cuts and that is due to the fact that higher energy is required to break smaller particles.

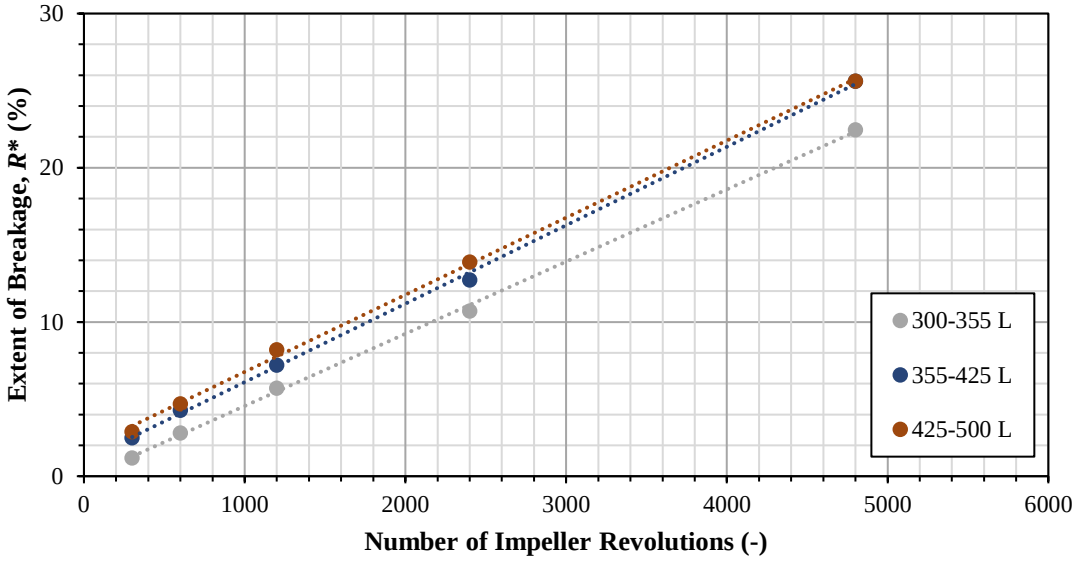

Figure 7-13 R of sodium chloride as a function of the number of impeller revolutions*

7.4.6 Effect of Impeller-Wall Clearance

The effect of clearance size between the impeller blade tip and the vessel wall was only studied after all the previous tests had been completed. Changing the clearance size involves shortening the laser sintered blade by grinding. Three different blade lengths of 24.5 (original), 22.5 and 20.5 mm were investigated here, which correspond to a gap size of 0.5, 1.25 and 2.25 mm. The effect of particle size and number of impeller revolutions were studied as a function of the impeller-wall clearance and the results are shown in Figure 7-14. L, M and S in the plot legend represent the blade length of 24.5, 22.5 and 20.5 mm, respectively. Unexpectedly, reducing the blade length causes no breakage to the sodium chloride at all regardless of the particle size and the number of impeller revolutions. Only a miniscule amount of fines were collected at the end of each test, indicating no particle breakage occur during the agitation. This suggest that the gap size between the blade tip and vessel wall plays a very important role in the breakage of sodium chloride observed in the previous tests.

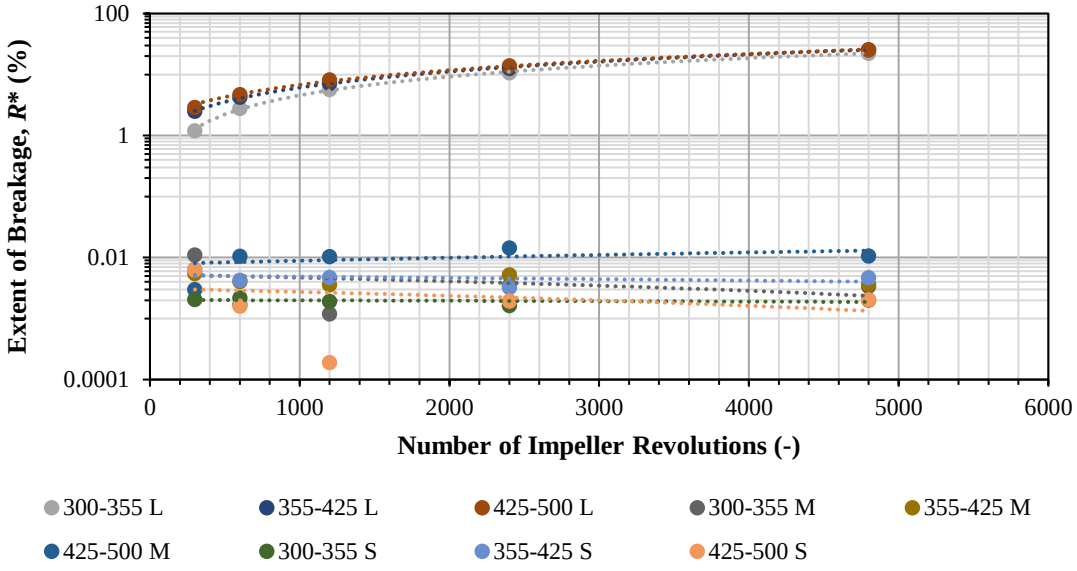

*Figure 7-14 Effect of particle size, blade length and number of impeller revolutions on R**

7.5 Breakage of Carbamazepine Dihydrate Crystals in The Agitated Filter Bed Dryer

7.5.1 Materials and Methods

The crystals used in this work were the CBZ.2H_2O_B2018. They are very platy crystals, more so compared to CBZ.2H_2O_B2016 as their length to width ratio is smaller. Nevertheless, the dominant face of the crystals is still the (h00) face, at which the cleavage planes (0k0) are perpendicular to and parallel to the longest crystal axis *c*. First, 1 g of dry sample was fed into the AFBD vessel, which filled up the vessel to about three times the impeller blade height. The impeller was then lowered down to 20 mm from the base before it started rotating at 10 RPM in an anti-clockwise direction to gently plough through (cutting and lifting) and condition the powder bed, while still going down until it reached the designated clearance. The impeller was then rotated in the same direction at fixed height to simulate the agitation process in an AFBD. Several process parameters were tested, and the detailed conditions used are discussed in each subsection accordingly.

After each process treatment, the crystals were collected, and their size distributions were measured using Morphologi G3 of Malvern Panalytical using dry dispersion technique. The lowest allowable dispersion pressure (0.5 barg) was used to disperse the sample, and the procedure to further analysing the size and shape of the sample is identical to the one discussed in Chapter 6. It was determined that 0.5 barg does not cause any observable particle breakage with it was compared to wet dispersion analysis. The extent of particle breakage is determined by assessing the degree of shifting of the particle size from the feed sample.

The size distribution of the feed sample is shown in Figure 7-15. Three different sizes are presented here, namely the square equivalent side length, length and width of the crystals. The square equivalent side length is defined as the side length of a square that has the same area as the projected shadow of the crystal captured using Morphologi G3. The mode of the length is approximately 350 µm, while the mode for the width is approximately 200 µm. The characteristic sizes of the distributions are shown in Table 7-1.

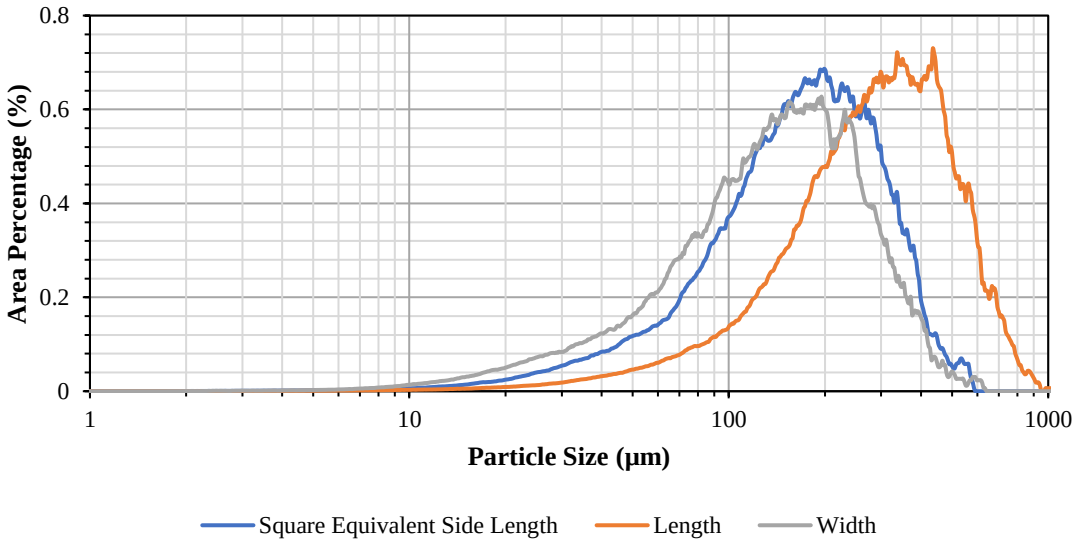

Figure 7-15 Distributions of the square equivalent side length, length and width of CBZ.2H$_2$O_B2018

Table 7-1 D-values of the square equivalent side length, length and width of CBZ.2H₂O_B2018

	Square Equivalent Side Length (µm)	Length (µm)	Width (µm)
D_{10}	62	109.8	44.8
D_{50}	168.7	287.9	140.9
D_{90}	325.1	539.2	290.4

7.5.2 Effect of Impeller-Base Clearance

The effect of impeller clearance from the base of the AFBD vessel was investigated by changing the gap size between the blade and the base of the vessel. The time and speed of the impeller rotation are 40 minutes and 120 RPM, respectively. Three different clearance sizes of 1, 3 and 5 mm were used. The ratio of particle diameter to clearance size is difficult to be quantified as the particles used had a full-size distribution, instead of a narrow size range. Compared to more equant particles like sodium chloride discussed in earlier section, carbamazepine dihydrate crystals have three very distinctively different dimensions, which correspond to the crystal length, width and thickness. The mode of the length distribution of the feed is used as a reference, owing to the high tendency of carbamazepine dihydrate to break along their largest dimension. The particle to clearance ratio is then worked out to be 2.8, 8.5 and 14.3 particles side lengths for clearance sizes of 1, 3 and 5 mm, respectively. The evolution of the particle size distribution as a result of changing the clearance size is shown in Figure 7-16. No distinguishable difference is seen from the PSDs of the crystals agitated in the AFBD at different impeller-base clearance sizes. The trend can only be seen when the plot is presented in the characteristic sizes, D_{10}, D_{50} and D_{90} (Figure 7-17). It can be seen that the characteristic sizes of all the samples agitated at different clearance size are smaller compared to the feed. The smaller the clearance size, the smaller the characteristic sizes of the treated samples. The extent of particle breakage as a function of the clearance size is shown in Figure 7-18. The smaller the clearance size, the larger the extent of breakage. The R^* of the sample agitated at an impeller-base clearance size of 1 mm is ~9%. The difference in R^* between the 3

and 5 mm clearance sizes is very small, compared to that of 1 mm, indicating that the particle breakage of both of these cases are due to the shear deformation of the powder bed induced by the impeller and not crushing.

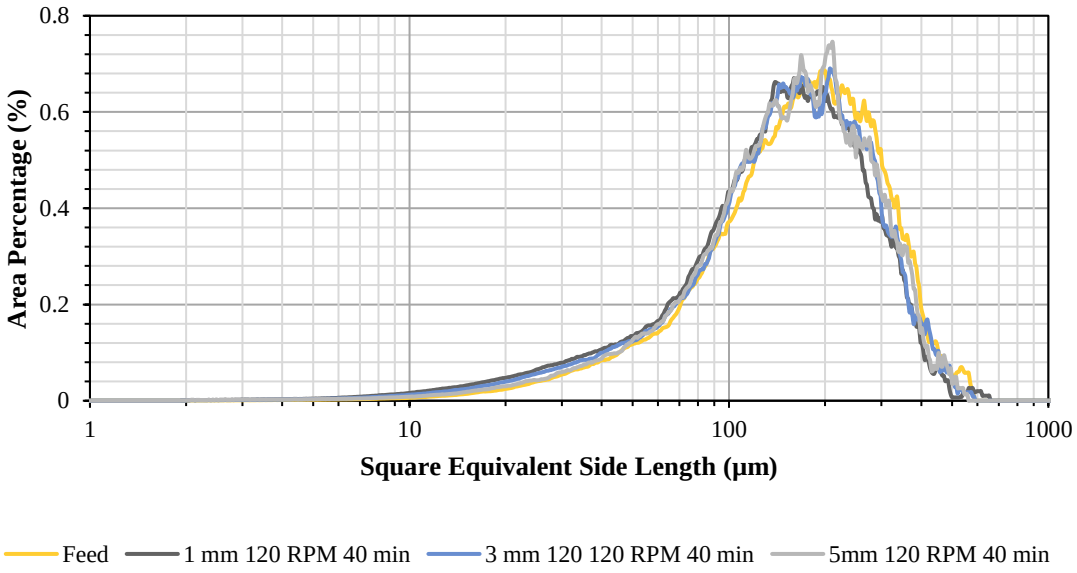

Figure 7-16 PSDs of broken CBZ.2H₂O as a function of clearance size

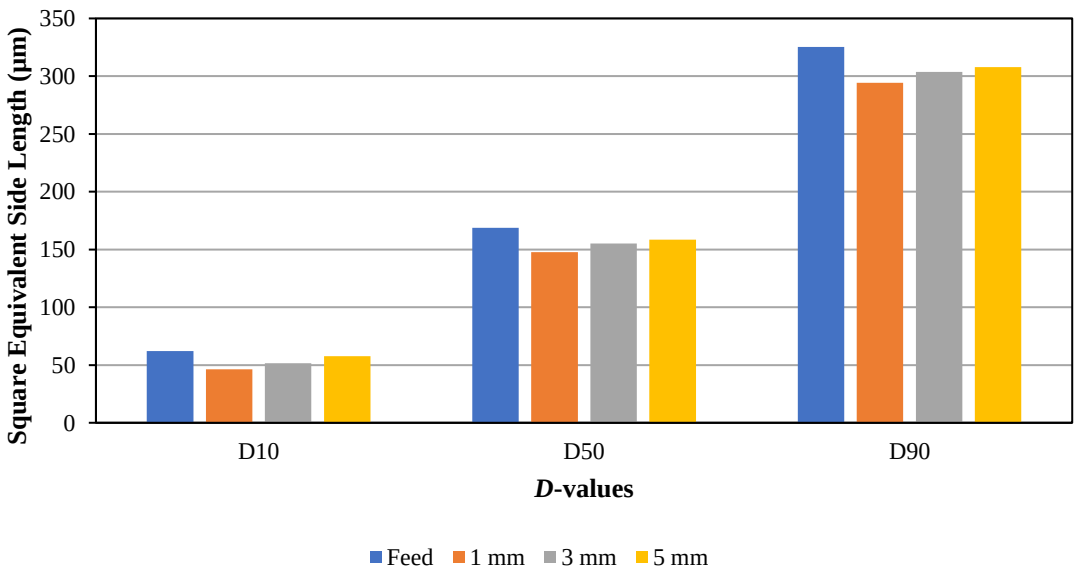

Figure 7-17 D-values of the broken CBZ.2H₂O as a function of clearance size at 120 RPM agitated for 40 mins

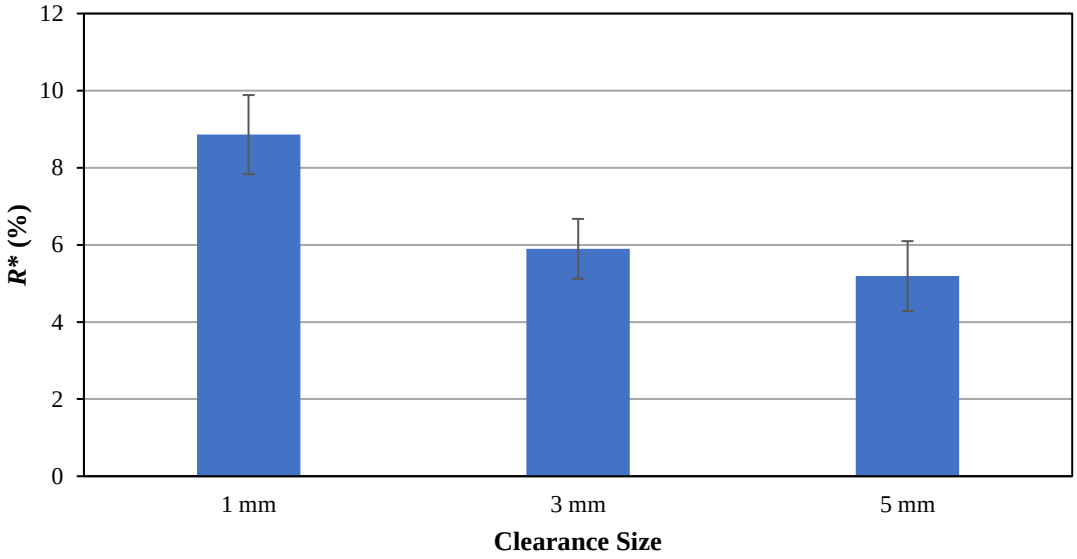

Figure 7-18 R of CBZ.2H$_2$O as a function of clearance size*

7.5.3 Effect of Impeller Speed

Three different impeller tip speeds were used to agitate the particle bed, while keeping the number of impeller rotations the same. The PSDs of the samples agitated at 30, 60 and 120 RPM are compared against the feed to assess the role of impeller tip speed in the breakage of carbamazepine dihydrate crystals (Figure 7-19). The characteristic D-values of the distributions are shown in Figure 7-20. A gradual decrease in the D_{90} is observed as the impeller tip speed is increased. However, the D_{10} and D_{50} of the distributions do not show such trend. The extent of particle breakage as a function of the impeller speed is shown in Figure 7-21. The breakage of carbamazepine dihydrate crystals is not sensitive to the impeller speed. Increasing the impeller rotational speed by four times increases the *R** by only 2%. Agitation at 60 RPM causes the highest breakage extent of carbamazepine dihydrate, at ~13%, but when compared to the other two impeller speeds tested, the difference is not significant.

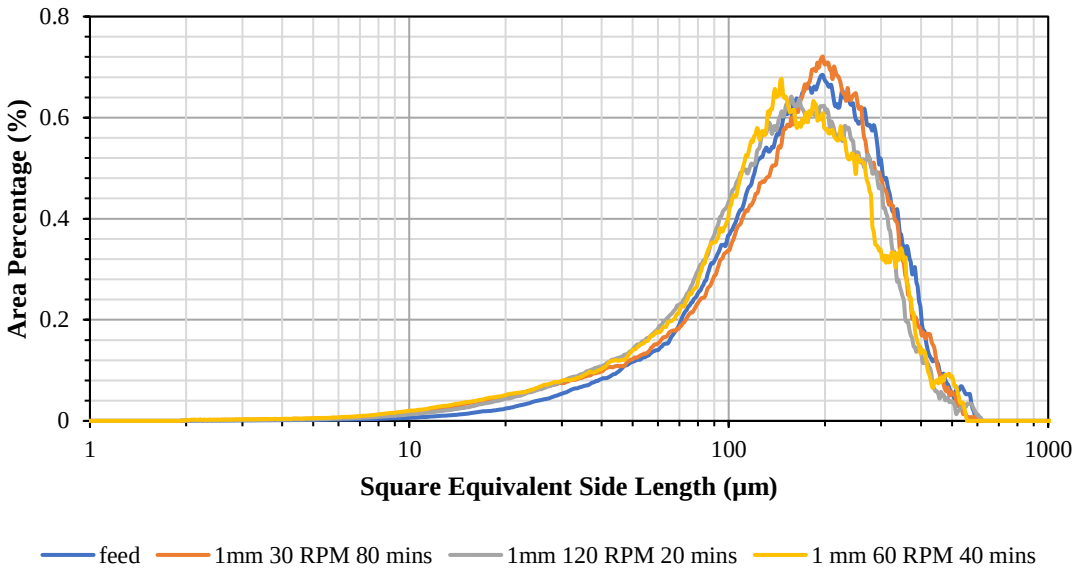

Figure 7-19 PSDs of broken CBZ.2H₂O as a function of impeller speed

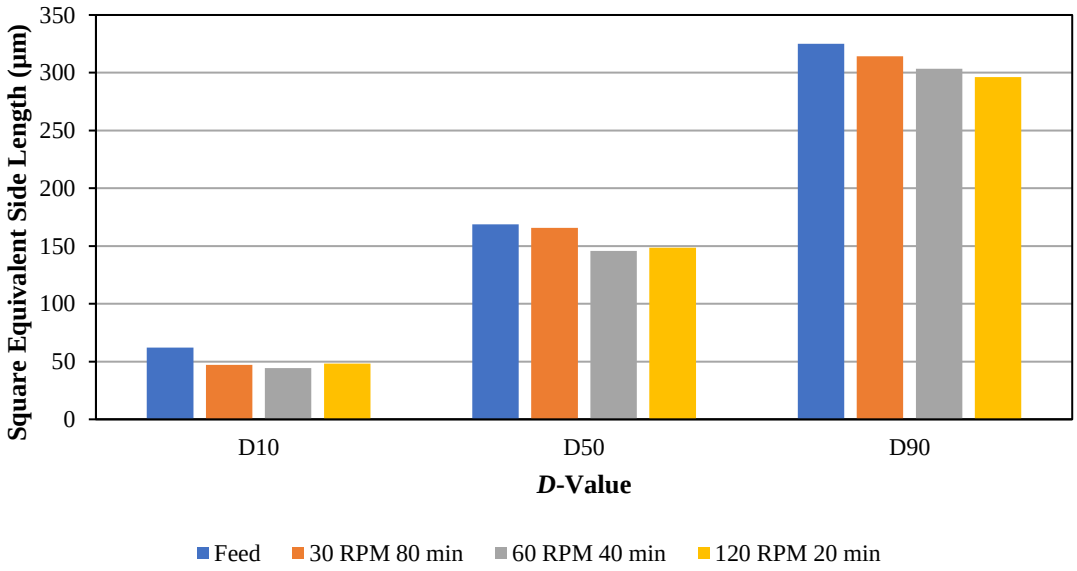

Figure 7-20 D-values of the broken CBZ.2H₂O as a function of impeller speed

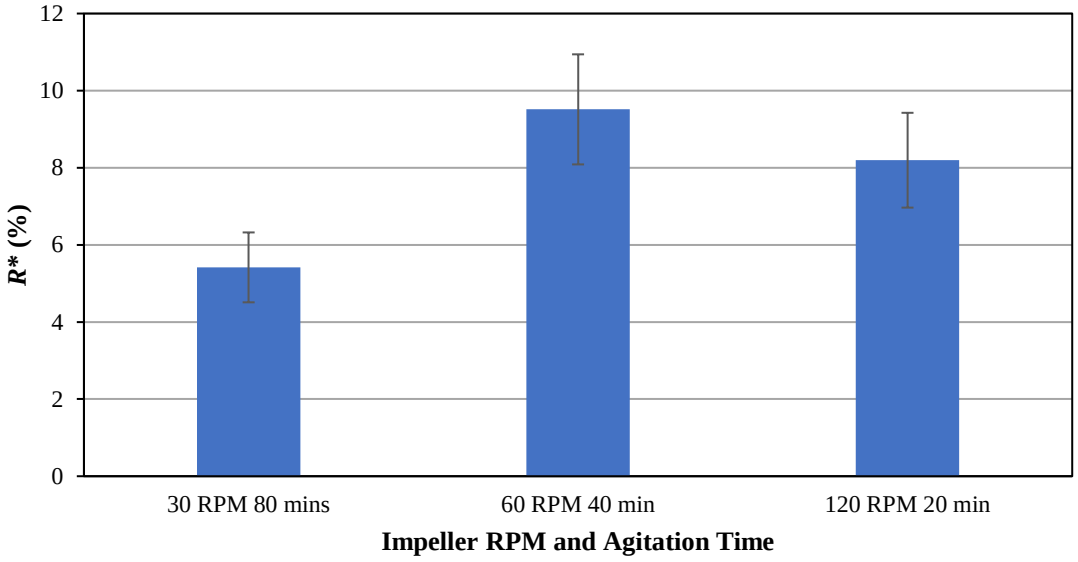

Figure 7-21 R of the broken CBZ.2H$_2$O as a function of impeller speed at 1 mm clearance*

7.5.4 Effect of Number of Impeller Revolutions

Particle breakage in an AFBD is a function of shear stress, shear strain and strain rate within the shear band induced by the rotating impeller. It is hypothesised that the longer the period of agitation, the higher should be the extent of particle breakage as the duration of particle being sheared are increased. This hypothesis is put to test by subjecting the carbamazepine dihydrate crystals to four different lengths of agitation time (5, 10, 15 and 20 mins) while keeping the rotational speed constant. The resulting PSDs of the crystals agitated for different lengths of time are shown in Figure 7-22 and the characteristic D-values are shown in Figure 7-23. The extent of particle breakage calculated as a function of agitation time is shown in Figure 7-24. Increasing the agitation time does increase the particle breakage to a certain degree but the trend is not always respected. At 10 minutes agitation, the calculated *R** is slightly less compared to 5 mins. A clear difference is seen when the agitation time is increased to 20 minutes but further increase in the agitation time to 40 minutes yields no further breakage of the crystals. Interestingly, when similar operating conditions were used but with 2 mm clearance instead of 1 mm, the breakage

of carbamazepine dihydrate crystal follow the trend hypothesized, which stipulates that the extent of particle breakage increases with the agitation time. It can be seen in Figure 7-25 that a gradual increase of the R^* is found when the agitation time is increased. It is also worth noting that the extent of breakage of the samples agitated at 2 mm clearance is generally higher than those samples agitated at 1mm clearance. The exact reason is unclear, but it could be attributed to fact that the particle bed having a very high void fraction. A clearance size of 1 mm corresponds to only ~3 particle length in a very dilated powder bed packing, and the amount of particles actually enter the breakage zone is very small compared to 2 mm clearance, hence resulting in the discrepancy observed.

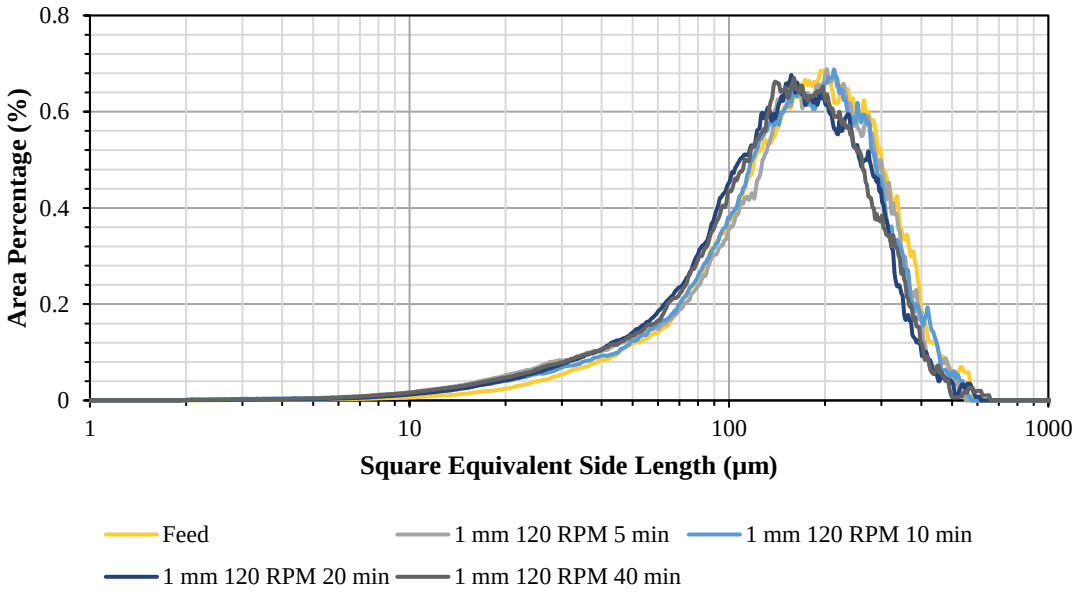

Figure 7-22 PSDs of the broken CBZ.2H$_2$O as a function of agitation time

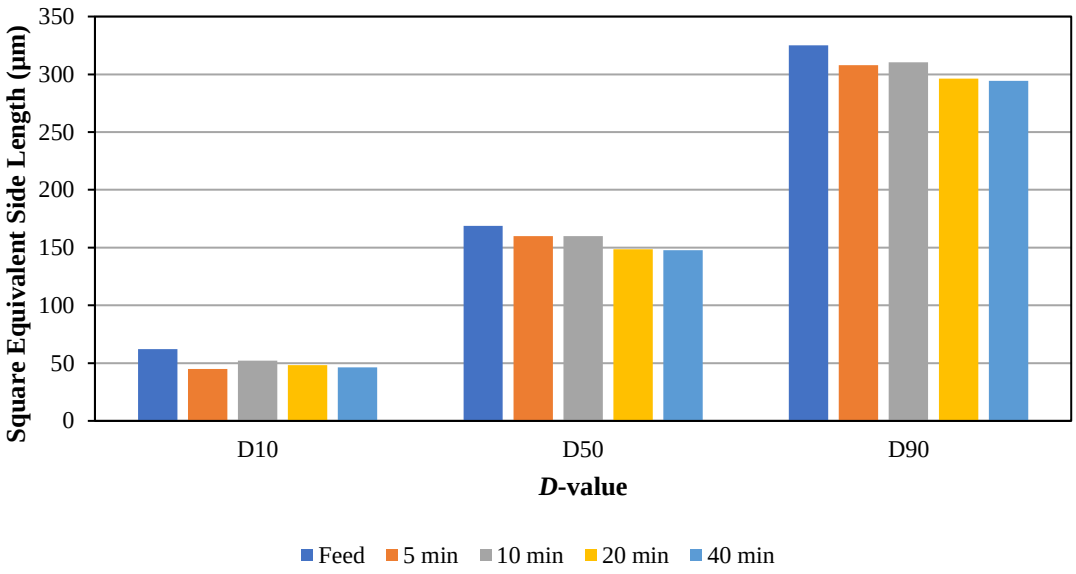

Figure 7-23 D-values of the broken CBZ.2H$_2$O as a function of agitation time at 1 mm and 120 RPM

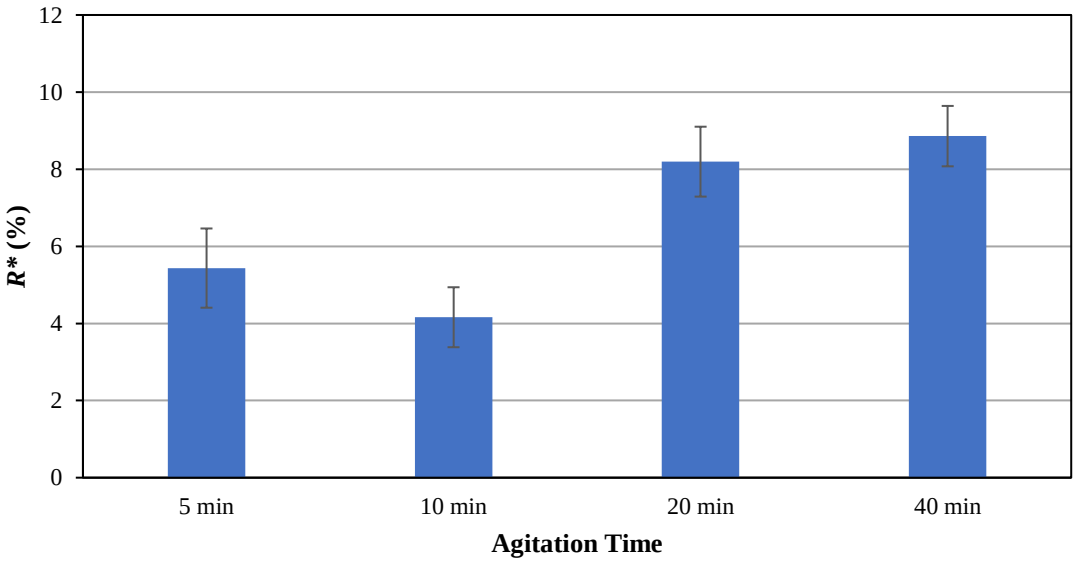

Figure 7-24 R of the broken CBZ.2H$_2$O as a function of agitation time at 1 mm clearance and 120 RPM*

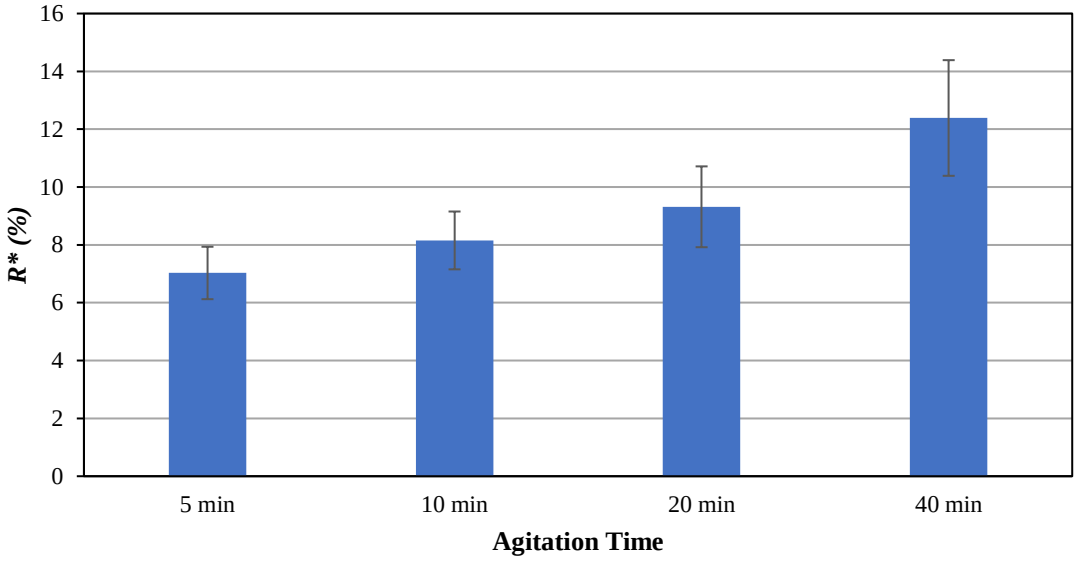

Figure 7-25 R of the broken CBZ.2H_2O as a function of agitation time at 2 mm at 120 RPM*

7.5.5 Effect of Vacuum Suction

Very often, vacuum suction is applied in an AFBD to speed up the drying process. In this work, a vacuum pump was connected to the bottom of the AFBD vessel to investigate the effect of vacuum suction application on the breakage of carbamazepine dihydrate crystals. the vacuum pump has a flow rate of 1.7 m^3/hr. Depending on the particle size and bed packing, the pressure drop across the powder bed varies from 50 – 250 mbar. Applying vacuum suction to the bottom of the AFBD vessel imposes additional normal load to the powder bed due to the pressure drop as the air percolates through the pack bed. The PSDs and extent of particle breakage as a function of impeller-base clearance with vacuum suction applied are shown in Figures 7-26 and 7-27. The first thing that can be noticed is that the extent of particle breakage is much higher compared to the same set of experiments performed without vacuum suction. At the clearance size of 1 mm, the resulting R^* is as high as 41%. The extent of breakage is reduced as the clearance size is increased. Going from 2 to 3 mm, a huge drop in R^* is observed. An approximate 20% of difference between them is obtained. The R^* at 3 and 5 mm clearance sizes is ~17 and

14%, respectively. This indicates that there may exist a critical clearance size somewhere between 2 and 3 mm, below which the particles experience a very high compressive and shear stresses, hence causing an increase in the shear stress that is responsible for the extensive particle breakage observed. Above the critical clearance size, the effect of clearance size diminishes and the R^* does not vary much with further increase in the clearance size. However, this could also be attributed to the fact that there simply is not enough sample above the impeller blades when the clearance size in increased as that hinder the formation of shear band. Another set of experiments were performed but with 2 g of sample instead. The PSDs and the R^* calculated for the new set of experiments is shown in Figures 1-28 and 1-29, respectively. The huge drop in R^* observed earlier is not seen in the new set of data. Comparing the difference between 2 and 3 mm clearance sizes, the decrease in R^* is reasonable. The decrease in R^* is gradual, unlike the previous dataset. Having compared the results from these datasets, it can be deduced that the sudden drop of R^* in the first dataset is indeed due to insufficient sample present above the impeller blades. In the second data set, where the sample mass is doubled, R^* is reduced at a steady rate as the impeller-base clearance is increased. The extent of breakage is high even for the largest clearance size (5 mm) tested, achieving a value of ~42%. This indicates that carbamazepine dihydrate crystals are very weak and prone to breakage.

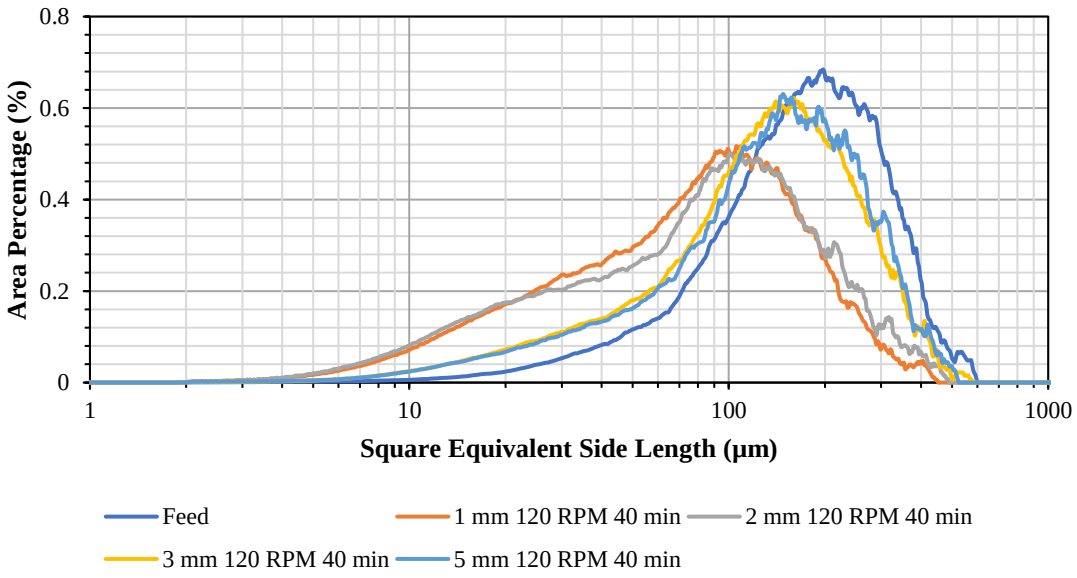

Figure 7-26 PSDs of the broken CBZ.2H$_2$O as a function of clearance size with vacuum suction applied

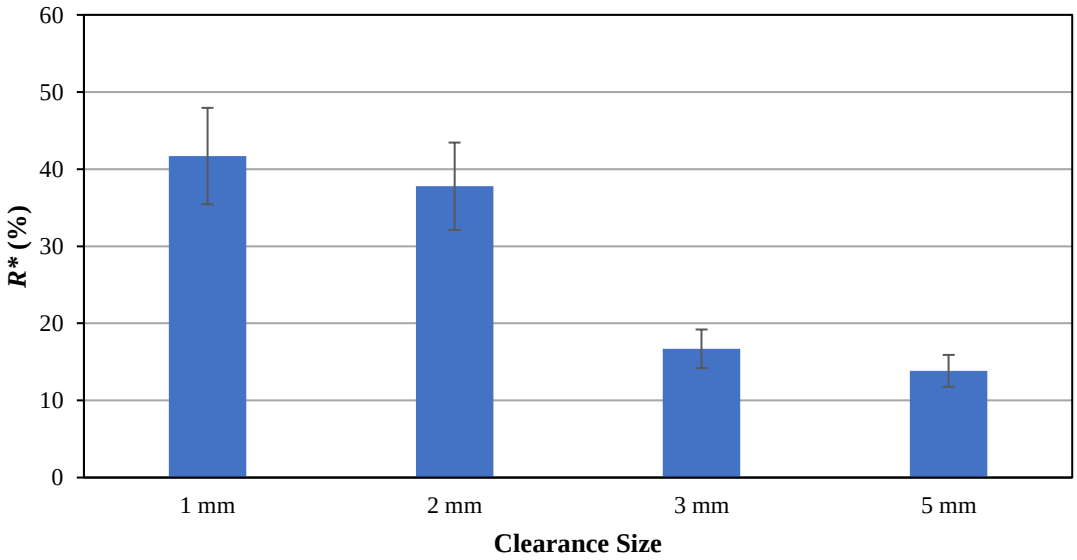

Figure 7-27 R* *of the broken CBZ.2H$_2$O as a function of clearance size at 120 RPM with vacuum suction applied*

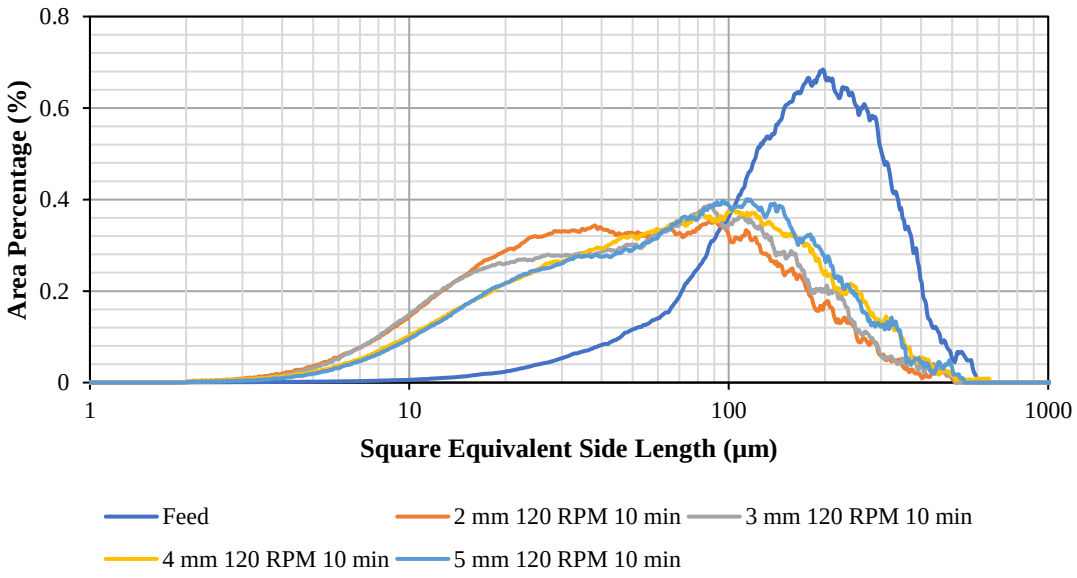

Figure 7-28 PSDs of the broken CBZ.2H$_2$O as a function of clearance size with vacuum suction applied (2 g)

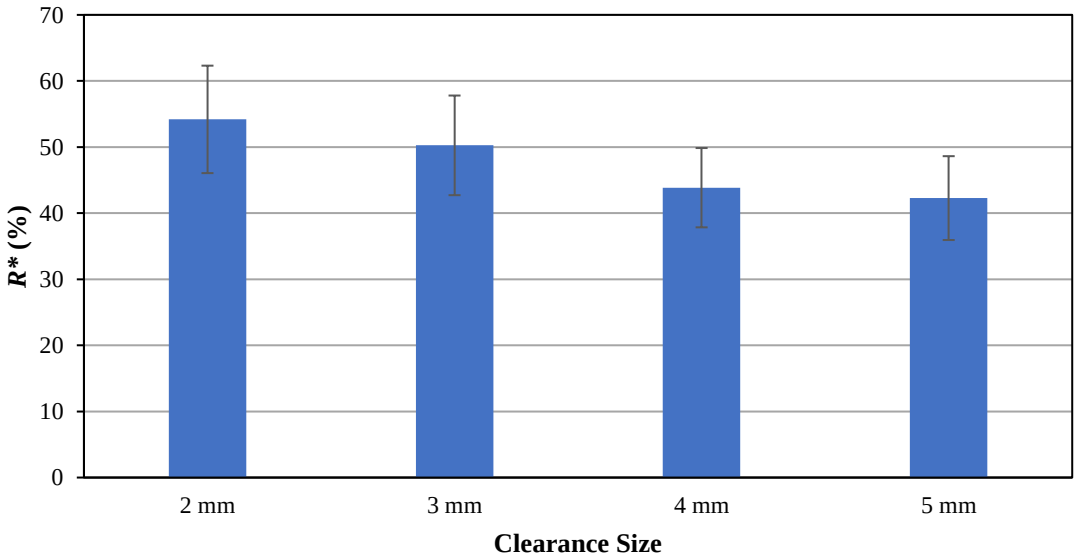

Figure 7-29 R of the broken CBZ.2H$_2$O as a function of clearance size at 120 RPM agitated for 10 min with vacuum suction applied (2 g)*

The effect of impeller rotational speed on the extent of CBZ.2H$_2$O breakage was investigated with vacuum suction applied. The PSDs of the carbamazepine dihydrate crystals agitated at different impeller speed is shown in Figure 7-30. Interestingly, the trend observed for the samples with vacuum suction applied is the same as those without. The *R** increases when the impeller rotational speed is increased from 30 to 60 RPM but reduces when it is increased to 120 RPM (Figure 7-31). Similar trend is also observed for

the samples agitated at a larger clearance size of 3 mm with vacuum suction applied as shown in Figure 7-32 and Figure 7-33. When the impeller is rotating, the particles in front of the blades are being lifted up and fall over to the back of the blades. The speed of those particle being lifted up by the impeller blade to fill the void behind the blades is dictated by the gravity and any additional normal load exerted on the powder bed, i.e. vacuum suction. Increasing the impeller rotational speed does increase the extent of particle breakage for carbamazepine, but only when the dynamic of the powder bed stays the same. At high rotational speed, the powder bed is in a constant dilated state as the speed of the particles being lifted up is now higher than settling down. In some extreme cases, the powder bed could get fluidised but that is not the case here due to the vacuum suction applied. The consistent trend shown by the three different datasets presented suggests that there is indeed a change of powder bed dynamic to a more dilated state when the impeller speed is increased from 60 to 120 RPM, hence causing less particle breakage.

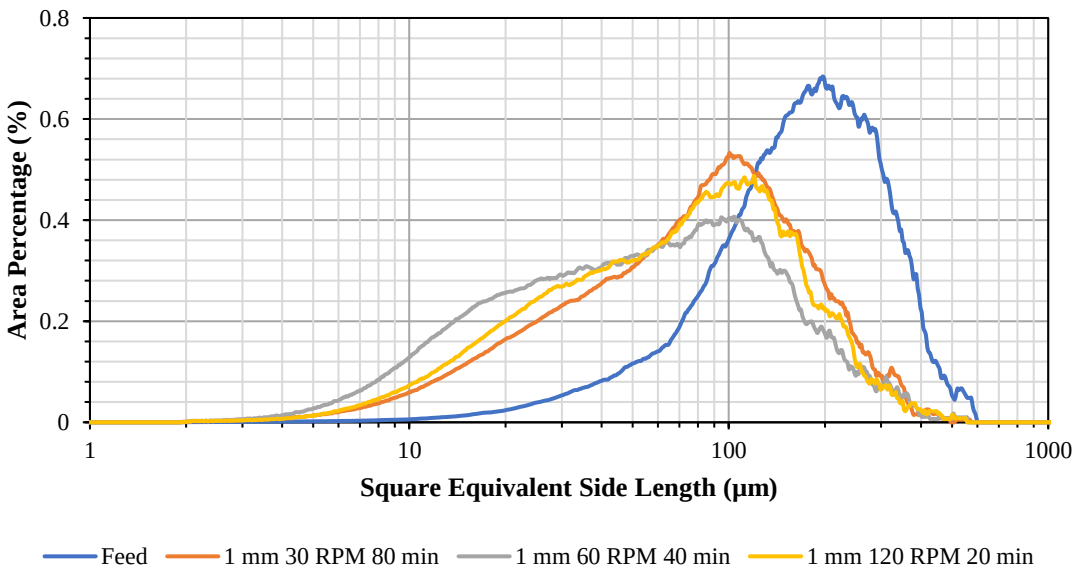

Figure 7-30 PSDs of the broken CBZ.2H₂O as a function of impeller speed with vacuum suction applied

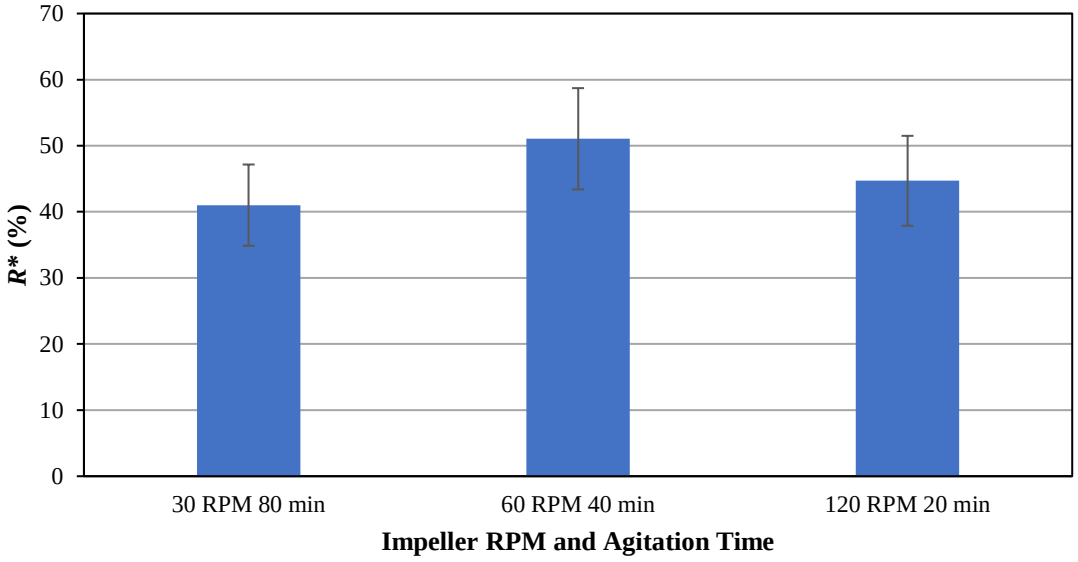

Figure 7-31 R of the broken CBZ.2H₂O as a function of impeller speed at 1 mm with vacuum suction applied*

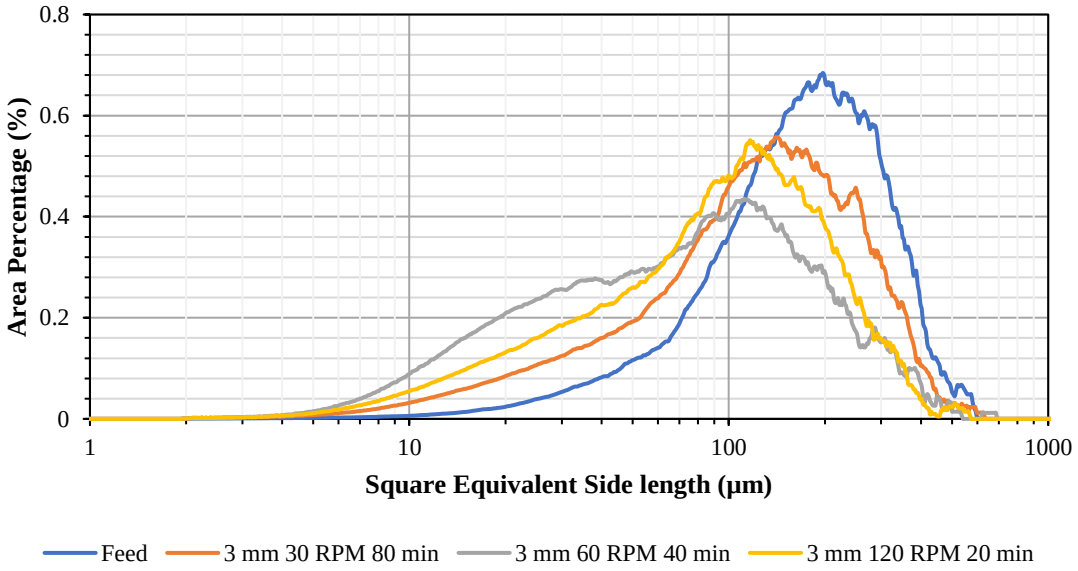

Figure 7-32 PSDs of the broken CBZ.2H₂O as a function of impeller speed and rotation time with vacuum suction applied (3 mm clearance)

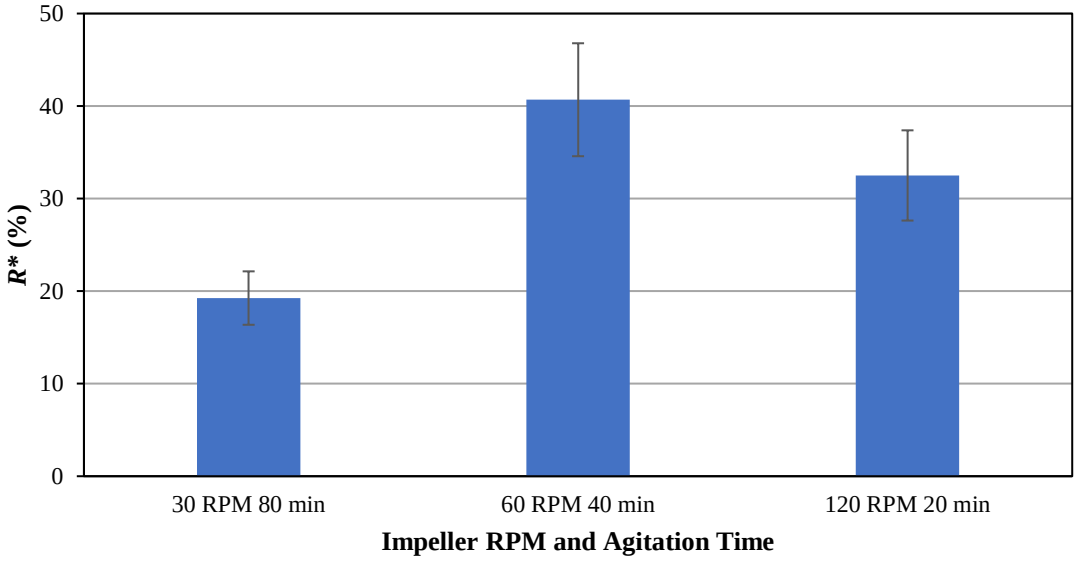

Figure 7-33 R of the broken CBZ.2H$_2$O as a function of impeller speed with vacuum suction applied (3 mm clearance)*

The PSDs and *R** of carbamazepine dihydrate crystals agitated at different periods of time with vacuum suction applied is shown in Figures 1-34 and 1-35, respectively. Again, applying vacuum suction incurs significant increase in the *R**. It can be seen that increasing the agitation time increases the extent of breakage of carbamazepine dihydrate. However, the system seems to have reached a plateau point when the particles are being agitated for 20 minutes as further increase in the agitation time results in no significant increase in *R**.

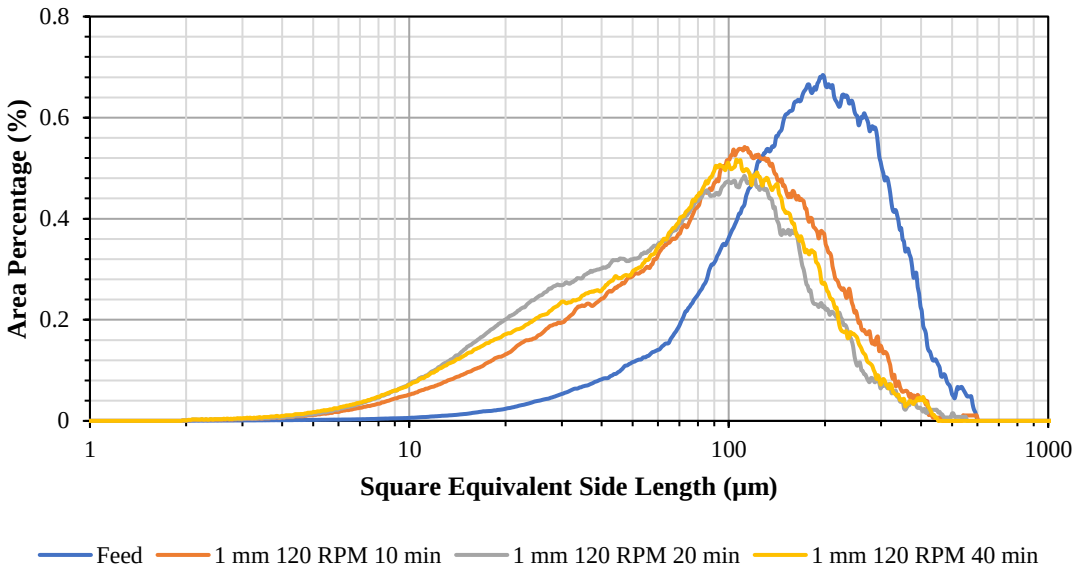

Figure 7-34 PSDs of the broken CBZ.2H₂O as a function of agitation time with vacuum suction applied

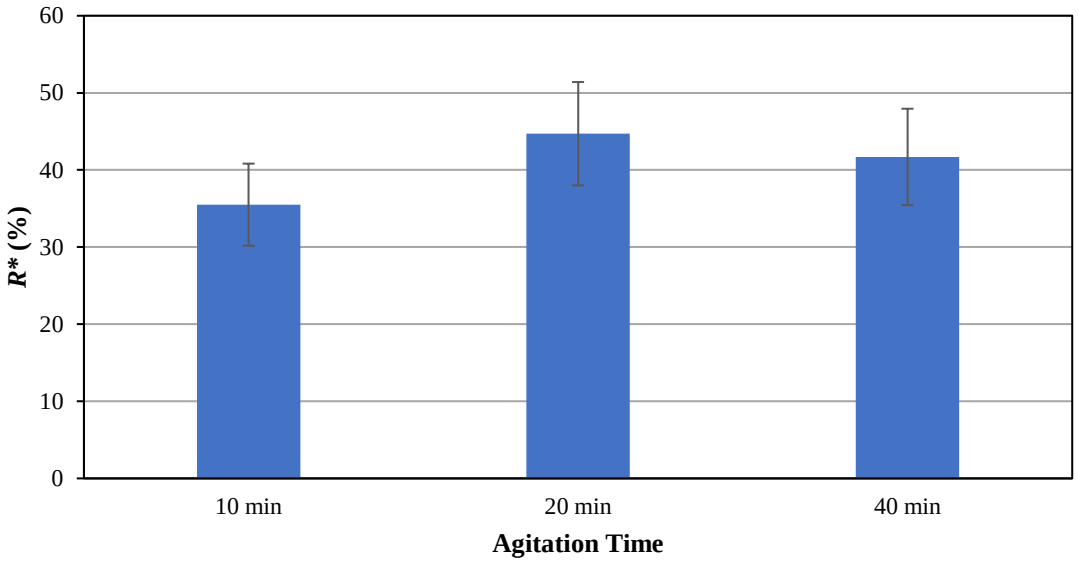

Figure 7-35 R of the broken CBZ.2H₂O as a function of agitation speed at 1 mm and 120 RPM with vacuum suction applied*

7.5.6 Effect of Solvent Content

The presence of solvent between the particles could influence the resistance to flow of the powder bed, and that is dictated by the type and amount of solvent presence in the powder bed. Carbamazepine dihydrate crystals in this work were crystallised using a water:ethanol solution. Water is an anti-solvent to the crystallisation process and the solubility of carbamazepine dihydrate in water is found to be very low, ~311.1 µg/ml (Kobayashi et al., 2000). To study the effect of solvent content present in the powder bed on the breakage behaviour of carbamazepine dihydrate, a slurry of carbamazepine dihydrate and water was first prepared. 2 g of carbamazepine dihydrate crystals were mixed with 10 ml of water and stirred gently using a spatula to wet the crystals thoroughly. The slurry was then filtered in the AFBD vessel until a desirable solvent content was reached. The reduction of solvent content by mass was monitored using the FT4 normal load sensor. The wet cakes with different solvent content were then agitated at 120 RPM with an impeller-base clearance of 2 mm to assess their role in the breakage of carbamazepine dihydrate in an AFBD. No vacuum suction was applied. Short intermittent agitation time (5 s) at 120 RPM was used as the wet crystals have a tendency to get suspended on top of the impeller blade due to the liquid bridges formed between the particles having higher attraction force compared to the gravitational pull. Hence, after every agitation step, the impeller blade was lifted up to 20 mm, well above the sample, and lowered back down to recondition the powder bed. The total agitation time was 5 mins and after that the sample is left in the AFBD vessel with vacuum suction applied to be air dried at room temperature for 2 hours. The dried samples were then collected for further analysis using Morphologi G3. Three solvent contents of 10, 25 and 50% by mass were tested, i.e, used at the start of shearing the bed by the impeller. The PSDs of the $CBZ.2H_2O$ samples agitated at different solvent contents are shown in Figure 7-36. It is evident that solvent content is influential on the reduction of particle size. The higher the

solvent content in the powder bed when it is being agitated, the higher the extent of breakage of the crystals. The *R** calculated for each solvent content is shown in Figure 7-37. At 10% solvent content, the *R** is about ~12% and it is increased to ~32% and 37% when the amount of water in the powder bed is increased, rising the solvent content to 25 and 50%. This is expected as a decrease in solvent content in the powder bed reduces the attraction force between the particle, which in turn lead to less resistance of the powder bed to flow upon being agitated by the impeller.

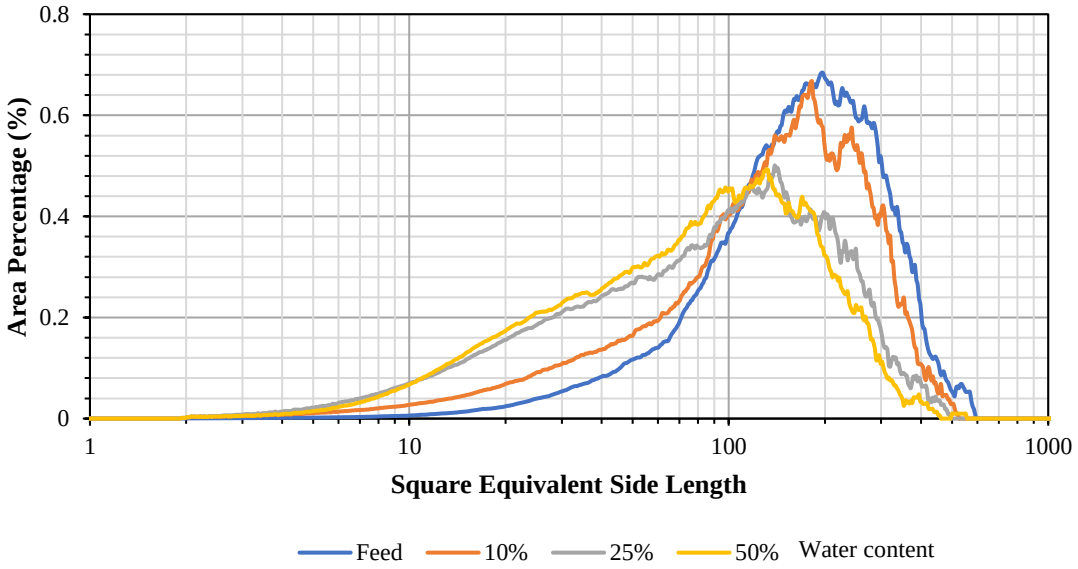

Figure 7-36 PSDs of the broken CBZ.2H₂O as a function of solvent content

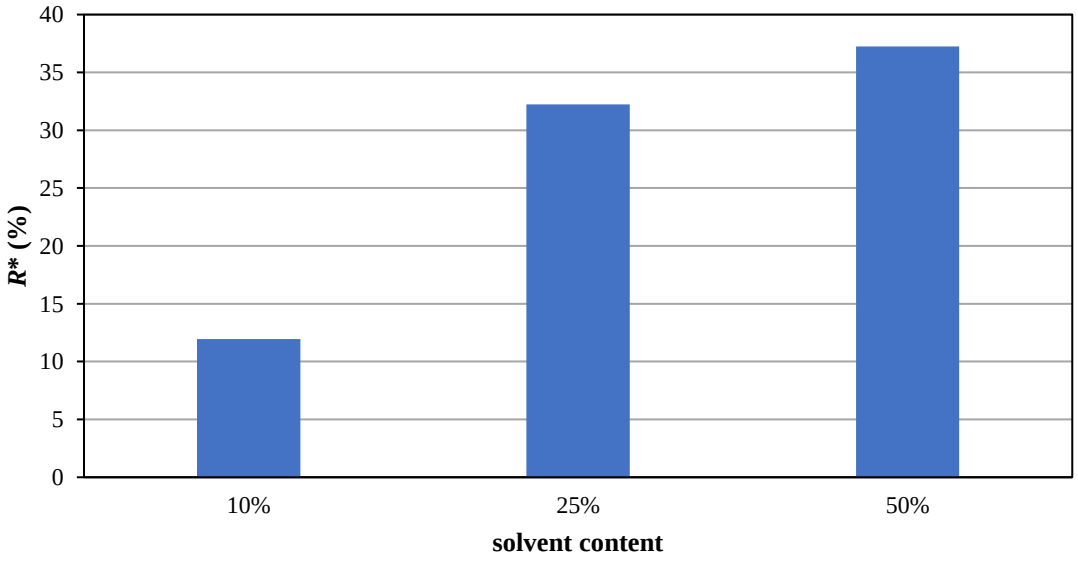

Figure 7-37 R of the broken CBZ.2H₂O as a function of solvent content*

7.5.7 Shape Analysis of the Broken CBZ.2H_2O

One interesting question arises as to how do CBZ.2H_2O crystals break in an agitated filter bed dryer? Carbamazepine dihydrate crystals used in this work are platy and acicular. Hence, the reduction of length and width of the crystals due to various process parameters could provide some insight into the breakage behaviour of the crystals. An overview of the reduction in width and length, expressed in their characteristic D-values is shown in Figure 7-38. Three series of datapoints can be seen in this plot. The blue one corresponds to D_{10}, orange to D_{50} and grey to D_{90} of the size distributions (length and width) of the broken particles due to different process treatments. Each data point corresponds to a set of process conditions tested in earlier section to break the crystals. The correlation between the length and width of the broken crystals subjected to different process treatments is fascinating. Strong linear relationship is observed for the characteristic sizes of the length and width distributions. The slope of the regression line of each data series gives a measure of the average aspect ratio of the broken crystals. D_{90} is associated with the biggest particle group in a distribution, while D_{10} represents the smallest particle group. The slope of the regression lines is found to be 0.39, 0.49 and 0.54 for D_{10}, D_{50} and D_{90}, respectively. This suggests that as the carbamazepine dihydrate crystals get broken down into smaller fragments, they become slender. The light micrographs of some of the biggest crystals of one of the agitated samples (with 10% solvent content) are shown in Figure 7-39. It can be seen that these crystals are generally very wide but not so long in length. Using the same dataset, the light micrographs of the smaller crystals are shown in Figure 7-40. It is very clear that those smaller crystals are slender in general which explains the trend that we observed in the plot earlier. Carbamazepine dihydrate could break either by chipping off the corner or snapping a long the longest dimension. A good example is shown in Figure 7-41 where a part of the crystal is obviously chipped

off and another part is snapped off due to the high bending moment it experiences in the powder bed.

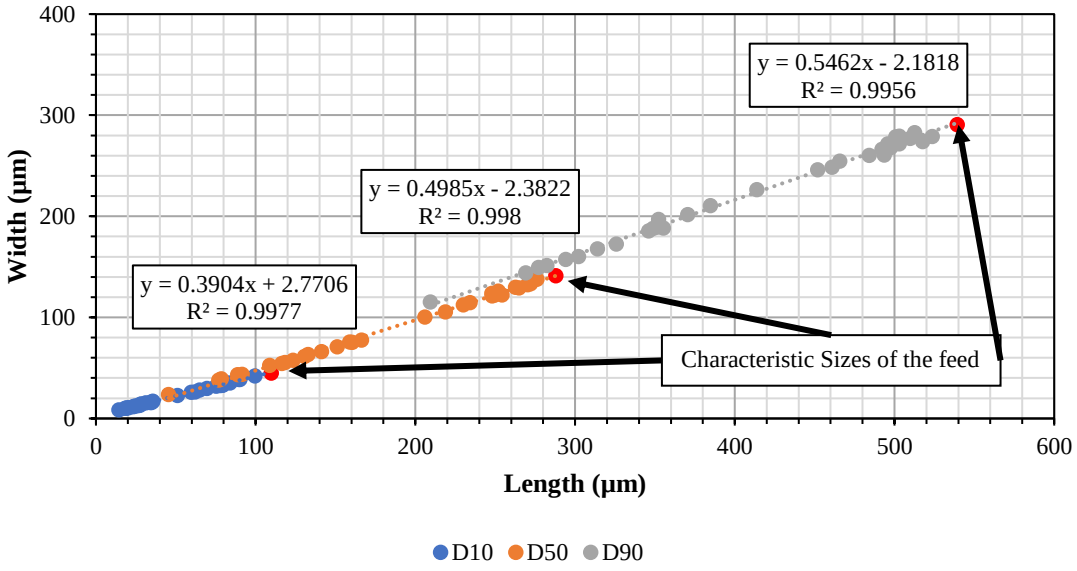

Figure 7-38 Scatter plot of the characteristic D-values of width and length distribution of CBZ.2H₂O

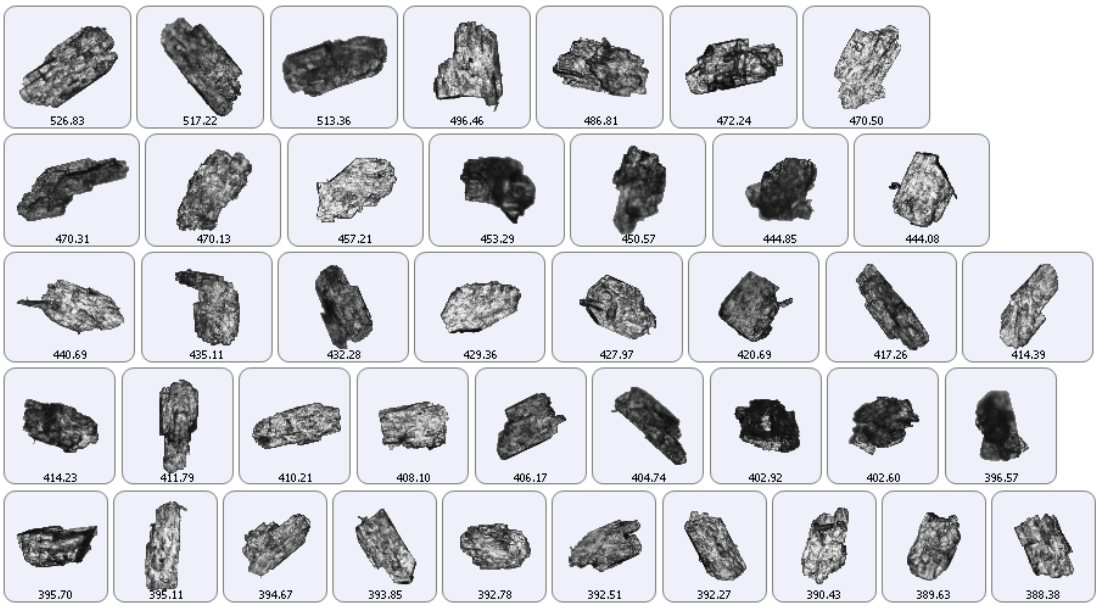

Figure 7-39 Light micrographs of big particles (treated sample)

Figure 7-40 Light micrographs of small particles (treated sample)

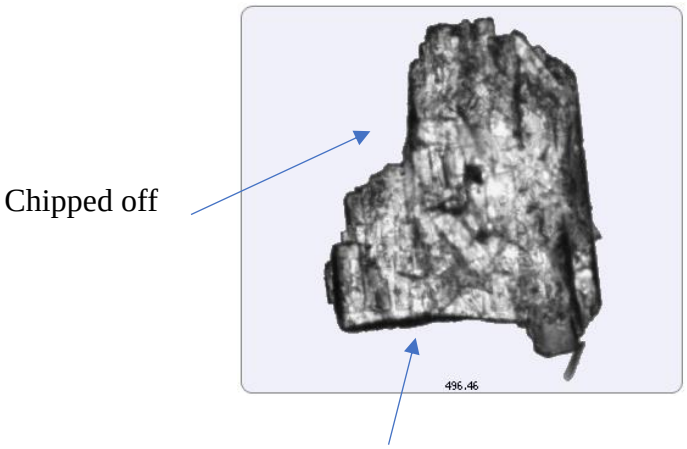

Figure 7-41 Breakage mechanism of CBZ.2H₂O

7.5.8 Energy Utilisation

During agitated filter bed drying, mechanical energy is transferred from the rotating impeller to the powder bed as a result of shearing. The mechanical energy transferred to the powder bed is spent on both agitating the powder bed and causing particle attrition. The input rotational energy to the powder bed can be calculated using the equation below:

$$E_{Rotational} = T\theta \qquad (7\text{-}2)$$

where T is the average torque and θ is the angular displacement travelled in radian. An example of the torque profile recorded with vacuum suction applied is shown in Figure

7-42. The negative sign indicates an anticlockwise rotation of the impeller blade. It can be seen that the magnitude of the torque increases sharply initially and then gradually before reaching a plateau. The region where the peak is observed correspond to the period where particle attrition happens. When agitation first starts, the big crystals in the powder bed are stationary and interlocked against each other. To shear the powder bed, a substantial amount of mechanical energy is needed and that explains the initial spike of the torque recorded. As the powder bed starts to flow, the shear deformation induced on the powder bed causes the particles to break. As the particles get smaller in size, their resistance to flow becomes less and hence a gradual decrease of the magnitude of the torque is observed. Using Eq. 6-1, the total energy being transfer to the bed can be calculated. The input mechanical energy for the experiments performed were calculated and the relationship between the R^* and the specific input energy is drawn shown in Figure 7-43. A reasonably good fit is obtained from linear regression. It is evident that the extent of particle breakage is proportional to the specific input energy.

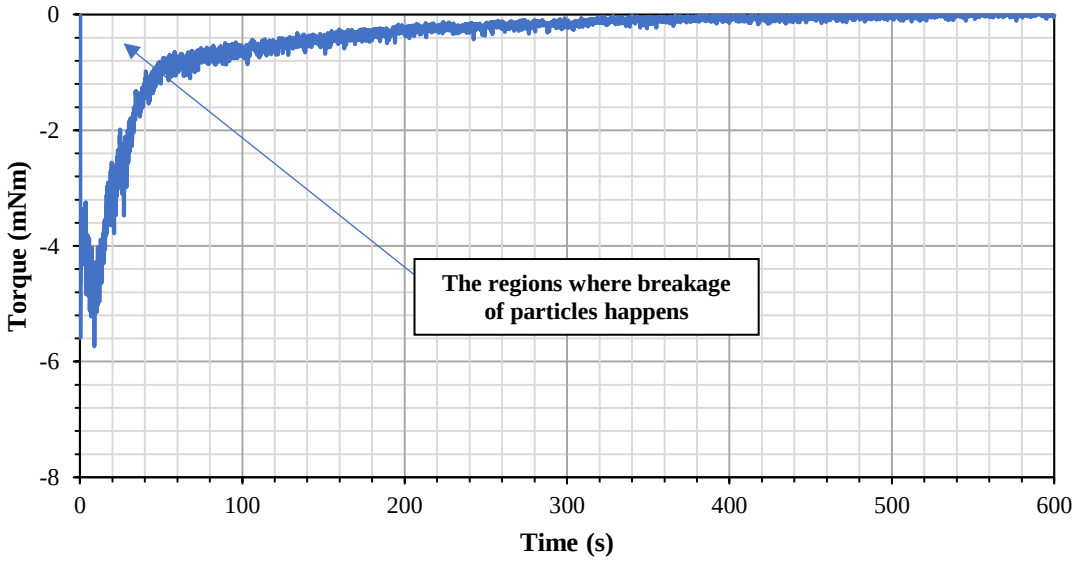

Figure 7-42 Torque profile recorded with vacuum suction applied

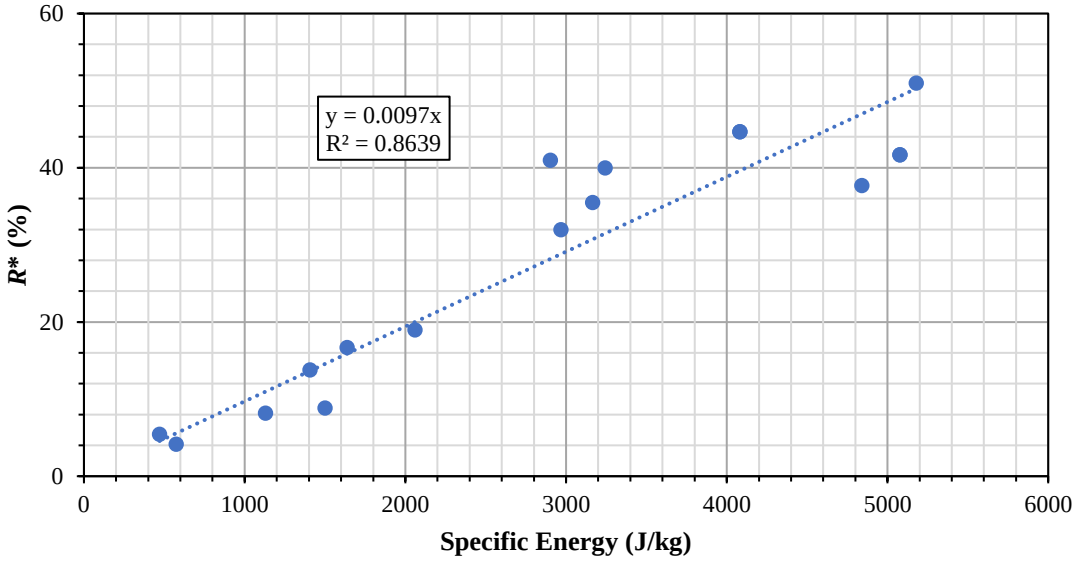

Figure 7-43 R vs specific input energy*

7.6 Conclusions

A new test rig to simulate agitated filter bed drying has been developed in collaboration with Freeman Technology using their existing FT4 powder rheometer. The device performs the essential features that an agitated filter bed dryer has. It picks up the change in the powder bed resistance (reflected in the torque profile) as the liquid carrier, IPA is dried off from sodium chloride crystals. The torque profile shows a positive parabolic shape which indicates the torque first increases when there is a high volume of solvent present in the system and then decreases when the solvent content is below a critical point, i.e. the resistance of the bed to flow is reduced.

A systematic study of the effect of process parameters on the breakage of equant particles of sodium chloride shows that impeller clearance has a significant effect on the breakage of sodium chloride. When the impeller clearance is less than 10 particle diameters, extensive breakage of the sodium chloride is observed. Impeller tip speed has little effect on the fractional broken mass, R^* calculated, but a full-size analysis shows a difference in the size distribution of the broken crystals. Chipping seems to be the dominant breakage mode here as plenty of chips are generated and the corner of the broken crystals appears to be rounded off. A strong linear relationship is found between the number of impeller revolution and extent of particle breakage of sodium chloride. The higher the number of revolutions, the higher the extent of particle breakage. Smaller particles break less as higher energy is required to break them. However, when the impeller blade length is reduced, no breakage is observed at all.

The new AFBD unit is used to assess the breakage of carbamazepine dihydrate crystals which are acicular and platy. Due to the acicular and platy shape of the crystals, optical imaging technique is used to measure the size distribution of the broken crystals. The extent of breakage, R^* is calculated using a new approach proposed earlier by

assessing the degree of shift of the size distribution of the broken crystals from the feed. R^* is increased when the impeller-base clearance in reduced. Impeller tip speed is influential to the breakage of carbamazepine dihydrate, even though the change of R^* is not huge across the velocity range tested. Increasing the number of impeller revolutions increases the extent of breakage of carbamazepine dihydrate. R^* increases significantly when vacuum suction is applied as now additional drag force is exerted on the powder bed. Solvent content is another major factor in AFBD that could cause significant particle breakage as demonstrated here with carbamazepine and water. At high water content (50%), the particles are held together strongly by the capillary bond between the particles. Agitating the powder bed at this stage causes significant particle breakage of carbamazepine. When the solvent content is lowered, the breakage of the crystals is reduced proportionally as the attraction force between the particles is reduced. Unlike sodium chloride which predominantly breaks by chipping, carbamazepine fragments easily due to the bending moment imposed by the impeller blade. The crystals become slender as they reduce in size. Both chipping and fragmentation are observed for carbamazepine dihydrate crystals.

The mechanical energy transferred from the impeller to the powder bed is calculated from the torque profile and related to the extent of particle breakage in an agitated filter bed dryer. It is found that the higher the energy input, the higher the extent of particle breakage.

Chapter 8

DEM Simulations of Agitated Filter Bed Dryer

8.1 Introduction

Agitated powder beds are found in many process industries for mixing and drying. The process performance is affected by the physical properties of the particles such as size and shape (Cho et al., 2006; Liang and Rajesh, 2013). Different packings of the bed give rise to different extents of resistance to flow and this may have adverse effects on particle breakage and transformations (Guises et al., 2009). DEM is used to study the stress distribution within the region of interest as a function of particle length to width ratio. Rounded cylinders are used to represent particles with different length to width ratios. Polyhedra geometry (Potapov and Donohue, 2013) is used to make the particles to simulate particle shape. When a particle bed is agitated, the stresses arising within the bed change over time because of the impeller agitation. The interactions between the particles and the impeller as well as the evolution of stresses are of particular interest in this study. The bed packing void fraction is analysed and the stresses are characterised for various particle length to width ratios.

8.1.1 Materials and Methods

8.1.1.1 Simulation Setup

DEM simulations were carried out using the ROCKY software (ESSS, Florianópolis, Brazil). Movement of individual particles in discrete element method was first described by Cundall and Strack (1979) as their translational and rotational motions governed by the equations below:

$$m_i \frac{dv_i}{dt} = \sum F_{c,i} + m_i g \tag{8-1}$$

$$\frac{d\left(I_i \omega_i\right)}{dt} = R_i \left(\sum M_{c,i}\right) \tag{8-2}$$

where m_i is the mass of the particle, *Ii* the moment of inertia, v_i the translational velocity, ω_i the rotational velocities and R_i the rotation matrix relating the global and local coordinate systems and $M_{c,I}$ the contact torque as a result of the contact forces, $F_{c,i}$ arising from rolling friction. The contact force in Rocky is described by a hysteretic linear spring model following the set of equations below first proposed by Walton and Braun (2002):

$$F_n^t = \begin{cases} \min\left(K_{nl} S_n^t, F_n^{t-\Delta t} + K_{nu} \Delta S_n\right) & \text{if } \Delta S_n \geq 0 \\ \max\left(F_n^{t-\Delta t} + K_{nu} \Delta S_n, \lambda K_{nl} S_n^t\right) & \text{if } \Delta S_n < 0 \end{cases} \tag{8-3}$$

$$\Delta S_n = S_n^t - S_n^{t-\Delta t} \tag{8-4}$$

where F_n^t and $F_n^{t-\Delta t}$ are the normal elastic-plastic contact forces at the current time, *t* and the previous time $t - \Delta t$. ΔS_n is the change in the contact normal overlap during the current time and is assumed to be positive as particles approach each other, and vice versa. S_n^t and $S_n^{t-\Delta t}$ are the overlap values at the current time and previous time, respectively. λ is a dimensionless small constant and is fixed at 0.001 in Rocky to ensure the normal

force will return to zero when the overlap decreases to zero during unloading. The loading and unloading contact stiffnesses are denoted as K_{nl} and K_{nu}. They are calculated as:

$$K_{nl} = \frac{K_{n1}K_{n2}}{K_{n1} + K_{n2}} \tag{8-5}$$

$$K_{nu} = \frac{K_{nl}}{\varepsilon^2} \tag{8-6}$$

$$K_{1,2} = E_{1,2}d_{p1,2} \tag{8-7}$$

where ε is the coefficient of restitution, E the Young's modulus, d_p the particle size and subscript 1 and 2 refers to the two entities in contact (particle-particle or particle-geometry). The tangential force, F_τ^t in Rocky is calculated using the equation below:

$$F_\tau^t = \min\left(F_\tau^{t-\Delta t} - K_\tau \Delta S_\tau, \mu F_n^t\right) \tag{8-8}$$

where ΔS_τ is the tangential relative displacement during the time step, μ is the friction coefficient (depending if sliding takes place, could be either static or dynamic friction coefficient).

Particle shape is modelled using polyhedra. Particles with length to width ratios in the range 1, 1.25, 1.5, 1.75, 2, 3 and 5 were investigated. As can be seen in Figure 8-1, spheres are used to represent particles with unity length to width ratio while particles with other length to width ratios are represented by rounded cylinders with different lengths and diameters. The volume of the particles is kept constant at an equivalent-volume diameter of 3 mm regardless of the change of particle length to width ratio throughout the simulations. The geometry of the impeller and vessel used in the simulation are reproduced as shown in Figure 8-2. The details of the geometry and simulation conditions are shown in Table 8-1. The vessel is initially fed with particles until the bed height (0.06 m) is approximately three times the blade height (0.018 m). The bed is then agitated at a speed of 1 rev/s for 5 s.

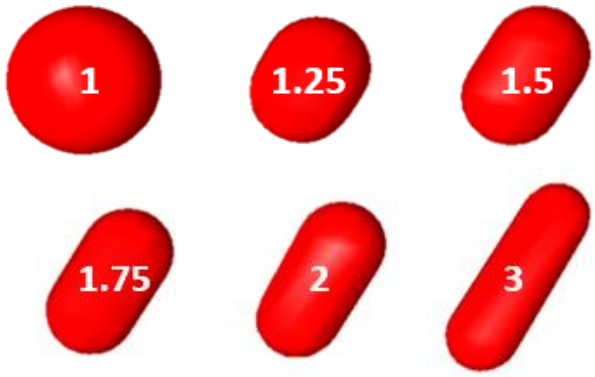

Figure 8-1 Sphere and rounded cylinders with different length to width ratios

Figure 8-2. Actual impeller and vessel (left) and its CAD representation (right)

Table 8-1 Geometry and simulation details

Operating Conditions

Vessel Inner Diameter (mm)	110
Number of Blades (-)	2
Blade Height (mm)	18
Blade Inclination (°)	60
Blade Diameter (mm)	98
Clearance Height (mm)	2
Angular Velocity (rev/s)	1
Particle Feed Rate (kg/s)	3
Particle Density (kg/m^3)	1.6
Young's Modulus (Pa)	10^7
Coefficient of Sliding Friction (-)	0.3
Coefficient of Restitution (-)	0.3
Simulation Time (s)	5

8.1.1.2 Determination of Particle Bed Void Fraction

Particles with different length to width ratios pack differently to form a bed and this in turn affects the prevailing shear stress (Guo et al., 2012). In this study, a cylindrical measurement cell with a height of 0.02 m is generated to measure the average void fraction of the particle bed (Figure 8-3). The measurement cylinder is placed right above the impeller blades and below the free surface of the bed to eliminate the situation where unwanted entities (such as impeller blades and area above free surface of the bed) are taken into the calculation of the average void fraction.

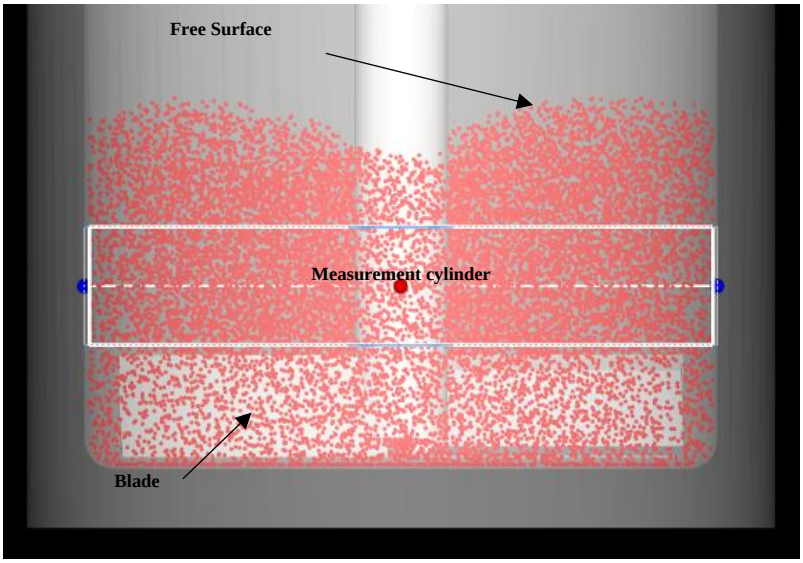

Figure 8-3. Position of measurement cylinder

8.1.1.3 Stress and Strain Analysis

In an agitated bed, as the impeller rotates, particles in front of the blades experience shear and get pushed over and fall behind the blade to a region where the bed is dilated. The prevailing stresses of the region of particle bed that comes into direct contact with the rotating bed are analysed. Experimentally, the stress distribution within a particle bed is too difficult to be determined, but this is made possible in DEM simulation by introducing measurement bins in the regions of interest (Hare et al., 2011). Five measurement bins created along the impeller blade that capture the particle interactions during each time

step within their own domain are shown in Figure 8-4. The stress tensor of each bin is calculated using the equation below developed by Bagi (Bagi, 1996),

$$\sigma_{ii} = \frac{1}{V}\sum_{1}^{N} F_{ii} \cdot r_p \tag{8-9}$$

where σ is the stress, V is the measurement bin volume, N is the number of particles within the bin and F is the force acting on a particle in direction ii with radius r_p. The average principal and deviatoric stresses are then given by equations 8-10 and 8-11:

$$\sigma_{ave} = \frac{P_1 + P_2 + P_3}{3} \tag{8-10}$$

where P_1, P_2 and P_3 are the three principal stresses, respectively. The deviatoric stress, σ_{dev} (Luding, 2008) can be calculated from the principal stresses and is defined as

$$\sigma_{dev} = \frac{\sqrt{(P_1 - P_2)^2 + (P_1 - P_3)^2 + (P_2 - P_3)^2}}{\sqrt{6}} \tag{8-11}$$

The calculation for both principal and deviatoric stresses is performed at each time step to capture the stresses experienced along the impeller blade. The size of the bin is kept in such a way that it has approximately more than 100 particles in each cell at each time step so that the dependency of individual particles is minimised while improving the statistical reliability for averaging the stress tensor in a measurement bin.

The breakage behaviour of particles is very much dependent on the strain rate. According to the work of Gong et al. (2018), particles break easier at lower strain rates and the progeny size distribution is strongly affected by the strain rate applied. The influence of the strain rate reduces when the input energy is increased. In this work, the strain rate applied to the powder bed is characterised by following the method suggested by Hare and Ghadiri (2015) and Remy et al. (2009, 2011). The five measurement bins created earlier are used in the calculation of the strain rate applied. The strain rate in the measurement cell is calculated using a simplified approach based on particle velocity

gradient across a distant in front of the impeller blade. That distance is assumed to be 5 particle diameters, which is the approximate width of a shear band. The strain rate can hence be calculated as the ratio between the shear band width and the maximum particle velocity in the measurement cell. According to Tardos et al. (2003), the strain rate, γ can be made dimensionless by using the correlation below:

$$\gamma_0 = \gamma \sqrt{d_p / g} \tag{8-12}$$

where γ_0 is the dimensionless strain rate, d_p the particle size and g the gravitational term.

Figure 8-4. Measurement bins along the impeller blade

8.2 Effect of Particle Length to Width Ratio

8.2.1 Particle Dynamics and Velocity Gradient

The velocity profile of the particle bed as the impeller is rotating could help identifying the shear band and its dependency on particle shape and impeller speed. To do that, a thin measurement bin is created that slices through the particle bed. The position of the measurement bin (blue box) is shown in Figure 8-5 at the left-hand column. The upper limit of the velocity is set as the maximum tip speed of the impeller. The snapshots on the left corresponds to the impeller position and those on right are the cross-sectional view from direction A as shown. The first snapshot is taken when the impeller blades are perpendicular to the measurement bin. The subsequent image is captured when the impeller has rotated 18 ° and the image acquisition process is continued until the blade has moved past the measurement. The series of snapshots captured could then allow the evolution of particle velocity as the impeller blades is rotating to be investigated. It can be seen that initially the particle velocity gradient of the cross-section A across the bed height is almost homogenous. Apart from the particles that are right beneath the free surface that can move freely, most of the particles are moving at the same velocity. As the impeller approaches the measurement bin, the velocity of the particles that are at the same level as the impeller blades gets increased as well (the impeller blade sweeping zone is represented by the red box on the right hand column of Figure 8-5 containing the particles). The difference becomes obvious when the angle between the blade and the measurement bin is less than 36 °. The particles that are neighbouring the vessel wall and impeller blade tips are moving at the highest velocity. However, the velocity of the particles decreases with their increase in vertical position in the particle bed. Interestingly, at 0 °C, the particles right at the top of the blade tip is almost stagnant. The shear band formed as a result of agitating the powder bed with a rotating impeller can be seen at 18 °. There is a region (encircled in yellow box) above the impeller blade that is of relative

higher velocity to the blade tip speed. That region, which is in fact the shear band, has a width of approximately 6 – 7 particle diameters. That agrees very well with the literature reported, that a shear band is typically around 5 – 10 particles diameter in size (Paramanathan and J. Bridgwater, 1983).

The velocity gradient across the horizontal area of the powder bed at different heights with regards to the lowermost position of the impeller blades is also studied. As can be seen in Figure 8-6, a cylindrical measurement bin is created with a diameter that is slightly bigger than the impeller diameter. It is first placed at a height that is in line with the lowermost position of the blade. The measurement is 5 mm in thickness and hence the first of the velocity gradient observed from direction B is on a surface that is 5 mm above the lowermost impeller height. For each subsequent snapshot, the measurement bin is moved 5 mm further upward. At 5mm, it is evident that particles around the blade tips are moving at the highest velocities. The regions of the particle bed that are perpendicular to the blade length appear to be stagnant and have particle velocities that are lower than 0.1 m/s. Similar pattern is observed height up until 20 mm. Beyond that height, particles are no longer in line with the impeller blade and gradual decrease of particle velocity is discerned. At 25 mm, stagnant regions above the blades start to form and they get wider as the height is increased. The mobility of the particles increased with their vertical position in the power bed. This is reflected in the velocity gradient where a gradual increase in particle velocity is observed when the measurement height is increased.

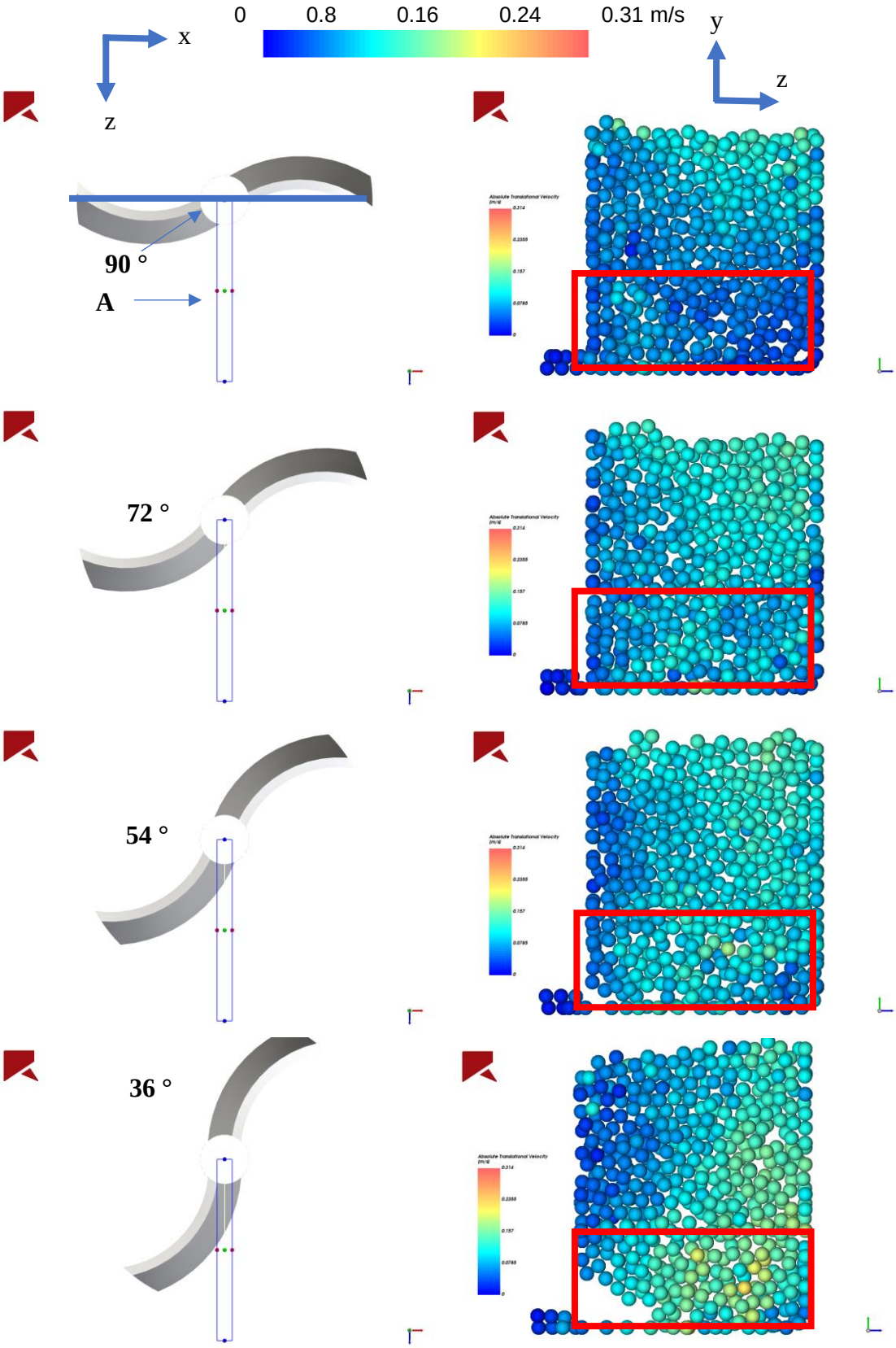
0
0.8
0.16
0.24
0.31 m/s
x
z
y
z
90 °
A
72 °
54 °
36 °

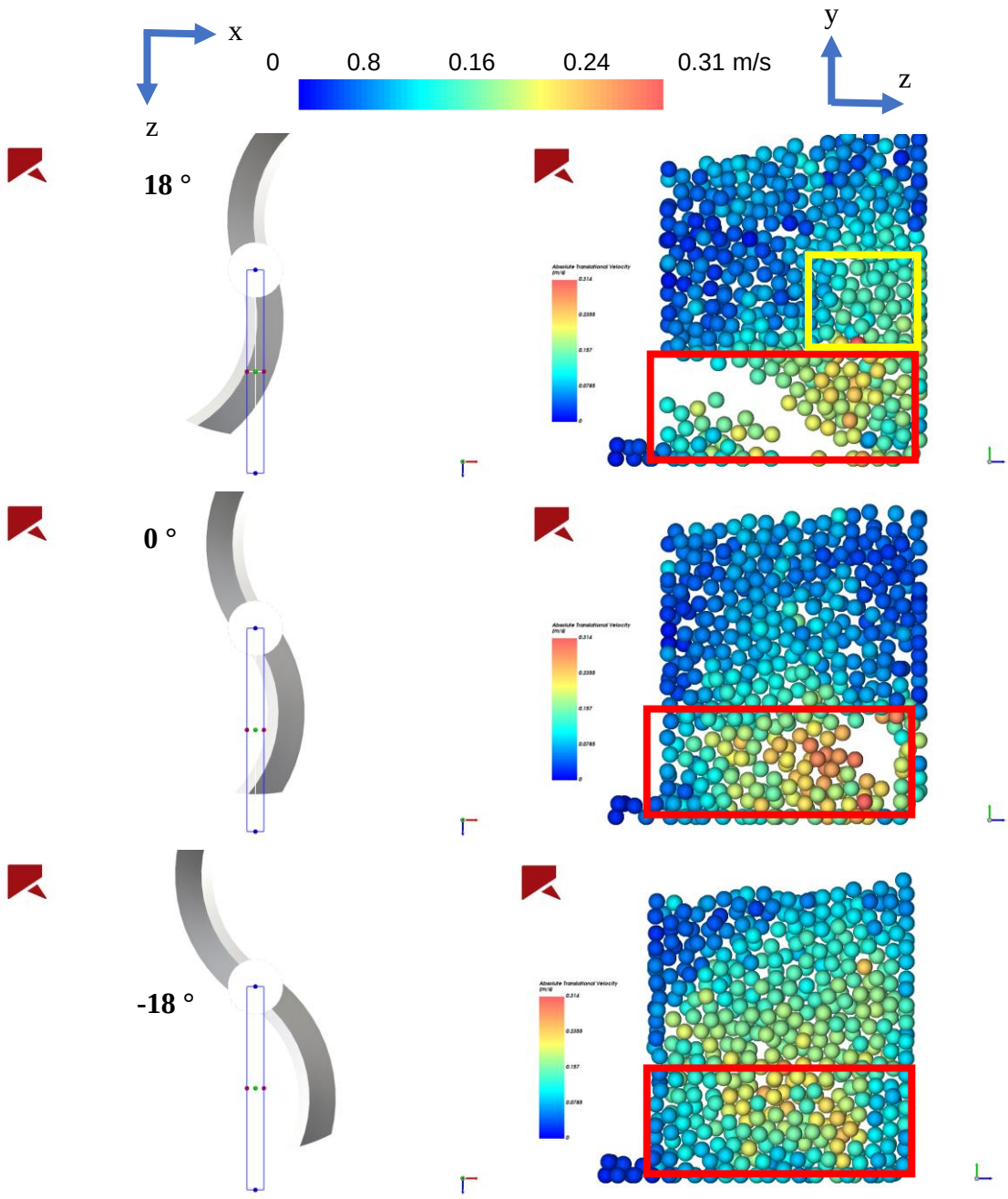

Figure 8-5 Velocity gradient of particles across the bed height at different Impeller positions

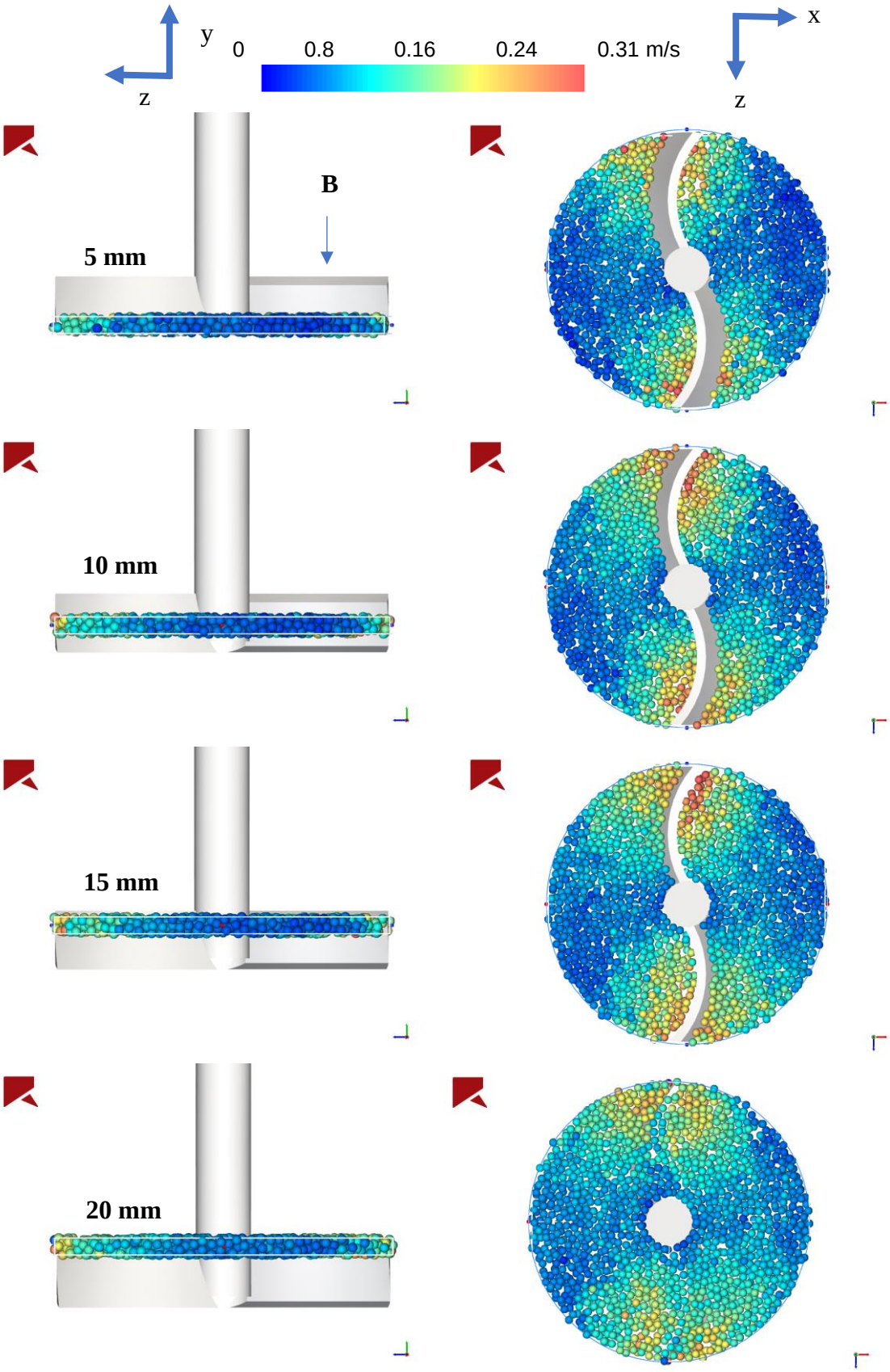
y
z
0
0.8
0.16
0.24
0.31 m/s
x
z
B
5 mm
10 mm
15 mm
20 mm

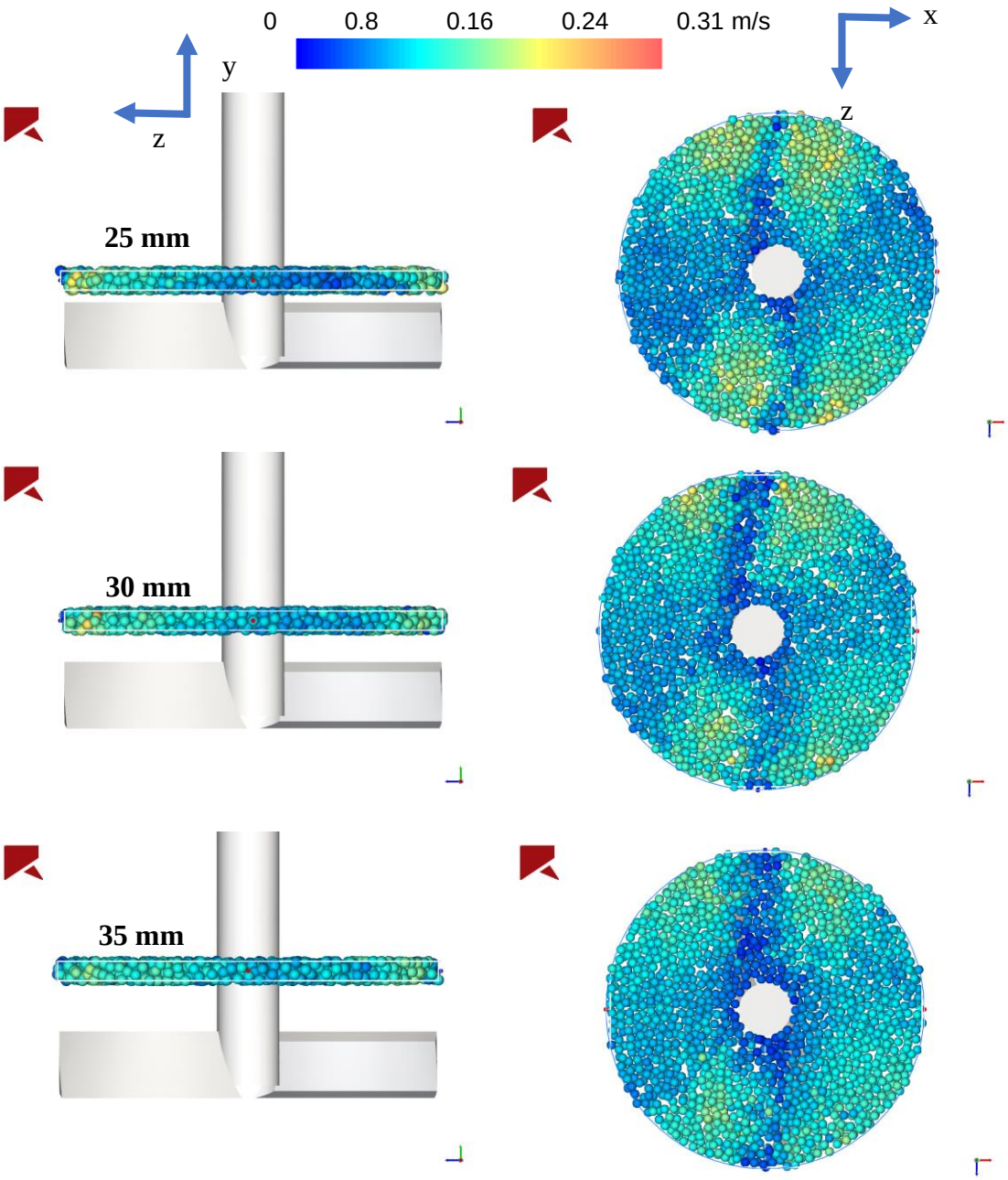

Figure 8-6 Velocity gradient of particles across the horizontal direction of the bed at different heights

Similar analysis is performed on acicular particles with a length to width ratio of 5 (Figure 8-7). The particles were packed by raining down the particle at the same orientation. The very first observation that stands out is the consistency of particle velocity along the radial position of the particle bed regardless of the vertical position of the particles. Unlike particle bed that is made up of spherical particles where stagnant regions can be identified, the particle bed made up of rounded cylinders seem to be constantly in motion in spite of the relative distance from the rotating impeller blade. This is an interesting observation as it signifies the role of particle shape in the flow dynamics of a packed bed. This difference is in fact due to the complex packing of the high length to width ratio particles that are being held together strongly, forming a bed. A good real-life example is bird nests, where their strong structure is actually supported by the twigs that are intertwined together. High length to width ratio particles could reach out further than just their surrounding particles, forming a network of support to the whole structure and hindering particle rearrangement. Particles can move and roll freely and rearrange themselves when they are spherical but not so much when they are elongated like the case here. Even though both cases have the same friction coefficients, their effective resistance to flow is different. The velocity gradient slightly changes when the impeller blade is passing through the measurement bin, around the tip of the blade at a relative angle of 18 °. A shear band is formed above the tip of the impeller blade and the width is approximately the diameter of 6 – 7 particles (equivalent spherical diameter). Another notable observation is the voids that form within the powder bed which are not seen when the bed is made up of spherical particles. They are the consequence of packing of high length to width ratio particles and are the hotspots for particle breakage due to the exerted compressive stresses and bending moments. The voids collapse when additional load is exerted, breaking the network of particles that support the structure, and the particles surrounding the voids could end up either: (i) reorienting themselves and become more

densely packed or (ii) breaking due the stress exerted being higher than the breakage strength of the particles. Breakage is not simulated here and hence no breakage is observed in this work.

The velocity gradient across the particle bed at different vertical positions is shown in Figure 8-8. Excluding the regions around the blade tips, the particle bed exhibits a very concentric velocity gradient profile, indicating the particles at the same radial position are moving at the same velocity. This observation is very different compared to the case of spheres, where stagnant regions are found parallel to the impeller blades. The concentricity of velocity gradient reduces with the increase in the vertical position, indicating the phenomenon of particle moving together as a block is most prominent at the bottom of the particle bed, where the particles are on the same level as the impeller blades. Above the blade, this effect is less prominent.

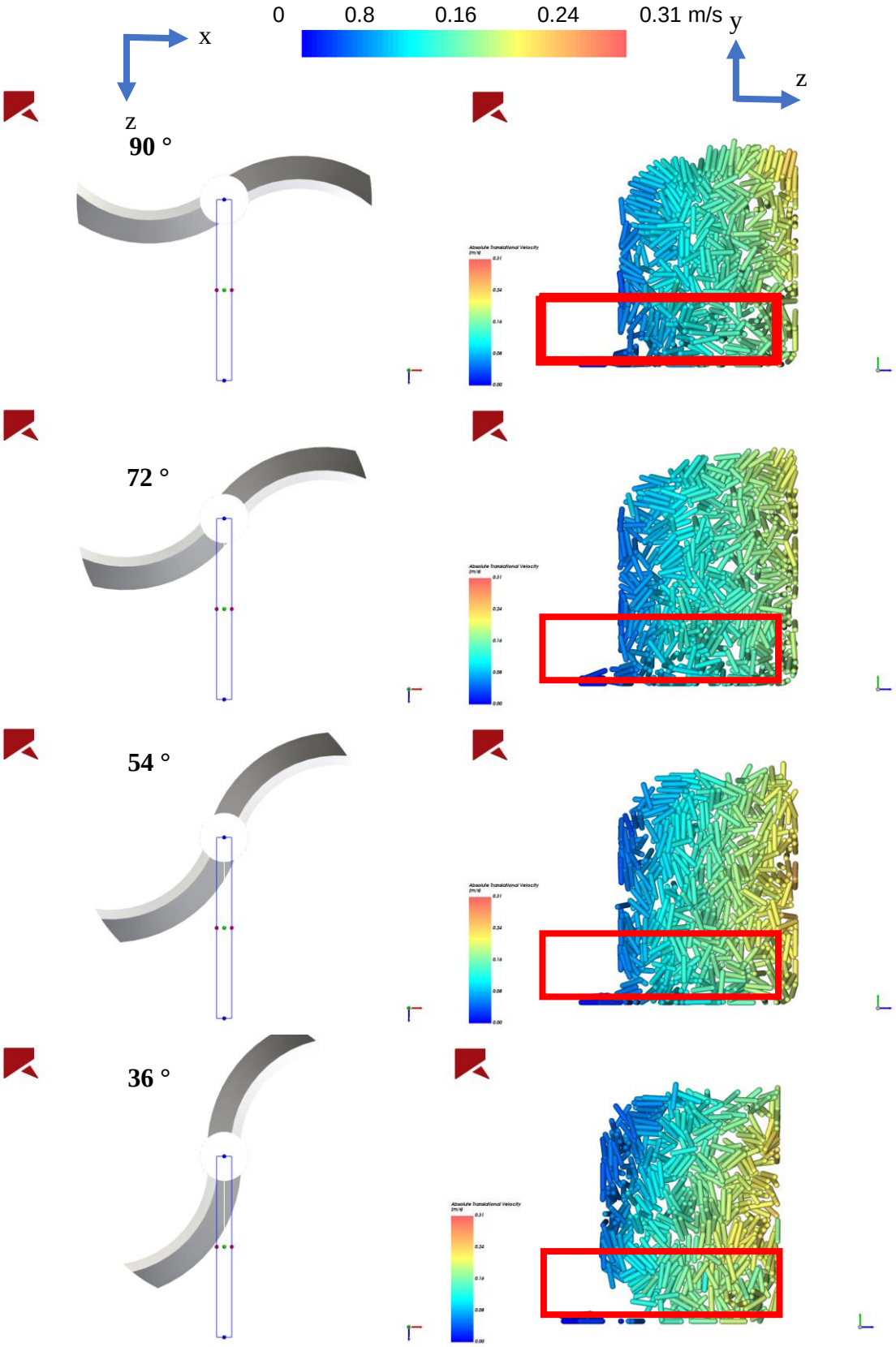
0
0.8
0.16
0.24
0.31 m/s
x
y
z
z
90 °
72 °
54 °
36 °

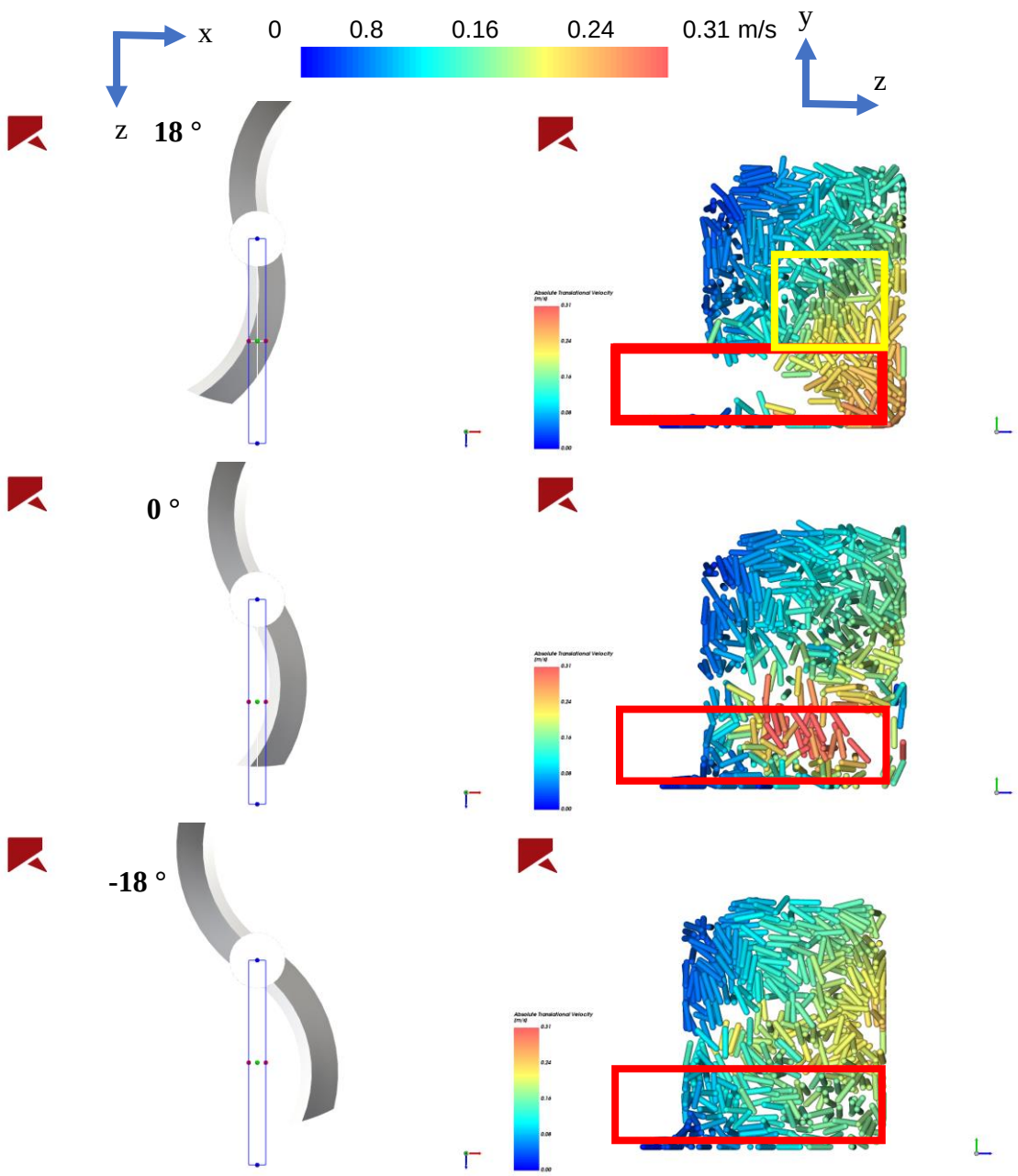

Figure 8-7 Velocity gradient of particles across the bed height at different impeller positions

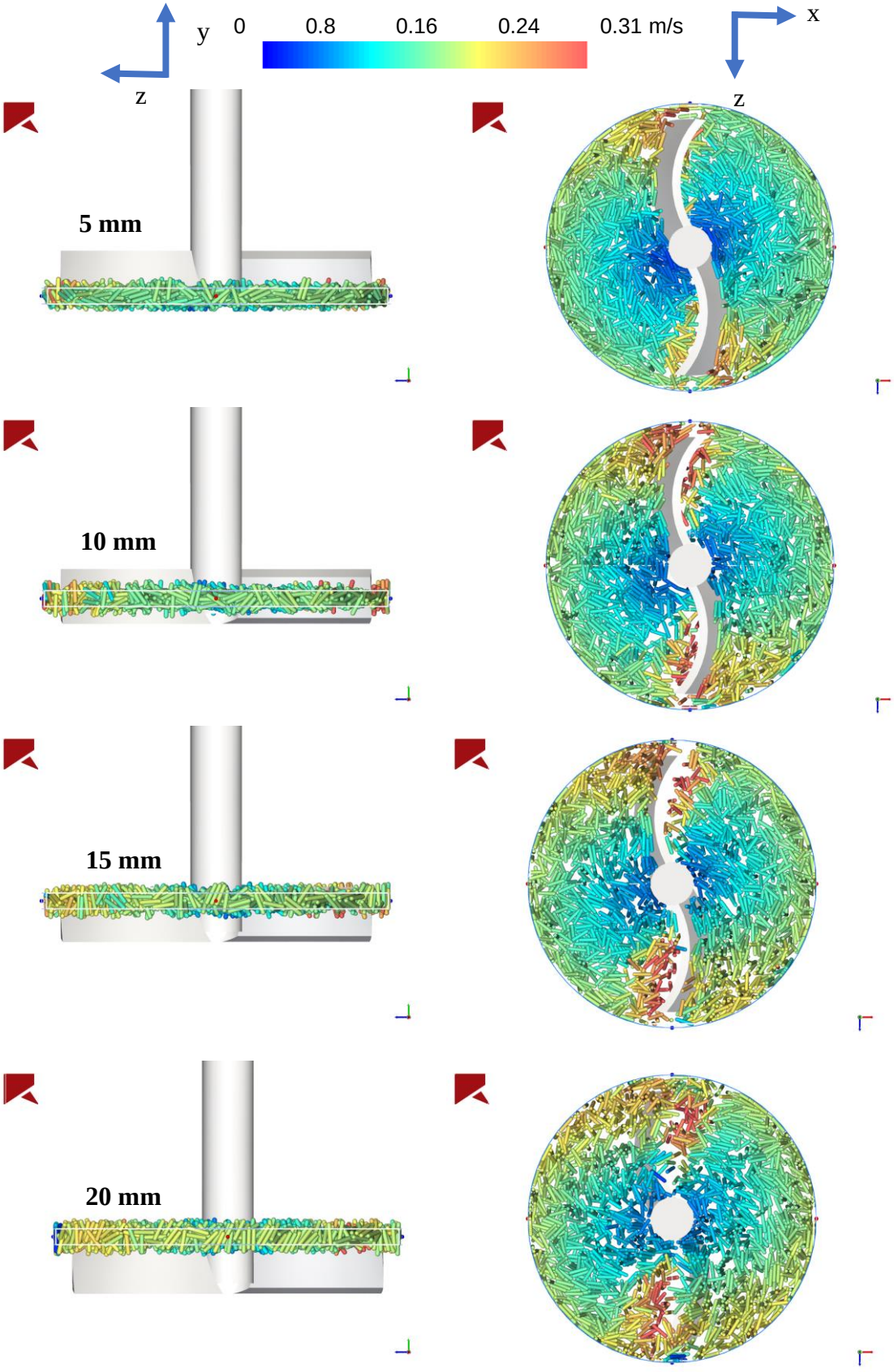
y
0
0.8
0.16
0.24
0.31 m/s
x
z
z
5 mm
10 mm
15 mm
20 mm

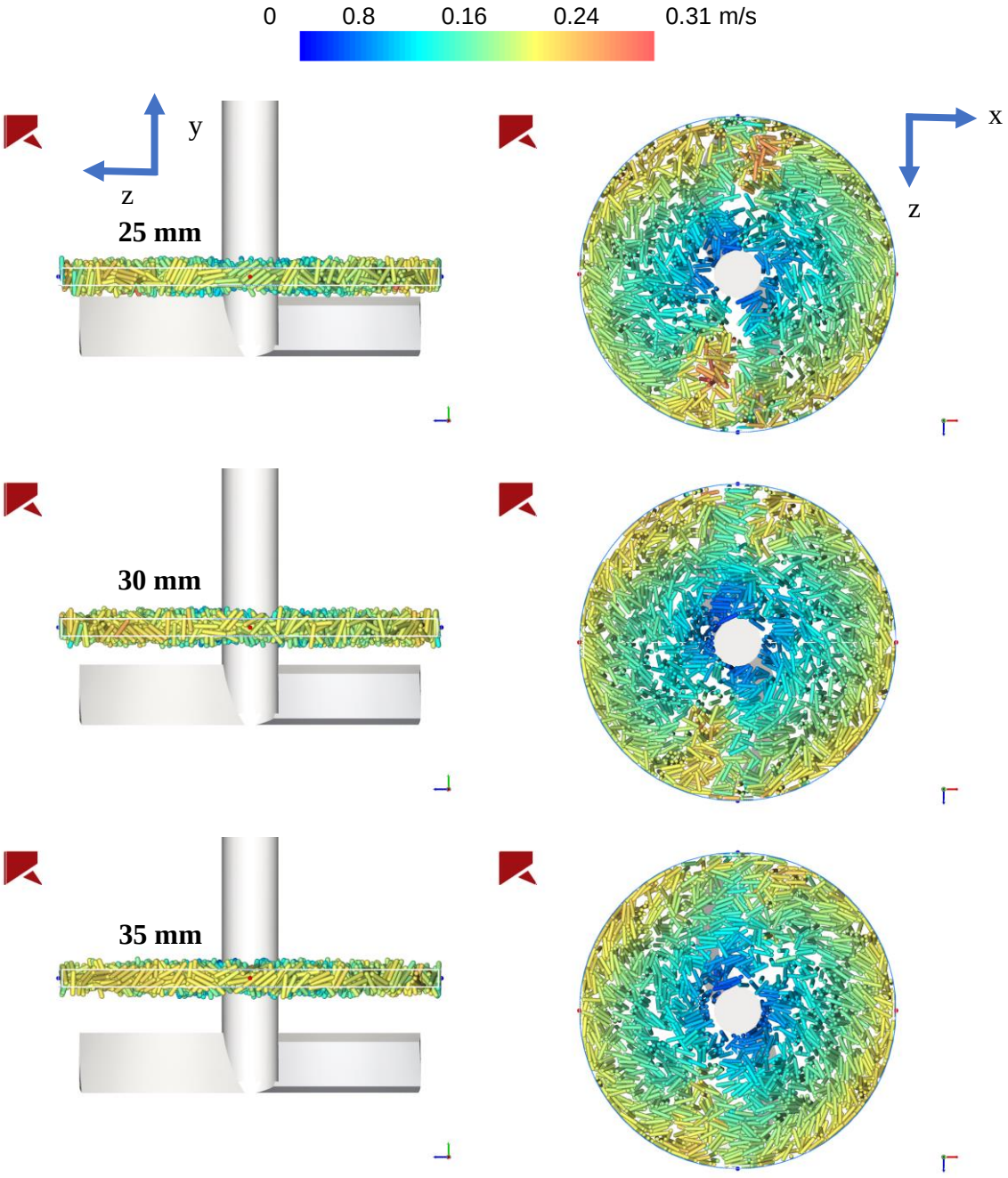

Figure 8-8 Velocity gradient of particles across the horizontal direction of the bed at different heights

8.2.2 Average Particle Velocity along the Impeller Blade

The average particle velocity along the impeller blade is calculated using the approach discussed earlier in which five measurement bins are created. The average particle velocity in each bin is calculated at different impeller blade positions, relative to the initial position of the blades, where the static measurement bins are created. The average particle velocity calculated for spherical particles is shown in Figure 8-9. Bin 1 is closest to the impeller tip and hence the average particle velocity calculated at different impeller blade positions is the highest. The closer the particles to the centre of the impeller, the lower their average velocity. This is expected because the linear speed of a rotating impeller is dictated by its radius and angular velocity. A relative angle of 0 ° in the plot represents that the measurement bins are right in front of the impeller blade. The further away the impeller blade is from the measurement bins, the lower the average particle velocities. A notable decrease of the average particle velocity is observed when the relative angle between the blade and the measurement bins is increased to 54 °, above which the change of average particle velocity is negligible. This is in line with the observation made earlier by looking at the velocity gradient, that at the stagnant regions that are located at the side of the impeller blade length, the particles are moving at a very low velocity.

The plot of the average particle velocity in each measurement bin calculated for rounded cylinders with length to width ratio of 5 shows a very different trend compared to the one for spherical particles (Figure 8-10). The difference between each consecutive measurement bins is smaller and unlike spherical particles, no sudden plummet of average particle velocity is seen in the case for rounded cylinder, suggesting that the whole particle bed is moving and there is no stagnant region within the bed. This agrees with the concentric velocity gradient profile observed for rounded cylinder in the previous section, further showing the role of particle shape in the particle bed dynamics. A further analysis involving rounded cylinders of length to width ratio of 3 reveals a plot of average particle

velocity, where the trend is very similar to the spherical particles, as shown in Figure 8-11. However, the effective relative angle of the particles from the impeller above which the average particle velocity is asymptotic is increased to 72 ° from 54 °. This indicates that the particles rearrange their orientation when their length to width ratio is decreased.

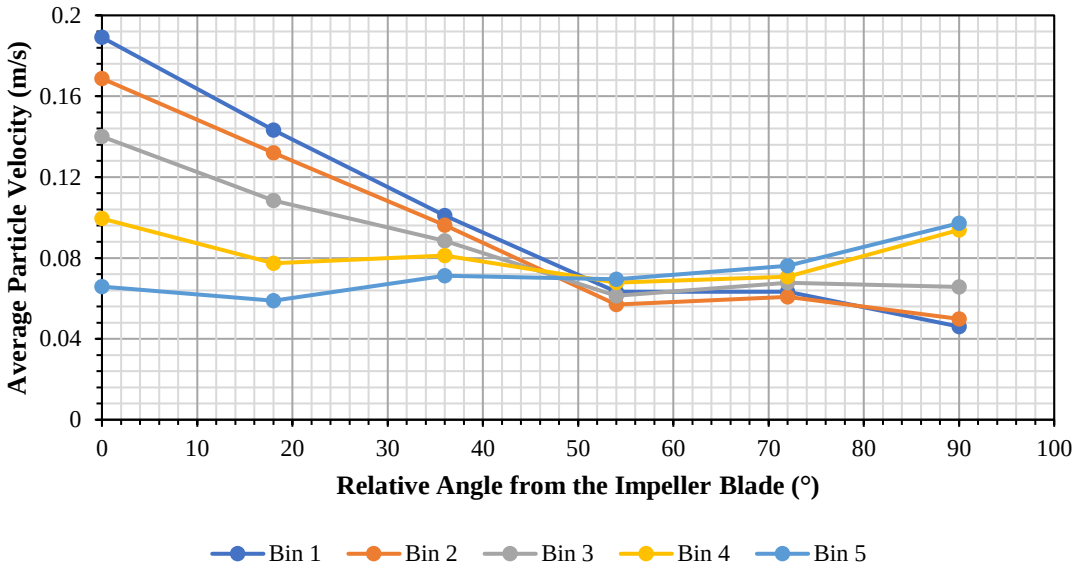

Figure 8-9 Average particle velocity in the measurement bin (spheres)

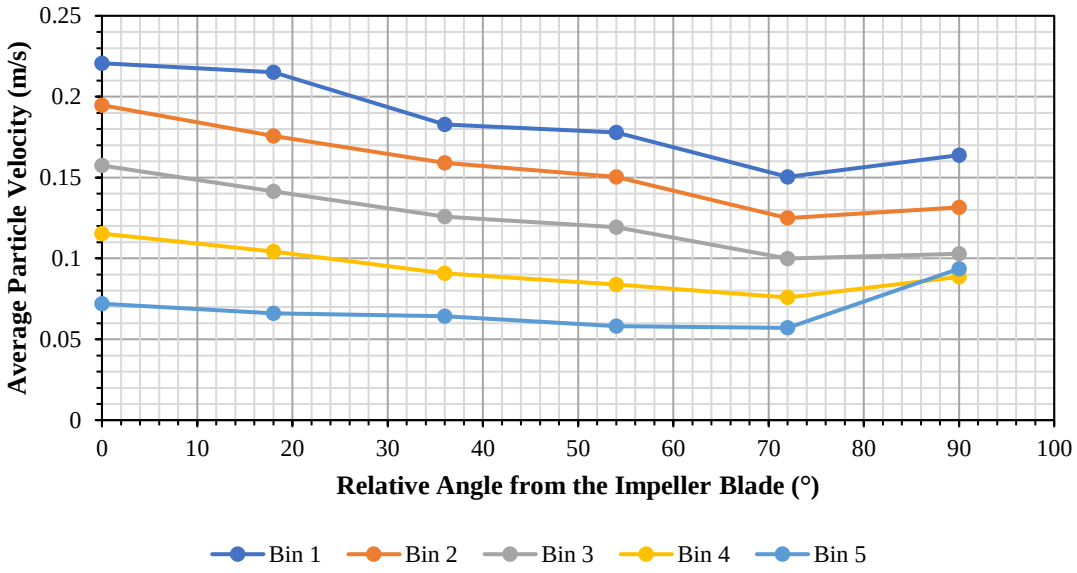

Figure 8-10 Average particle velocity in the bin (rounded cylinder, length to width ratio = 5)

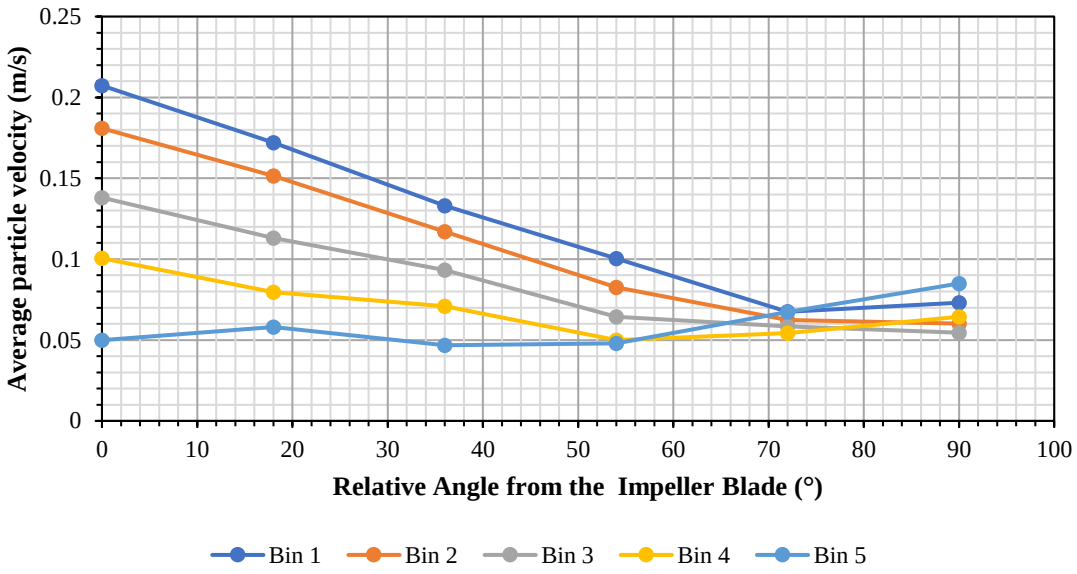

Figure 8-11 Average particle velocity in the bin (rounded cylinder, length to width ratio = 3)

8.2.3 Bed Packing

The void fraction of the static (when the vessel is first filled) and agitated beds for different particle length to width ratios is shown in Figure 8-12. A bed made with spherical particles (length to width ratio 1) appears to have a void fraction of 0.5 during static state. As the particle length to width ratio increases, the void fraction of the bed decreases initially. A minimum void fraction value is observed when the particle length to width ratio is 1.5. A further increase in the particle length to width ratio increases the void fraction. While the bed is agitated, higher void fractions of the particle bed are observed, suggesting that the bed is dilated when it is in motion. The arrangement of particles at the middle of the bed (cross sectional view at XY plane) when it is static (0 s) and agitated (5 s) is shown in Figure 8-13. At low length to width ratio from 1 to 1.75, the particle arrangement appears random for both static and dynamic cases. As the particle length to width ratio approaches 2, the tendency of the particles to reorientate themselves and align with the neighbouring particles becomes prevalent for both static and dynamic

cases. As the particle length to width ratio increases, the number of particles that cluster together increases as well. The effect is most significant and can be seen clearly for the case of particles with length to width ratio of 5. Even when the bed is agitated, the phenomenon of particles clustering as groups still prevails.

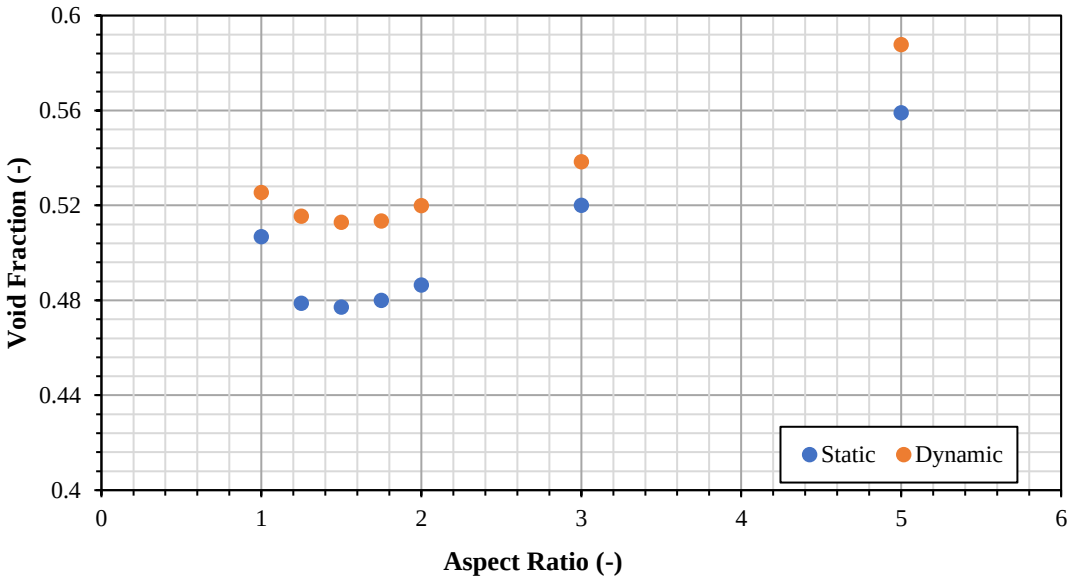

Figure 8-12. Void fraction for particle beds with different particle length to width ratios

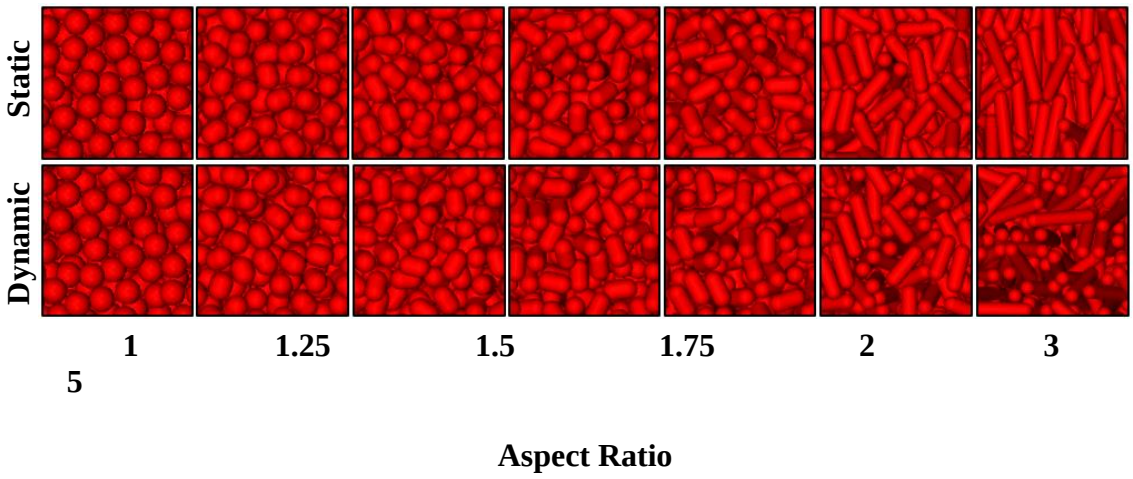

Figure 8-13 Particle arrangement in static and dynamic beds (cross sectional View at XY plane)

8.2.4 Impeller Torque

The impeller torque data obtained for the mono-sized particles are shown in Figure 8-14. A high torque is observed at the initial period when the impeller starts rotating. This is

due a number of reasons: (i) rapid acceleration of the impeller that immediately achieves the required velocity, (ii) particle bed dilation and (iii) ordering of crystalline-like structure that occurs when the particles are mono-sized. As the particle bed starts to move, the torque reduces and begins to plateau. Increasing the particle length to width ratio increases the impeller torque. However, for particle length to width ratios more than 1.5, the torque does not increase significantly with the length to width ratio. A plot of the average impeller torque versus the length to width ratio shows a better visualisation of the trend (Figure 8-15). The impeller torque increases fast initially and then beyond the particle length to width ratio of around 2, further rises are minor, suggesting that there is a limiting particle length to width ratio beyond which there is no significant effect on the impeller torque. Visual observation from Figure 8-13 suggested that the particles tend to align themselves and form groups of clusters that have preferred orientation when the length to width ratio is more than 1.75, which could potentially explain the trend observed. However, higher fluctuations of the impeller torque are observed as the particle length to width ratio increases and this could be attributed to the fact that particles with higher length to width ratio have a higher tendency of jamming.

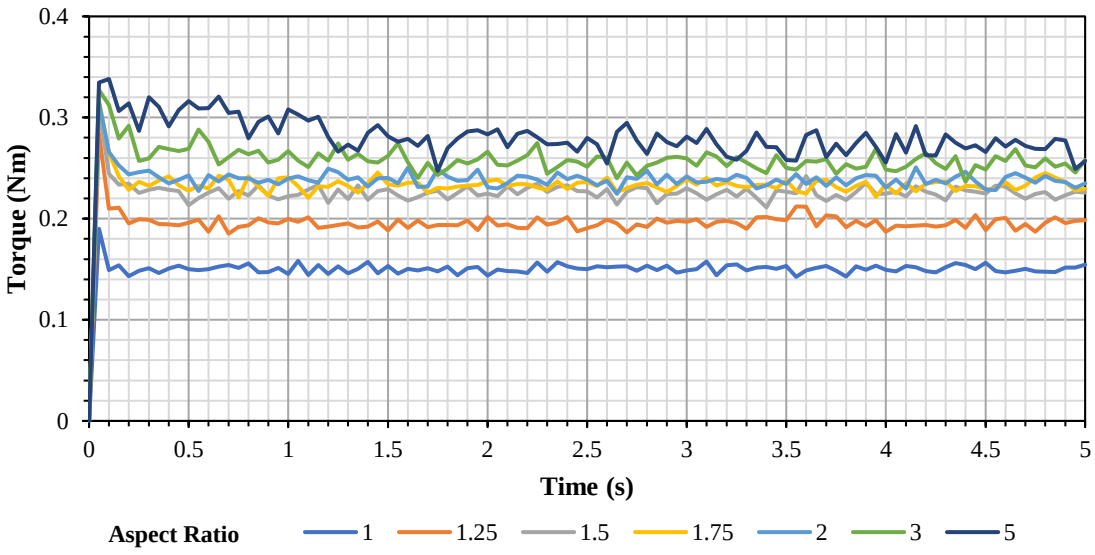

Figure 8-14 Impeller torque as a function of time for particle beds with different particle length to width ratios

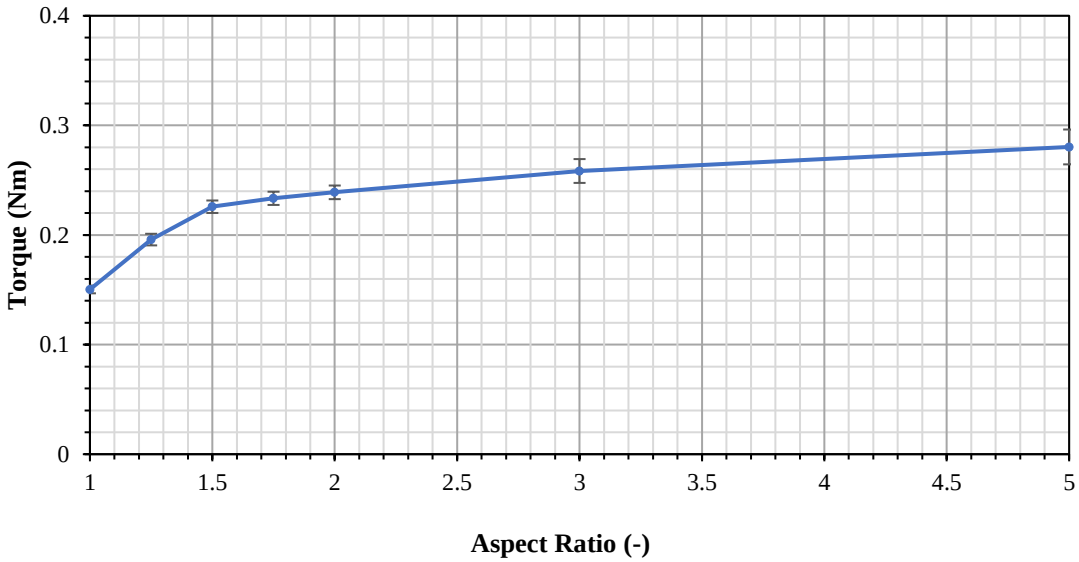

Figure 8-15 Average impeller torque versus particle length to width ratio

8.2.5 Principal and Deviatoric Stresses

When the impeller is rotating at 60 RPM, for every 0.5 s, a blade comes into direct contact with the measurement bins. The region in front of the blade is constantly being compressed, sheared and pushed over the blade to a region behind it where the particle bed is relaxed. The deviatoric stresses experienced at the region nearest to the wall (bin 1) over time are shown in Figure 8-16. As the blade approaches the bins, an increase in the deviatoric stresses is observed. Upon reaching a maximum value, the deviatoric stresses decrease as the blade moves past the measurement bins. This cyclical event is observed for every measurement bin for both principal and deviatoric stresses, but the results are not shown here. The average principal and deviatoric stresses experienced at the regions near the vessel wall (bin 1) and near the impeller shaft (bin 5) are shown in Figure 8-17 and Figure 8-18. The principal stresses increase with the increase of particle length to width ratio for both the regions near the vessel wall and near the impeller shaft but the rate of increase is different. Similar trend is observed for deviatoric stresses.

Compared to bin 5, a substantial increase of stresses (6 times) is observed at bin 1 as the particle length to width ratio is increased. This suggests that the particles are subjected to different extents of stresses at different radial positions. Both principal and deviatoric stresses show fluctuations as the particle length to width ratio is increased.

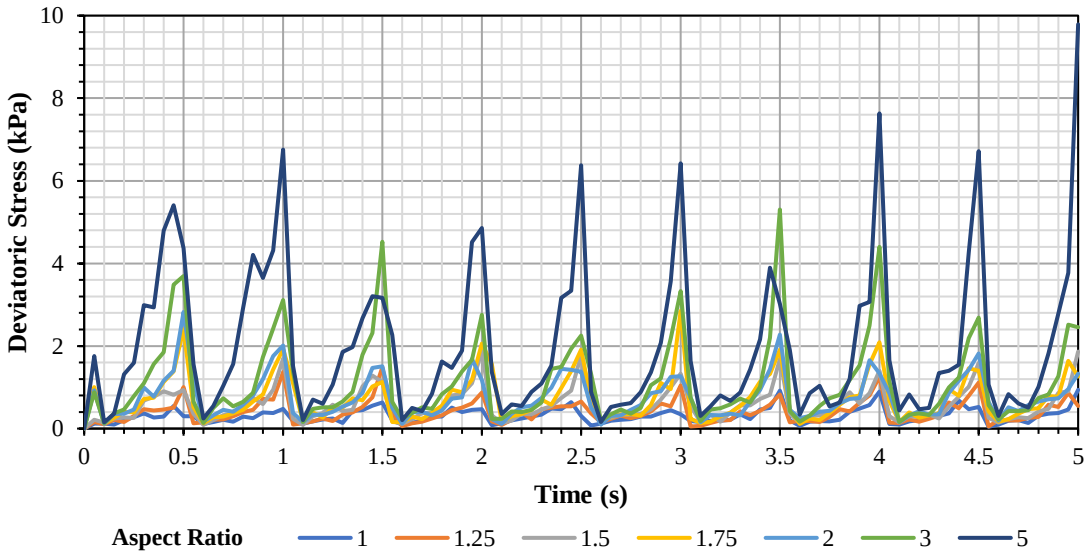

Figure 8-16 Deviatoric stress experienced at the region near the wall over time

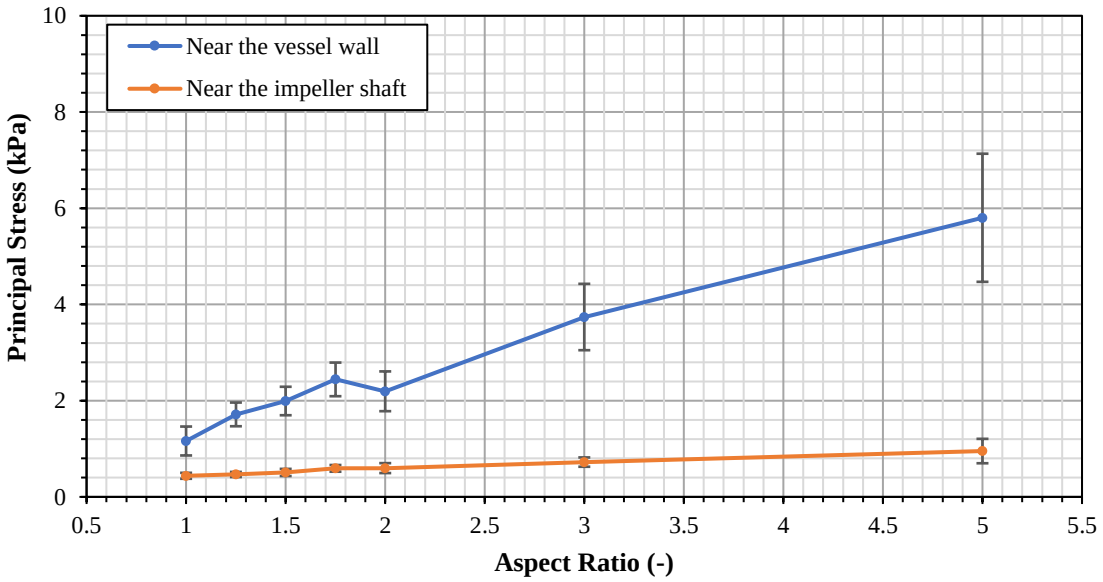

Figure 8-17 Average principal stress at the regions near the shaft and near the vessel wall

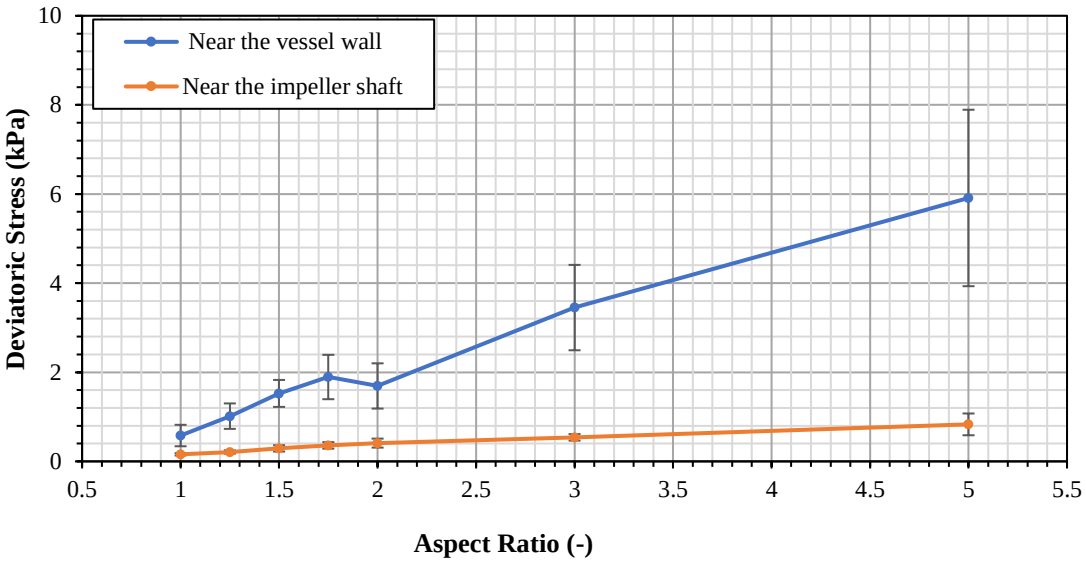

Figure 8-18 Average deviatoric stress at the regions near the shaft and near the vessel wall

8.2.6 Strain Rate Analysis

The normalised strain rate (using Eq. 8-12) increases linearly with the radial position of the particles as shown in Figure 8-19. This is expected as the linear speed along the blade increases with its radius. The particle length to width ratio, however, does not show any significant effect on the strain rate. The variation of the non-dimensionless strain rate is negligible within every measurement bin.

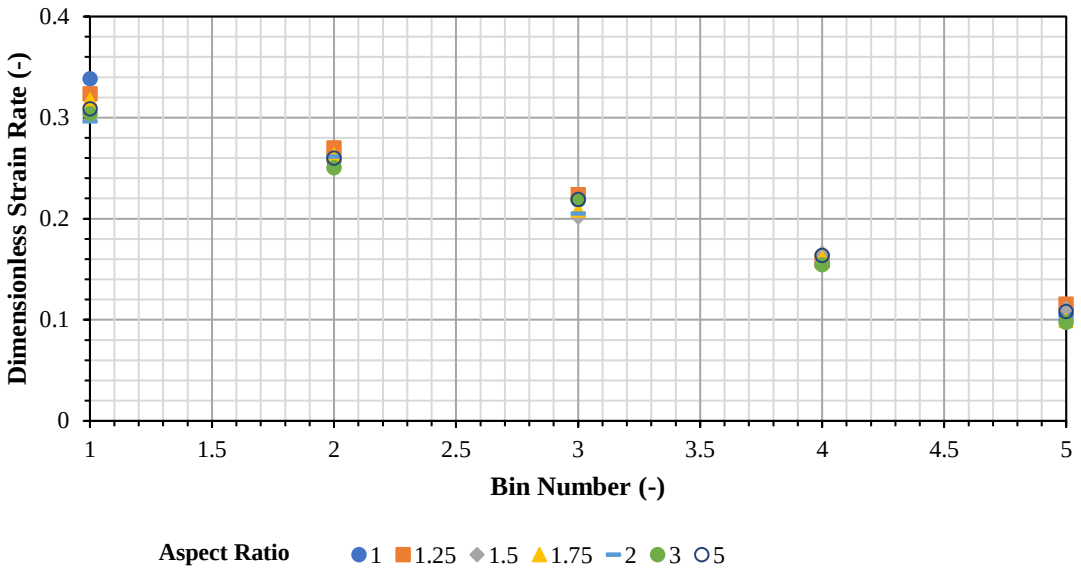

Figure 8-19 Relationship between strain rate and radial position of the particles

8.3 Effect of Particle Size Distribution

The effect of particle size distribution on the stress distribution and particle bed packing is studied by using four different particle size distributions of both spheres and rounded cylinder with length to width ratio of 5 as shown in Table 8-2. PSD 1 is mono size, which the rest has different cumulative percentages as shown.

Table 8-2. Particle size distributions used

Particle Size (mm)	Cumulative Percentage (%)			
	PSD 1	PSD 2	PSD 3	PSD 4
3.5	-	100	100	100
3	100	90	85	80
2.5	-	10	15	20

The void fraction of the powder bed when it is agitating is shown in Figure 8-20. As can be seen, changing the distribution does not change the void fraction of the particle bed. Similar trend is observed where there seems to be an optimal length to width ratio where the powder bed packing is the densest. Above that, the void fraction increases again when the particle length to width ratio is increased.

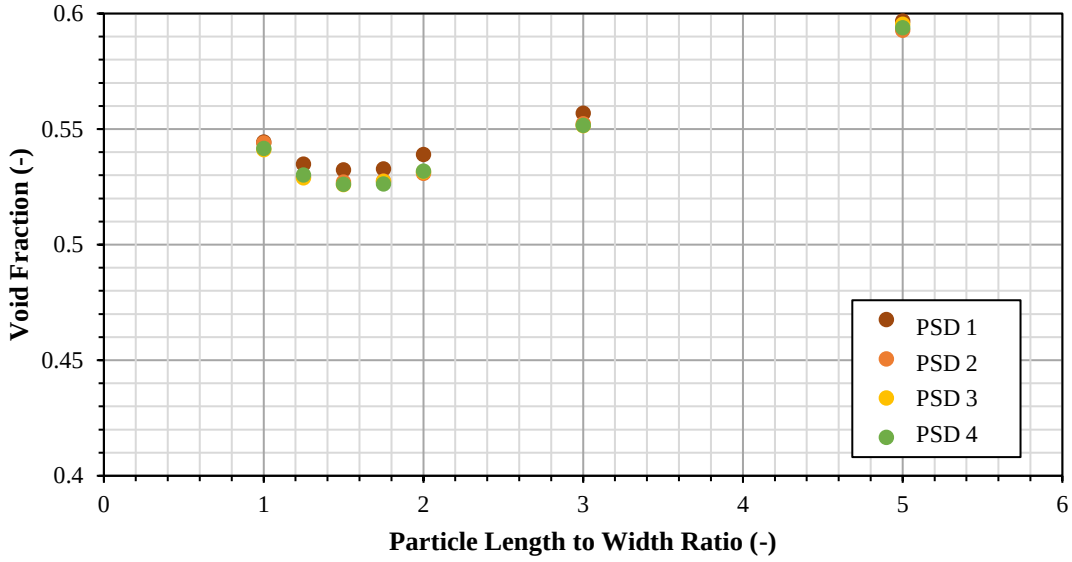

Figure 8-20 Void fraction of agitating particle bed made of particles with different size distributions

The average principal and deviatoric stress in the bin closest to the vessel wall (Bin 1) is calculated for each PSD and is shown in Figure 8-21. Compared to the mono-size particles, the other PSDs show higher average principal and deviatoric stresses. However, the difference amongst the PSDs, excluding mono-size particles, is negligible, indicating the particle size distributions tested in this work has no significant effect on the prevailing stresses in the particle bed.

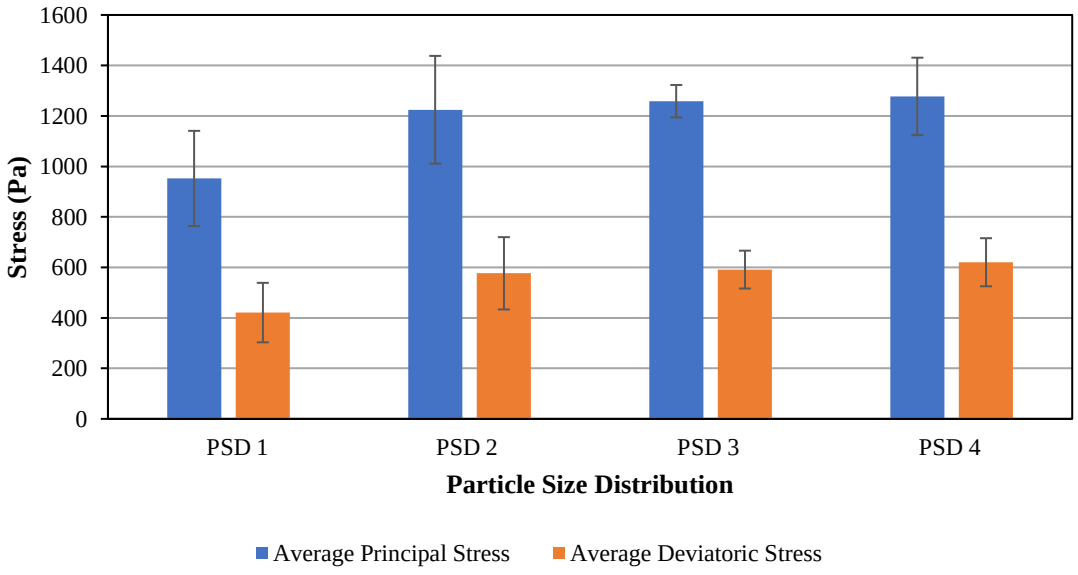

Figure 8-21 Average principal and deviatoric stresses vs different particle size distributions

8.4 Effect of Impeller Speed

The effect of impeller speed on the particle bed packing is shown in Figure 8-22. Increasing the impeller rotational speed does not increase the void fraction of the particle bed at the region above the impeller blade. The same trend is observed for spherical particles and rounded cylinder with an length to width ratio of 5. The dimensionless strain rate for spherical particles at each measurement bin at different impeller rotational speed is shown in Figure 8-23. It can clearly be seen that the strain rate of particles in front of the impeller blades is a function of the impeller rotational speed. The dimensionless strain rate increases with the impeller rotational speed. The strain rate at bin 1, which is closest to the vessel wall is the highest and it decays when it gets closer to the centre of the impeller. The same trend is observed for rounded cylinder with length to width ratio of 5 (Figure 8-24).

The stress analysis performed on bin 1 at different impeller rotational speeds for spherical particles is shown in Figure 8-25. It can be seen that the stresses, both average principal and deviatoric, remain asymptotic even when the impeller rotational speed is increased from 30 to 120 RPM. This suggest that the stresses experienced by the particles in an agitated bed is independent of the impeller tip speed. This holds true as long as the velocities tested are within the same flow regime, which in this case is quasi-static. The prevailing stresses are expected to behave very differently in the case where, the flow regime changes from quasi-static, to intermediate or rapid flow. Similar analysis is performed on the rounded cylinder and the results are shown in Figure 8-26. The stresses calculated, however, are very erratic and does not show a very clear trend. At 60 RPM the stresses increase but reduces when the impeller rotational speed is increased to 90 RPM. The reason for the trend is due to restructuring of the particle orientations with the strain rate.

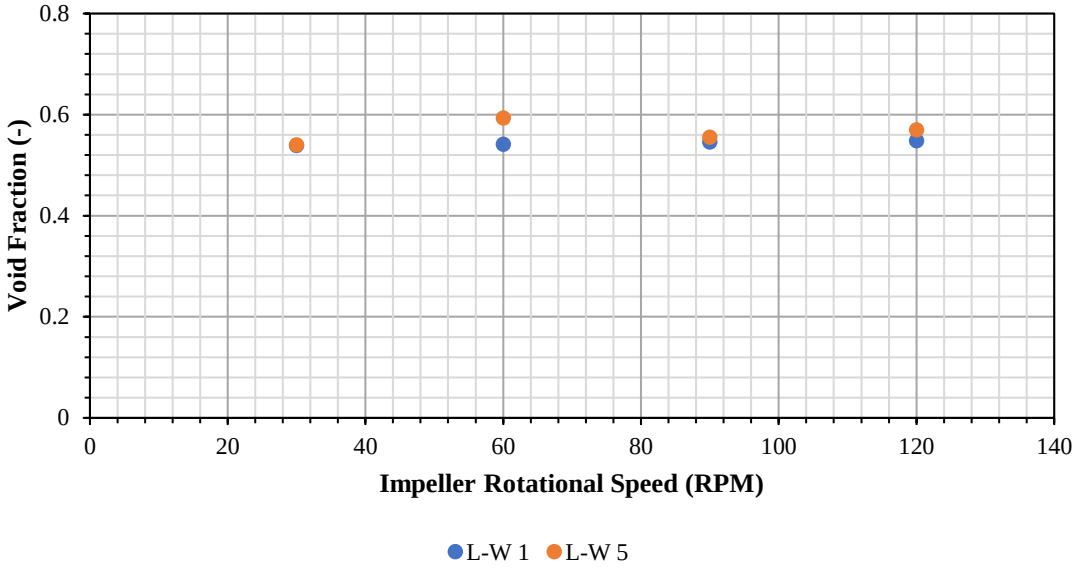

Figure 8-22 Void fraction vs impeller rotational speed

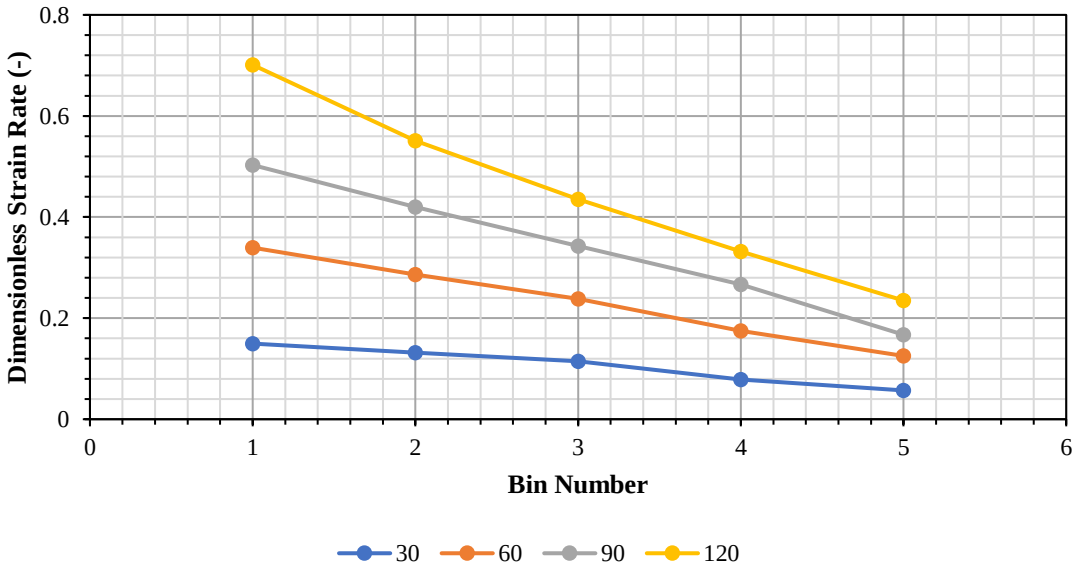

Figure 8-23 Relationship between dimensionless strain rate and impeller rotational speed (spheres)

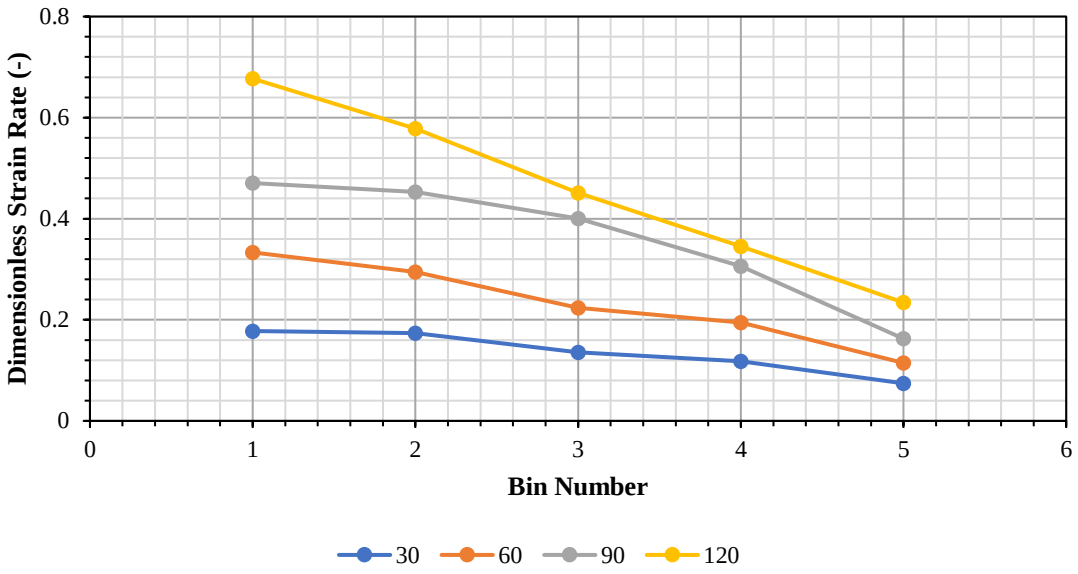

Figure 8-24 Relationship between dimensionless strain rate and impeller rotational speed (rounded cylinder)

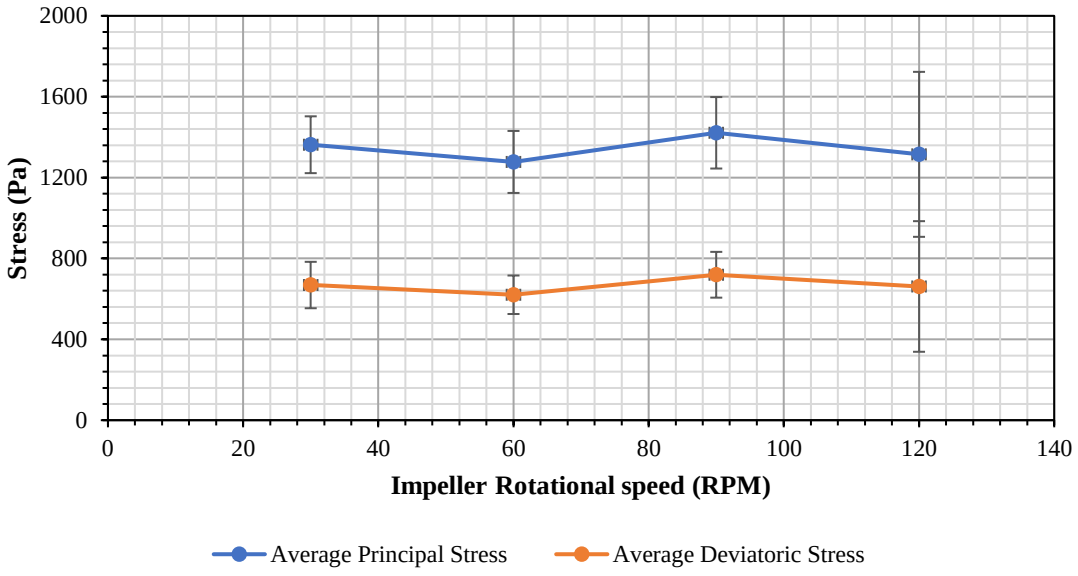

Figure 8-25 Average principal and deviatoric stresses at bin 1 at different impeller rotational speeds (spheres)

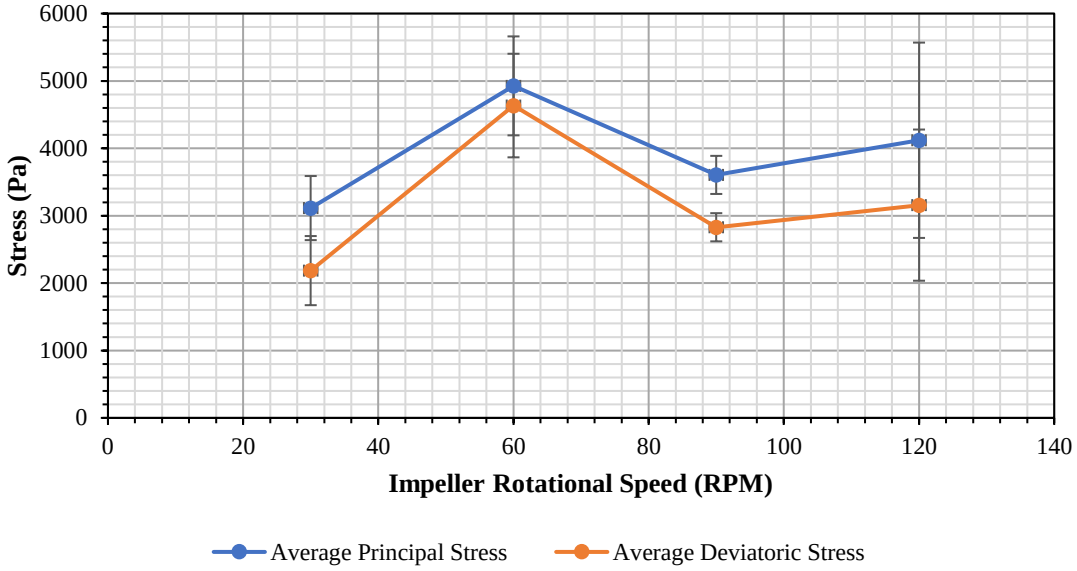

Figure 8-26 Average principal and deviatoric stresses at bin 1 at different impeller rotational speeds (rounded cylinder)

8.5 Conclusions

The velocity gradient profiles of spheres and rounded cylinders in the agitated filter bed dryer simulated in this work are very different from each other. The analysis reveals that there exist some stagnant regions in the particle bed of spheres that the particles are moving with relatively low speed. On the contrary, such stagnant region is not seen in particle bed made of rounded cylinders with high length to width ratio and all the particles tend to move together as a block. The packing of particle beds under shear deformation by an impeller is assessed using DEM for different particle length to width ratios of rounded cylinders from 1 to 5 and also for spherical particles for comparison. The void fractions of both static and agitated beds are calculated and compared. The beds undergo compression and dilation when being agitated. The impeller torque, which is a measure of the resistance of the bed to flow, is found to increase with the particle length to width ratio initially and it then reaches a plateau. Both principal and deviatoric stresses are evaluated at the regions of interest and are found to increase along the radial position. The simulation is further extended to study the effect of particle size distribution on the particle bed packing and the prevailing stresses in the particle bed. Changing the particle size distribution within the narrow range tested does not change the void fraction of the particle bed. The same applies to the prevailing stresses. Changing the particle size distribution does not incur a significant change in the average principal and deviatoric stresses. The impeller rotational speed is found to have no effect on the void fraction calculated for the agitating bed, both in the cases of spheres and rounded cylinder, presumably being in the quasi-static regime. The dimensionless strain increases with the radial position. The prevailing stresses in the particle beds of spheres and rounded cylinders are found to be independent on the impeller rotational speed. DEM technique has proven to be a very useful tool for investigating industrial processes involving

granular materials. The DEM simulations performed in this work have allowed the stress and strain distributions within the agitated particle bed to be investigated which are very difficult to obtain experimentally.

Chapter 9

Conclusions and Future Work

1.4 Conclusions

Attrition and phase changes during agitated filter bed drying is a complex process. Experimental work is coupled with simulation to study the breakage behaviour and dehydration as well as rehydration of carbamazepine dihydrate. The effects of mechanical and thermal stresses on the phase transformation of CBZ.2H_2O crystals have been investigated. Subjecting the crystals to impact and bulk crushing both yield a noticeable amount of crystal breakage, but no polymorphic transformation is observed.

CBZ.2H_2O is found to be susceptible to thermal stresses and dehydrates very easily at elevated temperature above 40 °C. The coupled effect of thermal and mechanical stresses is investigated, and the results show that CBZ.2H_2O crystals dehydrate readily when being stressed thermally but not mechanically. Subjecting partially dehydrated crystals to mechanical stresses does not increase the transformation rate of the hydrate to anhydrous carbamazepine.

The dehydration and rehydration of carbamazepine dihydrate are studied in this work. DVS experiments at 10% RH step suggest that the dehydration commences at below 10% RH and the rehydration of the dehydrated carbamazepine is dictated by the sorption temperature. The higher the temperature, the higher the critical RH for

dehydration. SEM analysis reveals macroscopic structural difference of CBZ.2H_2O dehydrated at different temperatures. As the temperature is increased, secondary crystal domains are found growing on the crystal surfaces and have been identified as Form I "whiskers" through PXRD. Further experiments involve subjecting the dehydrated crystals to 98% RH and found that the crystals are able to pick up water that is equivalent to the crystal water loss, indicating transformation back to the hydrate form of carbamazepine. At RH lower than 90%, the rehydration of carbamazepine is limited by the temperature. That limitation is broken when the surrounding air is saturated with water vapour, at 98% RH. The dehydration of CBZ.2H_2O has also been studied by ramping the RH from 90 to 0% at different ramping rate. There exists a transition region (~5-7 % RH) where the rate of dehydration changes significantly. The sorption and rehydration of dehydrated carbamazepine have also been studied using vapour sorption method. Ramping the RH from 0 to 100% reveals a series of transformation events of the dehydrated carbamazepine. The change of the crystal affinity to water suggests a polymorphic transformation of the dehydrated crystals.

A new assessment technique has been used to study the breakability of acicular particles of carbamazepine dihydrate using the G3 Morphologi dry dispersion to cause impact breakage. The shift of particle size, length, width and aspect ratio are analysed, indicating that carbamazepine dihydrate tend to break along their largest dimension, due to bending arising from the geometric effect of the high aspect ratio and in spite of the presence of cleavage planes. The breakability index of carbamazepine dihydrate is determined by plotting the graph of R^* versus $\sum_{i=1}^{n} \rho D U^2$, where a non-linear relationship is noted. There exists a transition point at which the rate of change the particle size is reduced, corresponding to a switch in the breakage mode. The first breakability index is higher than the second one and corresponds to the snapping of the particles along

their length, while the latter smaller one is associated with chipping. This work demonstrates that by using a combination of image analysis and modified impact breakage model, the role of crystal structure properties, particularly the existence of cleavage planes, together with the physical geometric properties on the breakage behaviour of carbamazepine dihydrate crystals can be isolated and studied individually.

A new test rig to simulate agitated filter bed drying has been developed in collaboration with Freeman Technology using their existing FT4 powder rheometer. The device performs the essential features that an agitated filter bed dryer has. A systematic study of the effect of process parameters on the breakage of equant particles of sodium chloride shows that impeller clearance has a significant effect on the breakage of sodium chloride. Impeller tip speed has little effect on the fractional broken mass, R^* calculated, but a full-size analysis shows a difference in the size distribution of the broken crystals. Chipping seems to be the dominant breakage mode here as plenty of chips are generated and the corner of the broken crystals appears to be rounded off. A strong linear relationship is found between the number of impeller revolution and extent of particle breakage of sodium chloride. The higher the number of revolutions, the higher the extent of particle breakage. The new AFBD unit is also used to assess the breakage of carbamazepine dihydrate crystals which are acicular and platy. Impeller tip speed is influential to the breakage of carbamazepine dihydrate, even though the change of R^* is not huge across the velocity range tested. Increasing the number of impeller revolutions increases the extent of breakage of carbamazepine dihydrate. R^* increases significantly when vacuum suction is applied as now additional drag force is exerted on the powder bed. Solvent content is another major factor in AFBD that could cause significant particle breakage as demonstrated here with carbamazepine and water. Agitating the powder bed at high solvent content causes significant particle breakage of carbamazepine. When the solvent content is lowered, the breakage of the crystals is reduced proportionally as the

attraction force between the particles is reduced. The mechanical energy transferred from the impeller to the powder bed is calculated from the torque profile and related to the extent of particle breakage in an agitated filter bed dryer. It is found that the higher the energy input, the higher the extent of particle breakage.

DEM simulation is used to study the effect of particle shape in an agitated filter bed dryer. The velocity gradient profiles of spheres and rounded cylinders are very different from each other. The analysis reveals that there exist some stagnant regions in the particle bed of spheres that the particles are moving with very low speed. On the contrary, such stagnant region is not seen in particle bed made of rounded cylinder with high length to width ratio and all the particles tend to move together as a block. The packing of particle beds under shear deformation by an impeller is assessed using DEM for different particle length to width ratios of rounded cylinders from 1 to 5 and also for spherical particles for comparison. Both principal and deviatoric stresses are evaluated at the regions of interest and are found to increase along the radial position. The simulation is further extended to study the effect of particle size distribution on the particle bed packing and the prevailing stresses in the particle bed. Changing the particle size distribution does not change the void fraction of the particle bed within the size range tested (2.5 – 3.5 mm). The same applies to the prevailing stresses. Changing the particle size distribution does not incur a significant increase or decrease of the average principal and deviatoric stresses. The dimensionless strain rate is a function of the impeller rotational speed and it increases with the radial position. The prevailing stresses in the particle beds of spheres and rounded cylinders are found to be independent on the impeller rotational speed. No significant change is observed.

9.1 Future Work

The work of dehydration and rehydration of carbamazepine reveals some very interesting observations. The only information available right now is gravimetric. An in-situ PXRD analysis under controlled environmental conditions is recommended to provide complementary data to support the DVS results.

The new impact breakage assessment technique developed should be tested with different materials with varying crystal structure. The current analysis is limited to acicular crystals but could be extended to equant particles. The breakability of the materials obtained can be compared with other methods such as single particle impact tester.

The breakage of carbamazepine dihydrate in an agitated filter bed dryer is studied. However, the effect of temperature and moisture content are not considered fully in this work. It is hence proposed here that this work could be extended to study the effect of temperature on the particle breakage as the particle bed is agitated. The newly developed AFBD test rig can also be used for drying studies of materials.

Particle breakage is not simulated in the DEM simulation performed as that will require substantially longer simulation time. The GPU technology has become more mature nowadays, further simulation work could attempt to incorporate breakage in the DEM simulation of an agitated filter bed dryer.

The suggestions above would further enhance the understanding the breakage and polymorphic transformation of particles in an agitated filter bed dryer.

References

Aitipamula, S., Banerjee, R., Bansal, A.K., Biradha, K., M.L., C. and Choudhury, A.R. 2012. Polymorphs, Salts, and Cocrystals: What's in a Name? *Crystal Growth & Design*. **12**, pp.2147–2152.

Ali, M. and Ghadiri, M. 2017. Analysis of triboelectric charging of particles due to aerodynamic dispersion by a pulse of pressurised air jet. *Advanced Powder Technology*. **28**(10), pp.2735–2740.

ANSYS® Academic Research. 2017. Ansys Fluent.

Arlin, J.B., Price, L.S., Price, S.L. and Florence, A.J. 2011. A strategy for producing predicted polymorphs: Catemeric carbamazepine form v. *Chemical Communications*. **47**(25), pp.7074–7076.

Arrhenius, s 1889. Über die Dissociationswärme und den Einfluss der Temperatur auf den Dissociationsgrad der Elektrolyte. *Zeitschrift für Physikalische Chemie*. [Online]. **4U**,p.96.

Bagi, K. 1996. Stress and strain in granular assemblies. **22**, pp.165–177.

Bagster, D.F. and Bridgwater, J. 1970. The Flow of Granular Material over A Moving Blade. *Powder Technology*. **3**(1), pp.323–338.

Barr, A.H. 1981. Superquadrics and Angle-Preserving Transformations. *IEEE Computer Graphics and Applications*. **1**(1), pp.11–23.

Bauer, J., Spanton, S., Henry, R., Quick, J., Dziki, W., Porter, W. and Morris, J. 2001. Ritonavir: An Extraordinary Example of Conformational Polymorphism.

Pharmaceutical Research. [Online]. **18**(6), pp.859–866.

Bauer, J.F. 2009. Drying Pharmaceutical Solids-Hydrates and Enantiotropic Polymorphs. *Journal of Validation Technology*. **15**(2), p.49.

Bauer, J.F. 2008. Polymorphism-A Critical Consideration in Pharmaceutical Development, Manufacturing, and Stability. *Journal of Validation Technology*. **14**(4), pp.15–23.

Bonakdar, T., Ali, M., Dogbe, S., Ghadiri, M. and Tinke, A. 2016. A method for grindability testing using the Scirocco disperser. *International Journal of Pharmaceutics*. **501**(1–2), pp.65–74.

Broitman, E. 2017. Indentation Hardness Measurements at Macro-, Micro-, and Nanoscale: A Critical Overview. *Tribology Letters*. **65**(1), pp.1–18.

Buckton, G. and Darcy, P. 1995. The use of gravimetric studies to assess the degree of crystallinity of predominantly crystalline powders. *International Journal of Pharmaceutics*. **123**(2), pp.265–271.

Buckton, G. and Darcy, P. 1996. Water mobility in amorphous lactose below and close to the glass transition temperature. *International Journal of Pharmaceutics*. **136**(1–2), pp.141–146.

Buist, A.R., Edgeley, D.S., Kabova, E.A., Kennedy, A.R., Hooper, D., Rollo, D.G., Shankland, K. and Spillman, M.J. 2015. Salt and Ionic Cocrystalline Forms of Amides: Protonation of Carbamazepine in Aqueous Media. *Crystal Growth and Design*. **15**(12), pp.5955–5962.

Buist, A.R., Kennedy, A.R., Shankland, K., Shankland, N. and Spillman, M.J. 2013. Salt forms of amides: Protonation and polymorphism of carbamazepine and cytenamide. *Crystal Growth and Design*. **13**(11), pp.5121–5127.

Burnett, D.J., Thielmann, F. and Booth, J. 2004. Determining the critical relative humidity for moisture-induced phase transitions. . **287**, pp.123–133.

Cares-Pacheco, M.G., Calvet, R., Vaca-Medina, G., Rouilly, A. and Espitalier, F. 2015. Inverse gas chromatography a tool to follow physicochemical modifications of pharmaceutical solids: Crystal habit and particles size surface effects. *International Journal of Pharmaceutics*. **494**(1), pp.113–126.

Cares-Pacheco, M.G., Vaca-Medina, G., Calvet, R., Espitalier, F., Letourneau, J.J., Rouilly, A. and Rodier, E. 2014. Physicochemical characterization of d-mannitol polymorphs: The challenging surface energy determination by inverse gas chromatography in the infinite dilution region. *International Journal of Pharmaceutics*. **475**(1–2), pp.69–81.

Carr, J.F. and Walker, D.M. 1968. An annular shear cell for granular materials. *Powder Technology*. **1**(6), pp.369–373.

Cho, G., Dodds, J. and Santamarina, J.C. 2006. Particle Shape Effects on Packing Density , Stiffness , and Strength : Natural and Crushed Sands. . **132**(May), pp.591–602.

Chou, S.H. and Hsiau, S.S. 2011. Experimental analysis of the dynamic properties of wet granular matter in a rotating drum. *Powder Technology*. **214**(3), pp.491–499.

Cleary, P. 2001. Modelling comminution devices using DEM. *International Journal for Numerical and Analytical Methods in Geomechanics*. **25**(1), pp.83–105.

Coats, A.W. and Redfern, J.P. 1963. Thermogravimetric Analysis. A Review. *The Analyst*. **88**(1053), pp.906–924.

Cundall, P.A. and Strack, O.D.L. 1979. A discrete numerical model for granular assemblies. *Geotechnique*. **1**, pp.47–65.

Datta, A. and Rajamani, R.K. 2002. A direct approach of modeling batch grinding in ball

mills using population balance principles and impact energy distribution. *International Journal of Mineral Processing*. **64**(4), pp.181–200.

Delaney, G.W., Morrison, R.D., Sinnott, M.D., Cummins, S. and Cleary, P.W. 2015. DEM modelling of non-spherical particle breakage and flow in an industrial scale cone crusher. *Minerals Engineering*. **74**, pp.112–122.

Descamps, M., Aumelas, A., Desprez, S. and Willart, J.F. 2015. The amorphous state of pharmaceuticals obtained or transformed by milling: Sub-Tg features and rejuvenation. *Journal of Non-Crystalline Solids*. **407**, pp.72–80.

Desprez, S. and Descamps, M. 2006. Transformations of glassy indomethacin induced by ball-milling. *Journal of Non-Crystalline Solids*. **352**(42–49), pp.4480–4485.

Duncan-Hewitt, W.C. and Weatherly, G.C. 1989. Evaluating the Deformation Kinetics of Sucrose Crystals Using Microindentation Techniques. *Pharmaceutical Research*. **6**(12), pp.1060–1066.

Duncan-Hewitt, W.C. and Weatherly, G.C. 1989. Evaluating the Deformation Kinetics of Sucrose Crystals Using Microindentation Techniques. *Pharmaceutical Research: An Official Journal of the American Association of Pharmaceutical Scientists*. **6**(12), pp.1060–1066.

Fischer-Cripps, A.C. 2011. *Nanoindentation*.

Gan, Z., Abe, H. and Doi, Y. 2002. Temperature-induced polymorphic crystals of poly(butylene adipate). *Macromolecular Chemistry and Physics*. **203**(16), pp.2369–2374.

Ganser, G.H. 1993. A rational approach to drag prediction of spherical and nonspherical particles. *Powder Technology*. **77**(2), pp.143–152.

Garnier, S., Petit, S. and Coquerel, G. 2002. Dehydration mechanism and crystallisation

behaviour of lactose. *Journal of Thermal Analysis and Calorimetry*. **68**(2), pp.489–502.

Ghadiri, M. 2006. Particle Impact Breakage *In*: H. Masuda, K. Higashitani and H. Yoshida, eds. *Powder Technology Handbook*. CRC Press, pp. 205–212.

Ghadiri, M., Bonakdar, T. and Nadimi, S. 2018. Particle breakage in gas phase *In*: *Powder Technology Handbook*. Taylor & Francis.

Ghadiri, M., Ning, Z., Kenter, S.. and Puik, E. 2000. Attrition of granular solids in a shear cell. *Chemical Engineering Science*. **55**(22), pp.5445–5456.

Ghadiri, M. and Zhang, Z. 2002. Impact attrition of particulate solids. Part 1: A theoretical model of chipping. *Chemical Engineering Science*. **57**(17), pp.3659–3669.

Gong, D., Nadolski, S., Sun, C., Klein, B. and Kou, J. 2018. The effect of strain rate on particle breakage characteristics. *Powder Technology*. [Online]. **339**, pp.595–605.

Grzesiak, A.L., Lang, M., Kim, K. and Matzger, A.J. 2003. Comparison of the Four Anhydrous Polymorphs of Carbamazepine and the Crystal Structure of Form I. *Journal of Pharmaceutical Sciences*. **92**(11), pp.2260–2271.

Guises, R., Xiang, J. and Munjiza, J.L.A. 2009. Granular packing : numerical simulation and the characterisation of the effect of particle shape. , pp.281–292.

Guo, Y., Wassgren, C., Ketterhagen, W., Hancock, B. and James, B. 2012. A numerical study of granular shear flows of rod-like particles using the discrete element method. . **713**, pp.1–26.

Gwyn, J.E. 1969. On the Particle Size Distribution Function and the Attrition of Cracking Catalysts. *AIChE Journal*. **15**(1), pp.197–206.

Han, J. and Suryanarayanan, R. 1998. Influence of Environmental Conditions on the

Kinetics and Mechanism of Dehydration of Carbamazepine Dihydrate. *Pharmaceutical Development and Technology*. [Online]. **3**(4), pp.587–596.

Hare, C. and Ghadiri, M. 2015. Attrition of paracetamol and aspirin under bulk shear deformation. *Chemical Engineering Science*. **125**,pp.13–19.

Hare, C., Ghadiri, M. and Dennehy, R. 2011. Prediction of attrition in agitated particle beds. *Chemical Engineering Science*. **66**(20),pp.4757–4770.

Hare, C.L. 2010. Particle Breakage in Agitated Dryers.

Harris, R.K., Ghi, P.Y., Puschmann, H., Apperley, D.C., Griesser, U.J., Hammond, R.B., Ma, C., Roberts, K.J., Pearce, G.J., Yates, J.R. and Pickard, C.J. 2005. Structural studies of the polymorphs of carbamazepine, its dihydrate, and two solvates. *Organic Process Research and Development*. **9**(6), pp.902–910.

Hassanpour, A., Ghadiri, M., Bentham, A.C. and Papadopoulos, D.G. 2004. Effect of temperature on the energy utilisation in quasi-static crushing of α-lactose monohydrate. *Powder Technology*. **141**(3), pp.239–243.

Hickey, M.B., Peterson, M.L., Scoppettuolo, L.A., Morrisette, S.L., Vetter, A., Guzmán, H., Remenar, J.F., Zhang, Z., Tawa, M.D., Haley, S., Zaworotko, M.J. and Almarsson, Ö. 2007. Performance comparison of a co-crystal of carbamazepine with marketed product. *European Journal of Pharmaceutics and Biopharmaceutics*. **67**(1), pp.112–119.

Iveson, S.M., Litster, J.D., Hapgood, K. and Ennis, B.J. 2001. Nucleation, growth and breakage phenomena in agitated wet granulation processes: A review. *Powder Technology*. **117**(1–2), pp.3–39.

Jenike, A.W. 1961. Gravity Flow of Bulk Solids. *Bulletin of the University of Utah*. **52**(29), p.322.

Jensen, R.P., Edil, T.B., Bosscher, P.J., Plesha, M.E. and Kahla, N.B. 2001. Effect of Particle Shape on Interface Behaviour of DEM-Simulated Granular Materials. *International Journal of Geomechanics*. **1**(1), pp.1–19.

Jensen, R.P., Plesha, M.E., Edil, T.B., Bosscher, P.J. and Kahla, N.B. 2001. DEM Simulation of Particle Damage in Granular Media - Structure Interfaces. *International Journal of Geomechanics*. **1**(1), pp.21–39.

Jiménez-Herrera, N., Barrios, G.K.P. and Tavares, L.M. 2018. Comparison of breakage models in DEM in simulating impact on particle beds. *Advanced Powder Technology*. **29**(3), pp.692–706.

Jørgensen, K., Bach, P. and Jensen, A.D. 2005. Impact and attrition shear breakage of enzyme granules and placebo particles-application to particle design and formulation. *Powder Technology*. **149**(2–3), pp.157–167.

Kachrimanis, K. and Griesser, U.J. 2012. Dehydration kinetics and crystal water dynamics of carbamazepine dihydrate. *Pharmaceutical research*. **29**(4), pp.1143–1157.

Khoo, J.Y., Heng, J.Y.Y. and Williams, D.R. 2010. Agglomeration effects on the drying and dehydration stability of pharmaceutical acicular hydrate: Carbamazepine dihydrate. *Industrial and Engineering Chemistry Research*. **49**(1), pp.422–427.

Khoo, J.Y., Shah, U. V., Schaepertoens, M., Williams, D.R. and Heng, J.Y.Y. 2013. Process-induced phase transformation of carbamazepine dihydrate to its polymorphic anhydrates. *Powder Technology*. **236**, pp.114–121.

Kissinger, H.E. 1957. Reaction Kinetics in Differential Thermal Analysis. *Analytical Chemistry*. [Online]. **29**(11), pp.1702–1706.

Klein, C., Hurlbut, C.S. and Dana, J.D. 1985. *Manual of Mineralogy* 20th ed. New York:

Wiley.

Kobayashi, Y., Ito, S., Itai, S. and Yamamoto, K. 2000. Physicochemical properties and bioavailability of carbamazepine polymorphs and dihydrate. *International Journal of Pharmaceutics*. **193**(2), pp.137–146.

Laine, E., Tuominen, V., Ilvessalo, P. and Kahela, P. 1984. Formation of dihydrate from carbamazepine anhydrate in aqueous conditions. *International Journal of Pharmaceutics*. **20**(3), pp.307–314.

Lawn, B.R. and Marshall, D.B. 1979. Hardness, Toughness, and Brittleness: An Indentation Analysis. *Journal of the American Ceramic Society*. **62**(7–8), pp.347–350.

Lee, H., Cho, H. and Kwon, J. 2010. Using the discrete element method to analyze the breakage rate in a centrifugal/vibration mill. *Powder Technology*. **198**(3), pp.364–372.

Lee, Y.Y., Wu, J.X., Yang, M., Young, P.M., Van Den Berg, F. and Rantanen, J. 2011. Particle size dependence of polymorphism in spray-dried mannitol. *European Journal of Pharmaceutical Sciences*. **44**(1–2), pp.41–48.

Lefort, R., Caron, V., Willart, J.-F. and Descamps, M. 2006. Mutarotational kinetics and glass transition of lactose. *Solid State Communications*. **140**(7–8), pp.329–334.

Lekhal, a., Girard, K.P., Brown, M. a., Kiang, S., Glasser, B.J. and Khinast, J.G. 2003. Impact of agitated drying on crystal morphology: KCl-water system. *Powder Technology*. **132**(2–3), pp.119–130.

Lekhal, a., Girard, K.P., Brown, M. a., Kiang, S., Khinast, J.G. and Glasser, B.J. 2004. The effect of agitated drying on the morphology of L-threonine (needle-like) crystals. *International Journal of Pharmaceutics*. **270**(1–2), pp.263–277.

Li, Y., Han, J., Zhang, G.G., Grant, D.J. and Suryanarayanan, R. 2000. In situ dehydration of carbamazepine dihydrate: a novel technique to prepare amorphous anhydrous carbamazepine. *Pharmaceutical development and technology*. **5**(2), pp.257–66.

Liang, X. and Rajesh, D. 2013. Dynamic simulation of particle packing influenced by size , aspect ratio and surface energy., pp.401–415.

Liss, K.-D., Bartels, A., Schreyer, A. and Clemens, H. 2003. High-Energy X-Rays: A tool for Advanced Bulk Investigations in Materials Science and Physics. *Textures and Microstructures*. **35**(3–4), pp.219–252.

Liu, W., Dang, L. and Wei, H. 2013. Thermal, phase transition, and thermal kinetics studies of carbamazepine. *Journal of Thermal Analysis and Calorimetry*. **111**, pp.1999–2004.

Luding, S. 2008. Constitutive relations for the shear band evolution in granular matter under large strain. *Particuology*. **6**, pp.501–505.

Mack, S., Langston, P., Webb, C. and York, T. 2011. Experimental validation of polyhedral discrete element model. *Powder Technology*. [Online]. **214**(3),pp.431–442.

Marigo, M., Davies, M., Leadbeater, T., Cairns, D.L., Ingram, A. and Stitt, E.H. 2013. Application of positron emission particle tracking (PEPT) to validate a discrete element method (DEM) model of granular flow and mixing in the Turbula mixer. *International Journal of Pharmaceutics*. **446**(1–2), pp.46–58.

Masuda, H., Higashitani, K. and Yoshida, H. 2006. Computer Simulation of Powder Flows *In*: *Powder Technology*. CRC Press, pp. 737–747.

Morgan, J.K. 2004. Particle Dynamics Simulations of Rate- and State-dependent Frictional Sliding of Granular Fault Gouge BT - Computational Earthquake Science

Part I *In*: A. Donnellan, P. Mora, M. Matsu'ura and X. Yin, eds. Basel: Birkhäuser Basel, pp. 1877–1891.

Morissette, S.L., Almarsson, ??rn, Peterson, M.L., Remenar, J.F., Read, M.J., Lemmo, A. V., Ellis, S., Cima, M.J. and Gardner, C.R. 2004. High-throughput crystallization: Polymorphs, salts, co-crystals and solvates of pharmaceutical solids. *Advanced Drug Delivery Reviews*. **56**(3), pp.275–300.

Neil, A.U. 1986. Particle Damage in Chemical Processing.

Neil, A.U. and Bridgwater, J. 1994. Attrition of particulate solids under shear. *Powder Technology*. **80**(3), pp.207–219.

Newitt, D.M. and Conway-Jones, J.M. 1958. A Contribution to the Theory and Practice of Granulation. *Transactions of Institute of Chemical Engineering*. **36**, pp.422–442.

Nye, B., Kulchitsky, A. and Johson, J. 2014. Intersecting Dilated Convex Polyhedra Method For Modeling Complex Particles In Discrete Element Method. *International Journal for Numerical and Analytical Methods in Geomechanics*. **38**, pp.978–990.

Olusanmi, D., Roberts, K.J., Ghadiri, M. and Ding, Y. 2011. The breakage behaviour of Aspirin under quasi-static indentation and single particle impact loading: Effect of crystallographic anisotropy. *International Journal of Pharmaceutics*. **411**(1–2), pp.49–63.

Olusanmi, D., Wang, C., Ghadiri, M., Ding, Y. and Roberts, K.J. 2010. Effect of temperature and humidity on the breakage behaviour of Aspirin and sucrose particles. *Powder Technology*. **201**(3), pp.248–252.

Otsuka, M., Matsumoto, T. and Kaneniwa, N. 1986. Effect of environmental temperature on polymorphic solid-state transformation of indomethacin during grinding. *Chemical & pharmaceutical bulletin*. **34**, pp.1784–1793.

Otsuka, M., Ofusa, T. and Matsuda, Y. 1999. Effect of environmental humidity on the transformation pathway of carbamazepine polymorphic modifications during grinding. *Colloids and Surfaces B: Biointerfaces*. **13**, pp.263–273.

Ouwerkerk, C.E.D. 1991. A micro-mechanical connection between the single-particle strength and the bulk strength of random packings of spherical particles. *Powder Technology*. **65**(1–3), pp.125–138.

Ozawa, T. 1965. A New Method of Analyzing Thermogravimetric Data. *Bulletin of the Chemical Society of Japan*. [Online]. **38**(11),pp.1881–1886.

Papadopoulus, D.G. 1998. Impact breakage of particulate solids.

Paramanathan, B.K. and Bridgwater, J. 1983. Attrition of Solids-I Cell Development. *Chemical Engineering Science*. **38**(2), pp.197–206.

Paramanathan, B.K. and Bridgwater, J. 1983. Attrition of solids—II : Material Behaviour and Kinetics of Attrition. *Chemical Engineering Science*. **38**(2), pp.207–224.

Pasha, M., Hare, C., Ghadiri, M., Gunadi, A. and Piccione, P.M. 2015. Effect of particle shape on flow in discrete element method simulation of a rotary batch seed coater. *Powder Technology*.

Perrenot, B. and Widmann, G. 1994. Polymorphism by differential scanning calorimetry. *Thermochimica Acta*. **234**(C), pp.31–39.

Porter, W.W., Elie, S.C. and Matzger, A.J. 2008. Polymorphism in carbamazepine cocrystals. *Crystal Growth and Design*. **8**(1), pp.14–16.

Post, R.M., Ketter, T.A., Uhde, T. and Ballenger, J.C. 2007. Thirty years of clinical experience with carbamazepine in the treatment of bipolar illness: Principles and practice. *CNS Drugs*. [Online]. **21**(1), pp.47–71.

Potapov, A. and Donohue, T. 2013. Computer Simulation of Coal Breakage in Conveyor Transfer Chutes with ROCKY Discreet Element Method Package.

Potapov, A. V. and Campbell, C.S. 1994. Computer simulation of impact-induced particle breakage. *Powder Technology*. **81**(3), pp.207–216.

Potyondy, D.O. and Cundall, P.A. 2004. A bonded-particle model for rock. *International Journal of Rock Mechanics and Mining Sciences*. **41**(8 SPEC.ISS.), pp.1329–1364.

Pratt, P.L. 1953. Cleavage deformation in zinc and sodium chloride. *Acta Metallurgica*.

Raman, C. V. and Krishnan, K.S. 1928. A New Type of Secondary Radiation. *Nature*. **121**(3048), pp.501–502.

Rauber, G. 2018. Examination of stress-induced transformations within multicomponent pharmaceutical crystals.

Remy, B., Khinast, J.G. and Glasser, B.J. 2009. Discrete Element Simulation of Free Flowing Grains in a Four-Bladed Mixer. . **55**(8), pp.2035–2048.

Remy, B., Khinast, J.G. and Glasser, B.J. 2011. Polydisperse granular flows in a bladed mixer : Experiments and simulations of cohesionless spheres. *Chemical Engineering Science*. [Online]. **66**(9), pp.1811–1824.

Remy, B., Kightlinger, W., Saurer, E.M., Domagalski, N. and Glasser, B.J. 2015. Scale-up of agitated drying: Effect of shear stress and hydrostatic pressure on active pharmaceutical ingredient powder properties. *AIChE Journal*. **61**(2), pp.407–418.

Rowe, R. 2006. *Handbook of pharmaceutical excipients*. London Greyslake, IL Washington, DC: Pharmaceutical Press American Pharmacists Association.

Rustichelli, C., Gamberini, G., Ferioli, V., Gamberini, M.C., Ficarra, R. and Tommasini, S. 2000. Solid-state study of polymorphic drugs: Carbamazepine. *Journal of*

Pharmaceutical and Biomedical Analysis. **23**, pp.41–54.

Saifoori, S. 2018. Impact Breakage of Acicular Particles in Morphologi G3.

Schuhmann, R. 1940. Principles of comminution, I. Size Distribution and Surface Calculation. *The American Institute of Mining, Metallurgical, and Petroleum Engineers (AIME) Technical Publication 1189*.

Seville, J.P.K., Ingram, A. and Parker, D.J. 2005. Probing Processes Using Positrons. *Chemical Engineering Research and Design*. **83**(7), pp.788–793.

Shi, F. and Kojovic, T. 2007. Validation of a model for impact breakage incorporating particle size effect. *International Journal of Mineral Processing*. **82**(3), pp.156–163.

Sinnott, M.D. and Cleary, P.W. 2015. Simulation of particle flows and breakage in crushers using DEM: Part 2 - Impact crushers. *Minerals Engineering*. **74**, pp.163–177.

Tardos, G.I., Mcnamara, S. and Talu, I. 2003. Slow and intermediate flow of a frictional bulk powder in the Couette geometry. . **131**, pp.23–39.

Tavares, L.M. 2017. A review of advanced ball mill modelling. *KONA Powder and Particle Journal*. **2017**(34), pp.106–124.

Tavares, L.M. 2007. Chapter 1 Breakage of Single Particles: Quasi-Static. *Handbook of Powder Technology*. **12**(21), pp.3–68.

Tavares, L.M. and de Carvalho, R.M. 2009. Modeling breakage rates of coarse particles in ball mills. *Minerals Engineering*. [Online]. **22**(7–8), pp.650–659.

Thielmann, F. 2004. Introduction into the characterisation of porous materials by inverse gas chromatography. *Journal of Chromatography A*. **1037**(1–2), pp.115–123.

Vogel, L. and Peukert, W. 2003. Breakage behaviour of different materials - Construction

of a mastercurve for the breakage probability. *Powder Technology*. **129**(1–3), pp.101–110.

Vollenbroek, J., Hebbink, G.A., Ziffels, S. and Steckel, H. 2010. Determination of low levels of amorphous content in inhalation grade lactose by moisture sorption isotherms. *International Journal of Pharmaceutics*. **395**(1–2), pp.62–70.

Walker, D.M. 1967. A Basis for Bunker Design. *Powder Technology*. **1**, pp.228–236.

Walton, O.R. and Braun, R.L. 2002. Viscosity, granular-temperature, and stress calculations for shearing assemblies of inelastic, frictional disks. *Journal of Rheology*. **30**(5), pp.949–980.

Wang, L., Park, J.Y. and Fu, Y. 2007. Representation of real particles for DEM simulation using X-ray tomography. *Construction and Building Materials*. **21**(2), pp.338–346.

Weibull, W. 1951. A statistical distribution function of wide applicability. *Journal of applied mechanics*. **18**, pp.293–297.

Willart, J.-F., Lefebvre, J., Danède, F., Comini, S., Looten, P. and Descamps, M. 2005. Polymorphic transformation of the Γ-form of d-sorbitol upon milling: structural and nanostructural analyses. *Solid State Communications*. **135**(8), pp.519–524.

Willart, J.F., Caron, V. and Descamps, M. 2007. Transformations of crystalline sugars upon milling. *Journal of Thermal Analysis and Calorimetry*. **90**, pp.125–130.

Willart, J.F., Dujardin, N., Dudognon, E., Danède, F. and Descamps, M. 2010. Amorphization of sugar hydrates upon milling. *Carbohydrate Research*. **345**(11), pp.1613–1616.

Willart, J.F., De Gusseme, a., Hemon, S., Odou, G., Danede, F. and Descamps, M. 2001. Direct crystal to glass transformation of trehalose induced by ball milling. *Solid State Communications*. **119**(8–9), pp.501–505.

Yang, Z., Fryer, P.J., Bakalis, S., Fan, X., Parker, D.J. and Seville, J.P.K. 2007. An improved algorithm for tracking multiple, freely moving particles in a Positron Emission Particle Tracking system. *Nuclear Instruments and Methods in Physics Research, Section A: Accelerators, Spectrometers, Detectors and Associated Equipment*. **577**(3), pp.585–594.

Yang, Z., Parker, D.J., Fryer, P.J., Bakalis, S. and Fan, X. 2006. Multiple-particle tracking-an improvement for positron particle tracking. *Nuclear Instruments and Methods in Physics Research, Section A: Accelerators, Spectrometers, Detectors and Associated Equipment*. **564**(1), pp.332–338.

Yoshihashi, Y., Yonemochi, E. and Terada, K. 2002. Estimation of initial dissolution rate of drug substance by thermal analysis: Application for carbamazepine hydrate. *Pharmaceutical Development and Technology*. **7**(1), pp.89–95.

Yu, L. and Ng, K. 2002. Glycine crystallization during spray drying: The pH Effect on Salt and Polymorphic Forms. *Journal of Pharmaceutical Sciences*. **91**(11), pp.2367–2375.

Yuregir, K.R., Ghadiri, M. and Clift, R. 1986. Observations on impact attrition of granular solids. *Powder Technology*. **49**(1), pp.53–57.

Zhu, H.P., Zhou, Z.Y., Yang, R.Y. and Yu, A.B. 2007. Discrete particle simulation of particulate systems: Theoretical developments. *Chemical Engineering Science*. **62**(13), pp.3378–3396.